NATIONAL TECHNICAL UNIVERSITY OF ATHENS

SCHOOL OF NAVAL ARCHITECTURE AND MARINE ENGINEERING

DIPLOMA THESIS

CORROSION SUSCEPTIBILITY OF AH36 AND S690 STEEL WELDMENTS

KRINIS IASONAS

Supervisor: Professor N. Tsouvalis

Examination Committee:

Prof. N. Tsouvalis, School of Naval Architecture and Marine Engineering

Prof. M. Samuelides, School of Naval Architecture and Marine Engineering

Assist. Prof A. Karantonis, School of Chemical Engineering

OCTOBER 2020

INTRODUCTION

One of the most challenging topics of the research in the marine field, in the last years, is the reduction of the weight which affects the fuel consumption and the payload capacity of the ship. The use of high-performance steels called HSLA (High Strength Low Alloy) steel aims at this topic. S690 HSLA steel provides strength, toughness, formability, weldability with high yielding point and better fatigue performance.

However, the application of this steel needs to be studied concerning several issues i.e. fatigue performance and corrosion behaviour, in comparison with conventional steel AH36.

The present thesis studies the corrosion behaviour of HSLA S690 structural steel and its weldment with conventional steel S690-AH36 and compare them with conventional parent metal AH36 and weldment AH36-AH36.

The steel specimens were provided by FINCANTIERI shipbuilding company, where the weldments were also performed, in the frame of RAMSSES EU funded project. Shipbuilding Technology Laboratory participates in this project as partner.

Electrochemical techniques were employed, applying DC and AC perturbation techniques, accompanied by study of the microstructure and micro-hardness. In particular Linear Polarization, Potentiodynamic polarization, Cyclic polarization and Electrochemical Impedance Spectroscopy. The experiments were performed mainly in simulated marine environment 3.5% NaCl. All the experiments were performed in the Shipbuilding Technology Laboratory, employing the relevant infrastructure, FRA, Potentiostat, Optical Microscope and Scanning Electron Microscope.

The present thesis consists of two main parts. The first part is the theoretical part, where the general characteristics of High Strength and HSLA steels, the properties and microstructure of welds, the corrosion of welds and generally the corrosion mechanism are presented, along with the fundamentals of the electrochemical techniques. The second part is the experimental part, where all the microstructure and electrochemical results are presented, along with detailed analysis of the results and relevant conclusions. Finally, in the appendix, the reader may find all the experimental results of the study.

ABSTRACT

The aim of the present thesis is to study the corrosion behaviour of HSLA S690 structural steel and its weldment with conventional steel S690-AH36 and compare them with conventional parent metal AH36 and weldment AH36-AH36. This study investigates the corrosion performance of this steel as an alternative of conventional steel AH36 for specific applications on the ship.

To this purpose, Electrochemical techniques were employed, applying DC and AC techniques, accompanied by study of the microstructure and micro-hardness. In particular Linear Polarization, Potentiodynamic polarization, Cyclic polarization and Electrochemical Impedance Spectroscopy. electrochemical techniques were accompanied by the study of the micro-structure in order to arrive into sound conclusions.

The experiments performed showed that **mechanism of corrosion**, is well described by an increase of current density with increasing potential in the anodic region, indicating active corrosion behavior without passivation. Both parent metals and welds present similar anodic dissolution determined by charge transfer (activation polarization) for long ranges of potential (CP) and long times of EIS experiment (8 hours) until the formation of oxide film that limits the dissolution. The cathodic polarization in determined by O_2 diffusion, meaning that the phenomenon is controlled by activation polarization, close to equilibrium and consequently by concentration polarization further than equilibrium. S690, and its weld AH36-S690 present faster transition from equilibrium to concentration polarization.

The **corrosion parameters obtained** prove no significant difference of S690 in comparison with AH36. The last one present slightly higher corrosion resistant. This can be attributed to the harder microstructure of S690, consisting of tempered martensite and bainite, along with ferrite. The Icorr values are similar for the parent metals and the welds and only AH36-AH36 weld presents higher corrosion susceptibility in Linear Polarization. Only in EIS technique S690 appears as the most corrosion resistant material. This difference can be explained by the difference of the perturbation applied on the specimen.

The aforementioned results prove that concerning the corrosion performance S690 can be introduced as an alternate material for specific spots in the ship. Whereas, it is useful to study the corrosion in combination with fatigue performance.

ΠΕΡΙΛΗΨΗ

Ο σκοπός της παρούσας διπλωματικής είναι η μελέτης της συμπεριφοράς απέναντι σε διάβρωση του χάλυβα υψηλής αντοχής και χαμηλής κραμάτωσης S690 και της συγκόλλησής του με το συμβατικό χάλυβα S690-AH36, καθώς και η σύγκρισή της συμπεριφοράς αυτής με αυτή του συμβατικού μετάλλου βάσης AH36 και της ομογενούς συγκόλλησής του AH36-AH36. Η μελέτη αυτή διερευνά την απόδοση του χάλυβα αυτού σε διάβρωση, ως μια εναλλακτική του συμβατικού χάλυβα AH36 για συγκεκριμένες εφαρμογές στο πλοίο.

Για το σκοπό αυτό, εφαρμόστηκαν ορισμένες ηλεκτροχημικές τεχνικές, με την εφαρμογή είτε σταθερού είτε εναλλασσόμενου ρεύματος, συνοδευόμενες από μελέτη ττης μικροδομής και της μικροσκληρότητας. Συγκεκριμένα, εφαρμόστηκαν οι τεχνικές της Γραμμικής Πόλωσης, της Ποτενσιοδυναμικής Πόλωσης, της Φασματοσκοπίας Ηλεκτροχημικής Εμπέδησης και της Κυκλικής Πόλωσης σε συνδυασμό με τη μελέτη της μικροδομής για την επίτευξη αξιόπιστων αποτελεσμάτων.

Τα πειράματα που διεξήχθησαν έδειξαν ότι ο μηχανισμός της διάβρωσης περιγράφεται από αύξηση της πυκνότητας ρεύματος με αύξηση του δυναμικού στην ανοδική περιοχή, υποδεικνύοντας έτσι ενεργή συμπεριφορά διάβρωσης χωρίς παθητικοποίηση. Τόσο τα μέταλλα βάσης όσο και οι συγκολλήσεις παρουσιάζουν παρόμοια ανοδική διάλυση η οποία καθορίζεται από μεταφορά φορτίου (πόλωση ενεργοποίησης) για μεγάλα εύρη δυναμικού (CP) και χρόνου στα πειράματα της εμπέδησης (8 ώρες) έως τη δημιουργία ενός στρώματος οξειδίων στην επιφάνειά τους, που εμποδίζει την περεταίρω διάλυση. Η καθοδική πόλωση καθορίζεται από διάχυση οξυγόνου, που σημαίνει ότι το φαινόμενο ελέγχεται από πόλωση ενεργοποίησης κοντά στο δυναμικό ισορροπίας και από πόλωση συγκέντρωσης πιο μακριά από αυτό. Ο S690 και η συγκόλληση AH36-S690 παρουσιάζουν πιο γρήγορη μετάβαση από την κατάσταση ισορροπίας στην πόλωση συγκέντρωσης.

Οι παράμετροι της διάβρωσης που εξήχθησαν από τα πειράματα αποδεικνύουν ότι δεν υπάρχει ουσιαστική διαφορά του S690 σε σύγκριση με τον AH36. Ο τελευταίος παρουσιάζει ελαφρώς υψηλότερη αντίσταση σε διάβρωση. Αυτό μπορεί να αποδοθεί στη σκληρότερη μικροδομή του S690, η οποία αποτελείται από μαρτενσίτη από επαναφορά, μπαινίτη και φερρίτη. Οι τιμές του Icorr είναι πταρόποιες για τα μέταλλα βάσης και τις συγκολλήσεις και μόνο η συγκόλληση AH36-AH36 παρουσιάζει μεγαλύτερη επιδεκτικότητα σε διάβρωση στην μέθοδο με Γραμμική πόλωση. Μόνο στη μέθοδο της εμπέδησης (EIS) ο S690 παρουσιάζει καλύτερη συμπεριφορά σε διάβρωση. Η διαφορά αυτή μπορεί να εξηγηθεί από τη διαφορά στη διακύμανση που εφαρμόζεται στο υλικό.

Τα αποτελέσματα αυτά δείχνουν ότι, όσον αφορά τη συμπεριφορά σε διάβρωση, ο S690 μπορεί να χρησιμοποιηθεί ως εναλλακτικό υλικό σε συγκεκριμένα μέρη του πλοίου. Ωστόσο, είναι χρήσιμο να μελετηθεί η διάβρωση σε συνδυασμό με τη συμπεριφορά σε κόπωση.

ACKNOWLEDGEMENTS

I want to express my gratitude towards my supervisor Prof. Nicholas Tsouvalis for assigning this thesis to me, guiding me throughout my studies and helping me whenever needed.

I would also like to thank Prof. Antonis Karantonis for his valuable advice on the electrochemical techniques, which were essential for the purposes of this study.

I want to express my gratitude to Mrs. Theodora Tsiourva, for presenting the idea of my thesis, for guiding and helping me in all stages of its implementation, and for all the bibliography and the scientific knowledge she provided (especially in Electrochemistry). Most importantly I consider Mrs. Theodora Tsiourva to be a great person of good quality and thus I am glad she supervised my work.

I also want to thank my fellow colleague Alexandros Ziakas, for an excellent collaboration which started and evolved during the experiments inside the laboratory and which became a true friendship outside of it.

I would like to thank my parents and my brother, Philippos, for encouraging me throughout my studies and for giving me the strength to keep going. They believed in me even when I didn’t. I wouldn’t have achieved anything without them.

A. THEORITICAL PART

1. HIGH STRENGTH AND HSLA STEELS

1.1. Introduction

The modern maritime industry shows strong demand for steel grades with improved structural performance and better resistance to fatigue damage initiation and evolution. Improved structural performance permits the use of plates with lower thicknesses, thus, resulting in significant savings in fuel consumption and engine requirements. High-Strength Low-Alloy steel grades exhibit a favorable strength-to-weight ratio when compared with conventional maritime steel grades, such as the AH36 High-Strength (HS) steel grade. HSLA steels have been extensively used in various offshore oil and gas applications, including pipelines. Recent developments in maritime transport policies and regulations have incited a constantly growing interest in HSLA steel grades in the shipbuilding industry.

The hull is the most important structural part of the ship. It is continuously subjected to cyclic loading caused by waves, cargo loading and unloading and engine vibration. Hull fatigue is mainly attributed to high loading cycles included by the ship's motion travelling through waves. Also, it is always exposed to highly corrosive conditions. Therefore, certain grades of steel must be used in order to withstand all those loadings and at the same time to offer good level of ductility, strength and of course, to be economically viable. That's the reason why AH36 is widely used for hull construction. On the other hand, S690 steel offers a very higher yield and tensile strength, good weldability and hardenability. However, it lacks the necessary ductility according to standards and is way too expensive to be used for hull construction, although it is suitable for the construction of other parts of the ship, with higher demands for fatigue (e.g. stiffeners). The characteristics of both the HS and HSLA steels are presented below in this chapter, along with the examples of AH36 and S690 steels.

1.2. General characteristics of High Strength Steels [20][27][56]

High Strength (HS) steel present higher yield and tensile strength than common carbon steel. It is mainly used in order to either increase the payload on an existing structure or to make the whole structure lighter. Also, it can be used to increase the safety margin to overloading. HS steel is preferred to common carbon steel due to its better behavior against buckling and fatigue.

These types of steel must be characterized by high hardenability, ductility in order to avoid brittle fractures, good weldability and of course, high strength. However, it is usually difficult to achieve the combination of all those factors because the improvement of one of them is accompanied by the reduction of another. For example, an increase of carbon will improve the material's strength but it will also reduce its weldability. Thus, there is a wide variety of High Strength steels where each one is characterized by some of these properties, depending the necessities of its use.

According to European standards, HS steels can be manufactured in two ways. The first way is through quenching and tempering, where the minimum yield strength is approximately 1100 MPa, whereas the second way is through thermo-mechanical controlled practice (TMCP), where the minimum yield strength is almost 500 MPa and offers high weldability.

Finally, prior to the weldment of these steels, pre-heating treatment at about 100-120$°C$ and after the weldment, post-weld treatment are required in order to avoid unwanted consequences, such as residual stresses, hydrogen embrittlement and many others.

1.2.1. AH36 steel [14][20][37][56][70]

High strength steel AH36 is widely used in shipbuilding industry and it consists of alternate bands of ferrite and pearlite, as shown in Fig.[1.1] Its main characteristic is that it can be killed or semi-killed, which means that the steel undergoes deoxidation before casting, in order to eliminate porosity. Ferritic micro-structure, which appears in the bright-color areas, covers larger area as expected due to the chemical composition of steel (0.18%). The grains of both the ferrite and the pearlite have intense orientation, which is caused by the production procedure (rolling) of the steel foil. The grain orientation is perpendicular to the direction of the load. The percentage is about 75% ferritic structure and 25% pearlitic structure.

An important characteristic of AH36 is that it can be killed or semi-killed as a steel. Killed steel is a steel that has been completely deoxidized by the addition of an agent before casting such that there is practically no evolution of gas during solidification. It is characterized by a high degree of chemical homogeneity and freedom from gas porosities and it's a method that is mostly used for thicknesses lower than 12.5mm. Semi-killed steel is mostly deoxidized steel, but the carbon monoxide leaves blowhole type porosity distributed throughout the ingot. The porosity increases the yield strength to approximately 90% by weight. Semi-killed steel is commonly used for structural steel with a carbon content between 0.15 and 0.25% carbon, because it is rolled, which closes the porosity and it's a method that is mostly used for bigger thicknesses. Its chemical composition and mechanical properties are presented in Ch.5, Experimental Procedure, according to ASTM-A131M standard and manufacturers' manuals, along with the chemical composition of the specific specimens via X-Ray Fluorescence (XRF) method.

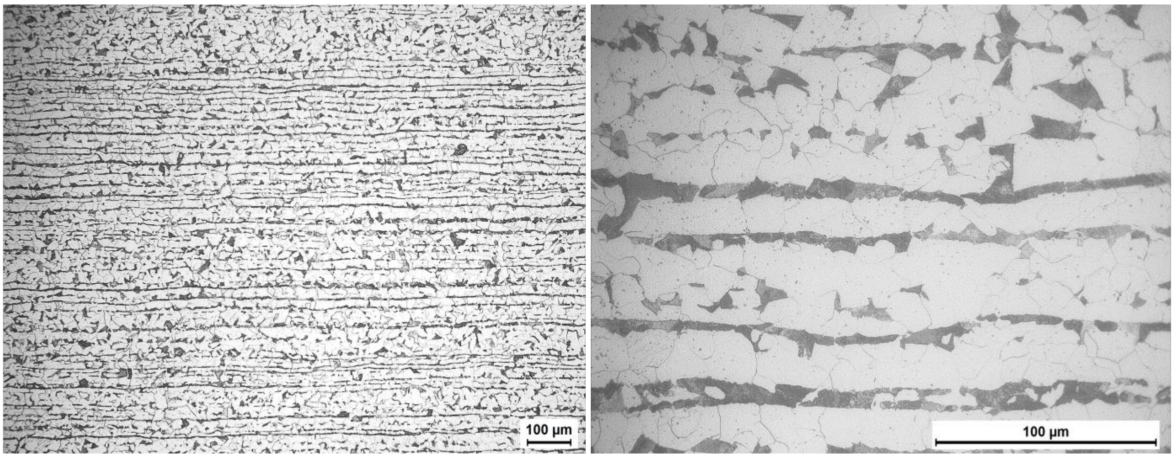

(a) (b)

Fig.[1.1] The ferritic- pearlitic microstructure of AH36 (a) x10, (b) x50.

Since AH36 consists of alternate bands of ferrite and pearlite, we conclude that the solidification rates are significantly low, Fig.[1.2], where, during its transition from the austenitic state, more time passes and its temperature decreases slower.

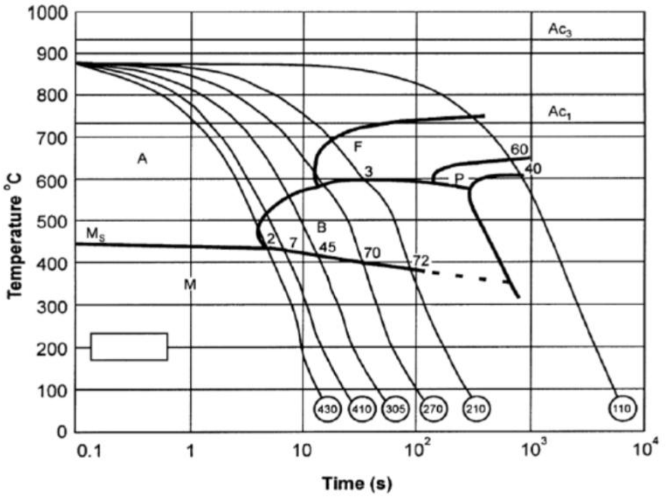

Fig.[1.2] CCT diagram of AH36.[37]

1.3. General characteristics of HSLA Steels [16][26][43][59]

High-strength low-alloy (HSLA) steels, or micro-alloyed steels, are important structural materials and contain small amounts of alloying elements, which enhance the strength through the formation of stable carbides, nitrides and carbonitrides and have effect on hardenability. Yield strength increments of two or even three times than that of plain carbon-manganese steel. They are aimed to provide better mechanical properties and greater resistance to atmospheric corrosion than conventional carbon steels and they are designed to meet specific mechanical properties, such as a yield strength greater than 275 MPa, rather than to obtain a specific chemical composition. The chemical composition of a specific HSLA steel may vary for different product thicknesses to meet mechanical property requirements.

Some factors that led to the initial development of micro-alloyed steels were:

- materials cost savings could be obtained directly by the application of HSLA steels due to savings in material, transport, handling and even welding procedures;
- in-service benefits could be obtained in the development of lighter structures;
- higher strength and improved fracture properties, such as crack arrest, could be obtained by using alloy elements;
- better weldability and weldment toughness due to lower carbon;

The HSLA steels used nowadays are obtained by means of a suitable combination of chemical composition and thermo-mechanical treatment parameters, such as hot rolling process, with the aim to achieve the proper balance between strength, toughness, ductility, formability and weldability. Their desirable properties are achieved basically through ferrite grain refinement and by the precipitation of micro-alloyed carbonitride particles. Prior to their use, they are subjected to heating and then accelerated cooling, as shown in Fig.[1.3], in order to obtain high strength and hardenability. Some alloy elements, such as Mo, Ni, Cr and Mn also contribute in the improvement of hardenability whereas, other alloy elements, such as Nb, Ti and V contribute in achieving a more fine-grained structure.

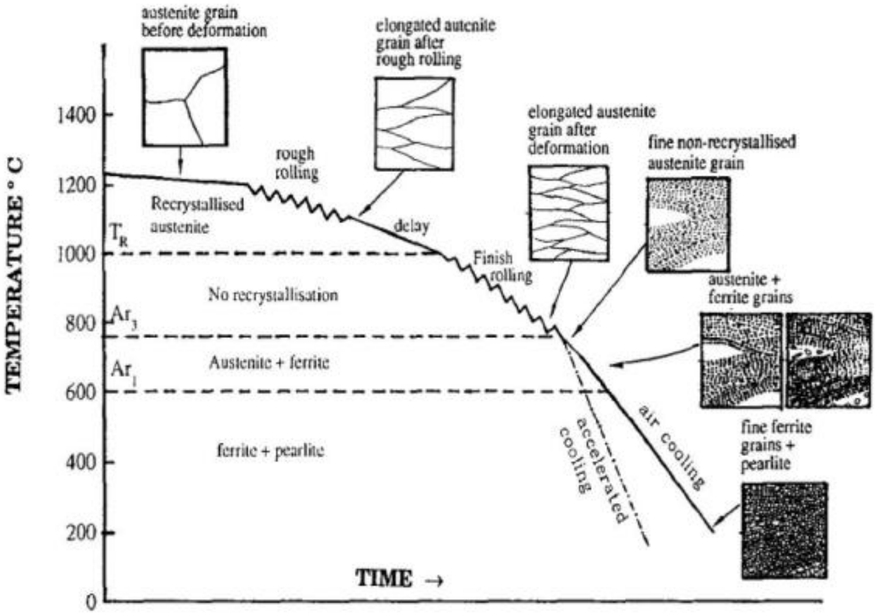

Fig.[1.3] Schematic diagram of the influence of accelerated cooling on the microstructure of HSLA steel.[16]

1.3.1. S690 steel [37][51][56][65]

S690 steel is a High Strength Low Alloy steel (HSLA) which is widely used in civil engineering constructions i.e. bridges, cranes, etc. Even though, it combines a very high yield strength with small weight and good weldability, its high cost and low ductility make it not suitable for hull construction, although it can be used for the construction of other parts of the ship, such as stiffeners or other areas with high fatigue strain. During the production of S690, thermo mechanical rolling is applied together with accelerated cooling and tempering. So, the microstructure of the parent steel S690 consists of a homogeneous mixture of tempered martensite and bainite, along with ferrite. The volume fraction of tempered martensite (bright-color areas) is usually higher than the one of bainite, Fig.[1.4]. Also, in contrast with AH36, grain orientation does not appear in S690, as a result of the thermo mechanical treatment.

Its complete name is S690QL where, S stands for Structural steel, 690 indicates the minimum yield strength which is 690 MPa, Q stands for Quenched, which means that the steel has been subjected to accelerated cooling and L indicates that the average strength values have been measured in Low temperatures, approximately at -40°C. Its chemical composition and mechanical properties are presented in Ch.5, Experimental Procedure, according to EN10025-6 standard and manufacturers' manuals, along with our own chemical composition measurements via XRF.

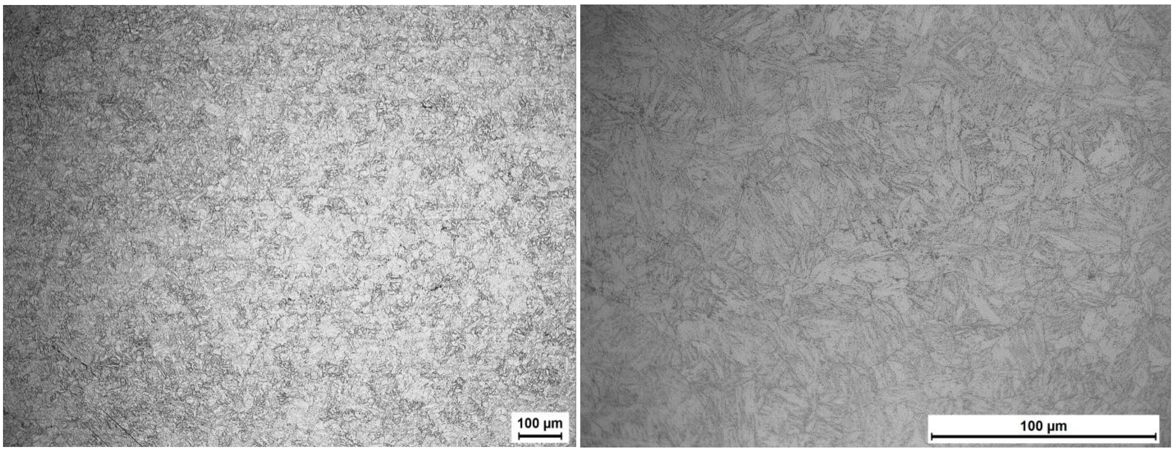

(a) (b)

Fig.[1.4] The ferritic, bainitic and martensitic microstructure of S690 (a) x10, (b) x50.

Since S690 contains bainitic and martensitic phases, we conclude that the solidification rates are much bigger than AH36, Fig.[1.5], where, during its transition from the austenitic state, less time passes and its temperature decreases significantly faster.

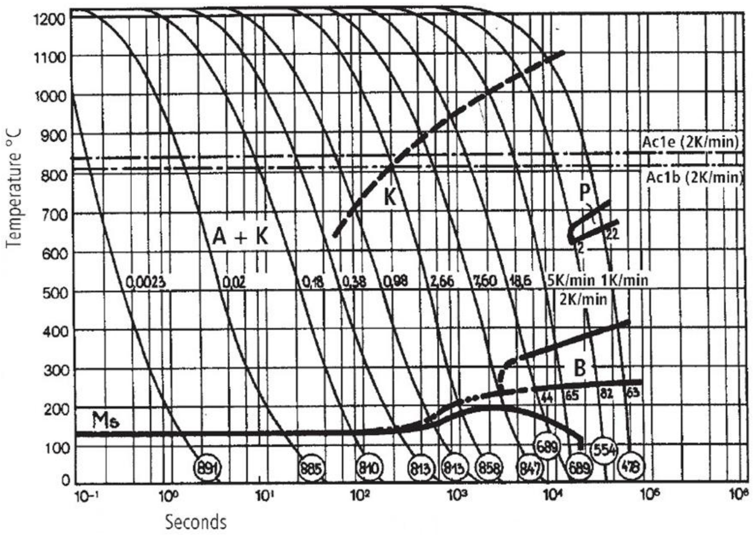

Fig.[1.5] CCT diagram of S690.[37]

1.4. Impact of alloy elements [13][20][30][38][62]

Carbon (C)

It is the basic alloy element for steel. Along with the increase of carbon amount, the hardness and resistance increase substantially. However, the tensile strength and yield point increase up to 0,8% carbon. The fragility increases above this value and the hardness does not increase more at the end of heat treatment due to residual austenite. The carbon amount of steels adversely affects the properties such as ductility, forgeability and weldability. There is a high cracking risk in the heat treatment of high carbon steels. Also, by increasing the amount of carbon we can achieve:

- Reduction of the grain size and thus, enhancement of the intergranular formation.
- More fine-grained ferritic regions in the boundary of the austenitic grains.
- High levels of ferrite lead to the formation of ferrite Widmanstatten.

Manganese (Mn)

Manganese is a deoxidizer and a degasifier and is typically used in combination with sulfur and phosphorus. Manganese helps to reduce brittleness and improves forgeability, tensile strength and resistance to wear. Manganese reacts with sulphur, resulting in manganese sulfides which prevents the formation of iron sulfides and enhance the forgeablity and weldability of the steel. Manganese is also added for better hardenability as it leads to slower quenching rates in hardening techniques. Excess oxygen can be removed in molten steel by using manganese. Manganese contributes to the formation of acicular ferrite (AF). AF is presented when Mn is approximately 1%, whereas, when the percentage is increased to 1.4-1.8% then, higher fragility occurs. Higher percentages lead to the formation of bainite and decrease of fragility. As the amount of Mn increases, the material strength and toughness increase (highest values at 1.4% Mn).

Silicon (Si)

Like manganese, silicon has also deoxidizing properties. It is always used in amounts lower than 0.5% because it causes unwanted results during welding and because, an even bigger increase of Si leads to the reduction of the yield strength. It increases the resistance and hardenability of material without decreasing its ductility and toughness since it is dissolved in the ferrite. The heat resistance of steels containing high silicon is also high. In general, it adversely affects the surface quality while it increases the hardenability, abrasion resistance and elasticity. The grain size of steel increases as the silicon amount increases.

Nickel (Ni)

Nickel increases strength, impact toughness and hardness without sacrificing ductility and toughness. It also increases resistance to corrosion and scaling at elevated temperatures when introduced in suitable quantities in high-chromium (stainless) steels, resulting in an even higher hardness. Austenitic stainless steels are most known for their high content in nickel and chromium.

Chromium (Cr)

Chromium is one of the most popular alloying metals for steel due to its high hardness and corrosion resistance. Higher chromium contents of 4 to up to 18% result in better corrosion resistance. In case the Cr is added at values up to 25%, it creates an oxide layer on the material surface and thus, ensures resistance to corrosion and adds a bright appearance to materials. It increases the tensile strength and heat resistance. It can lead to tempering brittle or decrease the ductility. It is mainly used with Ni and Mo with the aim of decreasing these impacts. The amount of Cr depends on the amount of Mn. As the Mn increases, the Cr must be reduced because, otherwise, bainite is formed against acicular ferrite.

Molybdenum (Mo)

Molybdenum increases strength, hardness, hardenability, and toughness, as well as creep resistance and strength at elevated temperatures. It improves machinability and resistance to corrosion and it intensifies the effects of other alloying elements. At amounts equal to 0.2-0.3%, Mo contributes to the formation of acicular ferrite, whereas, at higher percentages, it increases the formation of bainite and at the percentage of 0.5%, Mo completely eliminates acicular ferrite. A combination of molybdenum and titanium contributes significantly in the formation of acicular ferrite.

Titanium (Ti)

Titanium is used as a stabilizing element in stainless steels. It fixes carbon in inert particles, improving corrosion resistance and weldability. It has a grain refining impact. Small amounts of titanium in addition the existence of C-Mn contributes to the formation of acicular ferrite. Also, the addition of Ti increases the toughness but, it slightly decreases the ductility at the same time. Since Titanium is a rare element on Earth, this alloying element can be up to 200 times more expensive than regular carbon steel.

Boron (B)

As an alloying element, even small amounts of boron (0.001–0.003 %) can greatly increase hardenability. However, boron-steel is not easy to find as it only makes up to 0.003% of the alloy steels. It increases the hardenability of low and medium carbon steels in the most effective way. Also, in low-alloyed steels, the existence of boron nitride suspends the separation in the boundaries of the ferrite grains.

Aluminum (Al)

It is one of the most powerful deoxidizers. It reduces the grain coarsening and ageing in the heating. It has a property of grain refining. In low percentages of aluminum, the microstructure consists mostly of ferrite and acicular ferrite whereas, in higher percentages, the microstructure consists of upper bainite, which has negative effects on the hardness of the material.

Oxygen (O)

Oxygen affects the entire microstructure of the material, from small concentrations which lead to bainitic formation, to high concentrations, which lead to Widmanstatten ferrite. Generally, the optimum concentration of oxygen is 0.03-0.06% and for the HSLA steels, concentrations between 0.02 and 0.035% lead to the formation of acicular ferrite and present the best mechanical properties of the material.

Nitrogen (N)

Nitrogen has the ability to increase the hardness of the material like carbon but, it doesn't affect the microstructure that much. The amount of N must always be lower than 0.007%, depending on the amounts of Al and Ti. Although it increases the mechanical and corrosion resistance, it causes ageing.

Vanadium (V)

The vanadium like nickel is a significant grain reduced for steels. Even when it is used at an amount of 0,1%, it substantially prevents the grain coarsening during process. The vanadium increases its heat resistance as well as hardness depth. It ensures the increase of impact strength specifically at cutting parts and thus, it is effective in maintaining the forms of cutting edges for a long period.

Niobium (Nb)

Niobium has a grain refining impact it can increase the yield strength. It also increases the hardness thanks to its powerful carbide increasing property. However, both Nb and V can cause problems with hardness. Small amounts of Nb (<0.02%) and V (<0.05%) don't affect hardness, depending the concentration of Mn and the cooling rate.

Sulfur (S)

Sulfur is an undesired element and it is always tried to be decreased. As the sulfur amount increases, its ductility and impact strength decrease perpendicular to forming. When it is not balanced with manganese, it makes fragility at heat. Its weldability and hardenability get worse. The combination of O and S causes inclusions inside the material, whereas, the increase of S limits the formation of acicular ferrite and thus, it reduces the material's hardness and toughness.

Phosphorus (P)

It is an element which has a hazardous impact such as decreasing the material toughness. While it increases the steel resistance and hardenability, it decreases the ductility and impact strength. This impact is more clearly seen in high carbon steels. While it enhances the corrosion resistance of steel, it is tried to be kept as low as possible and the fewness of phosphor along with sulfur is the first criterion in terms of material quality.

Wolfram (W)

Wolfram is an alloy element which increases the resistance of steel. It increases strength, wear resistance, hardness and toughness. Also, wolfram steels have superior hot-working and greater cutting efficiency at elevated temperatures. Therefore, it is used as alloy element specifically in the high-speed steels, tool steels and heat treatable steels.

1.5. Comparison of AH36 and S690 properties [20][27]

In 2012, a research was conducted with the collaboration of two universities, the National Technical University of Athens and the University of Birmingham, and two organizations, AIMEN and Lloyd's Register, in order to compare these two materials and examine the possibility of the replacement of AH36 by S690 in maritime industry, in the framework of a European funded research project MOSAIC. The result of those experiments are presented below:

- The tensile test indicated that AH36 has an upper yield strength equal to 393 MPa and an upper tensile strength equal to 524 MPa, which are significantly lower values than those of S690.
- The Charpy impact tests confirmed that all these types of steel are in the upper region of the DBTT (Ductile Brittle Transition Temperature) curve at -20°C. It was observed that S690 had an increased ability for absorption of impact energy in comparison to AH36.
- The structure toughness test indicated that S690 presents values up to three times higher than those of AH36.
- The structure toughness test also concluded that it is difficult to predict precisely the factor K_{IC}, which is used in fracture mechanics to predict the stress state near the tip of a crack or notch, caused by a remote load or residual stresses.
- The experimental fatigue tests for crack propagation speed showed that S690 presents significantly higher crack resistance propagation than AH36. However, the values of critical elongation of S690 are below the necessary limits, in order to be used in certain segments in maritime industry, such as the ship's hull.
- The optical observation of the microstructure of AH36 showed that it contains high percentages of pearlite, whereas, S690 is proved to be a steel which was subjected to quenching and tempering.

2. WELDMENTS

2.1. Introduction

Welding is one of the most widely used hot-work processes used in the shipbuilding industry. The development in welding technology has enabled the industry to produce perfectly watertight and oil-tight joints. Welded joints as compared to riveted joints are much easier to produce and they reduce the cycle time of the project. Welded joints have also resulted in reduced steel weight and require less to negligible maintenance compared to rivet joints. The major contribution of welding technology to the shipbuilding industry is the possibility of producing smooth hull surfaces, therefore reducing the bare hull resistance and power requirements considerably. For these reasons, it is essential to perform a detailed study, in order to avoid undesirable effects during weldment, such as the effect of corrosion, which is the main aspect of this study.

In the following paragraphs, the microstructure of the weldments is presented, along with the major welding techniques in the maritime industry and the basic types of joints. The Flux Cored Arc Welding (FCAW) method is presented in a separate subchapter, since it is the technique used for the welding of the materials in this study and thus, needs to be thoroughly mentioned. Finally, the most common potential failures and the mechanical properties of the weldments are presented.

2.2. Microstructure of weldments [3][47][49]

Welding is a metal joining process where fusing is produced by heating up to proper temperature with or without filler metal. The heating and the consequent cooling of the fusion welds cause metallurgical transformations, owing to the distinct microstructures. This welding procedure generates a sequence of microstructures ranging from the unaffected base metal, to the weld metal. In the case of fusion welding, in literature, usually four distinct regions are identified: the melted zone, the partially melted zone, the heat affected zone and the base metal. This micro-structural transition is illustrated in Fig.[2.1]. Four zones are usually present in any given weld.

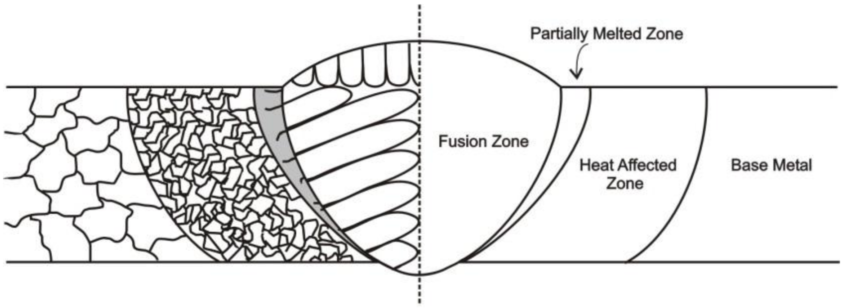

Fig.[2.1] The different zones present in a fusion weld. [47]

2.2.1. Fusion Zone

The Weld Metal (WM) is the central zone of a weldment and is delimited by the boundaries of the Partially Melted Zone (PMZ). It is the result of melting or fusion, that's why we often use the term Melted Zone (MZ) or Fusion Zone (FZ). It consists of small-sized and highly-orientated dendrites, which form due to rapid solidification from the liquid phase. The solidification rates that are developed are high, similar to the welding rates (up to a few mm/s). The orientation of the dendrites follows the direction of the isothermal curves.

The FZ is the result of melting, which fuses the base metal and the filler metal to produce a zone with a composition that is most often, different from that of the base metal. This compositional difference produces a galvanic couple, which can influence the corrosion process in the vicinity of the weld. This dissimilar-metal couple could produce macroscopic galvanic corrosion. The melted zone itself offers a microscopic galvanic effect due to micro-structural segregation resulting from solidification.

2.2.2. Partially Melted Zone

The Partially Melted Zone (PMZ) is a very narrow zone, between the melted zone and the heat affected zone. PMZ is not present in every weldment. For example, in welding of pure metals, this zone does not appear. Instead, in welding of impure or alloyed metals, this zone can be distinct and can be subjected to partial melting. In the case where a different composition filler metal is used during the welding process, the PMZ presents inhomogeneous composition and can be susceptible to corrosion. This zone can generally suffer from liquation cracking, and hydrogen cracking. Liquation cracking is induced in the grain boundary and can lead to loss of ductility.

2.2.3. Heat Affected Zone

The Heat Affected Zone (HAZ) lays between the partially melted zone and the base metal zone. HAZ undergoes a thermal cycle high enough to produce solid-state microstructural changes, however far from the melting point. Each point in the HAZ experiences a different thermal cycle, concerning the maximum temperature and the cooling rate. Consequently each point possesses a distinct microstructure. In the case of steel, HAZ includes the region where austenization due to heating has occurred. During cooling, many phase transformations may occur, depending on the cooling rate and the type of steel.

The HAZ can be divided into the following zones:

- Overheating Zone (T >> Ac_3), with very high temperature, inside the austenite region, where, increase of size of austenite grains can be detected. During cooling from these temperatures, austenite transforms according to the cooling rate to intergranular ferrite, Widmanstatten ferrite or acicular ferrite.
- Total Tempering Zone (T > Ac_3), with relatively lower temperatures, inside the austenite region, where, total tempering or normalizing conditions prevail, presenting fine-grained and uniform structures with high mechanical properties.
- Partial Tempering Zone (Ac_1 < T <Ac_3), where austenization isn't complete. During cooling, fine-grained ferrite-pearlite structures appear but, with some heterogeneity of the grain size.

2.2.4. Base Metal Zone

Base Metal or Parent Material Zone (BMZ), does not experience any thermal cycle, retaining its micro-structure unaffected by the welding process. However, the welding process imposes high residual transverse and longitudinal shrinkage stresses not only to the weld but also to the parent metal.

The cycle of heating and cooling that takes place during the welding process affects the microstructure and surface composition of welds and adjacent parent metal. Several transformation in the microstructure occur during the weld and can reduce its corrosion resistance. Some of these alterations are presented below:

- Micro-segregation
- Precipitation of secondary phases
- Formation of unmixed zone
- Recrystallization and grain growth in the heat affected zone
- Volatilization of alloying elements from the molten weld pool
- Contamination of the solidifying weld pool.

2.3. Common welding techniques in maritime industry [4][47]

2.3.1. Shielded Metal Arc Welding (SMAW) method

Shielded Metal Arc Welding (SMAW) is a manual welding process whereby an arc is generated between a flux- covered consumable electrode and the workpiece. The filler metal is deposited from the electrode and uses the decomposition of the flux covering to generate a shielding gas and to provide fluxing elements to protect the molten weld metal droplets and the weld pool, Fig.[2.2]. SMAW is one of the most used of various electric arc welding processes.

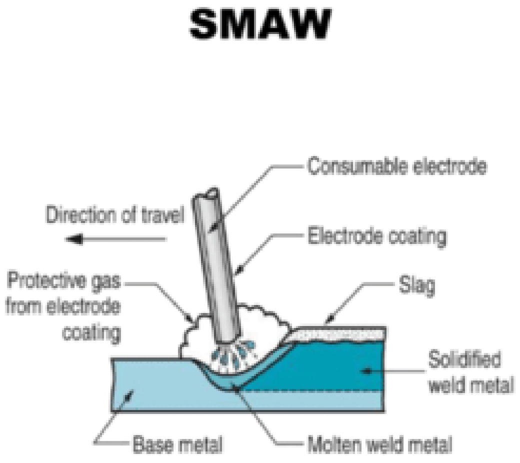

Fig.[2.2] Shielded Metal Arc Welding (SMAW) method.[22]

2.3.2. Gas Metal Arc Welding (GMAW) method

Gas Metal Arc Welding (GMAW) employs an electric arc, established between a consumable wire electrode and the workpiece to be joined. Heat from the electric arc melts the continuously fed metal wire and the metal workpiece surface to deposit a weld bead. An externally supplied gas or gas mixture acts to shield the arc and molten weld pool from the atmosphere, Fig.[2.3].

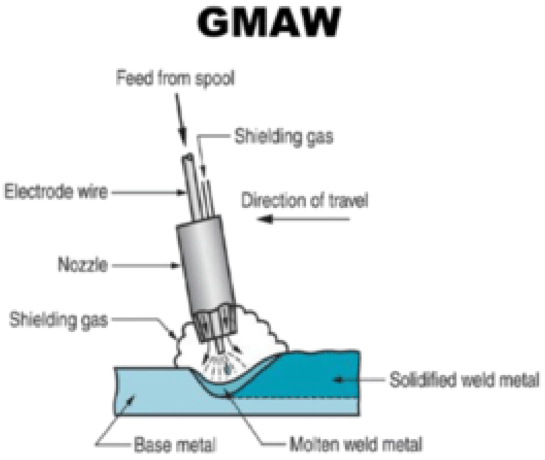

Fig.[2.3] Gas Metal Arc Metal (GMAW) method.[22]

2.3.3. Gas Tungsten Arc Welding (GTAW) method

Gas Tungsten Arc Welding (GTAW) derives the heat for welding from an electric arc, established between a non-consumable tungsten electrode and the workpiece to be welded. The arc zone must be flooded with an inert gas (Argon or Helium) to protect the tungsten electrode and molten metal from oxidation and to provide a conducting path for the arc current, Fig.[2.4].

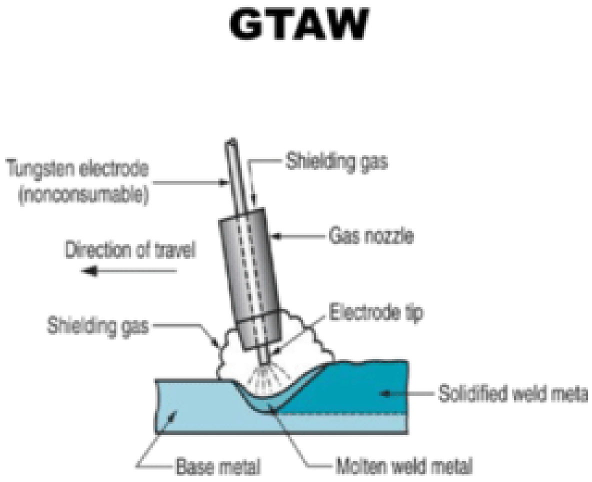

Fig.[2.4] Gas Tungsten Arc Welding (GTAW) method.[22]

2.3.4. Submerged Arc Welding (SAW) method

Submerged Arc Welding (SAW) is an arc welding process in which the arc is concealed beneath and shielded by a blanket of granular fusible material called flux and that is placed over the joined area ahead of the arc. Filler metal is obtained primarily from an electrode wire that is continuously fed through the blanket of flux into the arc and pool of molten flux, Fig.[2.5].

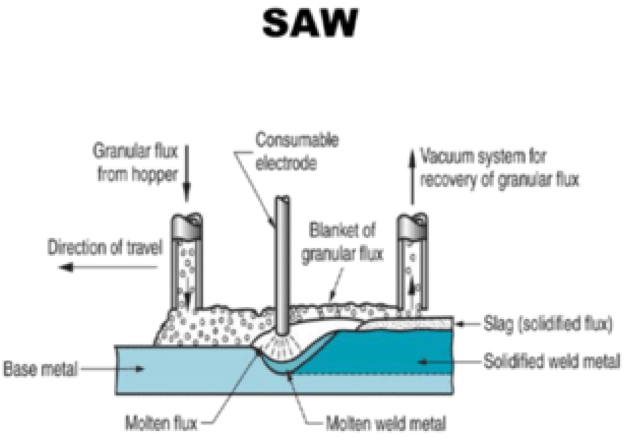

Fig.[2.5] Submerged Arc Welding (SAW) method.[22]

2.3.5. Flux Cored Arc Welding (FCAW) method

Because of the significance of this technique, as it is the technique used in this study, it will be thoroughly presented in Chapter 2.5.

2.4. Basic joint types [4][47][66]

Depending on the relevant position of the pieces-to-be-joined, various geometric assemblies can be produced, which can be distinguished into the following five basic joint types:

- *Tee joints*. They are named such because the two pieces of metal intersect at a 90° angle, which makes the joined edges come together in the shape of a "T". For these welds it is important to ensure effective penetration.
- *Edge joints*. It is not a very strong type of joint, since the pieces of metal are joined parallel together, but they are used mostly for sheet metal. This makes them bad for use with projects that will have to bear a ton of stress or impact. It also deeper penetration impossible.
- *Corner joints*. This type of joint only has the corners of the metals touching. The angle varies from joint to joint but it is usually 90°. Either side of the joint usually gets welded, but the inside corner is occasionally led without a weld. These joints can be closed, half-opened or fully open, they form an "L" shape and will melt down the overlapping edge so no filler metal gets added.
- *Butt joint*. It is the most common type of joint that gets used in pipe welding systems and it is also used for joining pipes together and other pieces of equipment, such as flanges, fittings and valves. This technique is applied in situations where a quality weld is necessary.
- *Lap joints*. These types of joints are used to join metals of different thicknesses together. These are fillet-type of weld and can be made to the one or more sides of the joint. These joints are so named because one piece of metal is overlaps another in the weld.

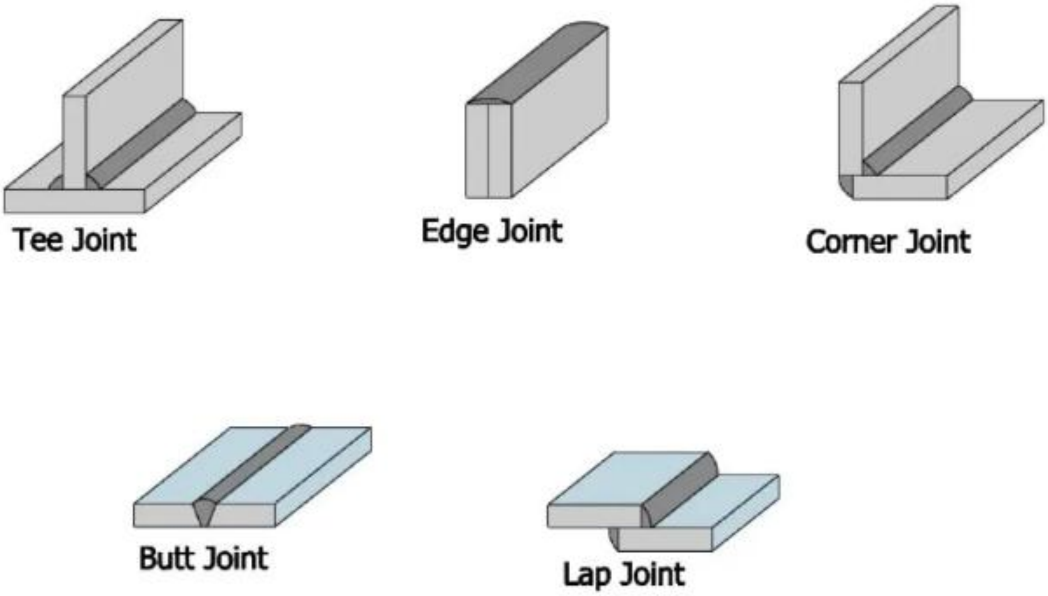

Fig.[2.6] Basic joint types of weldments.[66]

2.5. Flux Cored Arc Welding (FCAW) method

Flux Cored Arc Welding (FCAW) was introduced in 1957 to 1958 and it represented the first improvement in continuous welding over the solid wire gas metal arc welding (GMAW) technique. The difference between these two methods lays on the electrodes. In this welding method, the electrode is a metallic tube, which contains a specific flux in its core. This process is widely used in construction because of its high- welding speed and portability.

2.5.1. Fundamentals of FCAW [4][7][47]

FCAW is a semi-automatic or automatic arc welding which requires a continuously-fed consumable tubular electrode containing a flux and a constant- voltage or, less commonly, a constant- current welding power supply. An externally supplied shielding gas is sometimes used, but often, the flux itself is relied upon to generate the necessary protection from the atmosphere, producing both gaseous protection and liquid slag, as presented in Fig.[2.7].

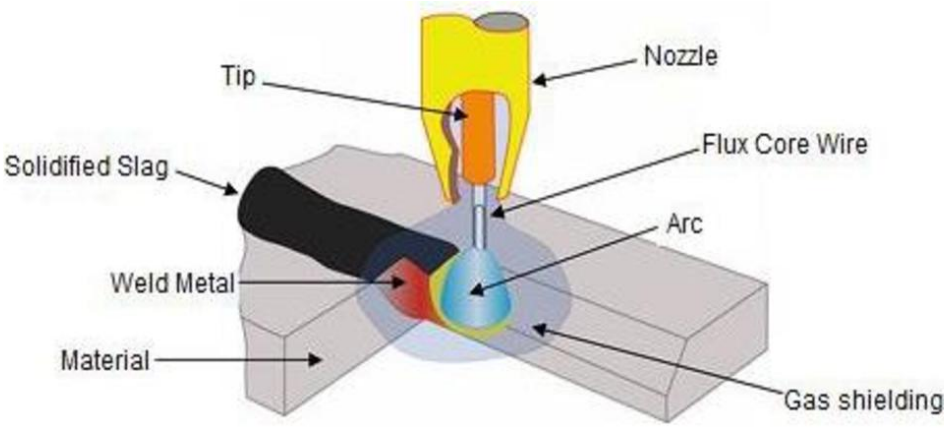

Fig.[2.7] Schematic illustration of the FCAW mechanism. [18]

FCAW electrodes are supplied in two distinct product types: Gas-shielded FCAW (FCAW-G) and Self-shielded FCAW (FCAW-S) process.

The first process (FCAW-G) uses an externally applied gas to assist in shielding the arc from oxygen and nitrogen in the atmosphere. The columnar flow of shielding gas, typically CO_2 or blends of argon and CO_2, protects the molten weld pool from atmosphere in the same manner as in the GMAW process. Additional protection from the intrusion of air is provided by the fluxing and slag- forming powders within the core ingredients, which form a molten slag cover over the weld pool. The use of CO_2 promotes deeper weld bead penetration and a more fluid weld puddle from the exothermal reactions. Argon (due to its higher energy of ionization) is more of a cooling gas than CO_2. Hence, the weld pool solidifies much more quickly and, the higher ionization promoted by argon stabilizes the welding arc. Finally, additives to the core ingredients can be used to stabilize the transfer, generate smaller droplets and promote less spatter around the weldment.

In the second process (FCAW-S), alloying, slug-forming and fluxing ingredients in the core protect the weld poll from atmospheric contamination. Because both oxygen and nitrogen can harm the weld poll by oxide contamination and porosity, respectively, different means of neutralization are employed. Combinations of lithium, magnesium and aluminum, in elemental and chemical compound forms, either limit nitrogen solubility or combine with it to form nitrides, preventing the nitrogen boil. Elements such as manganese, aluminum, magnesium and titanium are used to deoxidize the weld pool, combining with oxygen to form oxides, that help form a protective slag covering the weld pool.

2.5.2 Advantages and disadvantages of FCAW [4][47][61][69]

There are several important advantages to FCAW that make it a very popular choice for welding. These include:

- High deposition rate, which is the speed that the filler metal is applied.
- Can be used in all position with the right filler metal.
- Provides excellent weld penetration (bigger than SMAW and GMAW) and high welding productivity.
- Yields high-quality, consistent welds with fewer defects.
- No shielding gas needed with some wires making it suitable for outdoor welding and/or windy conditions.
- Possible welding of rusted or alloyed materials with CO_2 gas protection.
- Wide range of applications.

However, despite FCAW's many advantages, there are also some drawbacks, too. These include:

- Fume generation rates, directly proportional to deposition rates, are higher than the lower-deposition-rate processes (SMAW and GMAW); fume extraction may be required.
- Formation of rust, which must be removed.
- Complex equipment and thus, less portability.
- Higher electrode wire cost compared to solid electrode wires.
- Irregular wire feed, which is typically a mechanism problem.
- Porosity. The gases (specifically those from the flux core) don't escape the welded area before the metal hardens, leaving holes in the weld metal.

2.6. Potential failures [47]

The classification of the typical types of potential failures of weldments by the International Institute of Welding (I.I.W.) consists of six series of potential defects. This classification contains the following categories:

Series 100: Cracks

Crack is the material discontinuity due to fracture and is one of the most dangerous defects in weldments because, under specific conditions, they can propagate in high rates and cause structural failures. They are usually the result of corrosion, hydrogen adsorption or defective material. Based on the criterion of the cracking conditions, series 100 is distinguished in:

- Hot cracking, which usually occurs during the solidification of the metal, near the melting temperature.
- Cold cracking, which occurs after the solidification of the weld metal and is the result of high stresses. In the case of steels, it can also be mentioned as delayed cracking, since it occurs a long time after the solidification of the weldment, due to the accumulation of hydrogen.
- Lamellar tearing, which is the separation of the BM, mainly at levels parallel to the direction of the plate formation, which is due to high strains perpendicular to thickness.
- Solidification cracking, which can appear in several locations and orientations, but most commonly, is longitudinal center-line crack (coincident with the intersection of grains growing from opposites sites of the weld), or 'flare' crack, again longitudinal, but at an angle to the through-thickness direction.
- Reheat cracking, which occurs during the reheat process.

Series 200: Cavities

Cavities form on the welds due to the entrapment of gas during solidification. Depending on their form and distribution, cavities are divided into the following sub-categories:

- Uniformly scattered porosity.
- Cluster porosity.
- Linear porosity.
- Piping porosity.

Series 300: Solid inclusions

These are foreign substances that are trapped inside the weld metal. The basic types of inclusions are presented below:

- Slag inclusions.
- Flux inclusions.
- Oxide inclusions.
- Tungsten (wolfram) inclusions.
- Copper inclusions.

Series 400: Incomplete fusion and inadequate or incomplete penetration

Incomplete fusion means that the weld metal did not completely fill the entire space between the formed edges or that there is a gap between the metals or that there is a gap in the root of the weldment.

Inadequate or incomplete penetration occurs when the penetration of the weld metal inside the seam welding is less than the required and thus, the weldment is inadequate of the specific application.

Series 500: Unacceptable weld profiles

This category contains mainly the geometrical defects of the weldments and the most common of them are presented below:

- Undercut.
- Overlap.
- Underfill.
- Excessive reinforcement.
- Insufficient leg.
- Excessive convexity.

Series 600: Other types of defects.

The last category of potential failures contains defects that don't belong in none of the above series. Some of them are presented below:

- Arc strikes in the base metal.
- Excessive spatter.
- Craters.
- Melt-through.
- Dimensional defects.

2.7. Mechanical properties [29][47]

Residual stresses

During the fusion welding, the local heating of the metal causes the development of local stresses and strains, which can remain after the end of the weldment and affect its mechanical properties. High tensile residual stresses in the welding region can cause cracking and even premature structural failure. High compressive residual stresses in the base metal can reduce the plate's bending strength.

Hardness

The hardness experiments that were conducted for the purposes of this study and are thoroughly presented in Chapter 5 (Experimental procedure), showed that the maximum hardness values are presented in the HAZ of the weldment, the medium values are presented in the FZ and the minimum values are presented in the BMZ, which is the hardness values of the parent metals.

Tensile and Impact toughness properties

In recent experiments in HSLA steels, after Flux Cored Arc Welding method [29], during the tensile tests, all the specimens invariably failed in the unwelded region. This indicated that the weld region is comparatively stronger than the other regions and that the joined properties are controlled by weld region chemical composition and microstructure.

3. CORROSION OF WELDMENTS

3.1. Introduction

Corrosion is an inevitable issue in maritime industry due to the intricate service conditions which include the simultaneous action of high pressure, pH value, high temperature, multiphase flow and ion concentrations. Each part of the ship (from its hull, to the stiffeners, pipelines, tanks, plates) and their weldments are continuously subjected to highly corrosive conditions. Thus, the study of the corrosion of weldments is a very important parameter of the structural design and constitutes the main purpose of this thesis.

3.2. Corrosion of steels [6][33][48]

When a metal enters an acid environment, such as the sea, electrons start to be removed from its surface, causing a charge flow. This flow of electrons between the metal and the environment causes a potential change,E-e, from the equilibrium half-cell electrode potential, which is called polarization or overpotential. For cathodic polarization, η_c, electrons are supplied to the surface and for anodic porarization, η_a, electrons are removed from the metal's surface, causing its degradation or, corrosion. In every electrochemical corrosion cell there are four required components, an anode, a cathode, a conducting environment for ionic movement (electrolyte) and an electrical connection between the anode and the cathode for the flow of the electron current. If any of the above components is missing or disabled, the electochemical corrosion process will be stopped.

In a system that we study, where a metal (Fe^+) is in an acid solution (H^+), the anodic and cathodic reactions of H_2 are

$$H_2 \rightarrow 2H^+ + 2e^- \qquad (3.1)$$

$$2H^+ + 2e^- \rightarrow H_2 \qquad (3.2)$$

whereas, for the metal, in this case, iron, the anodic and cathodic reactions are

$$Fe \rightarrow Fe^{2+} + 2e^- \qquad (3.3)$$

$$Fe^{2+} + 2e^- \rightarrow Fe \qquad (3.4)$$

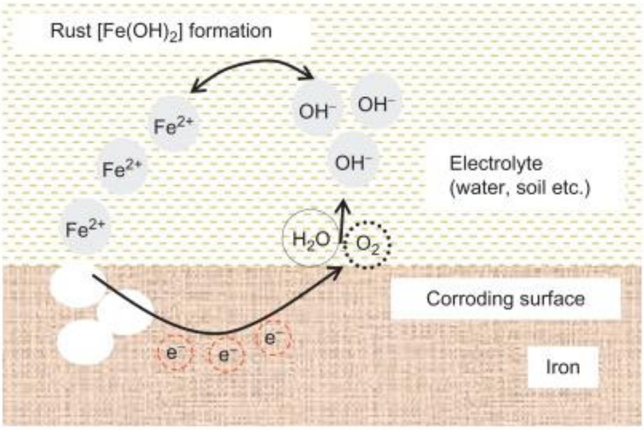

Fig.[3.1] Corrosion cell formed as a result of rusting of iron. [50]

To maintain charge neutrality in the metal both the anodic and the cathodic reactions must occur at the same rate, which means that the number of electrons produced and concumed per unit time must be equal (the total rate of oxidation must equal the total rate of reduction).

3.3. Parameters affecting the corrosion of weldments [6][33][37][47][48][49]

The majority of failures in welded structures are attributed to the corrosion. Even though the weldments in metallic structures are accomplished following standard procedures, methods and regulations and are consequently approved to avoid defects, corrosion failures in weldments still occur. Metals and alloys chosen for certain service environment prove to be prone to corrosion when they are welded. The most important parameters which determine the corrosion behavior of weldments, include:

- Welding technique, practice and sequence and also choice of filler metal, which determine the metallurgical and chemical compositional variations in the base metal, HAZ and weld metal, that results in a condition favoring galvanic corrosion.
- Moisture contamination that leads to Hydrogen-Induced Cracking of the weldment. Hydrogen in welding can result from improperly baked or stored electrodes, moisture in the flux, or the presence of moisture and other impurities on the components to be welded. This effect can be eliminated via post-welding heat treatment techniques (PWHT).
- Weld defects (e.g. incomplete weld penetration or fusion, porosity, cracks, surface flaws, which act as preferential sites for local corrosion attack).
- High stresses (external or residual) that lead to stress corrosion cracking (SCC).
- Final surface finish.

3.3.1. Welding techniques

In maritime industry, there are a lot of cases where different welding techniques must be applied. Thus, these techniques differ from one another and are used according to the necessary rules and regulations, concerning the base metals that need to be joint together, the loading that need to be subjected to and the environment in which it will be exposed. Different welding technique may lead to different welding and solidification rate, different effect on the microstructure of both the fusion zone and the heat affected zone, as well as, different effect on the thermal cycle. All these factors can affect in different ways the welded structures, including the corrosion behavior of the structure.

For example, in Gas Metal Arc Welding Technique (GMAW), a stable arc smooth metal transfer with low spatter loss and good weld penetration can be obtained, along with high deposition rates which allow for thick workpieces to be welded at high welding speed. In comparison, in Submerged Arc Welding (SAW), the spatter and the heat loss are eliminated even at high welding currents. Given the high deposition rates of SAW, thicker workpieces than GMAW can be produced. The relatively high heat input can reduce the weld quality and increase distortions.

3.3.2. Welding practice and sequence

One of the most important factors that affect the corrosion of weldments is the practice of the weldment. The number, the sequence and the direction of the passes, the heat input rate, the formation of the edges, the welding sequence and the dimensioning of the weldment are only some of the practice parameters that can affect the mechanical properties and the corrosion resistance of the weldment. Weldability of steels is important not only for initial fabrication, but also for future field repairs or modifications. Weld repairs and post-weld heat treatments (PWHT) can affect the mechanical properties of wrought components that have been processed by normalizing or quenching and tempering and can prevent severe corrosion damages (e.g. Hydrogen embrittlement).

3.3.3. Weldment microstructure and heat treatment

Fusion welding techniques, due to the thermal cycle that imposes to the base metal, leads to the creation of metallurgical transformation across the weld metal and HAZ. These distinct microstructures can significantly alter the intrinsic corrosion rate of the steel. The microstructure of the weld metal presents a high density of lattice defects and segregation of elements, depending on cooling rate and the peak temperature. Thus, a wide range of microstructures can be formed, conditional to the energy input, preheat, metal thickness, weld bead size, and reheating effects due to multipass welding. Due to the different peak temperatures, chemical compositions, and weld inclusions (oxides and sulfides), the microstructure of the weld metal is usually significantly different from this of the HAZ and base metal. Consequently corrosion behavior can also differ for the different microstructures in a weldment.

For example, metastable phases of steel (such as bainite and martensite), present higher hardness values and susceptibility to corrosion, due to high density of lattice defects and residual stresses. Proper design of all the heat treatments lead to the reduction of residual stresses and the formation of more metallurgical stable phases (such as ferrite and pearlite) and may reduce the susceptibility to corrosion of the weldment.

3.3.4. Geometrical factors-Defects

Corrosion of weldments often coexists with welding defects. In the weld defects dirt, soil or other particles may be accumulated enhancing corrosion, while weld defects are usually stress concentration points. The most common weld defects, strongly associated with corrosion of weldments include:

- Excess weld metal. This defect is appeared when excessive weld metal is added to the joint, Fig.[3.2] a. This defect is usually attributed to improper selection of welding technique or welding parameters.
- Undercut. This is a geometric discontinuity which may appear in the toe or in the root of the weld and is caused by insufficient deposition of the filler metal, Fig.[3.2] b. This defect is probably the most common shape imperfection during arc welding.
- Overlap. This accounts for the spread of the weld metal beyond the root or the toe of the weld, Fig.[3.2] c. This defect is usually caused by poor manipulation of the electrode or welding gun.
- Excessive penetration. This defect appears when weld metal is protruding through the root of a fusion (butt) weld made from one side only, Fig.[3.2] d. Penetration becomes excessive when the joint gap is too large, the root faces are too small, the heat input to the joint is too high or a combination of these causes.
- Incompletely filled groove. This defect occurs when insufficient filler metal is deposited for the formation of the weld, Fig.[3.2] e, and it is usually attributed to low current or wire feed, or high travel speed resulting in insufficient filling of the weld.

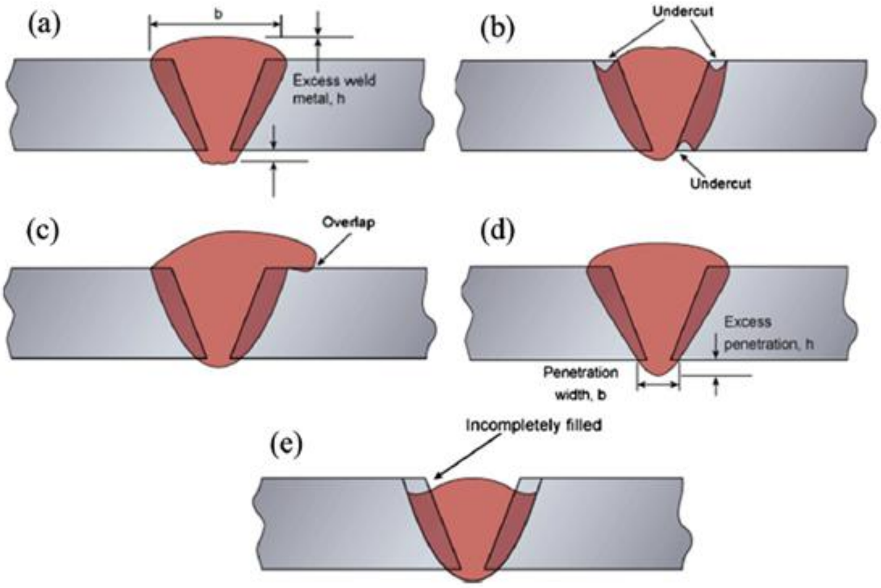

Fig.[3.2] Geometric defects: (a) excess weld metal, (b) undercut, (c) overlap, (d) excessive penetration, (e) incompletely filled groove. [49]

3.3.5. Residual stresses

The residual stress in welded structures mainly results from the non-uniform expansion and contraction of the weld and the base material in the vicinity, due to a non-uniform temperature field during welding. During welding, the base metal, HAZ, and underlying weld passes experience stresses due to thermal expansion and contraction. On solidification, high levels of residual stress, often close to the material yield stress, remain as a result of weld shrinkage. High residual stress within and near the weld zone may lead to brittle fracture, reduce the fatigue life and promote stress corrosion cracking during service. Thus, the residual stresses must be taken under consideration and specific measures must be taken to assure the integrity of the structure.

3.4. Corrosion of weldments [6][33][47][48][49]

Weldments present corrosion forms strongly related to the parameters induced to the metal due to the welding procedure: distinct microstructure, chemical composition, residual stresses. The above parameters along with the exposure of weldments in aggressive environment lead to the corrosion of weldments. The corrosion forms which are encountered in weldments consist a subsection of the usual corrosion forms, yet only related to micro-characteristics. In the following paragraphs the most common corrosion forms encountered in maritime industry are discussed thoroughly.

3.4.1. Uniform corrosion

This is the simplest and most common form of corrosion that occurs in an acid environment and is the most noticeable. For this form of corrosion, the corrosive environment must have the same access to all parts of the metal surface and the metal itself must be metallurgically and compositionally uniform. In some metals, such as steel, uniform corrosion produces a somewhat rough surface by removing a substantial amount of metal, which either dissolves in the environment or reacts with it to produce a loosely adherent, porous coating of corrosion products, Fig.[3.3]. An advantage of this form of corrosion is that it is widely spread through the entire surface of the metal and not concentrated to some points (which would be difficult to detect). It is predictable and the corrosion rate as long with the expected service life can be measured in the laboratory and be acceptable for the design.

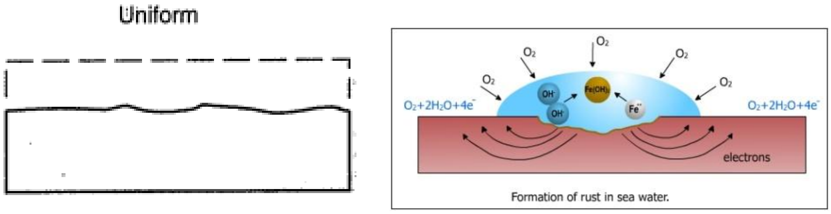

a) b)

Fig.[3.3] a) Uniform corrosion [33], b) Mechanism of uniform corrosion.[63]

3.4.2. Galvanic corrosion

Galvanic corrosion occurs when two or more dissimilar metals are immersed in a conductive solution and are electrically connected. The more active of the two metals becomes the anode and corrodes whilst the nobler one becomes the cathode and is protected, Fig.[3.4]. Filler metals employed in the majority of the welding techniques, along with the phase transformation induced by the thermal cycle during the weld, lead to the formation of distinctive areas, which present different susceptibility to corrosion. This phenomenon is attributed to the differences of the corrosion susceptibility, namely the electrochemical potential, among the different areas of the weld. If the weld metal (WM) and heat affected zone (HAZ) are anodic to the parent material (PM), then localized metal loss can take place in those regions. This phenomenon is accentuated by the small surface areas of the WM and HAZs compared to the large area of the parent material e.g. small anodic to large cathodic area. Despite the existing research and the protection applied, preferential corrosion occurs and failures are recorded either on the weld metal or in the HAZ.

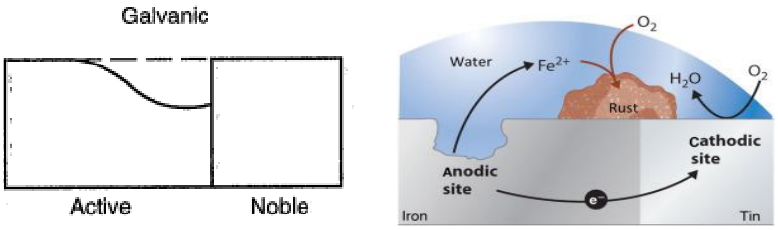

a) b)

Fig.[3.4] a) Galvanic corrosion [33], b) Mechanism of galvanic corrosion.[64]

Preferential Weld Metal Corrosion

The preferential weld metal corrosion refers to the anodic, active, behavior of the weld metal and depends on the chemical composition of the filler metal employed for the weld. Other important parameters of the preferential WM corrosion are: the type of steel, the heat input, the pre-heat treatment of the metal, the residual stresses and the grain size of the microstructure. The corrosion rate of the weld metal attack seems to be influenced by the Ni and Cr content of the filler metal and is less affected by base metal steel composition, although a steel with Cu, Ni, and Cr additions led to a nobler parent steel, hence accelerating weld metal attack. Matching weld consumables, with the same composition as the parent metal, have been shown to give the best resistance to PWMC, whereas both 1%Ni and 1%Si additions are detrimental.

Preferential Heat Affected Zone Corrosion

In the Heat Affected Zone, since there is no difference in composition, it is the wide range of microstructures formed, that causes preferential HAZ corrosion. Corrosion susceptibility of HAZ is considered highly dependent on the thermal cycle experienced by the metal. Close to the fusion boundary, the HAZ transformation to austenite on heating, will be followed on cooling by transformation to give either a ferrite-pearlite microstructure or bainite, or martensite or a mixture of them, depending on material composition, peak temperature, and cooling rate. Farther from the weld, the material will be exposed to a lower peak temperature, so only partial austenization occurs, and those areas heated below the ferrite-to-austenite transformation temperature (Ac_1) will not be significantly affected, other than by some carbide coarsening and tempering. Studying of the weldments microstructure in HAZ revealed that the coarsening of ferrite Widmastätten in the HAZ increased the corrosion resistance of carbon steel in acidic solutions containing NaCl.

3.4.3. Pitting corrosion

Pitting corrosion affects metals and alloys such as steel, iron, aluminum and more and is one of the most destructive forms of corrosion. It is usually constrained to specific areas. It penetrates and attacks rapidly and is difficult to detect. It most commonly occurs where the passive coating layer (film) is physically damaged or chemically attacked. This creates a weak point where water or corrosive solutions attack the substrate, Fig.[3.5]. Pitting corrosion occurs when the cathode (damaged coating) is large and the anode (exposed metal) is small. Typically the surface protection layer or film becomes the cathode when it is damaged and cracked. A small area of metal is then exposed and becomes the anodic. It is a very dangerous form of corrosion because it is unpredictable and cannot be detected due to deposits or corrosion products that can cover the pitted surfaces.

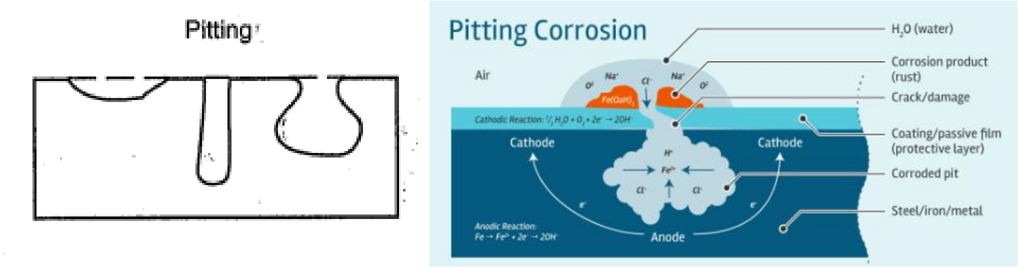

a) b)

Fig.[3.5] a) Pitting corrosion [33], b) Mechanism of pitting corrosion. [19]

The filler metal is most likely to be attacked due to micro segregation of the dendrite structure. Therefore, the selection of the proper alloy elements is very important. For example, the combination of low concentration of carbon with specified amount of nitrogen increases the material's resistance against pitting corrosion. Also, molybdenum is used as an inhibitor against pitting corrosion whereas, manganese has a negative effect in this form of corrosion, due to the sulfides of manganese (MnS) which are formed and become anodic regions in chloride media.

3.4.4. Environmentally Assisted Cracking (EAC)

Environmentally assisted cracking is common in the refining and power-generation industries where components frequently operate in aggressive environments. Environmentally assisted cracking or degradation can take many forms, ranging from local thinning caused by global corrosion attack, to SCC and hydrogen damage. The form of cracking or degradation depends on a number of factors, including the material, chemical composition and microstructure, weld metal and HAZ properties (including hardness), weld geometry, level of welding residual stresses, operating conditions, and environment.

Stress Corrosion Cracking (SCC)

Weldments can be susceptible to SCC under particular environmental conditions. The cracking results from the combined synergistic interaction of corrosive environment, susceptible microstructure, and tensile stress, Fig.[3.6] a. Welds often suffer from residual stress, to a level approaching the yield strength of the parent metal. Therefore, the heterogeneous microstructure of the weldment, the residual stress, and the exposure in corrosive environment make the weldment prone to SCC. Stress-corrosion cracks usually starts from corrosion pit, and proceeds transgranular or intergranular to the metal, Fig.[3.6] b. Cracking is often characterized by crack branching and usually has a delay time prior to crack initiation, while corrosion products are often found along the fracture.

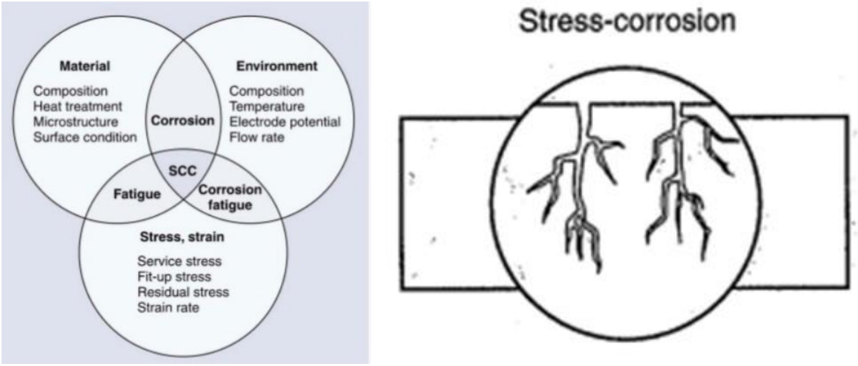

a) b)

Fig.[3.6] a) Synergistic interaction of environment, material and stress that lead to SCC [35], b) SCC propagation [33].

Welding parameters influence the amount and distribution of residual stress, because the extent of the stressed region and the amount of distortion are directly proportional to the size of the weld deposit; this deposit is directly related to the heat input. The thermal cycle of welding is often much localized, resulting in strains that can cause distortion and residual stress. These residual stresses can be important in the initiation and propagation of stress corrosion cracking. Post-weld heat treatment redistributes the localized load and reduces the residual tensile stress and decreases the SCC susceptibility.

Hydrogen- Induced or Cold Cracking (HIC)

Hydrogen induced cracking or cold cracking consists one of the most important issues in weldments, mainly in steel and high strength low alloy steels. This phenomenon is also referred as delayed cracking. Hydrogen coming from moisture in certain weld consumables or during non-optimal field welding conditions can become dissolved in liquid weld metal. This dissolved hydrogen can cause cracking during solidification, as well as embrittlement of the weld, due to the different dissolution in the different phases. Dissolved hydrogen in the material as a result of exposure to refinery wet H_2S service environments can also affect weldability and the subsequent performance of repair welds.

Hydrogen-induced cracking (HIC), is a phenomenon associated with welds in hardenable carbon and low-alloy steels and results from the combined action of the following parameters:

- Susceptible (“brittle”) microstructure
- Hydrogen presence in the weld metal
- Tensile stresses in the weld area
- Temperature range, from –100 to 200 °C

Cracking may occur several hours, days or weeks after the weld has cooled; consequently the term delayed cracking is also used. According to the location they are met, cracks are often described as toe cracking, root cracking, or underbead cracking, Fig.[3.7].

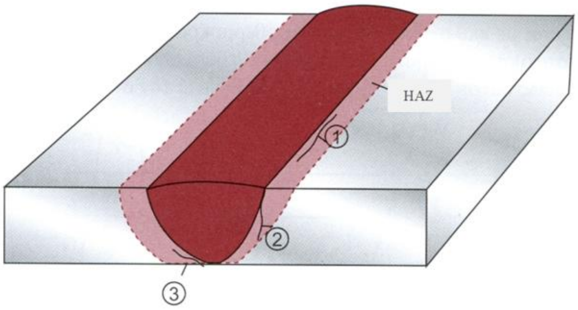

Fig.[3.7] Weld metal cracks in HAZ due to hydrogen induced cracking (1) underbead cracking, (2) toe cracking, (3) root cracking.[49]

HIC has been observed primarily in the parent metal and HAZ. Cracks in the HAZ are most often longitudinal. Under-bead cracks lie more or less parallel to the fusion line. They do not normally extend to the surface and may therefore be difficult to detect. Under-bead cracks will form at relatively low stress levels in martensite, when high levels of hydrogen are present. Toe cracks and root cracks start in areas of high stress concentration. Cracking may therefore occur in less susceptible microstructures or at relatively low hydrogen levels. This type of cracking is often delayed while the necessary hydrogen diffuses to the area. Transverse cracking in the HAZ is less common. It will occur in high-carbon martensite under conditions of high longitudinal stresses.

3.5. General prevention methods [1][46][47][48][49]

3.5.1. Material selection

The most common method of protection against corrosion is the selection of the most suitable metal or alloy, depending the environment where it's about to be exposed. Generally, pure metals present better corrosion resistance than those that contain impurities or small quantities of other elements. However, pure metals are more expensive and have low mechanical properties. The addition of alloys is used in order to improve the material's corrosion resistance. For example, the addition of Cu, Ni, Si and Cr in the HSLA weathering steels improve atmospheric corrosion significantly, by facilitating the formation of a protective, surface film. For the selection of the most suitable material there are combinations of corroding environment- metal alloy, which correspond to the highest corrosion resistance with the lowest cost.

In addition, we have to understand that it is almost impossible to find the perfect material for a certain application. Usually, there are opposite factors that need to be kept under concideration when selecting a material, such as the regulations that need to be followed, the environment, the strength and hardness of the material, the good weldability in some cases, the low (or better, the most acceptable and convenient) cost of production and maintenance, the corrosion resistance and many others. For example, martensitic structure offers hardness and a very high yield strength to the material with small weight but, its low ductility and welding difficulty make it inappropriate for some applications. So, depending on the factors we want to emphasize in each case, some tolerances should be established that will lead to selection of the most suitable material.

3.5.2. Design

The design of a structure is often as important as the selection of the material of this structure. The designer must take into consideration plenty of factors such as the strength requirements, corrosion rates, operationg conditions, environmental corrosivity, costs and much more. There is a plethora of rules that need to be followed in order to prevent, minimize or even rectify corrosion during the stage of design. Some of them are presented below:

- Corrosion causes loss of thickness, therefore, corrosion margin for thickness must be provided in the design.
- Careful selection of the materials.
- Conductive contact between dissimilar metals should be avoided in order to avoid galvanic corrosion.
- Any system must be designed to provide easy inspection and replacement of their components.
- Specific operation and maintenance procedures must be followed.

- Corners should be replaced where possible by curved section for several reasons, such as the stress concentration which can lead to SCC and the hot vapor concentration (in tanks with hot liquids).
- Avoid heterogeneity (metals, temperature, stresses, etc).

During the design stage, there are a lot of rules that need to be followed in order to eliminate the corrosion of weldments as well. Some of them are presented below:

- Selection of appropriate material and welding consumables in order to reduce compositional variations.
- Preparation of the surface eliminates the surface defects.
- Complete penetration and removal of slag after each pass are beneficial for the corrosion resistance. In addition, if flux is used, it should be thoroughly removed.
- Removal of sources of hydrogen (proper choice of consumables, drying of the flux, heat treatment) in order to avoic hydrogen embrittlement.
- Thorough inspection after completing the welding procedure. The surface should be smooth and uniformly oxidized, free of foreign particles and discontinuities.
- Pre- heat and post-weld heat treatment in order to reduce the residual stress gradients and also avoid hydrogen chacking.
- Protective coatings.
- Passivation treatment.

These are only a few general rules that need to be followed during the design stage. It's obvious that in each case, there are plenty more rules that need to be taken into consideration.

3.5.3. Cathodic protection

Cathodic protection is one of the most widely used methods of corrosion prevention. In principle, it can reduce or prevent the corrosion of any metal or alloy exposed to any aqueous electrolyte. In this case, we aim to prevent corrosion by achieving immunity with the decrease of potential, as shown at the Pourbaix diagram (E/pH) for iron, Fig.[3.8]. There are two types of cathodic protection: sacrificial anode cathodic protection and impressed current cathodic protection.

In the first case, cathodic protection is performed when the protected metal is connected to a less noble metal. The corrosion potential of the system must be less than the corrosion potential of the protected metal. Thus, the last becomes the anode an the less noble metal becomes the anode. For the protection of steel, we use Zn, Mg or Al as sacrificial anodes, which are less noble than steel.

In the second case, the anode consists of an inertial electron (eg graphite) and the corrosion potential of the structure-to-be-protected is reduced by an external direct current source.

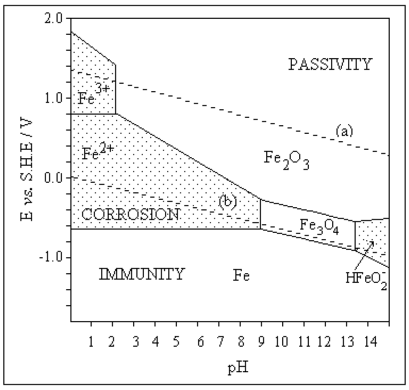

Fig.[3.8] Pourbaix diagram for iron in water.[28]

3.5.4. Anodic protection

Anodic protection is different from the cathodic protection because, in this case, the value of the corrosion potential increases, in order to achieve passivity (creations of a protective oxide film), Fig.[3.9], therefore, this method can only be applied to metals that have the ability to be passive (eg stainless steel). This method is secured by maintaining the equilibrium potential constant, between the protected structure and a reference electrode, via a potentiostat.

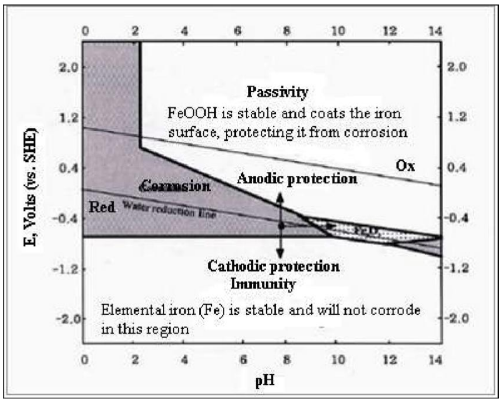

Fig.[3.9] In cathodic protection, the potential decreases in order to achieve immunity whilst, in anodic protection, the potential increases in order to achieve passivity.[28]

3.5.5. Coatings

Coatings have the ability to act as a physical barrier between the substrate and the corrosive environment, in order to prevent corrosion. In addition, they can preserve cosmetic appearance, which is often a major concern for structures and equipment routinely exposed to public view, such as the ship's hull. A coating, in order to effectively protect a metal from corrosion, must be continuous, cohesive and inert to the the environment and also, it is necessary to prepare the metal surface before applying them, by removing any oxidizing procucts or impurities. The coatings are distinguished into non-metallic and metallic.

As for non-metallic coationgs, they are paints, polymers and tarpaulins. Paints usually contain Zn or Al powders (less noble than steel), which act as anodes and serve as a reservoir for inhibiting compounds. Polymers that can be used for the metal protection against corrosion or either thermoplastic or thermosetting. Finally, some underground construstion are often protected by using tars or asphalt.

Metallic coatings act as a corrosion resistant barrier but may also provide sacrificial cathodic protection to exposed adjacent areas of a metal substrate of dissimilar composition. For exaple, zinc, which is more anodic than steel, act as a sucrificial anode to the galvanized components.

3.5.6. Inhibitors

Inhibitors are chemical compounds that deposit on exposed metal surfaces from the corrosive environment. They are those substances that, when added in small -but critical- quantities in a corrosive system, have the ability to reduce its corrosion rate. They may form a uniform film, which, like a coating, acts as a physical barrier. Inhibitors mainly act during the cathodic polarization (cathodic inhibitors). Thus, the corrosion element works under cathodic control and the corrosion current is reduced, Fig.[3.10]. There are a lot of types of inhibitors with different composition, such as vortex inhibitors, scavengers, oxidizers, vapor phase inhibitors and many others. These compounds are applied, depending on the metal, the corrosive environment, temperature and concentration. The concentration and the type of inhibitor are usually determined based on empirical applications and the information is provided by the manufacturer. However, despite the fact that inhibitors are an important parameter for the reduction of corrosion, there are restriction on their use. Since many inhibitors are toxic, the cannot be applied to specific environments (e.g. food industry) because they will infect it. Therefore, they should be used with caution.

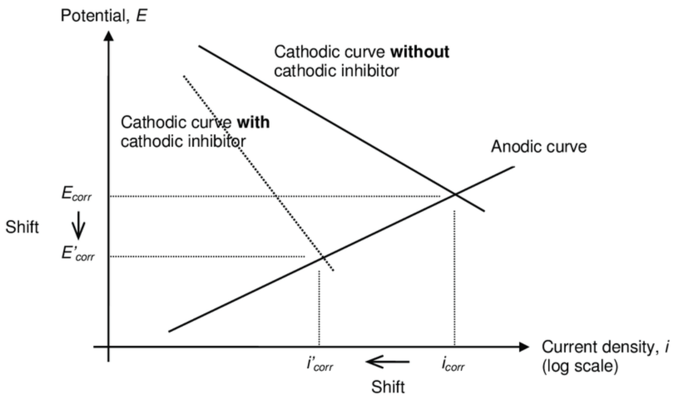

Fig.[3.10] Current density- potential diagram in a corrosion system with and without inhibitor.[44]

3.6. Bow Tie Analysis of Corrosion [6][17][33][47][48][49][55]

A 'bowtie' is a diagram that visualizes the risk you are dealing with in just one, easy to understand the picture. The diagram is shaped like a bow-tie, creating a clear differentiation between proactive and reactive risk management. The power of a Bow Tie XP diagram is that it gives you an overview of multiple plausible scenarios, in a single picture. In short, it provides a simple, visual explanation of a risk that would be much more difficult to explain otherwise. The main parameters of a bow tie diagram are presented below:

- Hazard (black and yellow). A hazard is something in, around or part of the organization which has the potential to cause damage.
- Top event (orange). This is the moment when control is lost over the hazard. There is no damage or negative impact yet, but it is imminent. This means that the top event is chosen just before events start causing actual damage.
- Threats (blue). The factors that will cause the top event.
- Consequences (red). The main results from the top event.
- Barriers (black). Barriers in the bowtie appear on both sides of the top event. Barriers on the left side interrupt the scenario so that the threats do not occur, and if they do, not result in a loss of control (the top event). These barriers are called Control Barriers. Barriers on the right side make sure that if the top event is reached, the scenario does not escalate into an actual impact (the consequences) and/or they mitigate the impact. These barriers are called Recovery Barriers.
- Escalation factors (yellow). Barriers are never perfect. Even the best hardware barrier can fail. Given this fact, what you need to know is why a barrier will fail. This is done using the 'escalation factor'. Anything that will make a barrier fail can be described in an escalation factor.
- Escalation factor barriers. The barriers that interrupt the negative effect of the escalation factors.

Bow Tie diagram is an important tool for visual representation of risk analysis. It can be very simple or highly detailed and thus, complicated. For the purposes of this study, a simple but, to-the-point bow tie representation was chosen, in order to describe the main corrosion characteristics. No escalation factors were included in this diagram, Fig.[3.11], in order to avoid a more complex analysis. Afterwards, all the threats and consequences will be mentioned, along with the protective and recovery barriers. Finally, in order to understand the simple role of the escalation factors in such a diagram, a simple example will be provided, based on this analysis.

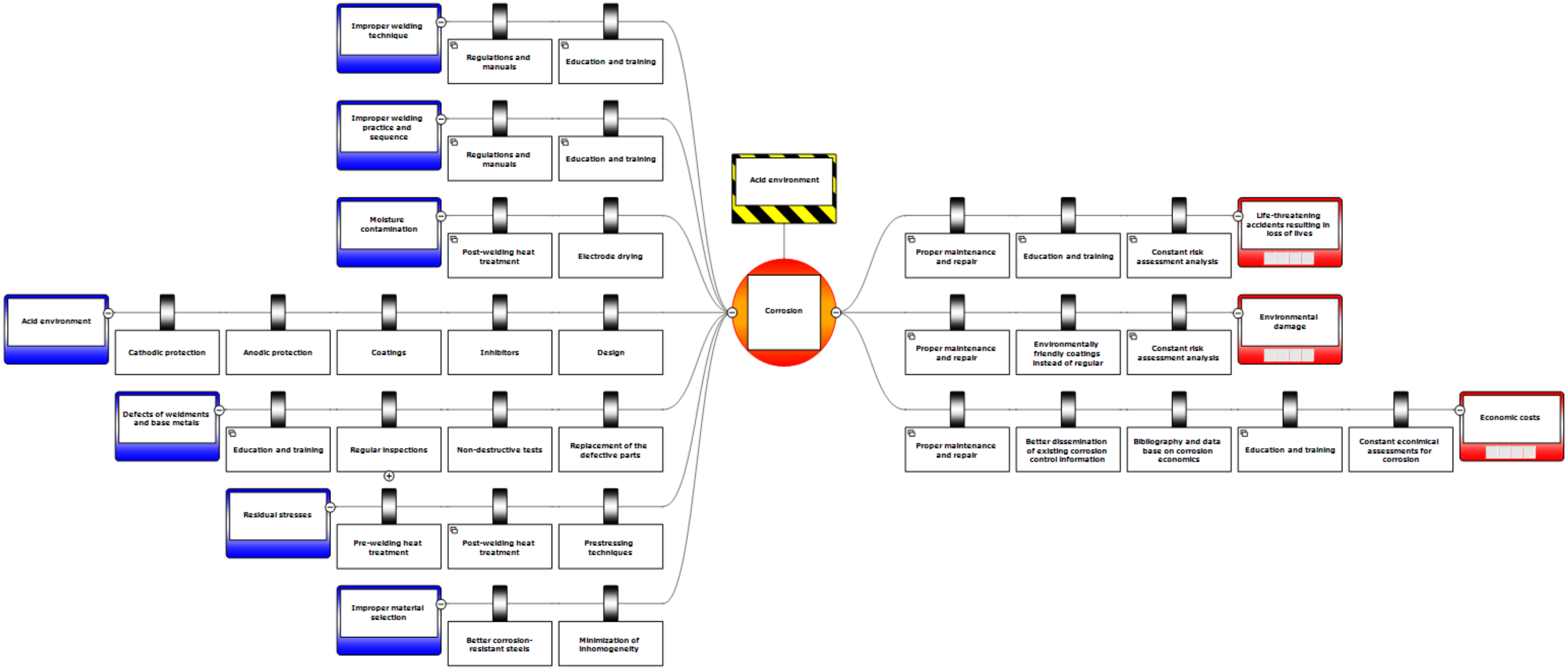

Fig.[3.11] Bow Tie diagram- Corrosion of weldments.

In Fig.[3.12], we observe the first steps of this Bow Tie diagram. In this case, the hazard is the acid environment and the top event is the corrosion of the weldments and of the materials in general. Some of the main threats of this event are presented below:

- Improper welding technique
- Improper welding practice and sequence
- Moisture contamination
- Acid environment
- Defects of weldments and base metals
- Residual stresses
- Improper material selection

Also, the main consequences of this effect are:

- Life-threatening accidents, resulting in loss of lives
- Environmental damage
- Economic costs

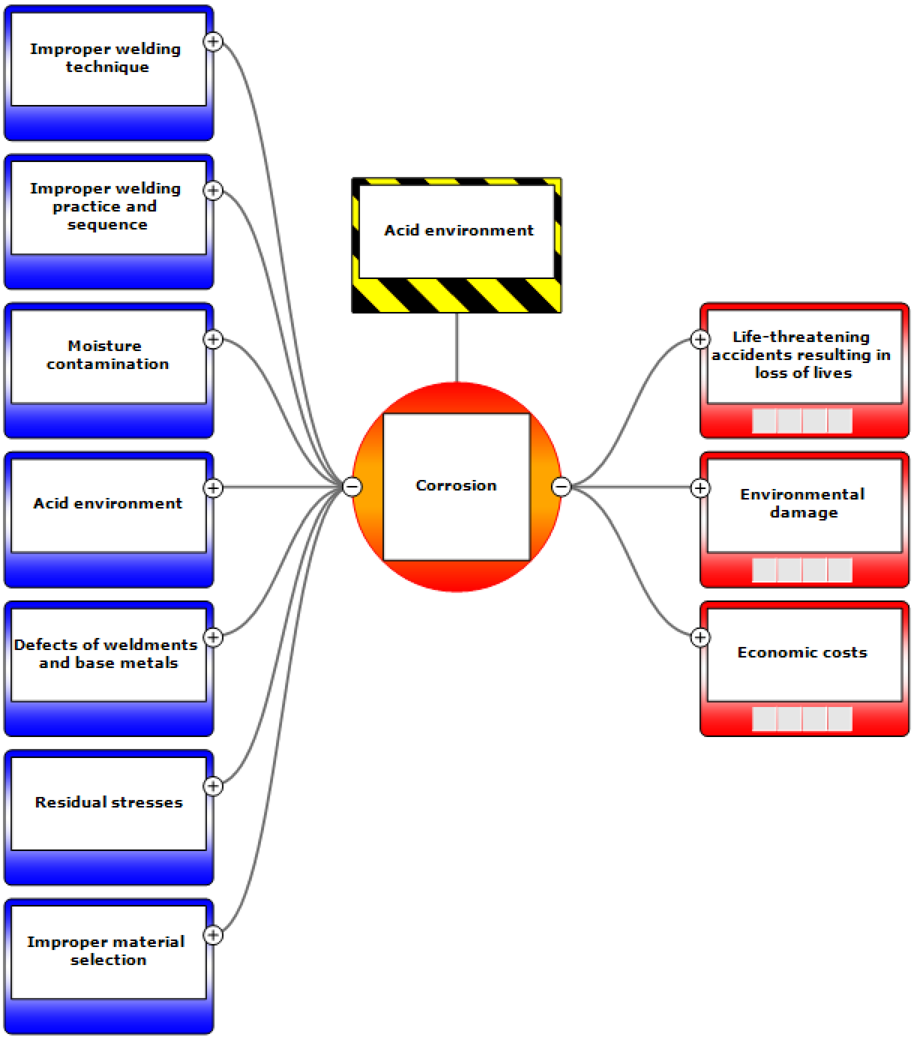

Fig.[3.12] First steps of the Bow-Tie diagram, including hazard, top event, threats and consequences.

In the figures below, some basic barriers are presented, either protective or recovey, in order to comprehend how this analysis works. It is important to mention that these barriers, these measures, are not the only barriers but some important barrier that are or should be used in order to avoid unpleasant consequences.

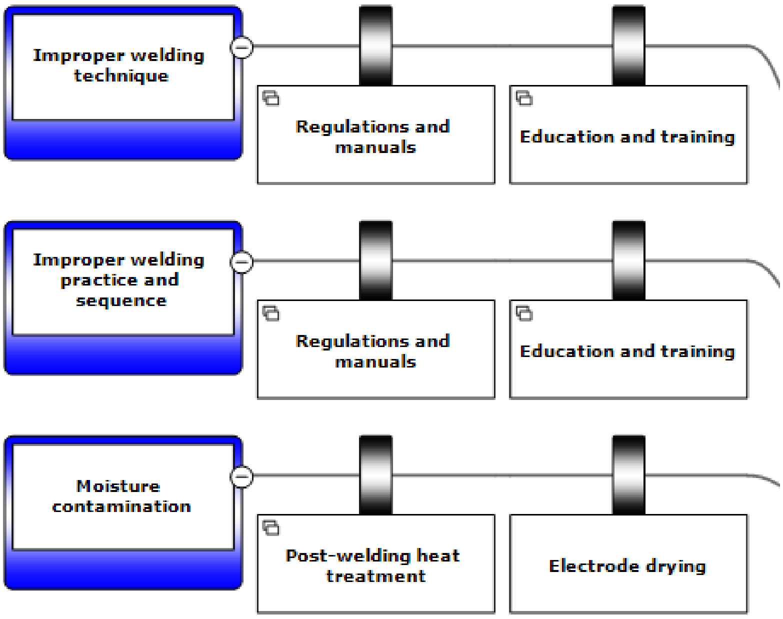

Fig.[3.13] Protective barriers against improper welding technique, improper welding practice and sequence and moisture contamination.

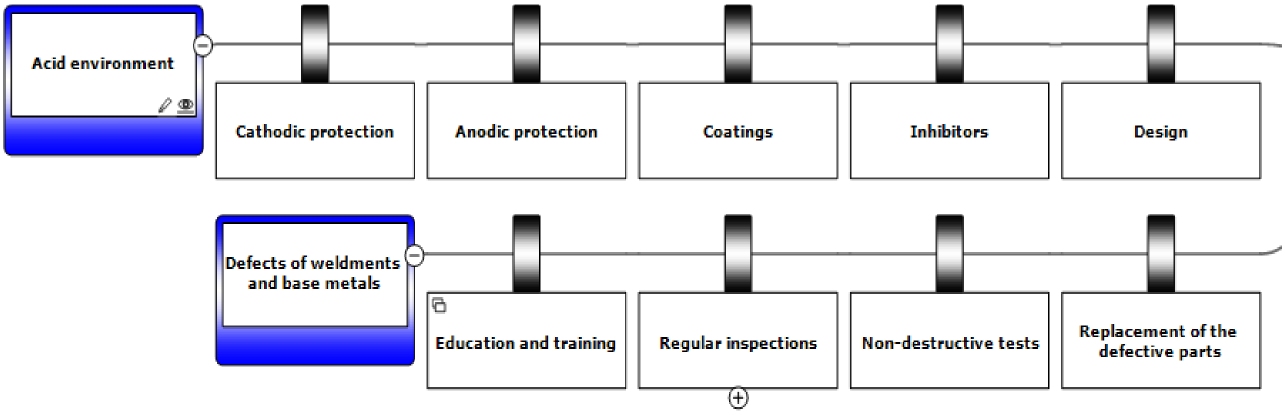

Fig.[3.14] Protective barriers against acid environment and defects of weldments and base metals.

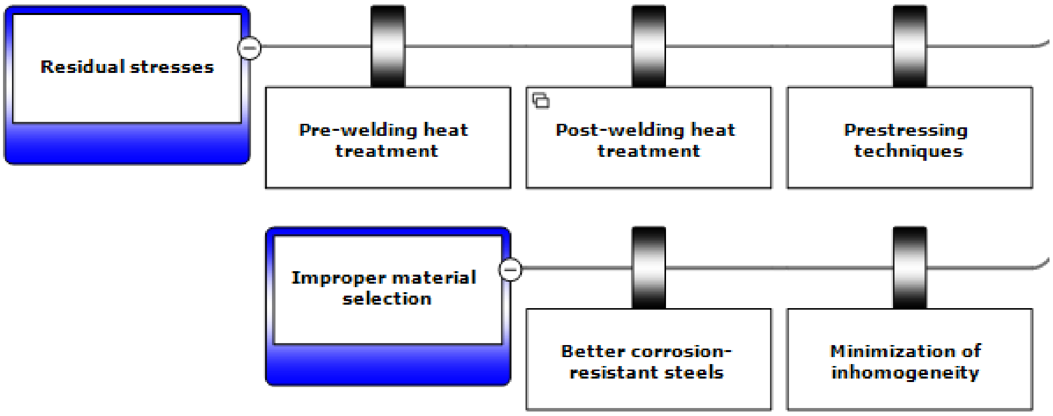

Fig.[3.15] Protective barriers against residual stresses and improper material selection.

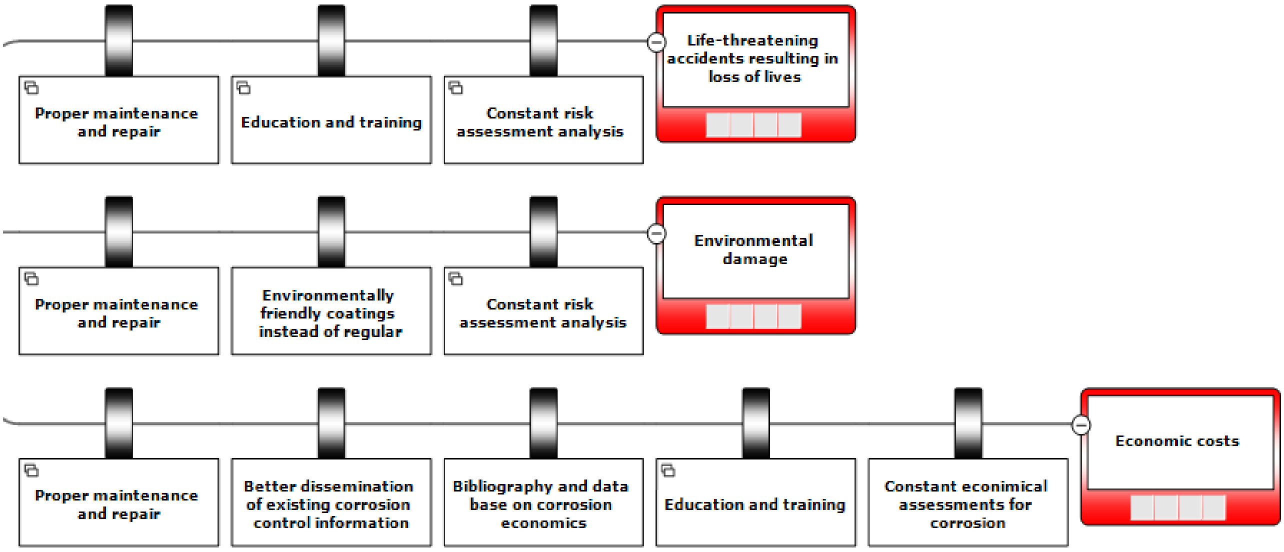

Fig.[3.16] Recovery barriers against life-threatening accidents, environmental damage and economic costs.

In Fig.[3.17], a simple example of an escalation factor is presented.

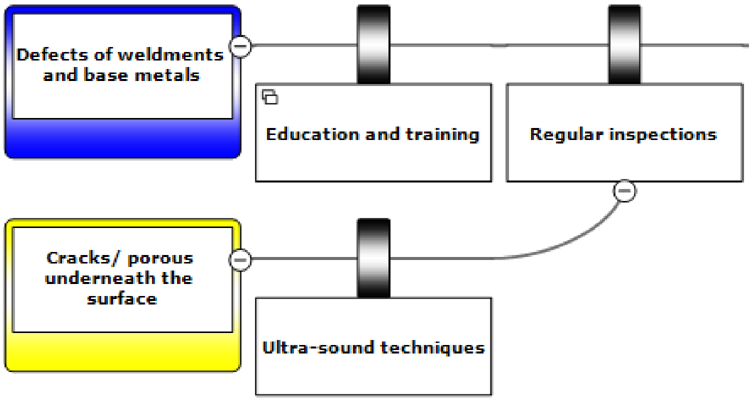

Fig.[3.17] Possible escalation factor that can mitigate the effect of a protective barrier.

4. EXPERIMENTAL TECHNIQUES

4.1. Electrochemical techniques

4.1.1. Introduction [10][33]

The corrosion mechanism in an aqueous phase is of electrochemical in nature. The electrochemical signal is one of the primary sources of information for the study of the potential, current and electrical charge of a corroding electrode. It arises from processes that cause corrosion and other electrochemical reactions. In order to estimate the corrosion behavior of a specimen (polarization resistance and corrosion rate) as well as its corrosion mechanism, electrochemical techniques are employed, which are modern and can produce reliable results for the determination of the corrosion rate.

In the following paragraphs, four electrochemical techniques are used for the determination of the corrosion rate and the polarization resistance of the metallic surface of our specimens:

- Linear Polarization Resistance (LPR), which includes both the anodic and the cathodic branches of potential E versus current density i plot.
- Potentiodynamic Polarization- Tafel Extrapolation technique (TE), which takes into account the linear segments of the anodic and cathodic branches of polarization, of the potential E versus the current density i plot.
- Electrochemical Impedance Spectroscopy (EIS), which requires alternating current, AC. The method’s output is a Nyquist plot for charge transfer or diffusion control that can be used to determine polarization resistance, Rct. Polarization resistance is the faradaic resistance of the reaction and is inversely proportional to the corrosion rate i_{corr}. This method also offers Bode diagrams of the |Z| and its phase versus frequency.
- Cyclic Polarization method (CP), which is used in order to measure the pitting corrosion of the specimens (via SEM in this study), presenting a plot similar to the Tafel extrapolation's, but with a wider ranger for the anodic branch.

In the following paragraphs, all of the four methods mentioned above are cited, Linear Polarization Resistance, Tafel Extrapolation technique, Electrochemical Impedance Spectroscopy and Cyclic Polarization method. These electrochemical methods display some important advantages in the determination of the corrosion rate:

- Corrosion rates can be determined in a very short time, only in a few minutes, whereas conventional methods, such as weight loss measurements, need several days or even more to produce results.
- These methods are sensitive and accelerating factors, e.g. elevated temperature, are not required in order to increase the rate of the reaction in the laboratory.
- Electrochemical Impedance Spectroscopy can be used repeatedly to measure consecutive corrosion rates on the same electrode, since this is a non-destructive method.

4.1.2. Linear Polarization Resistance (LPR) method [10][12][31][33]

Linear polarization resistance (LPR) methods can be used to characterize a material medium pair by scanning the current–potential (i–E) domain. Researchers have observed experimentally that there is a linearity at the origin of the polarization curve for overvoltages up to a few millivolts. Thus, the slope of this linear curve is inversely proportional to the corrosion rate and it is called polarization resistance R_P. It's an electrochemical technique which is adapted to rapid corrosion rate measurements, a condition necessary to its success in industrial monitoring corrosion operations.

For a system in which electrode processes involve a slow reaction step at the electrode surface, the rate of reaction is limited by activation overvoltage; the relationship between the reaction rate, or net current density *i*, and the driving force for the reaction, or potential *E*, is given by the Butler-Volmer equation. This equation relates *i*, for a single electrode process, such as

$$Fe \leftrightarrow Fe^{2+} + 2e^{-} \tag{4.1}$$

to *E* by the formula

$$\begin{aligned} i &= i_0 \left[\exp\left(\frac{anF\eta}{RT}\right) - \exp\left(\frac{(1-a)nF\eta}{RT}\right)\right] \\ &= i_0 \left[\exp\left(\frac{anF(E-Erev)}{RT}\right) - \exp\left(\frac{(1-a)nF(E-Erev)}{RT}\right)\right] \end{aligned} \tag{4.2}$$

where η is the overpotential, i_0 the exchange current density (rate of either the forward or reverse half-cell reaction) at the equilibrium potential *Erev*, α the transfer coefficient (usually close to 0.5, but must be between 0 and 1), and *n* the number of electrons transferred.

The graphical representation of the Butler-Volmer equation, as shown in Fig.[4.1] , is called the polarization curve.

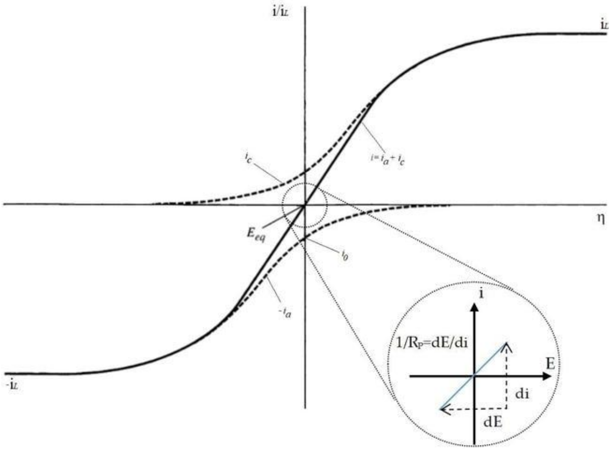

Fig.[4.1] Current density (i)-overpotential (η) curves for the system where α = 0.5 and $i_L,a = -i_L,c = i_L$. Partial current densities: ia, ic (dashed line), i_L limit current density (horizontal line), and RP the polarization resistance (circle).[10]

It is well known that the electrochemistry of corroding metals involves two or more half-cell reactions. Suppose there is a simple corrosion system, such as an iron metal Fe (a corroding working electrode) immersed in a sulfuric acid solution, in addition to (4.1), the following half-cell reaction also occurs:

$$H_2^{+}+2e^{-}\leftrightarrow H_2 \tag{4.3}$$

The dissolution of Fe takes place in the acid electrolyte. At equilibrium, the total anodic rate is equal to the total cathodic rate. In this case, the net rate of either Fe dissolution or hydrogen evolution can be measured at the electrode potential of the steady-state freely corroding condition. This potential refers to the corrosion potential *Ecorr*, which lies between the equilibrium potentials of the two individual half-cell reactions. At *Ecorr*, the net rate corresponds to the uniform corrosion rate, *icorr*, at free corrosion condition. In such system, the relationship between the overpotential (η, applied potential minus corrosion potential) and the current (flowing between the working electrode and the auxiliary counter electrode) is governed by the fundamental **Butler-Volmer** equation given as follows:

$$\begin{aligned} i &= i_0\left[\exp\left(\frac{anF\eta}{RT}\right) - \exp\left(\frac{(1-a)nF\eta}{RT}\right)\right] \\ &= i_0\left[\exp\left(\frac{anF(E-Erev)}{RT}\right) - \exp\left(\frac{(1-a)nF(E-Erev)}{RT}\right)\right] \end{aligned} \tag{4.4}$$

The two reactions are activation controlled and their experimental polarization curves can be drawn using the following relations:

$$i_{app,a}=i_a-i_c \tag{4.5}$$

$$i_{app,c}=i_c-i_a \tag{4.6}$$

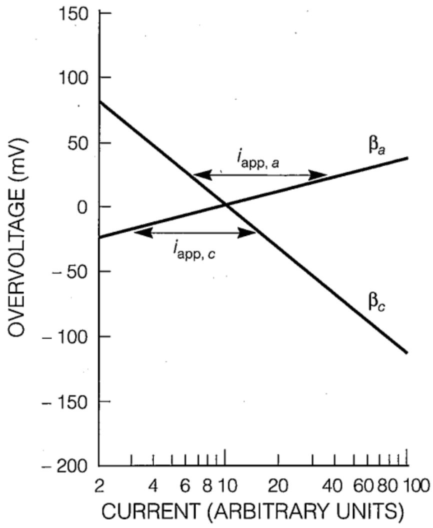

Fig.[4.2] Hypothetical anodic and cathodic polarization curves.[33]

where $i_{app,a}$ and $i_{app,c}$ are the applied anodic and cathodic current densities, i_c is the current density for the cathodic reduction reaction and i_a is the current density for the anodic oxidation reaction. To calculate R_P (units in ohms), the **Stern- Geary** equation can be used

$$R_p = \frac{B}{Icorr} \tag{4.7}$$

where Icorr is the corrosion current density and B is the proportionality constant for the particular corrosion system, which can be determined empirically from the anodic and cathodic slopes of a Tafel plot (β_a, β_c) as

$$B = \frac{\beta a\, \beta c}{2.3\ (\beta a + \beta c)} \tag{4.8}$$

The extent of the linear part of the polarization depends mainly to the values of the Tafel constants. When relatively high values for the Tafel constants are chosen, then the linearity of the polarization curve is extended. On the other hand, when low values are selected, then the linearity is limited. Moreover, when Tafel constants are unequal, the linearity is even more limited and the curve (i-E) doesn't present symmetry.

Two instrumental methods have been developed for the determination of the Linear Polarization Resistance. The galvanostatic or constant-current technique and the potentiostatic or potentiodynamic method.

Progress is made through competitive advantages between different measuring techniques, including rapidity in current measurement (generally rather quickly in a few minutes), where only a lower excitation is required (less than ±30 mV), so that the corrosion rate would not be affected by corrosion reactions, an easy measurement of low corrosion rates and measurements taken repeatedly, the LPR technique can be considered as a nondestructive technique and used for online corrosion monitoring of uniform corrosion rates useful for the field.

The main drawback of this technique is that the Tafel parameters must be known in advance in order to convert the polarization resistance into the corrosion rate. To tackle this problem, several numerical methods have been proposed to obtain both Tafel parameters and corrosion rate from the same polarization measurement in the vicinity of the corrosion rate. Nevertheless, the success is limited since the Tafel parameters thus determined will not be very accurate, which may compromise the non-destructive nature of the LPR technique. Another disadvantage of the LPR method lays in the fact that it will not work properly in low conductive media. Basically, the LPR technique can only be used to determine uniform corrosion rates; it can hardly provide information about localized corrosion.

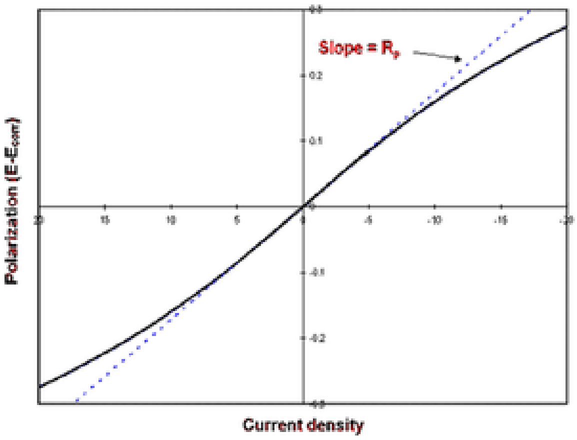

Fig.[4.3] Polarization resistance R_P, the slope of this linear curve[33].

The results obtained from the polarization of the specimens were elaborated employing EC Lab Software, a free software, which was used in order to determine the corrosion potential E_{corr} and current I_{corr} as well as the corrosion resistance Rp (polarization resistance) of the specimens. LPR measurements are simple and rapid (response time a few minutes) and give instantaneous corrosion rates.

The linear polarization resistance method consists of applying to the metal very small voltage variations (typically less than 30 mV) above and below its corrosion potential. The linearity near the origin is especially pronounced when relatively high values are selected for the Tafel constants, such as $\beta_a=\beta_c=0.118$ V.

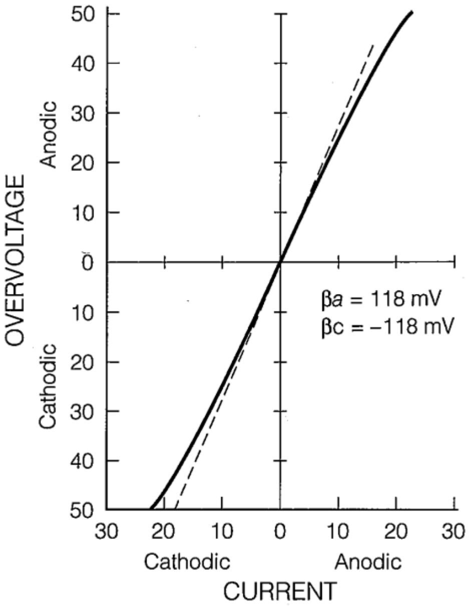

Fig.[4.4] Linear proximity near the origin for Tafel values $\beta_a=\beta_c=0.118$ V.[33]

As a result, the polarization resistance Rp was determined through a process of linear regression of the data obtained around E_{corr} within a range, which is set to 25 mV above and below E_{corr}, and with Tafel constants set to 120 mV. R_P is given by the inverse of the linear fit slope.

4.1.3. Potentiodynamic Polarization- Tafel Extrapolation method [10][12][[33][34][39]

The Tafel extrapolation method is a mathematical technique that estimates the corrosion current (I_{corr}) and the corrosion potential (E_{corr}) in an electrochemical cell, and by extension, the corrosion rate. Extrapolation involves extending a known sequence of linear values within a Tafel plot to determine these parameters. Extrapolation of the linear portion of the curve to E_{corr} is utilized to gain the corrosion current density. Presuming uniform corrosion, Faraday's law can be utilized to convert the corrosion density into the rate of penetration or weight loss. Using this technique, it is feasible not only to measure appreciably low corrosion rates but also to perform continuous monitoring of the system under investigation. Assume a system in which the following redox reactions take place:

$$M \rightarrow M^{+n} + ne^{-} \quad \text{(anodic reaction)} \tag{4.9}$$

$$2H^{+} + 2e^{-} \rightarrow H_2 \, \text{(cathodic reaction)} \tag{4.10}$$

When an excess of electron flow is applied, current density i_{app}, the equilibrium of the system is disturbed. The electrode potential shifts positively or negatively from E_{corr} to E. Simultaneously, the excess of electron flow forces the rates of both reactions to change. The rate of the oxidization becomes i_a from i_{corr} and the rate of the reduction moves to i_c from i_{corr}, too. It is obvious that the absolute difference between i_a and i_c equals to the i_{app}, according to the principle of charge conservation:

$$i_{app}=|i_a-i_c| \tag{4.11}$$

If numerous values of current density i_{app} are applied to the redox system and each pair of i_{app} and of counterpart E is plotted on a diagram of potential versus log i_{app}, then a polarization curve is created. A polarization curve is the result of polarizing from the corrosion potential anodically and/or cathodically. Figure [4.5] shows typical cathodic polarization data for iron in an acid solution, with extrapolation of the cathodic Tafel slope back to the corrosion potential, E_{corr}, and the intersection gives the corrosion rate or corrosion current density, i_{corr}.

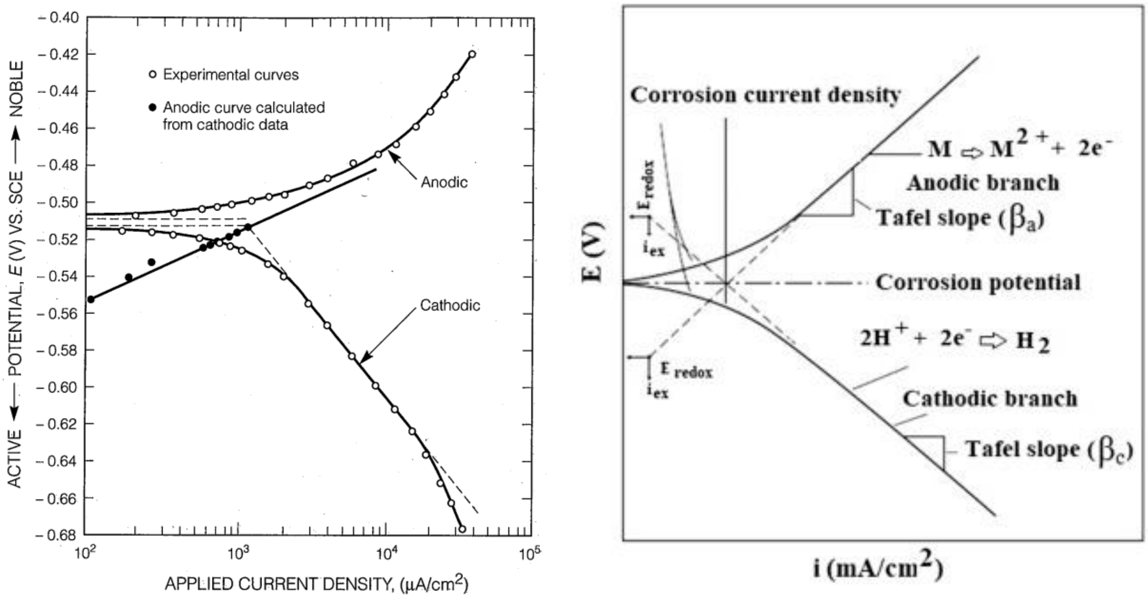

a) b)

Fig.[4.5] a) Cathodic polarization data showing Tafel behavior, b) Tafel curves-anodic branch for the metal and cathodic for hydrogen. [33]

The existence of a linear relationship between *E* and log *I* has been demonstrated when the electrode is polarized at sufficiently large potentials, and far away from the corrosion potential both in anodic and cathodic directions, as can be seen in the polarization curve depicted in Fig.[4.5] b. The portions in which such relationships prevail are called Tafel portions or Tafel regions. This can be mathematically expressed as:

$$\begin{aligned} I &= I_{corr}\left[\exp\left(\frac{2.303\eta}{\beta a}\right) - \exp\left(\frac{2.303\eta}{\beta c}\right)\right] \\ &= I_{corr}\left[\exp\left(\frac{2.303(E-Eoc)}{\beta a}\right) - \exp\left(\frac{2.303(E-Eoc)}{\beta c}\right)\right] \end{aligned} \tag{4.12}$$

where *Ecorr* is the corrosion potential, *E* the applied potential, η the overpotential (difference between *E* and *Ecorr*), *I* the current, *Icorr* the corrosion current, and βa and βc are the Tafel constants or Tafel parameters derived from $E - \log I$ plots as the anodic and cathodic slopes in the Tafel regions, respectively.

Extrapolating from the Tafel portions of either anodic or cathodic or both, an intersection point is obtained at *Ecorr*, from which *Icorr* is readily available from the log *I* axis. Therefore, it is possible to obtain simultaneously the corrosion current, *Icorr*, and the Tafel parameters (i.e., βa and βc) from this method.

In order to obtain the Tafel portions in the anodic and cathodic regions, the electrode has to be polarized far away from its corrosion potential, e.g., ±250 mV away from *Ecorr*. (4.11) can be rearranged, as appropriate, to choose one single polarization direction, either anodic or cathodic way. The linear parts of the curve on a semilog plot are called Tafel behavior. They obey Tafel's relationship, which connects polarization to current density i_a or i_c. For anodic and cathodic polarization respectively, the relationships are:

$$\eta_a = \beta_a \log \frac{I}{Icorr} \quad (4.13)$$

$$\eta_c = \beta_c \log \frac{I}{Icorr} \quad (4.14)$$

Where: β_a, β_c: Tafel constants for anodic and cathodic reactions, respectively.

Tafel plots are generated by plotting both anodic and cathodic data in a semilog diagram as *E*-log *I*. From the plot, three values are determined: the anodic Tafel slope, the cathodic Tafel slope, and *Icorr* (from back-extrapolation of both anodic and cathode curves to *Ecorr*).

The Tafel extrapolation method presents some limitations when used for determining corrosion rates:

- At least one of the branches of the polarization curves has to be activation controlled.
- Anodic or cathodic parts, which show Tafel behavior, need to exist and be well-defined.
- Large current densities are often required to generate the complete Tafel plots. The use of large current densities can alter the surface conditions of the specimen (e.g., permanent change or surface damage), thereby distorting the results and increasing complications due to mass transport and uncompensated electrolyte resistance.
- The anodic and the cathodic reactions which occur at the corrosion potential are also the only reactions which occur during determination of the polarization curves. This means that changes in electrode potential does not induce additional electrode reactions.
- Corrosion has to be general in nature and localized corrosion should not occur.
- The measurement of current density over a wide potential range may also distort the results if the adsorption of some species is potential dependent. Since this method applies a large overpotential to the metal surface (e.g., anodic polarization), therefore, the technique is rather destructive and can hardly be used for online corrosion monitoring purposes and in particular in the field.
- The polarization curves are for the steady-state.

In this study, where the specimens were set in a 3.5% NaCl solution for all the Tafel extrapolation experiments, the anodic reaction is the dissolution of Fe:

$$Fe \rightarrow Fe^{2+} + 2e^{-} \quad (4.15)$$

whereas, the predominant cathodic half-cell reaction is

$$O_2 + 2H_2O + 4e^{-} \rightarrow 4OH^{-} \quad (4.16)$$

rather than the hydrogen evolution reaction which occurs in acid solutions. As a result of the oxygen's reduction, the cathodic polarization curve displays a limiting diffusion current i_L, while the anodic dissolution of iron obeys Tafel's law, Fig.[4.6] . Thus, the cathodic process is controlled by concentration polarization rather than activation polarization.

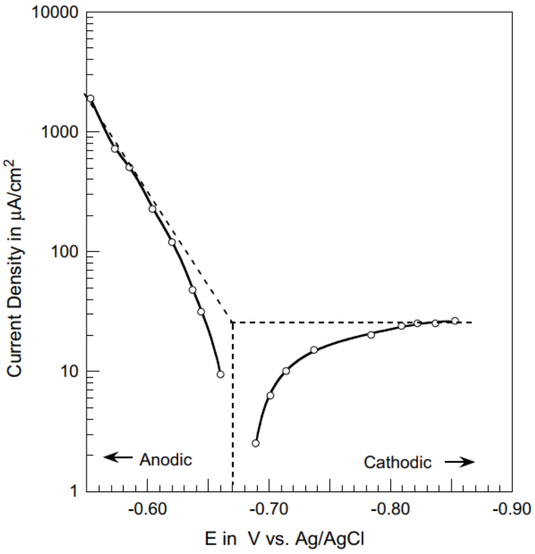

Fig.[4.6] Polarization curves for iron in NaCl solution- diffusion display of the cathodic branch. [39]

Nevertheless, both branches can be extrapolated back to E_{corr} in order to give i_{corr}, as, at the open-circuit corrosion potential, the net rate of iron dissolution is equal to the net rate of oxyden reduction, i_L.

In this study, EC Lab Software was used for the data elaboration, in order to define the Tafel parameters, as long as the corrosion rate of the speciments. The equivalent weight of each speciment was measured and estimated individually via XRF, and was inserted in the software, along with the density and the surface area before the elaboration. On the point of the intersection of the linear regressions, the corrosion potential, corrosion current, the Tafel parameters, and the corrosion rate were calculated. Corrosion rate is estimated through the following function

$$\mathrm{CR}=\frac{Icorr\ K\ EW}{d\ A} \qquad (4.17)$$

where K is a constant that defines the units of the corrosion rate, EW is the equivalent weight is equal to the molar mass of the tested metal devided by the number of the electrodes involved in the redox reaction, d is the density of the tested metal and A is the sample area.

There is a possibility that Tafel and corrosion parameters do not provide a satisfying fit, when the redox reaction has not a Stern behavior but rather a mass transport limited behavior or when passivation occurs. Then, satisfying parameters may be obtained and the error minimized by minimizing x^2,

$$\mathrm{x}^2=\frac{1}{N}\sqrt{\frac{\sum_{i=1}^{N}(Imeas,i-ICalc,i)^2}{Imeas,i+10^{-9}}} \qquad (4.18)$$

4.1.4. Electrochemical Impedance Spectroscopy (EIS) method [8][10][12][33][54]

The electrochemical impendance spectroscopy, EIS, is a technique for the analysis of the response of corroding electrodes to small-amplitude alternating potential signals of widely varying frequency. The EIS technique normally uses a typical three-electrode cell system controlled by a potentiostat, similar to that used in the LPR technique, but with a Frequency Response Analyzer (FRA). Unlike the previous time-resolved techniques, where the current system response is either the consequence of a large voltage perturbation from the steady-state condition (Tafel extrapolation) or from a smaller perturbation (LPR method), in the EIS approach, by applying a small varying perturbation over a range of frequency, it is possible to probe the full response of the electrochemical system, and not just the resistive components.

In that respect, a small AC signal, i.e., alternating potential or voltage $V(\omega)$ typically a *sine* wave of amplitude ±10 mV of the corrosion potential, is applied over a wide range of frequency (typically from 10^5 down to 10^{-2} Hz) at a number of discrete frequencies (typically 5–10 frequencies per decade), and the alternating current response, $i(\omega)$, is measured at each frequency, ω (i.e., the ac polarization or angular frequency, $\omega = 2\pi f$). When a sinusoidal alternating potential signal V(t) is applied to an electrode surface, the time-dependent current response I(t) is expressed through an angular dependent impedance Z(ω). The relationship connecting these three parameters is:

$$Z(\omega)=\frac{V(t)}{I(t)} \tag{4.19}$$

Where:

$$V(t)=V_o \sin(\omega t) \tag{4.20}$$

$$I(t)=I_o \sin(\omega t+\theta) \tag{4.21}$$

θ: phase angle between V(t) and I(t). Several processes on the electrode surface absorb electric energy in different frequencies. As effect, they create a time lag between excitation and response. These processes are simulated by resistive-capacitive electric networks.

The impedance Z(ω), may be expresses in terms of real, Z'(ω), and imaginary, Z"(ω), as

$$Z(\omega) = Z'(\omega) + Z''(\omega) \tag{4.22}$$

where $\omega = 2\pi f$. The impedance behavior of an electrode may be expressed in Nyquist plots of the imaginary component of Z as a function of the real componenent of Z, as in Fig.[4.7] a,or in Bode plots of log|Z| and log(Phase) versus the logarithmic scale of the frequency f in Hertz, as in Fig.[4.7] b.

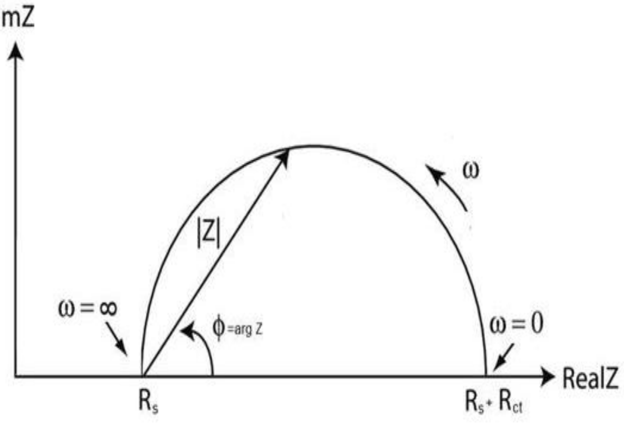

a)

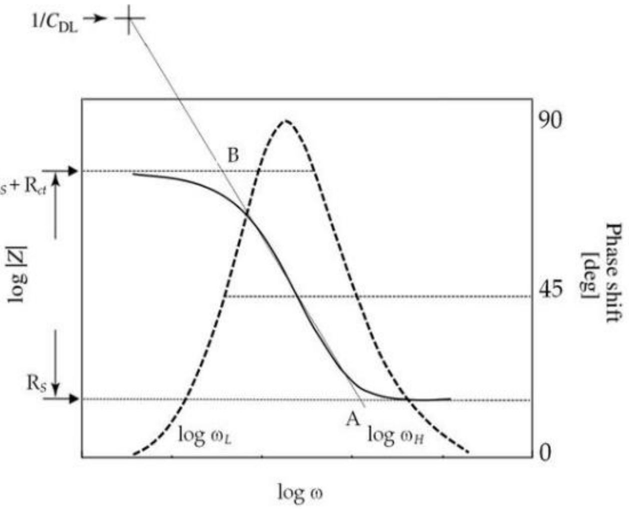

b)

Fig.[4.7] Electrochemical Impedance Spectroscopy: a) Nyquist plot, b) Bode plot.[10]

The Nyquist plot shows a semicircle, with increasing frequency in a counterclockwise direction, Fig.[4.7] a. At very high frequency, the imaginary component disappears, leaving only the solution resistance, R_Ω (R_1 in our experiments via EC Lab). At very low frequency, the imaginary part disappears again, leaving the sum of R_Ω and the polarization resistance, Rp (R_2 in our experiments via EC Lab).

A typical example is shown in Fig.[4.8], where R_S, R_{CT}, and CPE represent labels for the solution resistor, the Faradaic charge transfer resistor, and the Constant Phase Element (CPE), Q, respectively. The CPE impedance is frequency dependent, just like the capacitor's impedance, C. The difference between them is that in the case of Q, the Nyquist plot corresponds to a straight line in the imaginary part (-Im(Z)>0) with an angle with the real axis ($-\alpha\pi/2$), whereas, in the case of C, the same plot corresponds to a vertical straight line in the imaginary positive part.

The CPE is associated with the separation of charges at the electrode/electrolyte interface as in the case of a working electrode having a surface film (e.g., AISI 304 stainless steel immersed in a 0.5 M H_2SO_4 electrolyte), in which case the capacity of the equivalent circuit can be associated with the capacity of the passive oxide surface film and the resistor in parallel with the CPE is considered as the charge transfer resistance, R_{CT} (or the polarization resistance, R_P, under *EIS*-free corrosion conditions), while the ohmic resistance in solution, R_S, between the working electrode and the reference electrode is in series with the parallel resistor and the CPE, Fig.[4.8].

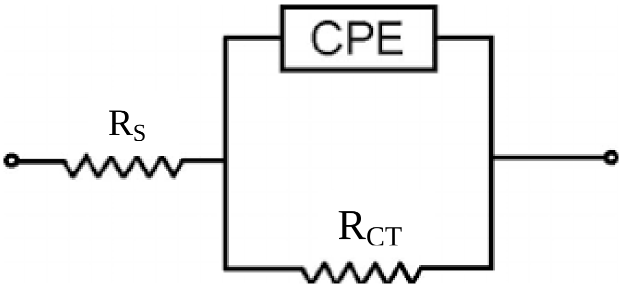

Fig.[4.8] The ohmic resistance in solution, R_S, between the working electrode and the reference electrode is in series with the parallel resistor and the CPE. [10]

The situation struggles when diffusion processes govern the corrosion behavior. When a redox system is controlled by the diffusion rate in the electrolyte, which reveals concentration polarization, in a surface film or coating, the electric circuit changes and an additional resistive element is introduced. This element is called Warburg impedance, W, and it affects the Nyquist plot as it is presented on the following graph, Fig. [4.9].

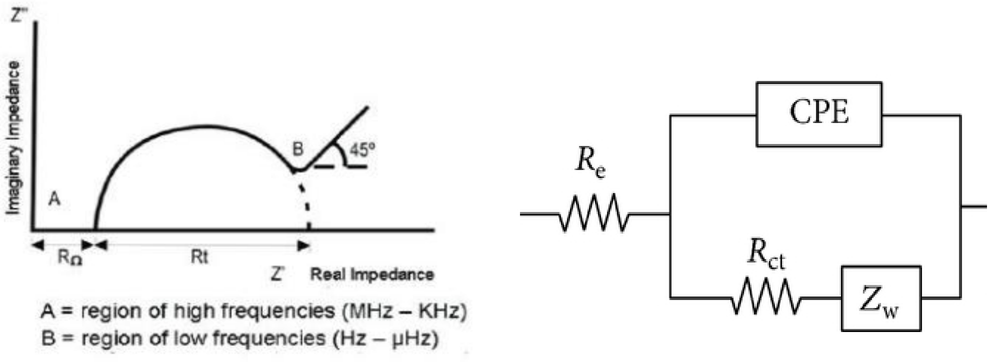

Fig.[4.9] Nyquist plot of a circuit with Warburg impedance. [54]

The Warburg impedance does not appear at high frequencies. In the Nyquist plot, this impedance will result in a straight line at a constant phase angle at 45°. However, the effect of the Warburg impedance can complicate the correct estimate of the *RP* value in certain cases.

It is important to mention that Electrochemistry Impedance Spectroscopy produces invalid measurement for polarization resistance, R_P, when the exchange current density applied to the system is very large. These experimental conditions approach simple direct-current electric circuit and more complex instruments are needed so that valid measurements are obtained. However, this method is really useful as it offers unambiguous results for polarization resistance and corrosion rate, corrected for ohmic interferences due to solution resistance.

Moreover, it can reveal important information about reaction mechanism through frequency response of the corroding electrode.

Impedance analysis is a powerful tool to determine the mechanism involved in an electrochemical reaction and the values of the kinetic parameters of this mechanism. Thus, its data analysis allows the user to propose an electrochemical reaction mechanism to define the system. The EC Lab Software was used to elaborate the experimental data and to determine the specimen’s resistance to corrosion. The software offered a wide variety of number as well as type of elements or components for the equivalent circuit. The EIS section of analysis menu is dedicated to the analysis of EIS data. Also, it is possible to simulate various EIS diagrams with Z Sim tool, or to fit with various electrical circuits an existing diagram with Z Fit tool. In this case, the chosen equivalent circuit consisted of a resistance R_1, the solution resistance, in series with a constant phase element Q_2 (CPE) and a resistance, R_2, the resistance of the specimen, connected in parallel, Fig.[4.10].

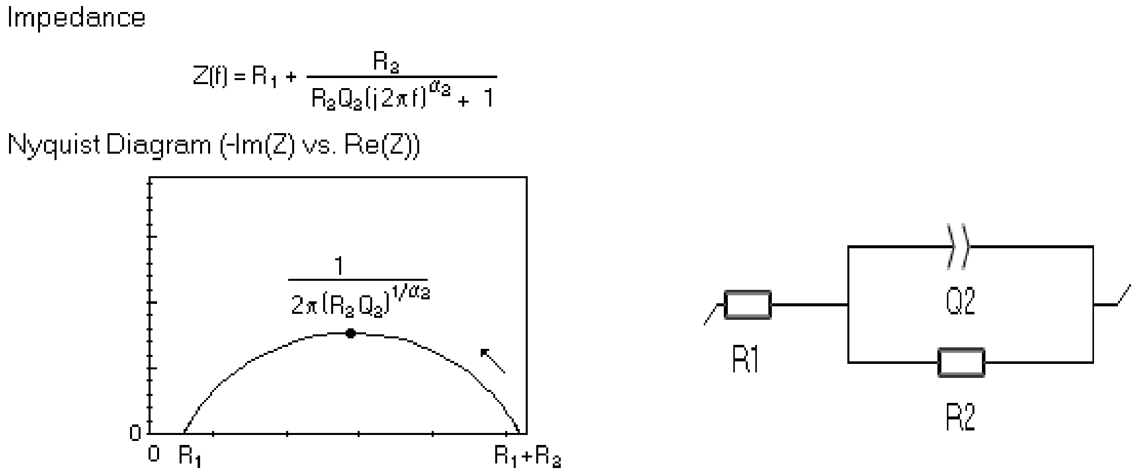

Fig.[4.10] EIS method on EC Lab, with R_1,Q_2 and R_2 parameters.[12]

For each one of the parent metals and different weld combinations, after the elaboration of the data, the following plots were obtained:

- Nyquist plots
- Bode plot of impedance |Z| vs frequency
- Bode plot of phase vs frequency

In this chapter of the study, two figures were obtained for each EIS experiment. The first one is the Nyquist plot (-Im|Z| vs Re|Z|), while the second figure is the combination of the two Bode plots (impedance |Z| vs frequency and phase vs frequency), along with their fitting curves. The last point of the fitting curve of the Nyquist plot (R_2) is equal to the first point of the fitting curve of the Bode plot of impedance |Z| vs frequency (Rp). Thus, in the end of our analysis we will refer to these values as Rp.

4.1.5. Cyclic Potentiodynamic Polarization (CPP) method [12][21][33][52][58]

Uniform corrosion is one of the most common forms of corrosion in metals, but, in some cases, it can be prevented due to passivity. Passivity is defined as a condition of corrosion resistance due to formation of thin surface films under oxidizing conditions with high anodic polarization (e.g. stainless steel). However, localized corrosion (pitting corrosion, crevice corrosion and stress corrosion cracking) can occur by breakdown of the passive film in the presence of aggressive ions. Electrochemical investigation of passivity is used to evaluate the materials' resistance to localized corrosion. Thus, Cyclic Potentiodynamic Polarization (CPP) method is a suitable way for investigation of the beginning of passivity, breakdown of oxide film, susceptibility to repassivation and calculation of the rate of pitting corrosion due to the vast range of scanning potential.

General shape of CPP curve is as follows; after passing through the region of active corrosion, the current density decreases to a critical potential, called "Flade potential" or "primary passivation potential". This decrease is due to the formation of the passive layer on metal surface. The passive current density is the current density in the passive region. With further increase in the potential in the passive region, a rapid rise in the anodic current can be detected. This rise is due to either the evolution of oxygen by the decomposition of water, or the breakdown of the passive film, the initiation of pitting and occurrence of localized corrosion.

In order to assess the localized corrosion susceptibility of the materials CPP measurements should be carried out according to the defined ASTM standards (F2129, G61). After the preparation of the test of the specimen for stabilizing the rest potential Er (the potential of working electrode to the reference electron under the Open Circuit condition- as in every method used so far in this study), the specimen is immersed in a prepared electrolyte. Then, the potential scan starts at the OC and moves in the noble direction in a cyclic path with a slow scan rate, between the working electrode and auxiliary electrode. Finally, the scanning potential is reversed to the starting point. The interpretation of the CPP scan is difficult. The extracted parameters from the cyclic curves are not constant and vary from material to material. They are empirical parameters and change in different experimental conditions. The parameters used to interpret the CPP curves include: pitting potential, repassivation or protection potential, potential of anodic to cathodic transition, hysteresis and active passive transition (anodic nose). In the CPP method, relative position of pitting and repassivation potential with respect to the corrosion potential are the most important parameters for evaluating the pitting corrosion behavior.

In the anodic polarization scan , scanning starts from corrosion potential after reaching the steady state. Before reaching the potential of O_2 evolution, a rapid increase in the current density may occur due to either some defects of the surface film or the breakdown of the oxide film and occurrence of the pitting corrosion in the presence of aggressive ions. The potential at which the current density increases rapidly in that way is called *pitting corrosion* potential. For some metals, the pitting potential coincides with the corrosion potential, which occurs when there is an oxide film on the material surface prior to the polarization, Fig.[4.11]a. Due to the intersection of the cathodic branch with the transpassive region of the anodic branch, the value of pitting potential is the same as corrosion potential.

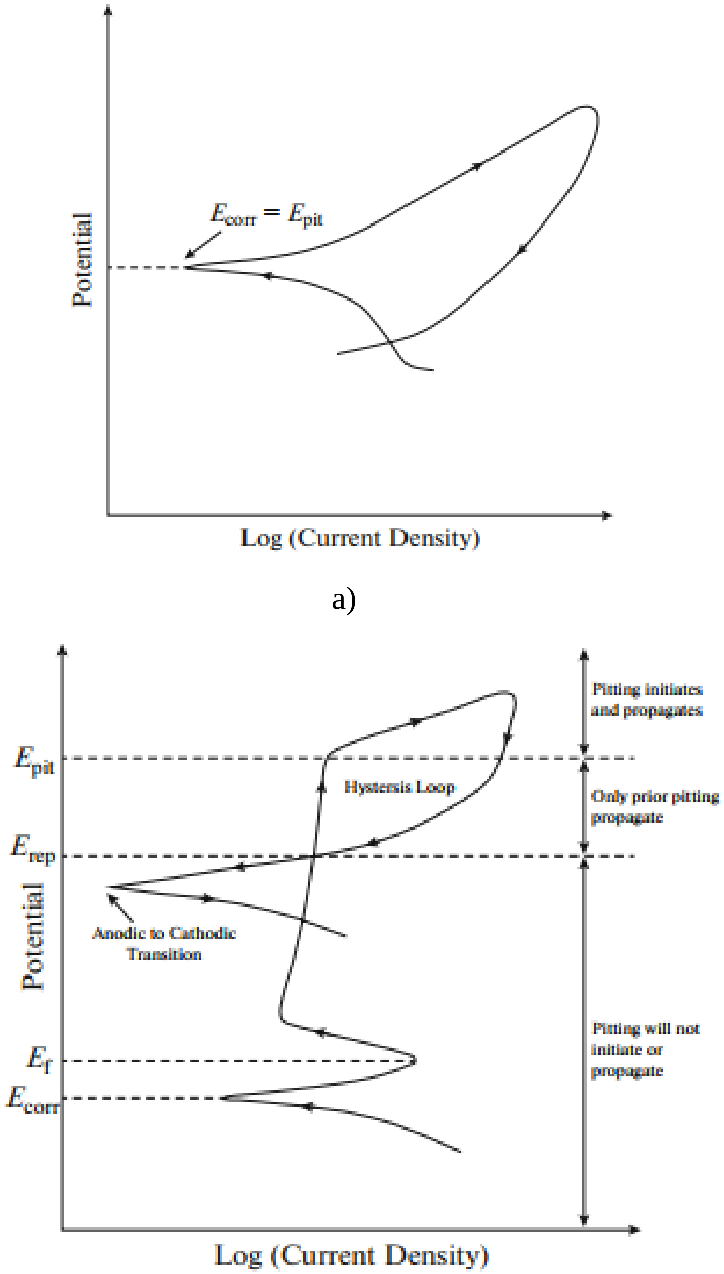

a)

b)

Fig.[4.11] Schematic illustration of a) CPP of Al in 3.5 wt % NaCl solution, b) CPP curve and corrosion parameters.[21]

In the CPP curve, after the increase of the current density at pitting corrosion, the scanning direction changes and then, with the potential reduction toward the negative potentials, the current density in the reverse scan may be different than that in the forward scan (hysteresis), as shown in Fig.[4.11] b. The scan continues until the reverse curve crosses the forward polarization curve and the intersection point is called protection potential. At the potentials between the protection potential and corrosion potential, the passive film is stable and no pits will initiate or grow. This region is called perfect passivity. At the potentials between the pitting potential and protection potential, only old pits propagate and no new pits are formed. Finally, at potentials above the pitting potential, new pits will initiate and develop.

The difference between forward and reverse current densities at the same potential demonstrates the size of hysteresis. The bigger size of hysteresis loop means more passive film disruption, following with more difficulty for restoring the damaged passive film. There are two types of hysteresis at the more positive potentials: *positive hysteresis* is related to the decrease of the passivity due to the localized corrosion that causes the increase of the current density in reverse scan, in comparison to the current density in the forward scan, at the same potential, Fig.[4.11] b. *Negative hysteresis* happens when the degree of surface passivation is greater at more noble potentials, which causes the current densities in the reverse scan to be lower than those in the same potentials of the forward scan, Fig.[4.12] a. The absence of hysteresis loop during the potential scan (the forward curve coincides with the reverse curve) means that the localized corrosion does not occur but it could be a sign of an active surface and general corrosion. The difference between the pitting potential and the protection potential and also the area of the hysteresis loop indicate the probability of pitting corrosion. The higher the difference between Epit and Erp and the larger area of positive loop demonstrate the probability of low pitting corrosion resistance.

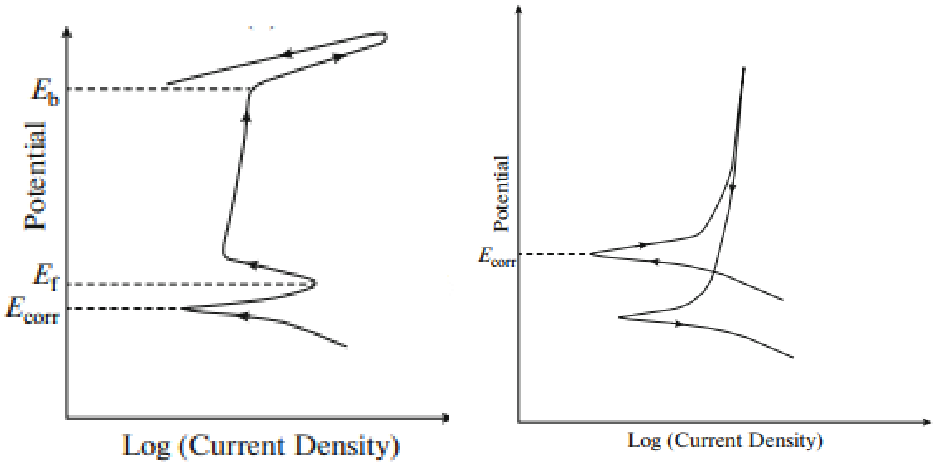

a) b)

Fig.[4.12] a) Schematic illustration of CPP curve with negative hysteresis, b) schematic illustration of CPP curve of Al alloy without hysteresis loop. [21]

The Anodic to Cathodic Transition potential is the potential at which the anodic current density varies to the cathodic current density. At the reverse curve, the decrease of the corrosion current density at a potential called active-passive transition potential (anodic nose) that is more noble than Ecorr occurs for alloys that are susceptible to passivity and restore the damaged oxide film, Fig.[4.11] b or the alloys that are not susceptible to pitting corrosion, Fig.[4.12] b. For these two groups of alloys, the difference between the anodic to cathodic transition potential and Ecorr are used to determine the persistence of the passive film.

According to the place of anodic to cathodic transition potential relative to the Ecorr, the passive layer stability is evaluated. If in the reverse scan, the anodic to cathodic transition potential is more noble than Ecorr, the passive layer will not be stable at Ecorr, Fig.[4.11] b, while the passivity will persist, if Ecorr gets more noble than the anodic to cathodic transition potential.

Finally, there are a lot of critical parameters which affect the CPP curve. Those are the solution resistivity, the scan rate, the point of scan reversal, the effect of aggressive ions, the effect of corrosion inhibitor and the effect of some metallurgical variables, such as heterogeneity at grain boundaries, disorder in the passive film by impurity atoms or inclusions. Some additional parameters that may affect the CPP curve are the temperature and the pH values, the dissolved gases in the electrolyte, the immersion duration, the fluid velocity and the surface roughness. Thus, it is very important to take under consideration a lot of different factors, in order to study the behavior of the CPP curve of a specimen.

The plotting of CPP curve on EC Lab was similar to that of the Tafel Extrapolation method (Ewe/V [y-axis] vs log[|I/mA|]), but with a very wider range in the anodic scan.

Finally, we obtained images of the pits of our specimens via SEM, by scanning the sample with a focused beam of electrons. The interaction of the electrons with the sample material produces signals that contain information about surface topography and composition, measuring the size of the pits.

4.2. Experimental procedures principles

4.2.1. Introduction

In the following section, the equipment used in this study is presented, along with relevant theory. A stereo microscope, an optical microscope and a Scanning Electron Microscope were used for the observation of the microstructure of the specimens, as well as their surface topography after each electrochemical technique. The micro hardness and the chemical composition were also measured using Vickers testing and X-ray Fluorescent (XRF) spectroscopy,respectively.

4.2.2. Stereo microscope [24][41]

The stereo or dissecting microscope is an optical microscope variant designated for low magnification observation of a sample using incident light illumination rather than transillumination. It works by using two separate optical paths instead of just one. The two objectives and two eyepieces provide the eyes with slightly different viewing angles. In essence, the left and right eye are seeing the same object but in a different way. Thus, it produces a three-dimensional visualization of the specimen. Stereomicroscopy overlaps macro photography for recording and examining solid samples with complex surface topography, where a three-dimensional view is essential for analyzing the detail.

The stereo microscope is often used to study the surface of solid specimens or to carry out close work such as dissection, microsurgery, circuit board manufacture or inspection of fracture surfaces. Thus, it is widely used in large numbers in manufacturing industry for manufacture, inspection and quality control. In this study, a Leica MZ6 stereo microscope was used for the observation of the specimens' surface, Fig.[4.13], especially after the application of each electrochemical technique.

Fig.[4.13] Stereomicroscope Leica MZ.

4.2.3. Optical microscope [20][42]

Microscopes are effectively just tubes packed with lenses, curved pieces of glass that bend (or refract) light rays passing through them. The simplest microscope of all is a magnifying glass made from a single convex lens, which typically magnifies by about 5–10 times. Microscopes used in homes, schools, and professional laboratories are actually compound microscopes and use at least two lenses to produce a magnified image. There's a lens above the object (called the objective lens) and another lens near your eye (called the eyepiece or ocular lens). Each of these may, in fact, be made up of a series of different lenses. Most compound microscopes can magnify by 10, 20, 40, or 100 times, though professional ones can magnify by 1000 times or more. For greater magnification than this, scientists generally use electron microscopes.

In this study, a Leica DM ILM optical microscope was used for the observation of the specimens' microstructure, Fig.[4.14]. Its main features are presented below:

- A light source
- Lenses that direct the light beam (eyepiece lens and objective lens)
- A diaphragm
- A stage, where the specimen is set
- A reflecting mirror

Fig.[4.14] Microscope Leica DM ILM.

4.2.4. Scanning Electron Microscope (SEM) [24][45]

The Scanning Electron Microscope (SEM) is used to observe and characterize surface features over large (or small) surface of the specimen. The primary electron beam interacts with the specimen surface to produce secondary electrons, backscattered electrons and X-rays. With detectors mounted just above the specimen, these electrons and X-rays can be collected and analyzed to provide important information about the specimen surface. Subsequently, we look at each interaction. In Fig.[4.15], the basic operating principles of a Scanning Electron Microscope are presented.

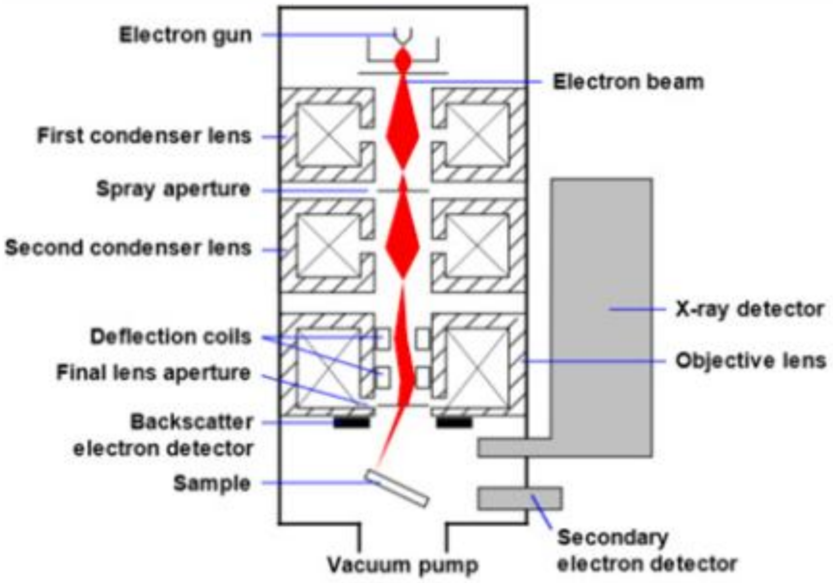

Fig.[4.15] Schematic representation of a Scanning Electron Microscope. [45]

The backscattered electrons are those electrons that are scattered from the specimen surface and can be collected as the primary beam scans the specimen surface. The collected backscattered electron image of the specimen surface is displayed on a cathode ray tube (CRT) and can be photographed. There is some energy loss during the backscattering process.

The higher the atomic number of the elements in the sample, the greater the degree of backscattering (less energy loss). This means that elements with higher atomic numbers (e.g. Fe, with an atomic number of 26) will appear brighter on the backscattered electron image on the CRT than elements with lower atomic numbers (e.g. O_2, with an atomic number of 8).

Secondary electrons, on the other hand, are the result of the interaction of primary beam electrons with the electrons contained within the atoms in the sample. The primary electrons can actually knock the loosely held orbital electrons from atoms, which are called secondary electrons and have much lower energy than the backscattered electrons. Thus, the secondary electrons can only be detected from the surface and near-surface regions of the specimen, because those from deeper regions are easily absorbed by the sample. As a result, the secondary electrons yield a secondary electron image on the CRT that reveals surface topography and produces an image with enhanced depth of field, which makes the SEM one of the most useful microscopes.

X-rays are also emitted from the sample, because of the interaction of the primary and backscattered electrons with the inner shell electrons of atoms in the sample. The primary/backscattered electrons have sufficient energy to knock inner shell electrons out of orbit. Where an electron is knocked out of a particular inner electron shell, an X-ray is emitted when an electron moves into space. The X-rays have a characteristic energy and wavelength for the particular atomic species present. Because of this, they are called characteristic X-rays, which means that every X-ray that is collected has an energy and wavelength that is unique to the particular element present in the sample. The importance of collecting these X-rays is that compositional information can be obtained. Generally, in a SEM, only the X-ray energy is analyzed.

In this study, the JEOL JSM-6390 Scanning Electron Microscope was used, Fig.[4.16], in order to measure and evaluate the pitting corrosion of the specimens tested.

Fig.[4.16] JEOL JSM-6390 Scanning Electron Microscope.[24]

4.2.5. Micro hardness [20][25]

For the parent metals, a hardness testing was conducted at LME, using Wolpert Wilson Instruments 402 MVD, Fig.[4.17a]. This is actually a pressure testing with a penetrator of known geometry and mechanical properties, and with the application of a small load to the specimen. We used Vickers micro-hardness testing method, in which, the penetrator is a diamond in the form of a square-based pyramid, with face angles of 136°. The applied load was F=2.940N (=299.8 gr) and the loading time was 15 seconds (according to standard ASTM E 384). On the surface of the specimens appeared an indent of a diamond shape after the test, Fig.[4.17b]. The lengths of the two diagonals d_1 and d_2 of the resulting square indent are measured by the micro hardness tester and their average value d is used in order to calculate hardness HV, as:

$$\mathrm{HV} = \frac{1854.4\,P}{d^2} \qquad (5.1)$$

where P is the applied force in gr and d is the mean diagonal length in mm.

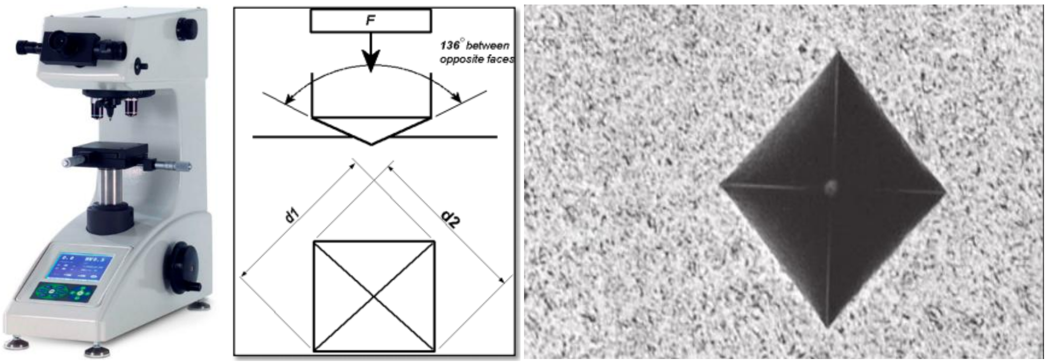

a) b) c)

Fig.[4.17] a) Wolpert Wilson Instruments 402 MVD, b) Vickers testing mechanism, c) Example of a well-formed Vickers indentation (400X) [15].

4.2.6. X-Ray Fluorescent spectroscopy (XRF) [57][67]

X-ray Fluorescence (XRF) spectroscopy was used in order to calculate the chemical and elemental composition of the materials. It is the measurement and analysis of samples excited by incident radiation. The two primary components of an XRF spectrometer are an X-ray output and a sensitive detector capable of determining fluorescent X-rays from the incident light. An XRF spectrometer works because if a sample is illuminated by an intense X-ray beam, known as the incident beam, some of the energy is scattered, but some is also absorbed within the sample in a manner that depends on its chemistry. When this primary X-ray beam illuminates the sample, it is said to be excited. The excited sample in turn emits X-rays along a spectrum of wavelengths characteristic of the types of atoms present in the sample.

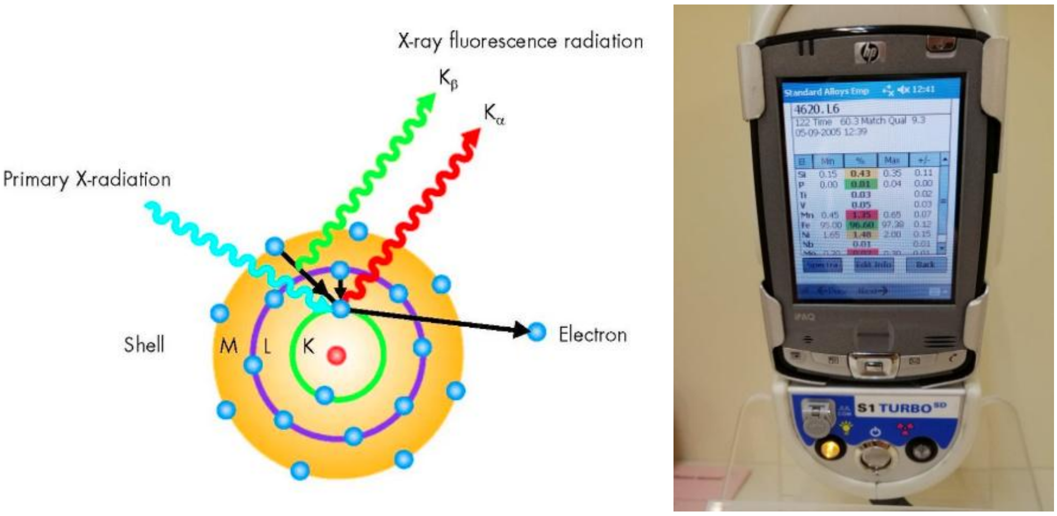

a) b)

Fig.[4.18] a) The principle of X-ray fluorescent spectroscopy [23], b) XRF S1 Turbo Bruker.

The atoms in the sample absorb X-ray energy by ionizing, ejecting electrons from the lower energy levels. The ejected electrons are replaced by electrons from an outer, higher energy orbital. When this happens, energy is released due to the decreased binding energy of the inner electron orbital compared with an outer one. This energy release is in the form of emission of characteristic X-rays indicating the type of atom present. For the purposes of this study, an XRF S1 Turbo Bruker portable device was employed for the analysis of the elemental composition of the specimens, Fig.[4.18].

B. EXPERIMENTAL PART

The aim of the present thesis is the study of the corrosion behavior of welded AH36-S690 and AH36-AH36 specimens, as well as the behavior of their parent metals AH36 and S690. The study of the corrosion behavior was accomplished employing electrochemical techniques applying AC and DC excitation techniques. For the interpretation of the results obtained and the completion of the study, detailed study of the microstructure (Optical Microscopy, Micro-hardness, XRF analysis) was also performed.

The specimens were provided by FINCANTIERI Shipbuilding Company, in Italy, where they were welded, cut and sent to Shipbuilding Technology Laboratory. The specimens were provided for the project RAMSSES (Realisation and Demonstration of Advanced Material Solutions for Sustainable and Efficient Ships) which is funded by EC. Both of these steel grades are specified according to the EN 10025 standard.

5. EXPERIMENTAL PROCEDURES - CHARACTERIZATION OF THE MATERIALS

In order to study the corrosion behavior of the FCAW weldments of the HS steel AH36 and the HSLA steel S690, several electrochemical techniques were applied. However, for the complete study of these weldments and the parent metal, additional techniques were required. The microstructure of the specimens, for both the parent metals and the welds, has been studied employing micro-hardness measurements, optical observation with the stereoscope and study of the metallography with optical microscope. In the following paragraphs, the laboratory procedure followed is presented, along with the basic characteristics of the instruments employed.

5.1. Laboratory experimental procedures

To accomplish the corrosion study of the specimens, electrochemical techniques with AC and DC current excitation were employed. In particular Linear Polarization, Potentiodynamic polarization employing Tafel extrapolation, Electrochemical Impedance Spectroscopy for both welds and parent metals were employed, along with the Cyclic Potentiodynamic Polarization, in order to observe the specimens' behavior against pitting corrosion.

More experimental methods were employed to study the material and to interpret the results: Optical microscopy, micro-hardness for the parent metals and X Ray Fluorescence analysis. The experimental procedures employed are described in the following paragraphs.

Study of the microstructure

The specimens for the study were in prismatic shape both the welds and the parent metals. The dimensions 100x100x10 mm.

For the study of the microstructure and the corrosion experiments 20x20x10 mm specimens were prepared. The welded specimens were cut vertically to the weld cord. Thus, the specimens had to be prepared as following:

- Firstly, specimens were cut with a discotom, Fig. [5.1]

Fig.[5.1] Discotom of LME.

- The specimens then were mounted in epoxy resin mixture with hardener (25 parts resin, 3 parts hardener, Struers Epofix resin and hardener), for the consequent grinding, polishing, etching and corrosion testing, Fig.[5.2]

Fig.[5.2] Metal specimens mounted in epoxy resin.

- During grinding, grit emery papers of #80, #120, #180, #320, #500, #800, #1000, #1200, #2000, #4000 where used, for 4 minutes each. During polishing, aluminum and diamond pastes of 1 μm and 0.1 μm were used with a velvet polishing disc (cloth), for 10 minutes each. The machine used for both techniques was Struers Labopol-5, Fig.[5.3] Finally, all specimens were cleaned by distilled water and degreased in pure ethanol. It is worth mentioning that grinding and polishing were repeated after the end of each experimental procedure (e.g. chemical etching and optical observation, hardness testing, corrosion experiments etc).

Fig.[5.3] Struers Labopols-5.

- In order to observe the microstructure of the samples through the microscope, they were etched by Nital 3% solution, consisting 97% v/v ethanol and 3% v/v nitric acid. They were left in the solution for 10-15 seconds and they were again cleaned by distilled water and ethanol. This process was carried out so that grain boundaries were etched and could easily be observed through the modular stereomicroscope (Leica MZ 6), and microscope (Leica DM ILM), using LAS Hardware.

- For the parent metals, a hardness testing was conducted at LME, using Wolpert Wilson Instruments 402 MVD. Vickers micro-hardness testing method was used , in which, the penetrator is a diamond in the form of a square-based pyramid, with face angles of 136°. The applied load was F=2.940N (=299.8 gf) and the loading time was 15 seconds.

- X-ray Fluorescence (XRF) spectroscopy was used in order to calculate the chemical and elemental composition of the materials, both the parent metals and the welds.

Electrochemical techniques for the Corrosion Study

- The basic part of this thesis was the corrosion testing. The specimens were exposed to sea water solution, consisting of 3.5% w/v NaCl and distilled water and all experiments were conducted in ambient temperature, using a three-electrode electrochemical cell, Fig.[5.4]a, where, the exposed area was 1 cm^2. The working electrode was the tested specimen, the auxiliary electrode was a platinum wire and the reference electrode was a saturated calomel electrode (SCE) in KCl. During each experiment, potential excitation was applied and current response was measured via the potentiostat Versa Stat 4, Fig.[5.4]b, which was connected to the Versa Studio Hardware. For the evaluation of the corrosion resistance of the specimens four (4) electrochemical techniques were employed i.e., the Linear Polarization Resistance (LPR) method, the Potentiodynamic Polarization/Tafel Extrapolation Method, the Electrochemical Impedance Spectroscopy (EIS) and the Cyclic Potentiodynamic Polarization (CPP) Method.

a) b)

Fig.[5.4] a) Three-electrode electrochemical cell, b) VersaStat 4 potentiostat.

In order to apply each electrochemical experimental technique, certain parameters were set at Versa Studio, which are mentioned below.

Table [5.1] Electrochemical techniques' parameters- Versa Studio.

Method	Parameters	Values
Linear	**Step Properties**	Initial potential: -0.02 V vs OC
		Final potential: 0.02 V vs OC
	Scan Properties	Step height: 0.2 mV
		Step time: 0.2 s
EIS	**AC Properties**	Start frequency: 10000 Hz
		End frequency: 0.01 Hz
		Amplitude: 10 mV RMS
	Scan Properties	Point spacing: Logarithmic
		Number of points: 30
		Points per decade: 10
		Data quality: 1
		Measurement delay: 0 sec
Tafel	**Endpoint Properties**	Initial potential: -0.25 V vs OC
		Final potential: 0.25 V vs OC
	Scan Properties	Step height: 0.5 mV
		Step time: 3 s
CP	**Endpoint Properties**	Initial potential: -0.1 V vs OC
		Vertex potential: 1.2V vs ref.
		Final potential: 0 V vs OC
	Scan Properties	Step height: 1 mV
		Step time: 1 s

For the majority of the experiments that were conducted (LPR, Tafel, CP and 3 EIS experiments back to back), the exposed area of each specimen to the solution was of 1 cm^2 and the solution was aerated solution of 3.5% w/v (0.6 M) NaCl, as it maximizes relative corrosion rate [5] and represents the conditions of the seawater environment.

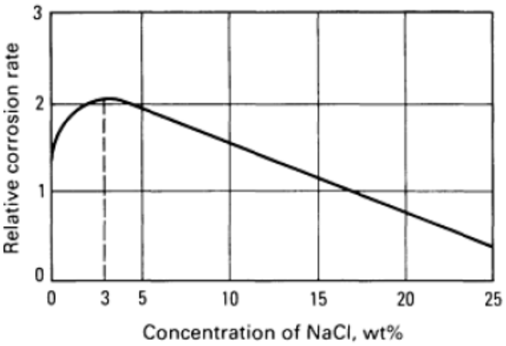

Fig.[5.5] Effect of NaCl concentration on the corrosion rate of iron in aerated room-temperature solutions. [5]

Also, for the second series of EIS experiments with a duration of 25 hours, the solution was aerated solution of 0.29% w/v (0.05 M) NaCl, and the exposed area of each specimen to the solution was of 1 cm^2. The density of each specimen was 7.85 g/cm^3 and the equivalent weight (EW), which we used during the elaboration of data via EC Lab at the Tafel Extrapolation Method in order to measure the corrosion rate, was calculated as,

$$EW=Neq^{-1} \tag{5.1}$$

$$Neq=\Sigma\left(\frac{fi}{Mi/zi}\right)=\Sigma\left(\frac{fi\,zi}{Mi}\right) \tag{5.2}$$

where fi,zi and Mi are mass fraction, electrons exchanged and atomic weight respectively of i^{th} alloying element. Equivalent weight, EW, is calculated, neglecting all minor elements below 1%, as measured by XRF.[2]

Table [5.2] Equivalent Weight as measured via XRF.

	Neq	**EW**
AH36	0.03567	28.036
S690	0.03550	28.167
AH36-AH36	0.03556	28.121
AH36-S690	0.03558	28.104

- EC Lab software was used for the plot and the elaboration of the data obtained from Versa Studio.
- Scanning Electron Microscope (SEM) was used for the study of pits in pitting corrosion procedure (Cyclic Potentiodynamic Polarization- CP).
- Finally, after each corrosion technique, the specimens were cleaned again with distilled water and ethanol and were observed via modular stereomicroscope and microscope.
- The aforementioned experimental procedures applied are summarized in the table below:

Table [5.3] The experimental procedures applied in each specimen.

Experimental procedure		AH36	S690	AH36-AH36	AH36-S690
Optical Microscopy		v	v	v	V
Scanning Electron Microscopy (SEM)		v	v		
Microhardness		v	v		
X-Ray Fluorescence		v	v	v	V
Electrochemical techniques	Open circuit (Short)	v	v	v	V
	Linear	v	v	v	V
	Potentiodynamic	v	v	v	V
	EIS short time	v	v	v	V
	EIS 24h	v	v	v	V
	Cyclic Polarization	v	v	v	V

5.2. Materials' Characterization

5.2.1. Parent metals AH36 and S690- General properties [9][14][40][51][56][65][70]

In the following paragraphs the results the study of the microstructure, micro-hardness and chemical composition by XRF are presented, complemented with data from the literature where necessary.

5.2.1.1. Chemical composition and mechanical properties

AH36 belongs to High Strength Steels, with minimum yield stress of 355MPa. It contains several alloying elements to enhance its microstructure, corrosion resistance and welding properties. AH36's chemical composition according to DNV Rules and Regulations is cited in Table [5.4], showing the maximum values of each element. In order to define the precise values of the main alloying elements X-Ray Fluorescence method was employed, Table [5.5].

It has to be mentioned that XRF method does present values for C and for elements with content lower than 0.01. Comparing the alloying it is obvious that the chemical analysis of the steel specimen is in agreement with the rules by DNV for AH36.

In Table [5.6] the mechanical properties of AH36 are presented, obtained from the literature.

Table [5.4] AH36 chemical composition, from manuals.

Grade	C max	Si max	Mn	P max	S max	Al min	Ti max	Cu Max	Cr max	Ni max	Mo max	Nb	V
AH36	0.18	0.50	0.90-1.60	0.035	0.035	0.015	0.02	0.35	0.20	0.40	0.08	0.02-0.05	0.05-0.10

$$Ceq = C + \frac{Mn}{6} + \frac{Cr+Mo+V}{5} + \frac{Ni+Cu}{15} = 0.48(\%) \qquad (5.4)$$

Table [5.5] AH36 chemical composition, via XRF.

Grade	Si	Mn	P	S	Cu	Cr	Ni
AH36	0.28	1.39	0.02	0.01	0.03	0.02	0.04

Table [5.6] AH36 mechanical properties.

Grade	Yield Stress (MPa)	Tensile Strength (MPa)	Elongation to Failure (%)	Charpy Impact Energy Long. (J)
AH36	355	490-620	21	34 (0^{o})

In Table [5.7] the S690's chemical composition is cited, showing the maximum values of each element, as provided by the steel company SSAB. As with AH36, the chemical composition of S690's was obtained employing XRF, Table [5.8], with the same constraints for C and elements lower than 0.01%. In Table [5.9] the mechanical properties of S690 are presented.

Table [5.7] S690 chemical composition.

Grade	C max	Si max	Mn max	P	S	N	B	Cu Max	Cr max	Ni max	Mo max	Nb max	V max
S690	0.20	0.80	1.70	0.020-0.025	0.010-0.015	0.015	0.05	0.50	1.50	2.00	0.70	0.06	0.12

$$Ceq = C + \frac{Mo}{6} + \frac{Cr+Mo+V}{5} + \frac{Ni+Cu}{15}\ (\%)=0.65\% \qquad (5.5)$$

Table [5.8] S690 chemical composition, via XRF.

Grade	Si	Mn	P	Mo	Cu	Cr	Ni	Nb	Sn	W
S690	0.31	1.21	0.01	0.17	0.01	0.29	0.05	0.01	0.01	0.01

Table [5.9] S690 mechanical properties.

Grade	Yield Stress (MPa)	Tensile Strength (MPa)	Elongation to Failure (%)	Charpy Impact Energy Long. (J)
S690	690	770-940	14	40 (0^{o})

Comparing the chemical composition of the two steel grades AH36 and S690, it is clear that there is a higher amount of manganese on the S690 steel, contributing to the higher strength and hardenability of this steel with respect to the AH36 steel. The S690 steel also includes grain-refining elements such as aluminium, niobium and titanium. The phosphorus and sulphur contents are lower in the S690 steel grade, since these elements have adverse effects on ductility and toughness, especially on quenched and tempered steels like S690.

5.2.1.2. Microstructure of the parent metals AH36, S690 and the welds AH36-AH36, AH36-S690

The microstructure of the specimens, for both the parent metals and the welds, has been studied employing micro-hardness measurements, optical observation with the stereoscope and study of the metallography with optical microscope. In the following paragraphs the results are presented.

High strength steel **AH36** consists of alternate bands of ferrite and pearlite, as shown in Fig.[5.6]. Ferritic structure, which appears in the bright-color areas, covers larger area as expected due to the chemical composition of steel (0.18%). The grains of both the ferrite and the pearlite have intense orientation, which is caused by the production procedure (rolling) of the steel foil. The grain orientation is perpendicular to the direction of the load. The percentage is about 75% ferritic structure and 25% pearlitic structure.

Micro-hardness measurements present consistency and is in accordance with the literature, presenting AH36 HV equal to 153 HV, Table [5.10].

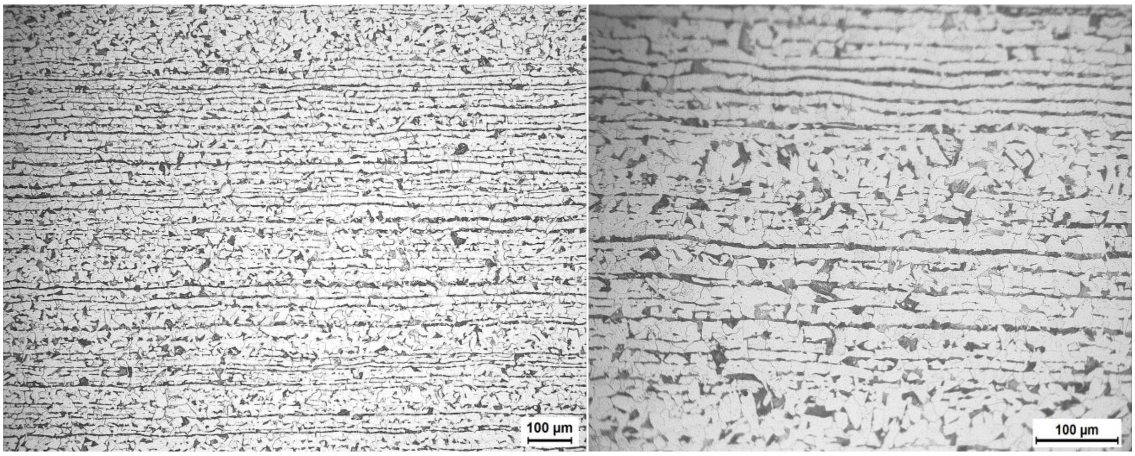

(a) (b)

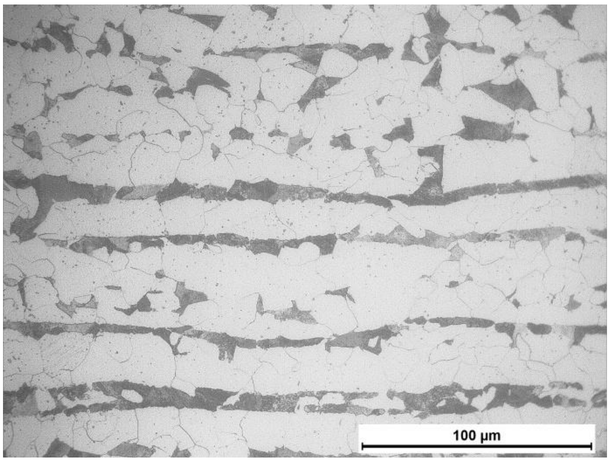

c)

Fig.[5.6] The ferritic- pearlitic microstructure of AH36 a) x100, b) x200, c) x500.

Table [5.10] AH36 hardness.

Grade	Hardness (HV0.3)						
	1	2	3	4	5	Average	Stdev
AH36	150.2	160.3	154.9	151.6	150.1	**153.4**	4.3

S690 steel is a High Strength Low Alloy steel (HSLA). During the production of S690, thermo mechanical rolling together with accelerated cooling and tempering is applied. So, the microstructure of the parent steel S690 consists of a homogeneous mixture of tempered martensite and bainite, along with ferrite. The volume fraction of tempered martensite (bright-color areas) is usually higher than the one of bainite. Also, in contrast with AH36, grain orientation does not appear in S690, as a result of the thermo mechanical treatment. In this case, the S690 BM (rolled and direct quenched), exhibits a fine elongated ferrite- bainite microstructure, Fig.[5.7].

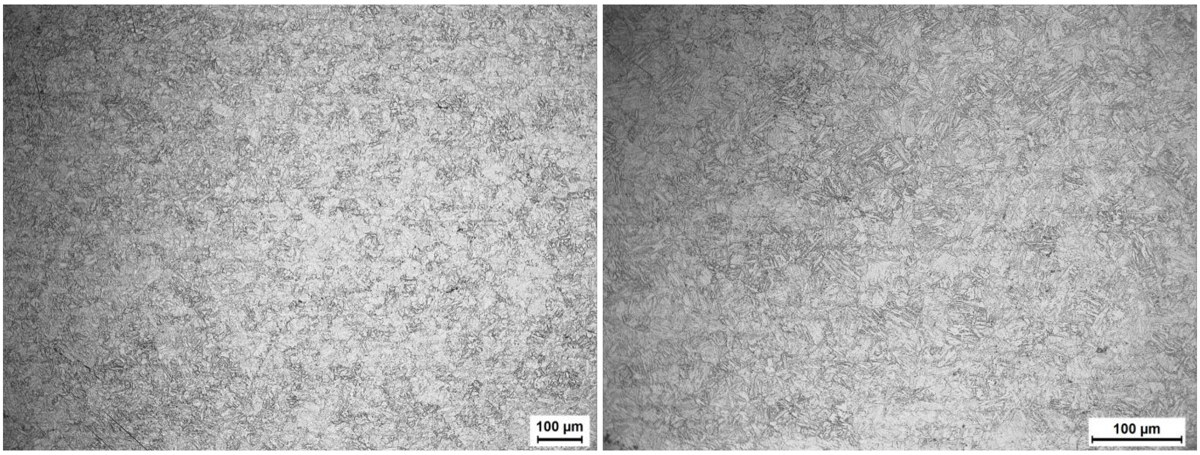

(a) (b)

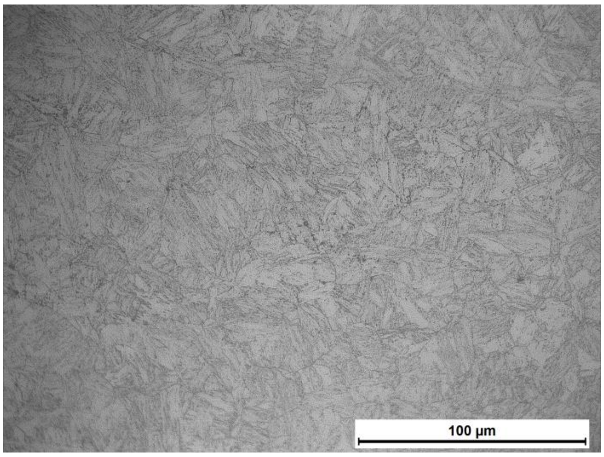

c)

Fig.[5.7]The ferritic, bainitic and martensitic microstructure of S690 a) x100, b) x200, c)x500.

Table [5.11] S690 hardness.

Grade	Hardness (HV0.3)						
	1	2	3	4	5	Average	Stdev
S690	272.4	279.7	281.9	290.1	274.0	**279.6**	7.1

Micro-hardness measurements of S690 present significant higher values than AH36, i.e. 280 HV. This difference is attributed to the microstructure and is consistent with the higher yield stress of S690, Table [5.11].

5.2.2. Homogeneous weldment of AH36-AH36 [53]

The welding technique applied, for both homogeneous and heterogeneous welds, is the Flux-cored arc welding (FCAW) with active gas shield. This method is widely used in the marine field due to its welding speed and portability.

The welded specimens were manufactured with the FCAW method in the Fincantieri shipyard of Riva Trigoso with the following characteristics:

- Welding machine: ESAB ORIGOMIG 520 MAGMA
- Surface preparation technique: edge plasma or flame cutting, double V joint $\alpha = 50°$
- Gas composition: 100% CO_2;
- Welding speed: 180÷250 mm/min.

The following welding consumables approved by BV were used by FC

- ESAB OK TUBROD E71T-1 φ 1,2 mm
- FILARC PZ 6116S φ 1,2 mm

In the following paragraphs, the chemical composition (as measured via XRF) and the micro hardness of the homogeneous FCAW weldment of AH36-AH36 are presented, along with the microstructure of the weldment.

5.2.2.1. Chemical composition- XRF and micro hardness

X-ray Fluorescence (XRF) spectroscopy was used in order to calculate the chemical and element composition of the materials. It is the measurement and analysis of samples excited by incident radiation.

Table [5.12] AH36-AH36 weld chemical composition, via XRF.

Grade	Si	Mn	P	S	Cu	Cr	Mo	Ti	V	Nb
AH36-AH36	0.50	1.35	0.01	0.05	0.02	0.02	0.02	0.02	0.03	0.01

The microhardness measurements of the homogeneous weldment of AH36-AH36 are obtained from Report "*Realisation and Demonstration of Advanced Material Solutions for Sustainable and Efficient Ships*" RAMSSES project, and were performed according to ISO 17693/ ISO 9015-2.

Line I was obtained on the upper part of the weld, while line II was performed on the toe of the weld. The values in Table [5.13] and the Fig.[5.9] show that on the tow the values are lower due to the annealing caused by the following passes. Moreover, in line I more distinct values are observed for each area of the weld. Thus, in Fusion Zone the values are higher than the parent metal, while the highest values are observed on the HAZ. In some points they are as high as 337HV. This is attributed to the specific microstructure which is developed in the HAZ.

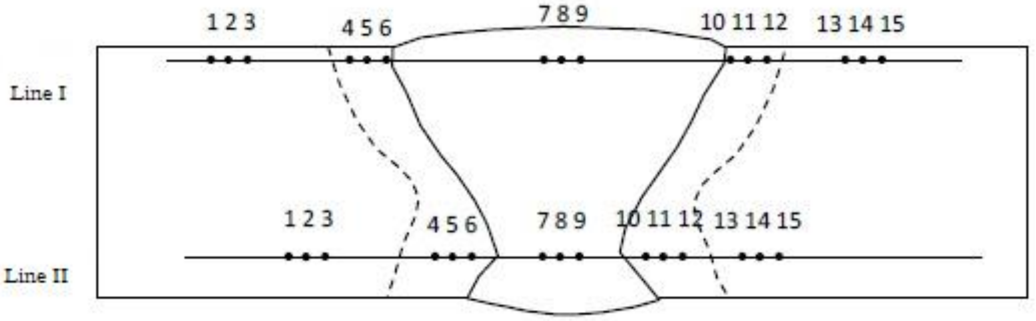

Fig.[5.8] Hardness measurements sketch on AH36-AH36 weldment.[53]

Table [5.13] AH36-AH36 weld micro hardness.

	Hardness (HV10)														
AH36-AH36	**BMZ**			**HAZ**			**FZ**			**HAZ**			**BMZ**		
Points	1	2	3	4	5	6	7	8	9	10	11	12	13	14	15
Line I	147	152	169	183	303	337	211	213	207	257	257	171	172	147	144
Line II	151	158	175	175	180	199	199	183	181	178	173	172	160	152	152

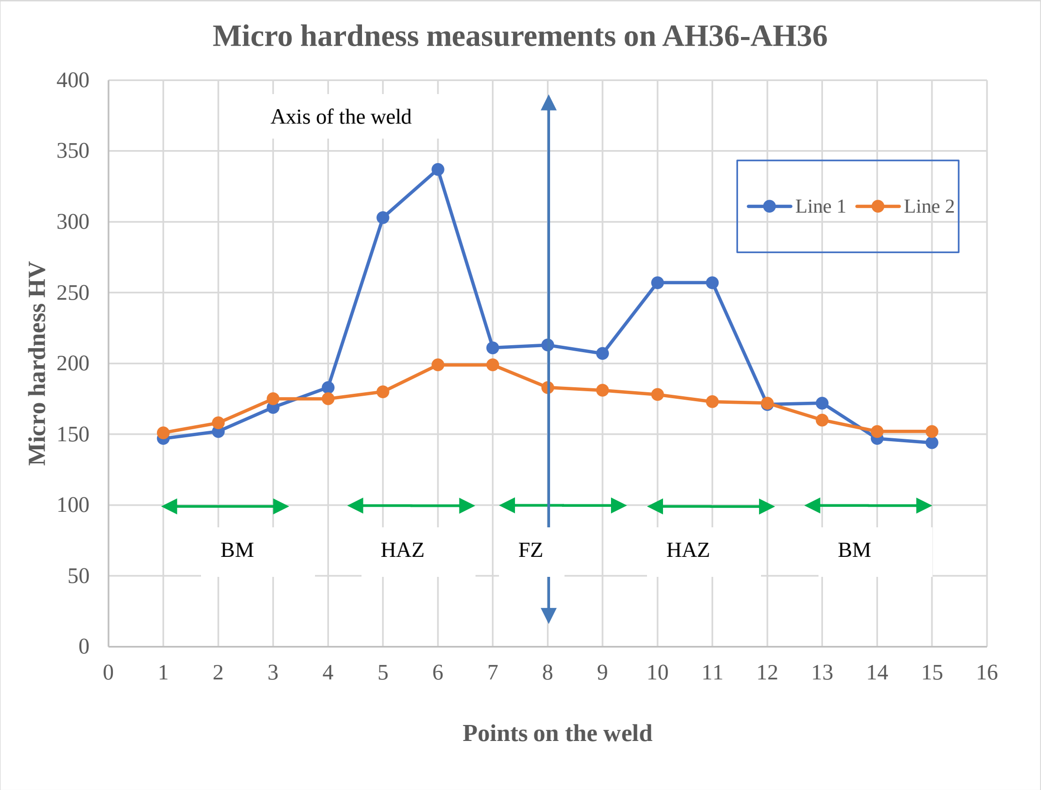

Fig.[5.9] Microhardness measurements on AH36-AH36 weldment.

5.2.2.2. Microstructure- optical microscopy

The microstructure of the AH36-AH36 weld has been studied employing the stereoscope to observe the different welding passes and welding areas (HAZ,WZ,BM) and employing optical microscope to reveal the microstructure of the weld. The section of FCAW AH36-AH36 is presented in Fig.[5.10], where the Base Metal (BM), the Heat Affected Zone (HAZ) and the Fusion Zone (FZ) of the weldment can be clearly distinguished.

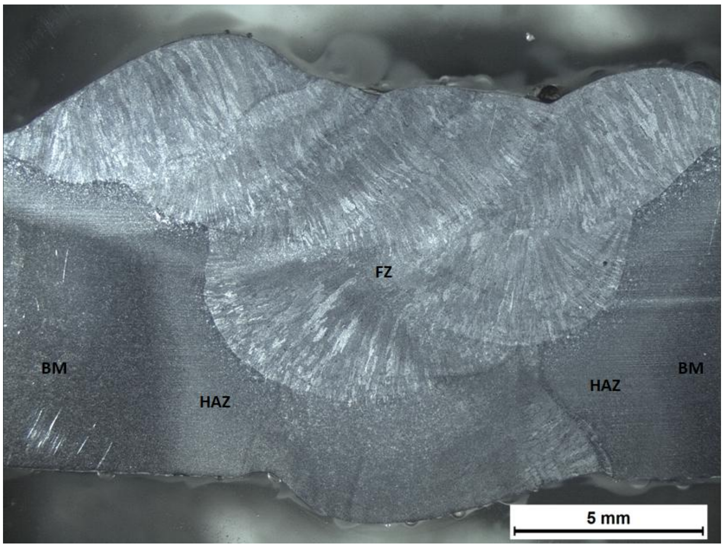

Fig.[5.10] The intersection of AH36-AH36 in the stereoscope.

In this case, concerning the homogeneous weldment of AH36-AH36, a region in the start of the HAZ is presented. From the left part of the figure to the right, the unaffected zone of ferrite and pearlite, the tempered zone, the partially austenized and tempered zone and finally, the fine-grained austenite zone can be detected, Fig.[5.11].

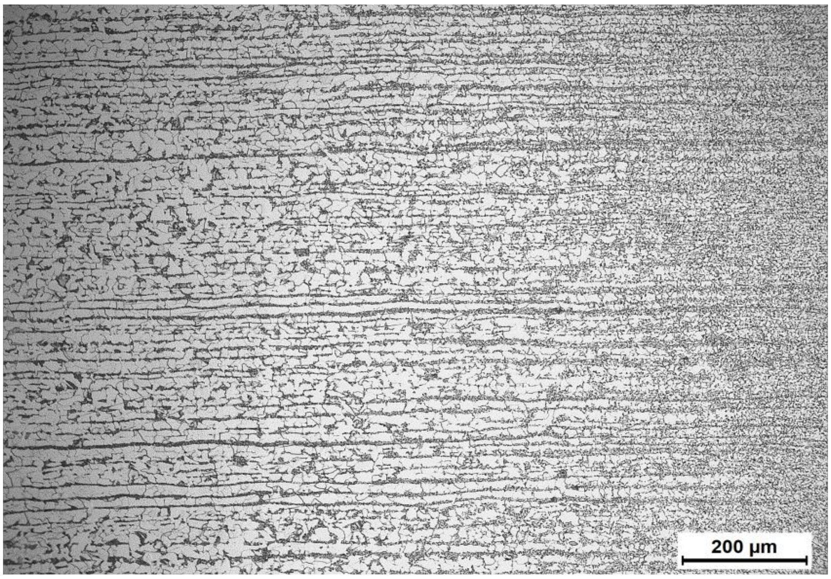

Fig.[5.11] AH36-AH36 microstructure at the beginning of the Heat Affected Zone.

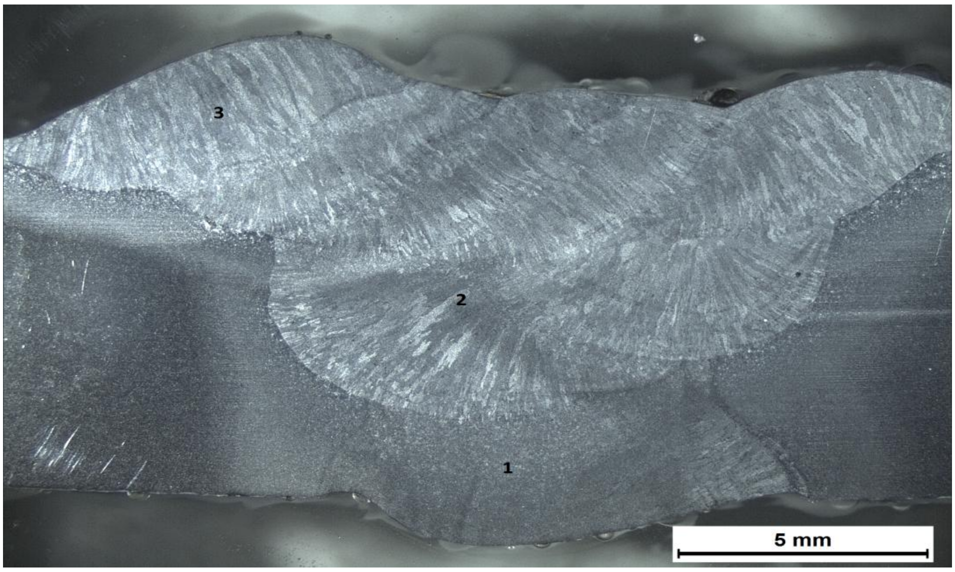

Fig.[5.12] Different regions of weldment of AH36-AH36.

In Fig.[5.13], the microstructure of the Fusion Zone of the homogeneous weldment in the first pass is presented, in a region below the point 1 Fig.[5.12].

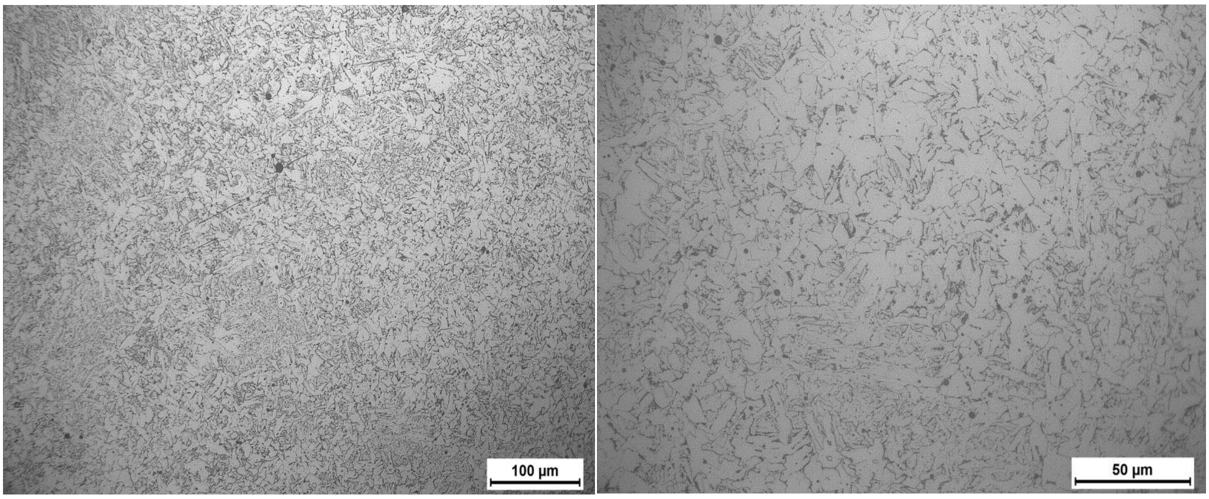

a) b)

Fig.[5.13] AH36-AH36 Fusion Zone of the first pass of the weldment, a) x200, b) x500.

Studying the microstructure Fig.[5.13], a ferrite-bainite microstructure is observed, with bigger percentages of ferrite than in Fig.[5.15]. The differences between the grain sizes in the two cases lays in the fact that these regions have undergone tempering during the welding procedure.

In Fig.[5.14], AH36-AH36 Fusion Zone of the last pass of the weldment is presented, in a region near the point 2 of Fig.[5.11].

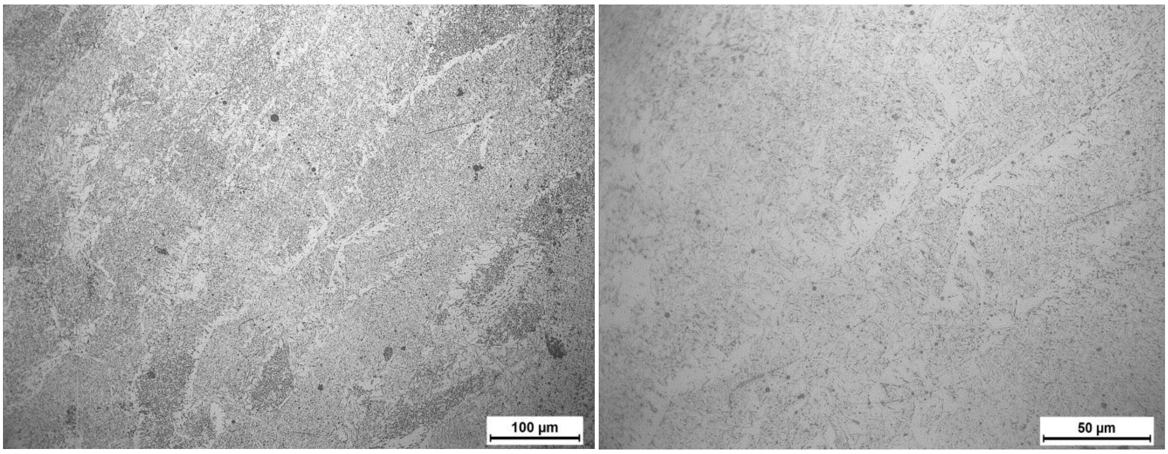

Fig.[5.14] AH36-AH36 Fusion Zone of the central region of the weldment, a) x200, b) x500

In Fig.[5.15], the microstructure of the Fusion Zone of the homogeneous weldment in the last pass is presented, in a region near the point 3, of Fig.[5.12].

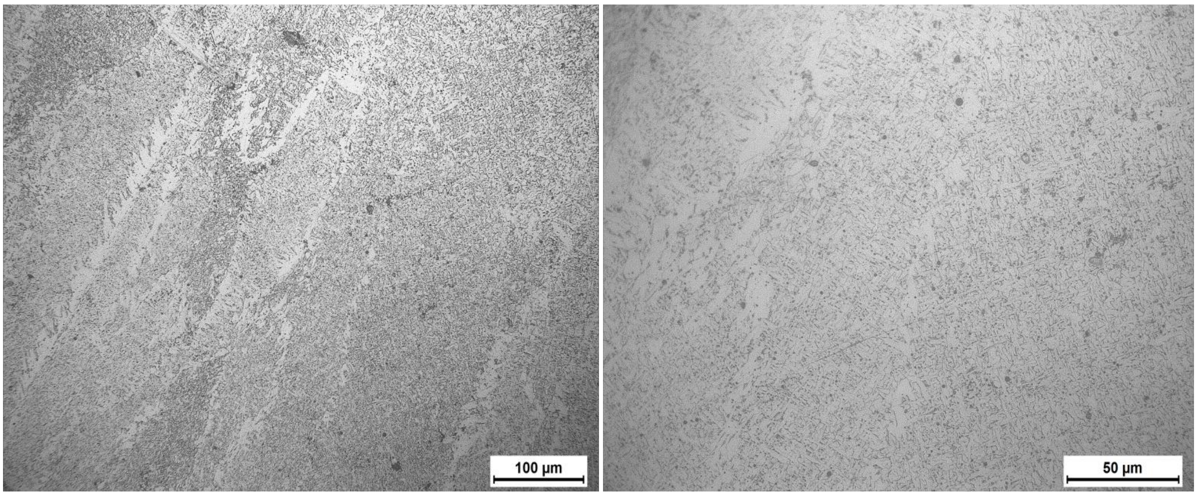

a) b)

Fig.[5.15] AH36-AH36 Fusion Zone of the last pass of the weldment, a) x200, b) x500.

Studying the microstructure of these specific bright- color regions in Fig.[5.15], a ferrite-bainite microstructure is also observed. The grains form dendrites due to the rapid cooling during the welding procedure. The solidification orientation is perpendicular to the isothermal curves. Also, Widmanstätten ferrite is locally observed in the fusion zone.

5.2.3. Heterogeneous weldment of AH36-S690 [53]

In the following paragraphs, the chemical composition (as measured via XRF) and the micro hardness of the heterogeneous FCAW weldment of AH36-S690 are presented, along with the microstructure of the weldment..

5.2.3.1. Chemical composition- XRF and micro hardness

X-ray Fluorescence (XRF) spectroscopy was used in order to calculate the chemical and elemental composition of the materials. It is the measurement and analysis of samples excited by incident radiation. The two primary components of an XRF spectrometer are an X-ray output and a sensitive detector capable of determining fluorescent X-rays from the incident light. This array emits a beam of X-rays into the sample, exciting electrons within the sample's inner atoms and displacing them from their orbital shells.

Table [5.14] AH36-S690 chemical composition, via XRF.

Grade	**Si**	**Mn**	**P**	**Cr**	**Mo**	**Ti**	**Ni**	**Nb**
AH36-S690	0.42	1.20	0.01	0.07	0.04	0.02	1.11	0.01

The microhardness measurements of the heterogeneous weldment of AH36-S690 are obtained from Report on "*Realisation and Demonstration of Advanced Material Solutions for Sustainable and Efficient Ships*" RAMSSES project, and were performed according to ISO 17693/ ISO 9015-2.

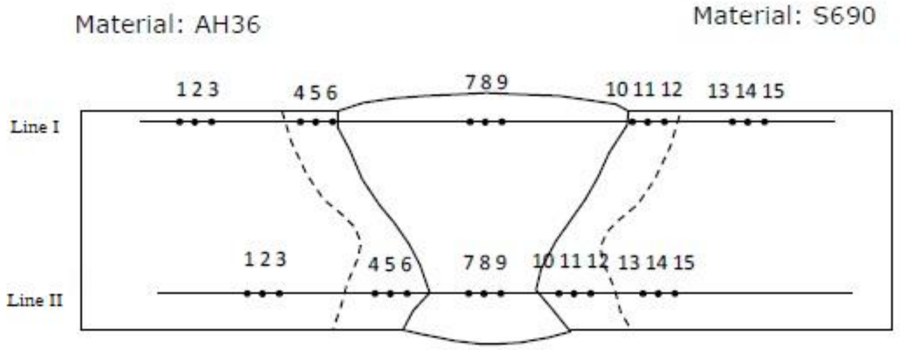

Fig.[5.16] Hardness measurements sketch on AH36-S690 weldment.[53]

Table [5.15] AH36-S690 hardness.

	Hardness (HV10)														
AH36-S690	**BMZ**			**HAZ**			**FZ**			**HAZ**			**BMZ**		
Points	1	2	3	4	5	6	7	8	9	10	11	12	13	14	15
Line I	147	149	166	176	236	278	209	221	212	314	340	364	252	271	272
Line II	146	148	165	174	170	174	201	190	191	275	268	229	245	273	275

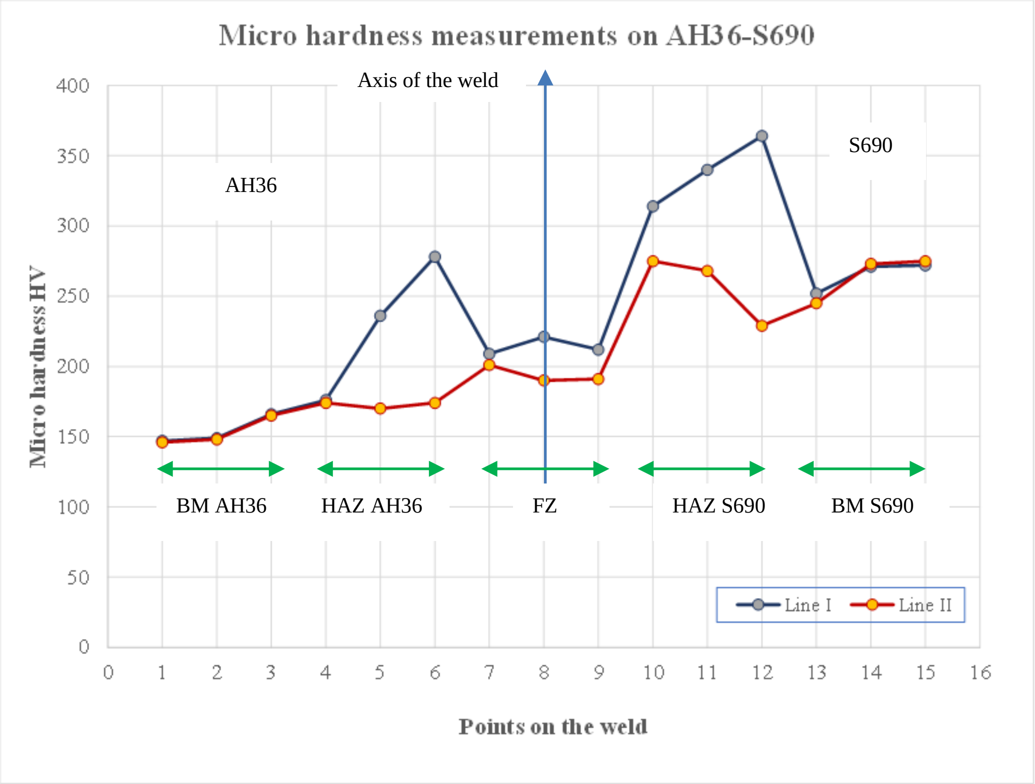

Fig.[5.17] Microhardness measurements on AH36-s690 weldment.

The values in Table [5.15] and Fig.[5.17] show that as in homogeneous weld line II on the toe of the weld, presents lower values due to annealing of the subsequent passes. FZ presents higher values only than AH36, since the combination keeps the values of FZ in low level. However, tha HAZ values are very high, especially in S690 side, where these are as high as 364HV.

5.2.3.2. Microstructure- optical microscopy

The section of FCAW AH36-S690 is presented in Fig.[5.18], where the Base Metal (BM), the Heat Affected Zone (HAZ) and the Fusion Zone (FZ) of the weldment can be clearly distinguished.

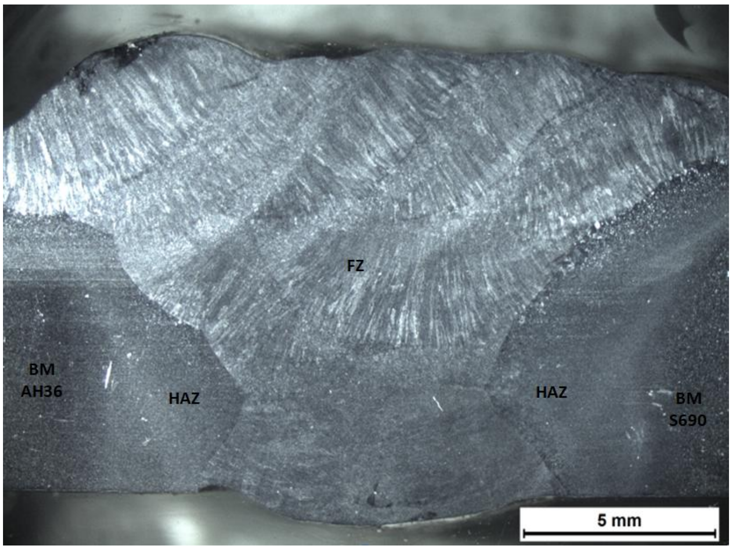

Fig.[5.18] The intersection of AH36-S690 in the stereoscope.

In Fig.[5.19] Heat Affected Zone from the side of the parent metal S690 the is presented.

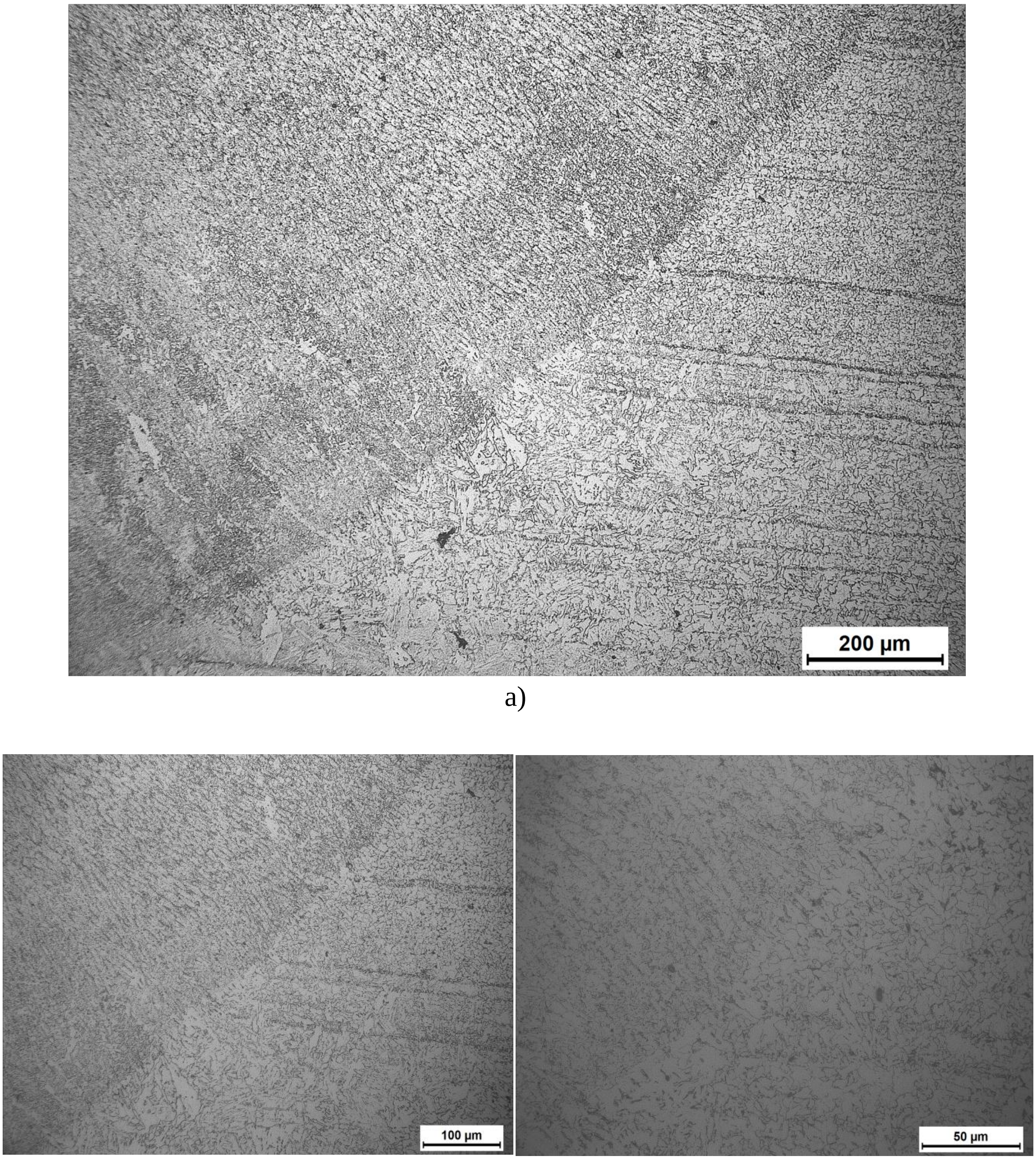

a)

b) c)

Fig.[5.19] Heat Affected Zone from the side of the parent metal S690, a) x100, b) x200, c) x500.

The region of the HAZ from the side of S690 presents a microstrusture that consists mostly of tempered martensite, along with a small amounts of remaining austenite, ferrite and bainite. This region presents an increased hardness, due to its complex microstructure.

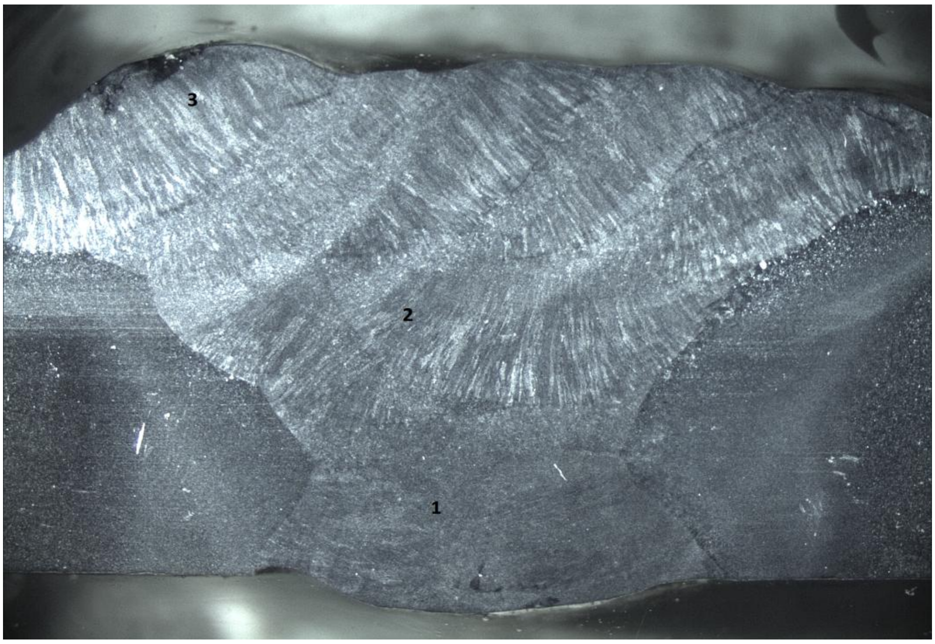

Fig.[5.20] Different regions of weldment of AH36-S690.

In Fig.[5.21], AH36-S690 Fusion Zone of the first pass of the weldment is presented, in a region near the point 1 of Fig.[5.20]. This zone presents a ferrite-bainite microstructure, with a higher percentage of ferrite. This is the reason for the reduced hardness of the region, in comparison to the HAZ. The grains have a characteristic dendrite microstructure, due to the rapid cooling during the weldment.

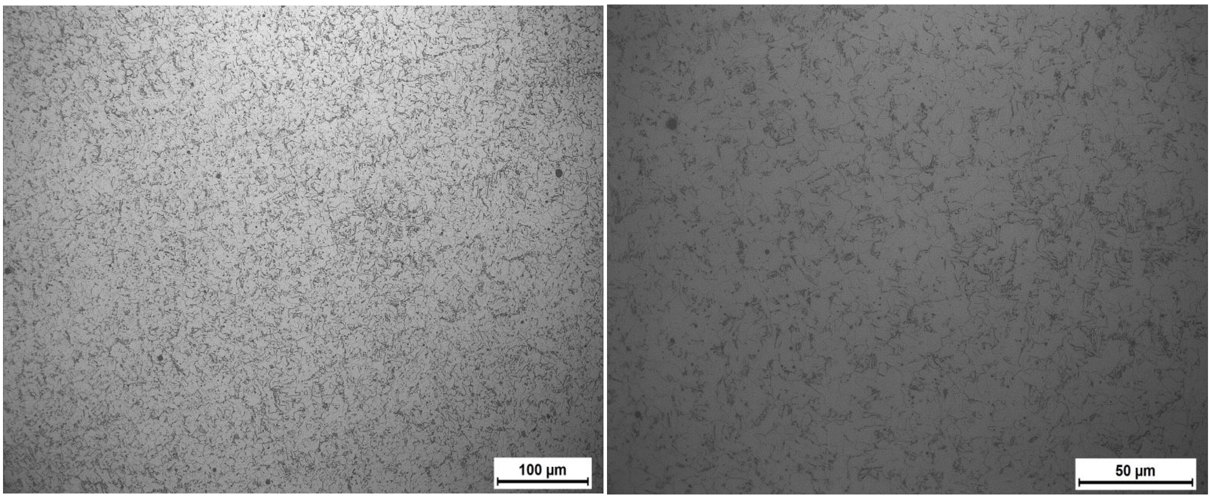

a) b)

Fig.[5.21] AH36-S690 Fusion Zone of the first pass of the weldment, a) x200, b) x500.

In Fig.[5.22], AH36-S690 Fusion Zone of the central region of the weldment is presented, in a region near the point 2 of Fig.[5.20].

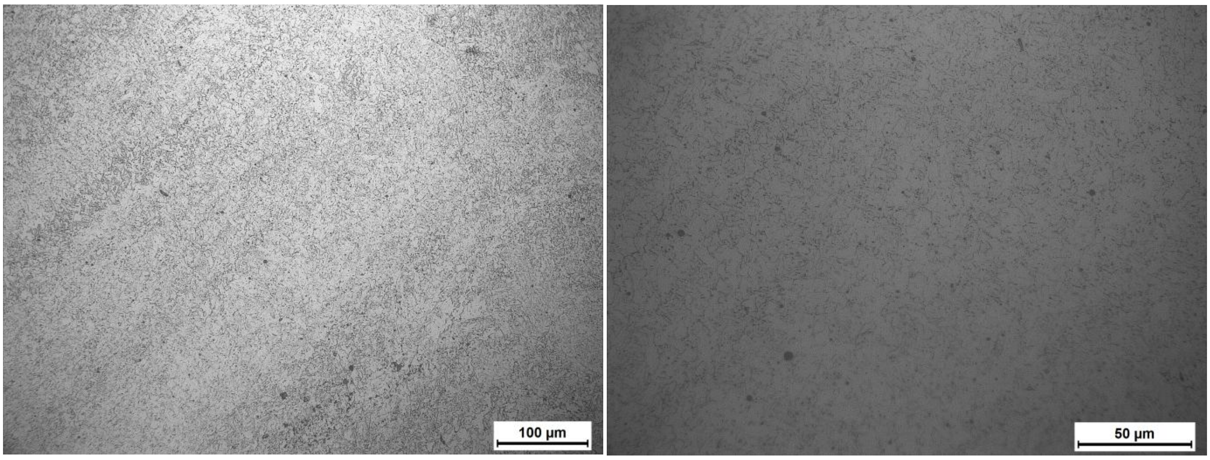

a) b)

Fig.[5.22] AH36-S690 Fusion Zone of the central region of the weldment, a) x200, b) x500.

In Fig.[5.23], AH36-S690 Fusion Zone of the last pass of the weldment is presented, in a region near the point 3 of Fig.[5.20].

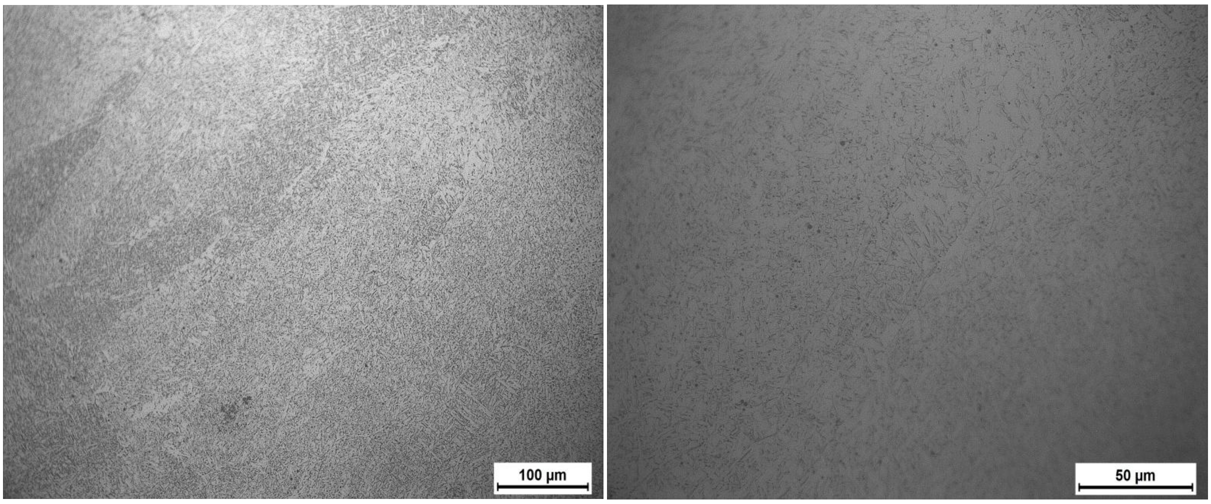

a) b)

Fig.[5.23] AH36-S690 Fusion Zone of the last pass of the weldment, a) x200, b) x500.

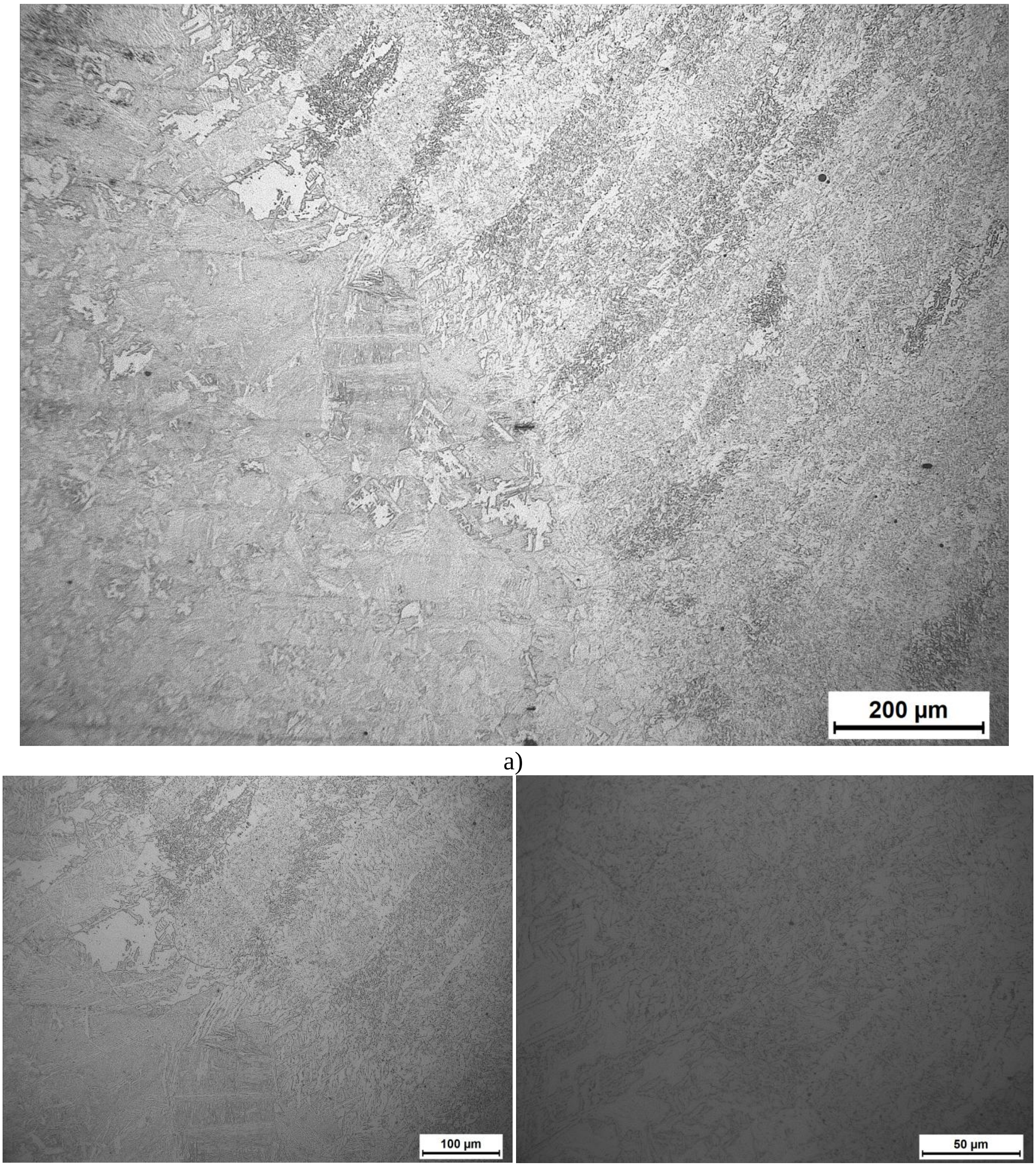

a)

a) b)

Fig.[5.24] Heat Affected Zone from the side of the parent metal AH36, a) x100, b) x200, c) x500.

The region of the HAZ from the side of AH36 presents a microstrusture that consists mostly of bainite, along with a small amount of ferrite. During the observation of these regions of the weld, it becomes obvious that the grain size is getting bigger closer to the HAZ than in the parent metal.

C. ELECTROCHEMICAL EXPERIMENTS -RESULTS

With the completion of the analysis of the specimens' microstructure, a thorough analysis of the corrosion behavior of these specimens was performed. The study of the corrosion behavior was accomplished employing electrochemical techniques applying AC and DC excitation techniques. For the elaboration of the results obtained and the completion of the study, several electrochemical methods (Linear Polarization, Tafel Extrapolation, Impedance Spectroscopy and Cyclic Potentiodynamic Polarization) were employed.

6. LINEAR POLARIZATION

6.1. Introduction

As already mentioned in Chapter 4, Linear Polarization consists an electrochemical technique, applying DC perturbation. This excitation scans over a small range of potential, 10-15mV negative (cathodic) and consequently positive (anodic) to Open Circuit Potential. Thus, graphs of Current (Y axis) versus Voltage (X) axis and measure the slope which is the Polarization Resistance Rp. Thus, Rp to icorr is converted using Stern-Geary equation:

$$\Delta V/\Delta I = Rp = \frac{\beta a \, \beta c}{2.3 \text{ Icorr } (\beta a+\beta c)} \tag{6.1}$$

where

Rp = Slope of the graph= Polarization Resistance (Ohm)

Icorr = corrosion current (μA/ cm^2)

βα, βc = Tafel constants from a Tafel curve, 120 milivolts/decade of current, according to literature.

In the present thesis the elaboration of the results has been performed employing EC Lab Software. For each specimen, six (6) experiments were conducted, giving one diagram each. In this chapter, only one of them is presented (the one with values that are closer to the average values of the three experiments), along with the common diagrams and the rest of the diagrams for each experiment are presented in Chapter 12. Annex (12.2.1).

6.2. Results

In Fig.[6.1] an example of a Linear Polarization Resistance fitting via EC Lab software is presented, in order to help with the comprehension of the LPR method used for the data elaboration.

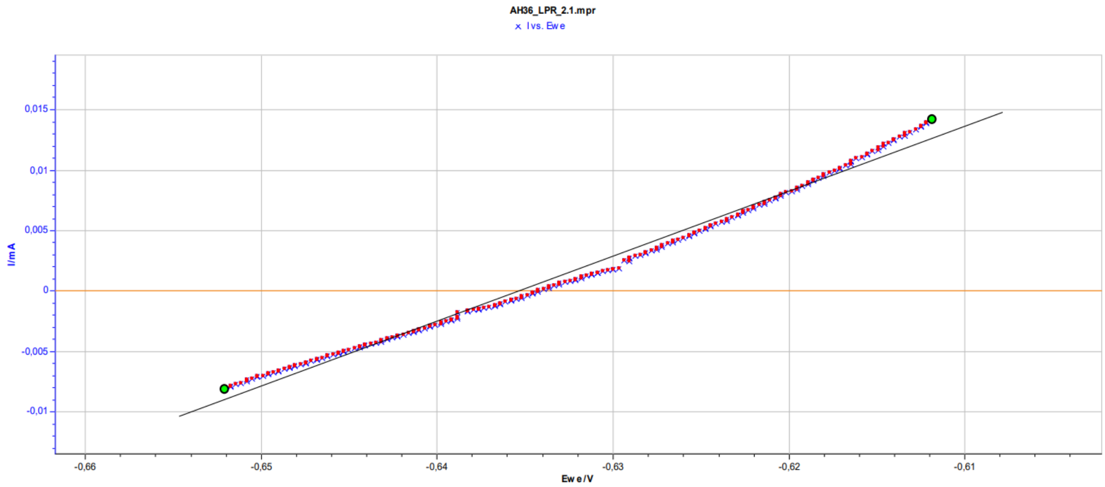

Fig.[6.1] LPR plot of parent metal AH36, exp.1, **Blue**/**Red** trace: points, **Black** line LPR fit.

6.2.1. Parent metals

In the present paragraph, the summary diagrams, Fig.[6.2] and Fig.[6.3] and corrosion parameters tables, Table[6.1] and Table [6.2] of the parent metals AH36 and S690 are presented, along with comparison diagram, Fig.[6.5] and Table [6.3]. For all the graphs log(|I/mA|) is presented on y-axis vs E we/V on x-axis.

Concerning parent metal AH36 Linear Polarization technique proves that the mean value for Ecorr is -629 mV and Icorr values are also rather stable at 15 μA/cm^2. The mean value of the Rp has been 1857 Ohm.

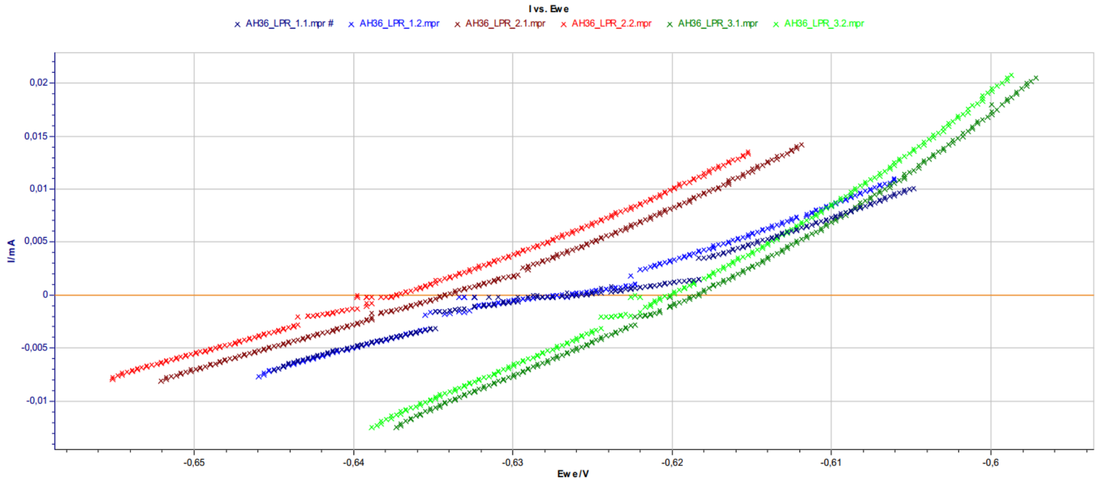

Fig.[6.2] LPR **AH36**, 6 experiments : **Maroon** exp. 1, **Red** exp. 2, **Navy** exp. 3, **Blue** exp. 4, Green exp.5, **Lime** exp. 6.

Table [6.1] Corrosion and LPR parameters for parent metal AH36.

	Ecorr (mV)	Icorr (μA/cm^2)	Rp (Ohm)	Correlation
AH36.1	-635.4	14.011	1862	0.995
AH36.2	-638.6	13.463	1938	0.996
AH36.3	-627.4	10.296	2534	0.985
AH36.4	-628.5	11.404	2288	0.992
AH36.5	-619.9	20.583	1267	0.994
AH36.6	-621.5	20.814	1253	0.994
Average	**-628.6**	**15.095**	**1857**	**0.993**
Stdv	7.4	4.546	522	-

In Fig.[6.3] and Table [6.2], the results of parent metal S690 Linear Polarization technique are presented. According to Fig.[6.4], all the experiments present very good repeatability. The results show that the mean value for Ecorr is -626 mV and Icorr mean value is 18μA/cm^2. The values of the Rp have been 1461 Ohm.

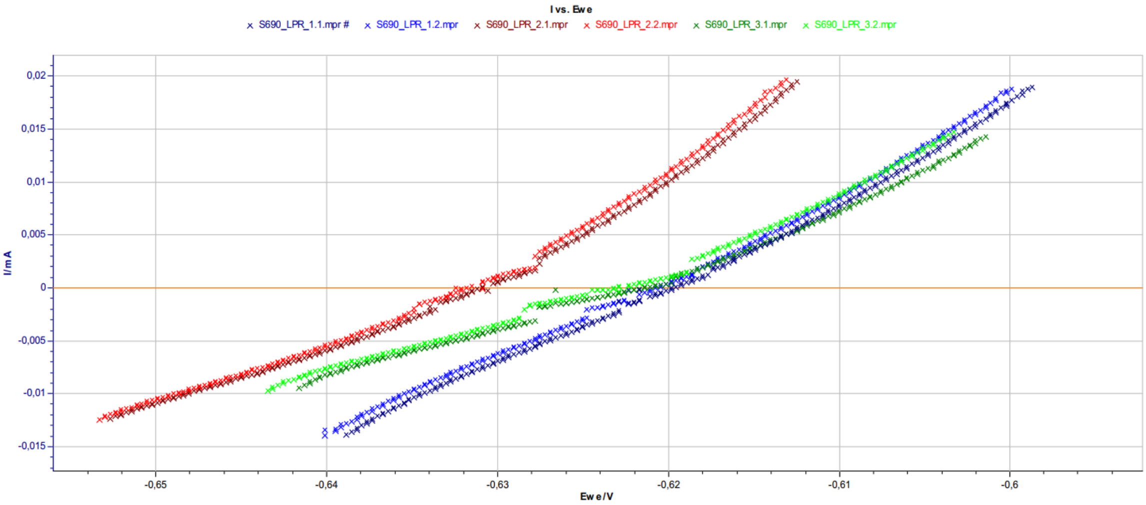

Fig.[6.3] LPR **S690**, 6 experiments : **Maroon** exp. 1, **Red** exp. 2, **Navy** exp. 3, **Blue** exp. 4, Green exp.5, **Lime** exp. 6.

Table [6.2] Corrosion and LPR parameters for parent metal S690.

	Ecorr (mV)	Icorr (μA/cm^2)	Rp (Ohm)	Correlation
S690.1	-633.2	19.758	1320	0.985
S690.2	-634.0	19.897	1311	0.986
S690.3	-620.7	20.308	1285	0.997
S690.4	-621.7	20.208	1291	0.997
S690.5	-623.5	14.408	1811	0.992
S690.6	-625.0	14.926	1749	0.990
Average	**-626.3**	**18.251**	**1461**	**0.991**
Stdv	6.0	2.788	248	-

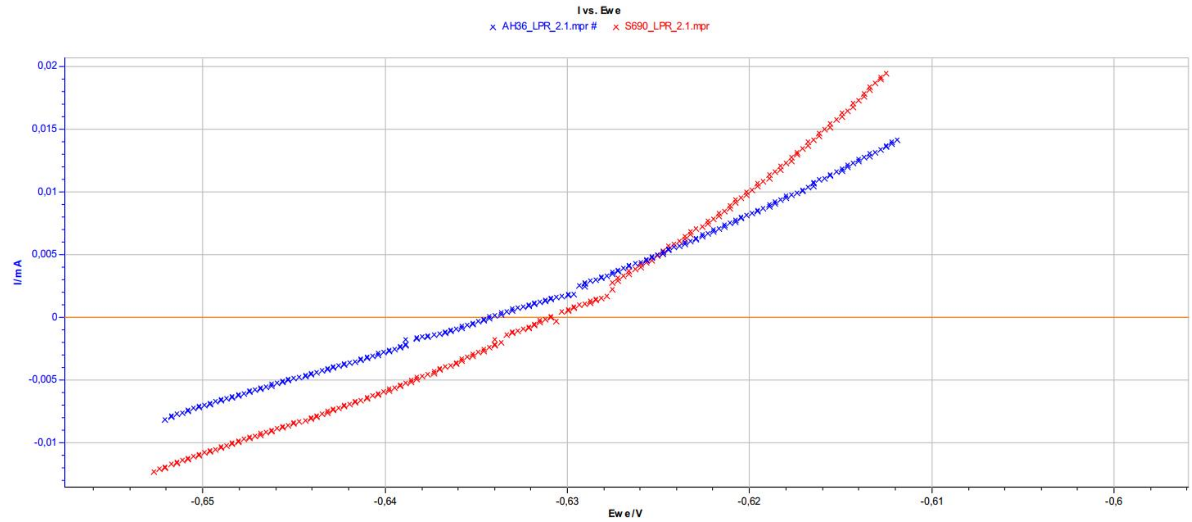

Fig. [6.4] Comparison of LPR for parent metals **AH36** and **S690**, **Blue:** AH36. **Red:** S690.

Table [6.3] Average corrosion and LPR parameters for parent metals AH36 and S690.

	Ecorr (mV)	**Icorr (μA/cm^2)**	**Rp (Ohm)**	**Rp Stdev(Ohm)**
AH36	-628.6	15.095	1857	522
S690	-626.3	18.251	1461	248

6.2.2. Weldments

In the present paragraph, the summary diagrams, Fig.[6.5] and Fig.[6.6] and corrosion parameters tables, Table[6.4] and Table [6.5] of the weldments AH36-AH36 and AH36-S690 are presented, along with comparison diagram, Fig.[6.7] and Table [6.6].

Homogeneous weldment AH36-AH36 presents Ecorr of -696 mV and Icorr of 30 μA/cm^2. The mean Rp value of the homogeneous weldment has been 872 Ohm. These values are evidently higher than the parent metal AH36, proving that the corrosion rate is higher than the parent metal.

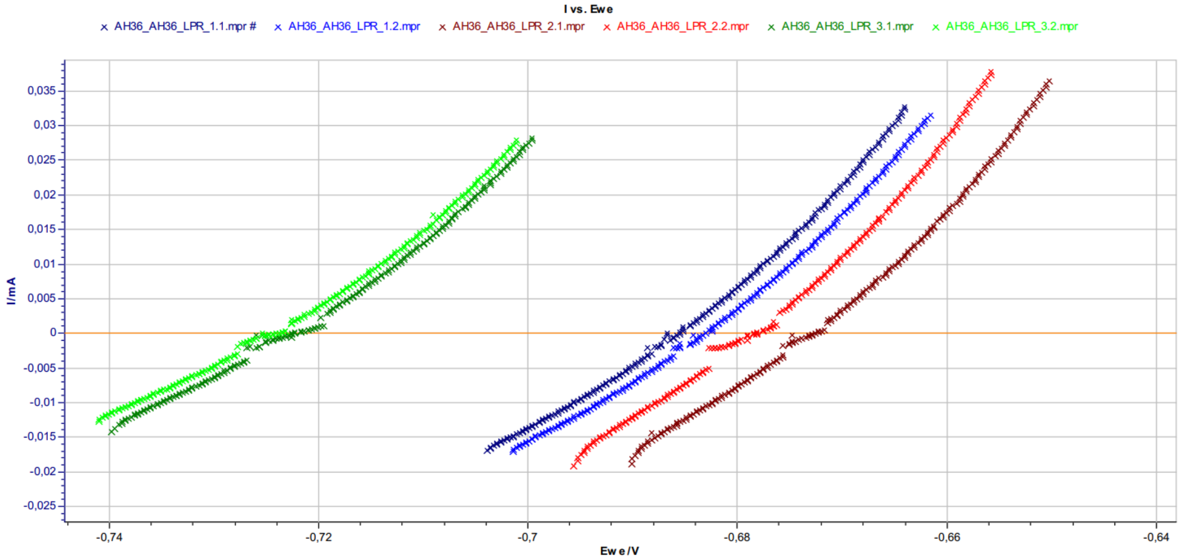

Fig.[6.5] LPR plot of homogeneous weldment of **AH36-AH36**, 6 experiments : **Maroon** exp. 1, **Red** exp. 2, **Navy** exp. 3, **Blue** exp. 4, Green exp.5, **Lime** exp. 6.

Table [6.4] Corrosion and LPR parameters for homogeneous weldment of AH36-AH36.

	Ecorr (mV)	Icorr (μA/cm^2)	Rp (Ohm)	Correlation
AH36-AH36.1	-684.6	30.869	845	0.992
AH36-AH36.2	-687.2	31.413	830	0.992
AH36-AH36.3	-674.3	33.713	774	0.991
AH36-AH36.4	-679.9	34.721	751	0.991
AH36-AH36.5	-723.9	26.080	1000	0.991
AH36-AH36.6	-725.7	25.361	1029	0.992
Average	**-695.9**	**30.360**	**872**	**0.992**
Stdv	22.8	3.871	116	-

The experiments performed on heterogeneous weld AH36-S690 present mean value of –642 mV for Ecorr and 19μA/cm^2 for Icorr. The experiments present very good repeatability. For the Rp 1376 Ohm.

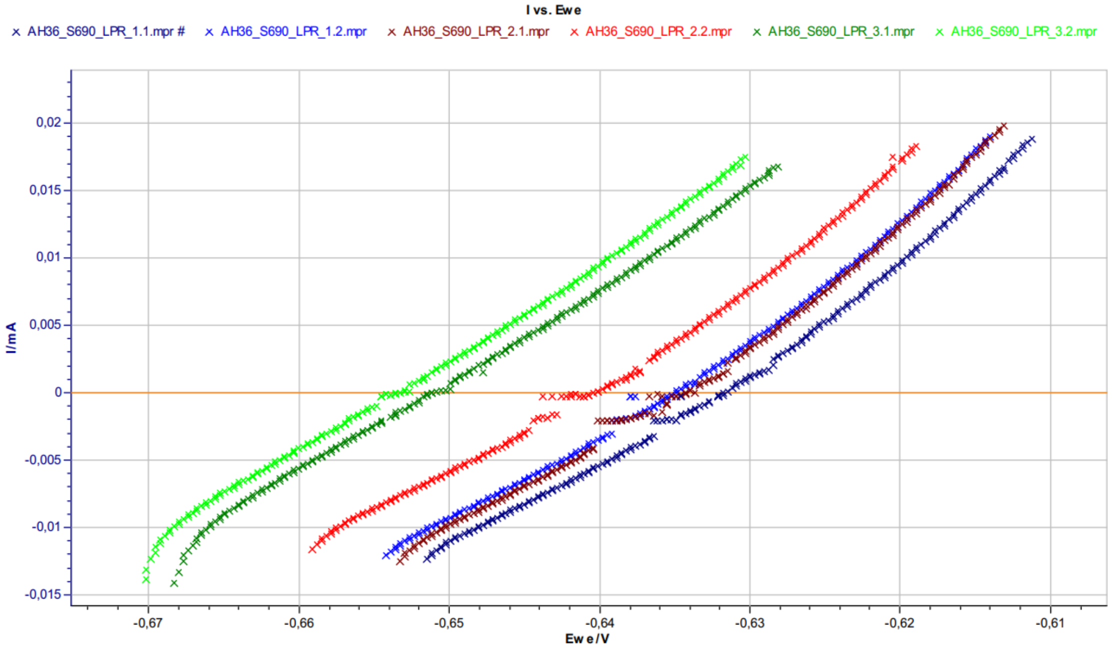

Fig.[6.6] LPR plot of heterogeneous weldment of **AH36-S690**, 6 experiments : **Maroon** exp. 1, **Red** exp. 2, **Navy** exp. 3, **Blue** exp. 4, Green exp.5, **Lime** exp. 6.

Table [6.5] Corrosion and LPR parameters for heterogeneous weldment of AH36-S690.

	Ecorr (mV)	**Icorr (µA/cm^2)**	**Rp (Ohm)**	**Correlation**
AH36-S690.1	-633.3	19.420	1343	0.994
AH36-S690.2	-636.4	19.469	1340	0.994
AH36-S690.3	-635.8	20.000	1304	0.994
AH36-S690.4	-641.7	18.493	1411	0.994
AH36-S690.5	-651.4	18.096	1442	0.999
AH36-S690.6	-653.8	18.391	1418	0.999
Average	**-642.1**	**18.978**	**1376**	**0.996**
Stdv	8.6	0.753	55	-

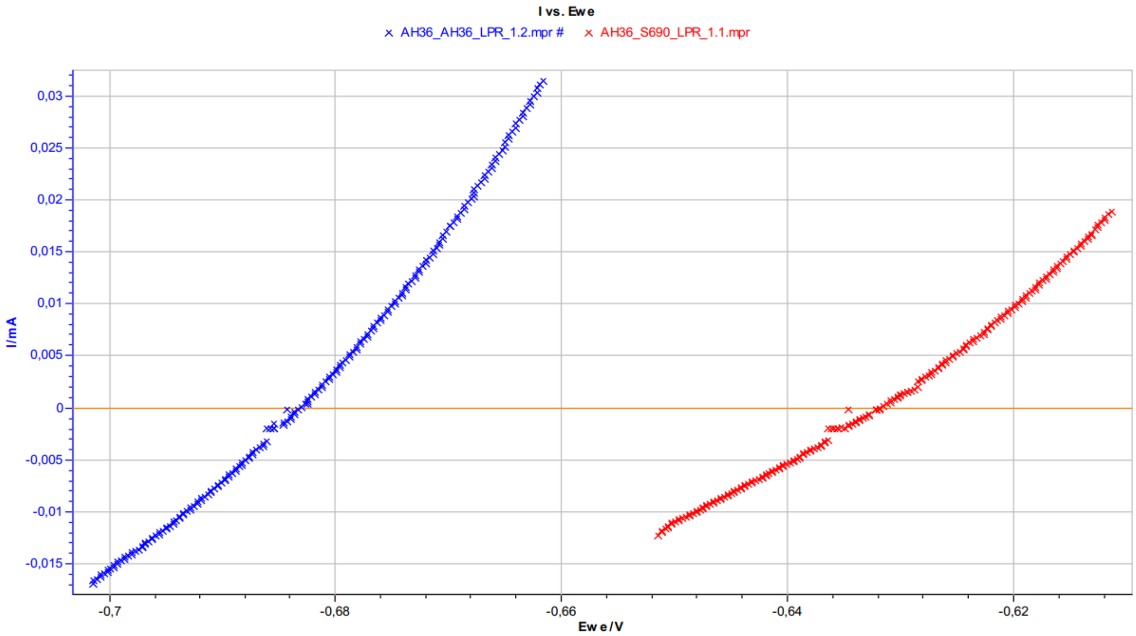

Fig.[6.7] Comparison of LPR plots of weldments **AH36-AH36** and **AH36-S690**, **Blue:** AH36-AH36, **Red:** AH36-S690.

Table [6.6] Average corrosion and LPR parameters for weldments AH36-AH36 and AH36-S690.

	Ecorr (mV)	Icorr (μA/cm^2)	Rp (Ohm)	Rp Stdev (Ohm)
AH36-AH36	-695.9	30.360	872	116
AH36-S690	-642.1	18.978	1376	55

6.3. Total results- Conclusions

Firstly, comparing the parent metals, the Ecorr values do not present significant differences, indicating similar corrosion potential for all the specimens. However, the Icorr (18μA/cm^2) values for S690 are slightly higher, while the polarization resistance Rp is lower, indicating worse corrosion behavior than AH36 (Icorr =15μA/cm^2).

Concerning the two weldments, the Ecorr values do not present significant differences here too, but the Icorr (30μA/cm^2) values are much higher for the weldment of AH36-AH36 than that of AH36-S690 (19μA/cm^2), indicating worse corrosion behavior for the homogenous weldment.

Finally, comparing the parent metals with their weldments, we observe that the Rp values of S690 are similar to those of the weldment AH36-S690 and that there is a very big difference between the Rp values of AH36 and the weldment AH36-AH36 in this case.

In the present paragraph, the summary diagram, Fig.[6.8] and corrosion parameters table, Table[6.7] of the parent metals AH36 and S690 and the weldments AH36-AH36 and AH36-S690 are presented.

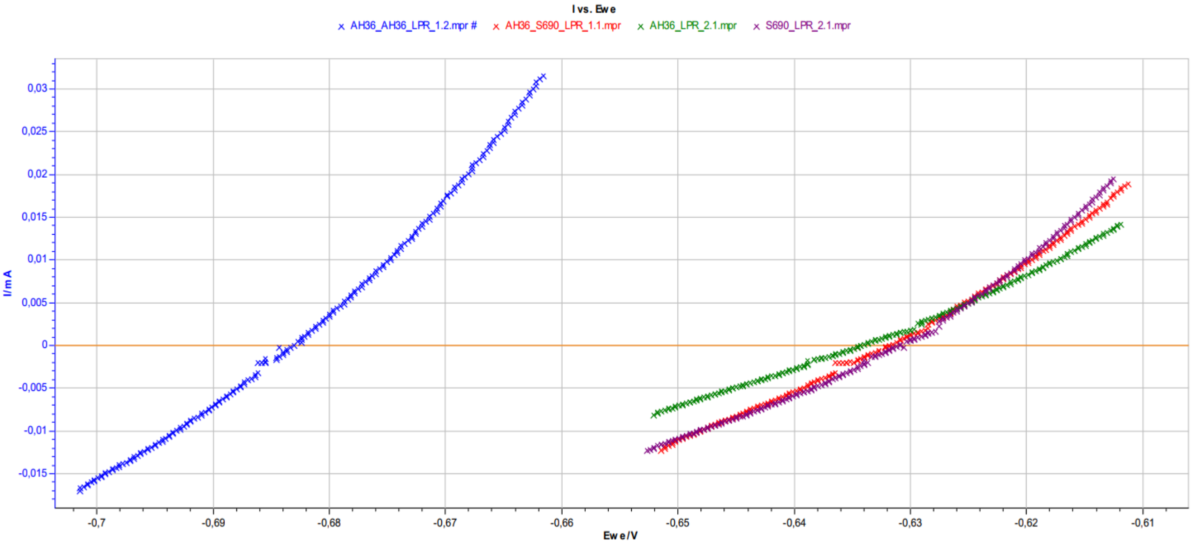

Fig.[6.8] LPR for parent metals AH36, S690 and weldments AH36-AH36 and AH36-
Blue: AH36-AH36, **Red:** AH36-S690, **Green:** AH36, **Purple:** S690**.**

Table [6.7] Average values of corrosion and LPR parameters of all the specimens.

	Ecorr (mV)	**Icorr (µA/cm^2)**	**Rp (ohm)**
AH36	-628.6	15.095	1857
S690	-626.3	18.251	1461
AH36-AH36	-695.9	30.360	872
AH36-S690	-642.1	18.978	1376

7. POTENTIODYNAMIC POLARIZATION- TAFEL EXTRAPOLATION METHOD

7.1. Introduction

As already mentioned in Chapter 4, potentiodynamic polarization consists an DC perturbation of the specimen over a large range of potential of 250mV catholically (negative) and anodically (positive) versus the Open Circuit Potential. This excitation returns graphs of potential (Voltage, Y axis) vs log (current). For practical reasons the negative cathodic currents are replaced by their positive values. Potentiodynamic polarization is explained by mixed potential theory (see Chapter 4), and consequently the Butler-Volmer equation describes the relation between the potential and the current (kinetics) in a mixed potential system :

$$I = Ia + Ic = I_{corr}\left[\exp\left(\frac{2.303(E-Eoc)}{\beta a}\right) - \exp\left(\frac{2.303(E-Eoc)}{\beta c}\right)\right] \qquad (7.1)$$

where
I = cell current (A)
Icorr = corrosion current (A)
E = applied potential (V)
Eoc = Corrosion Potential (V)
βa = anodic Tafel constants
βc = cathodic Tafel constant

The aim is to calculate the corrosion current Icorr, as well as the Tafel constants βa and βc. The method applied is referred as Tafel extrapolation method (see Chapter 4).

For each specimen, three (3) experiments were conducted, giving one diagram each. In this chapter, only one of them is presented (the one with values that are closer to the average values of the three experiments), along with the common diagrams. The diagram of every experiment performed is presented in Chapter 12. Annex (12.2.2). The fitting of the graphs obtained is performed employing ECLab Software. For all the graphs current is presented as log(|I/mA|) on x-axis while potential E as we/V on y-axis.

7.2. Results

In the following paragraphs the potentiodynamic polarization graphs and the results obtained of the parent metals AH36, S690 and the welded specimens AH36-AH36 and AH36-S690 are presented. In Fig.[7.1] an example of a Tafel Extrapolation fitting via EC Lab software is presented, in order to help with the comprehension of the Tafel method used for the data elaboration.

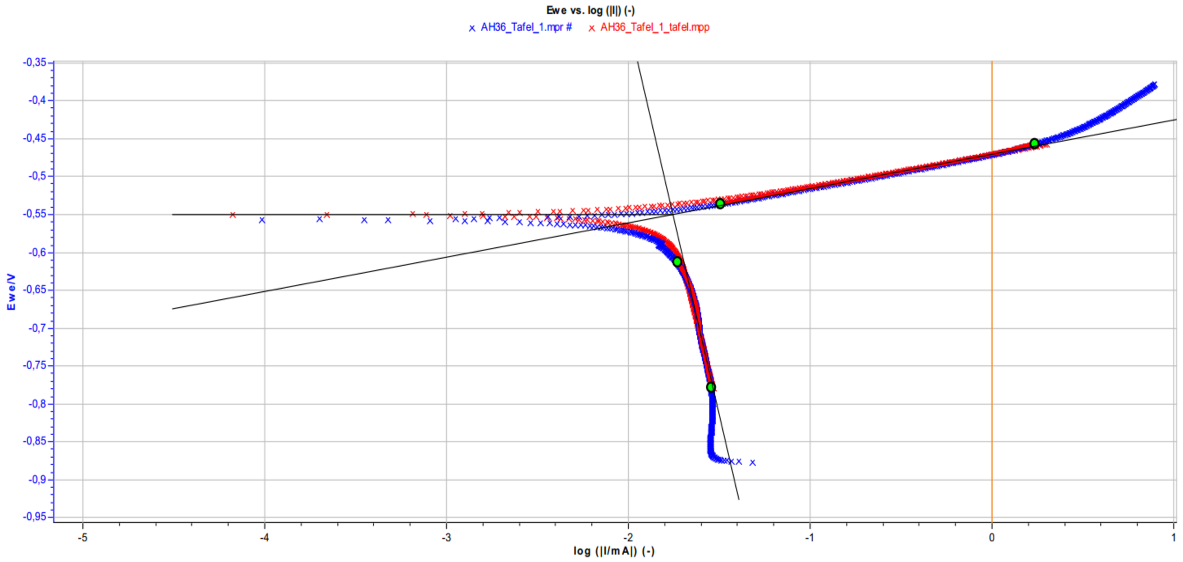

Fig.[7.1] Polarization curves and Tafel extrapolation method of parent metal **AH36**, exp.1.
Blue: AH36, **Red**: Tafel fitting via EC Lab.

The polarization curve in Fig.[7.1] presents two branches: the anodic branch and the cathodic branch. The shape of the anodic branch proves that AH36 presents continuous anodic dissolution, without evidence of passive behavior. The dissolution should be well represented by the anodic reaction of:

$$Fe \rightarrow Fe^{2+} + 2e^{-} \qquad (7.2)$$

Possibly, other alloying elements present anodic reactions, however of minor importance.

The shape of the cathodic branch shows that cathodic behavior is dominated by the O_2 diffusion in the electrolyte solution. Close to Ecorr, the reduction of hydrogen is observed :

$$2H^{+} + 2e^{-} \rightarrow H_2 \qquad (7.3)$$

while for lower potential values O_2 diffusion in the almost neutral solution defines the cathodic behavior:

$$O_2 + 2H_2O + 4e^{-} \rightarrow 4OH^{-} \qquad (7.4)$$

Acccording to Tafel extrapolation method, the crossing point of :

- the tangent to the linear part of the anodic branch
- the tangent to the linear part of the cathodic branch
- the line through the Ecorr parallel to the x-axis

defines the Icorr value on x-axis.

The corrosion rate can be calculated by

$$CR=\frac{Icorr\ K\ EW}{d\ A} \tag{7.5}$$

where K is a constant that defines the units of the corrosion rate, EW is the equivalent weight is equal to the molar mass of the tested metal devided by the number of the electrodes involved in the redox reaction, d is the density of the tested metal and A is the sample area.

From Tafel extrapolation method the values of Tafel constants βa and βc, can also be obtained. These are the values of the slope of anodic βa and cathodic βc branch of the polarization curves in mV/decade. However, in diffusion controlled cathodic curves the βc values cannot be defined.

7.2.1. Parent metals

In the present paragraph, the summary diagrams, Fig.[7.2] and Fig.[7.3] and corrosion parameters tables, Table[7.1] and Table [7.2] of the parent metals AH36 and S690 are presented, along with comparison diagram, Fig.[7.5] and Table [7.3].

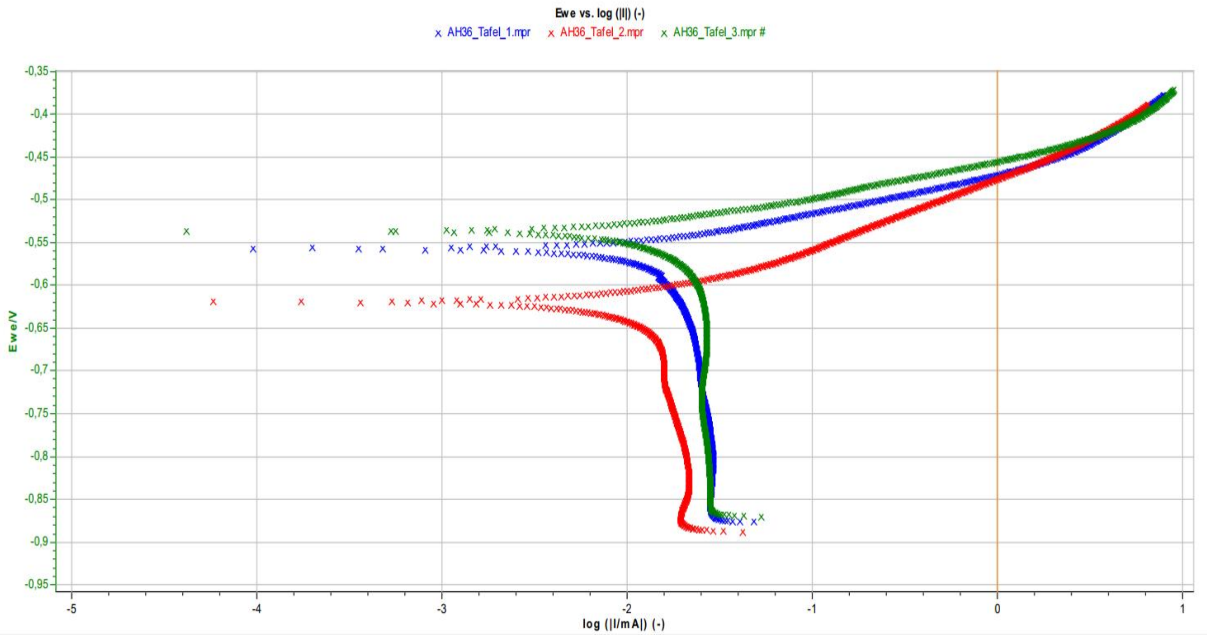

Fig.[7.2] Polarization curves **AH36**, all 3 experiments. **Blue**: exp.1. **Red**: exp. 2. **Green** exp. 3.

Fig.[7.2] shows that all the experiments present very good repeatability. All of them present anodic dissolution and O_2 diffusion controlled cathodic polarization. Corrosion potential Ecorr has mean value of -567 mV while Icorr has an average of 18 μA/cm^2. Anodic Tafel constant βa is 57 mV/decade, while cathodic Tafel constant βc are very high, higher than 200 mV and cannot be taken as credible, due to O_2 diffusion..

The corrosion rate has been calculated according to equation (7.5) and equals to 8 mpy.

Table [7.1] Corrosion and Tafel parameters for each AH36 experiment.

	Ecorr (mV)	**Icorr (μA/cm^2)**	**βc (mV)**	**βa (mV)**	**CR (mpy)**
AH36.1	-549.7	17.556	1033.9	45.1	8.076
AH36.2	-624.8	15.591	1372.7	83.1	7.172
AH36.3	-525.3	20.351	2142.2	41.3	9.362
Average	**-566.6**	**17.833**	**1516.3**	**56.5**	**8.203**
Stdev	51.6	2.392	567.9	23.1	1.101

The shape of the anodic branch proves that S690 presents continuous anodic dissolution, without evidence of passive behavior, attributed to anodic reduction of Fe (see eq. 7.2). The shape of the cathodic branch shows that cathodic behavior is dominated by the O_2 diffusion (see eq. 7.4) in the electrolyte solution. The cathodic area becomes very fast dominated by O_2 diffusion.

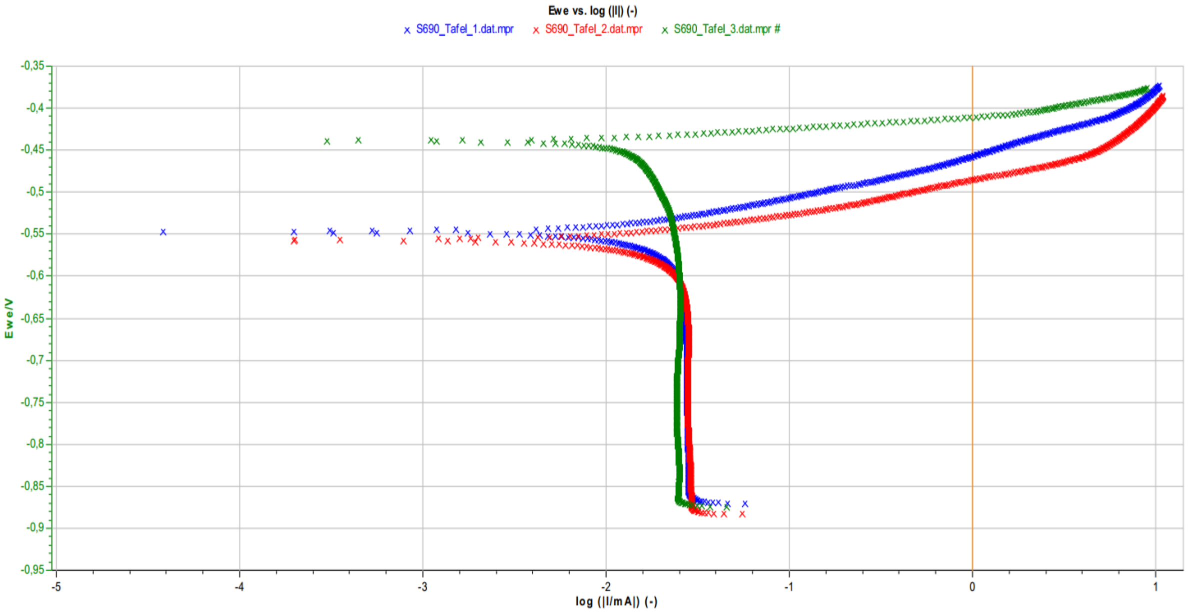

Fig.[7.3] Polarization curves **S690**, all 3 experiments. **Blue**: exp.1. **Red**: exp. 2. **Green** exp. 3.

Fig.[7.3] shows all the experiments present performed on S690. All of them present very good repeatability. All of them show anodic dissolution and O_2 diffusion controlled cathodic polarization. Corrosion potential Ecorr has mean value of -505 mV while Icorr has an average of 25 μA/cm^2. Anodic Tafel constant βa is 34 mV/decade, while cathodic Tafel constant βc are very high, higher than 200 mV and cannot be taken as credible, due to O_2 diffusion. The corrosion rate calculated according to (7.5) and equals to 11mpy.

Table [7.2] Corrosion and Tafel parameters for each S690 experiment.

	Ecorr (mV)	**Icorr ($\mu A/cm^2$)**	**βc (mV)**	**βa (mV)**	**CR (mpy)**
S690.1	-533.2	25.656	6097.9	46.1	11.857
S690.2	-550.1	26.177	6120.0	41.0	12.098
S690.3	-432.4	22.619	5334.1	13.8	10.454
Average	**-505.2**	**24.817**	**5850.7**	**33.6**	**11.470**
Stdev	63.6	1.922	447.5	17.4	0.888

In Fig.[7.4] the most representative polarization curves of AH36 and S690 parent metal are presented, for the comparison of the two metals. According to this, both parent metals present similar anodic dissolution determined by charge transfer (activation polarization). The cathodic curve shows that the phenomenon is dominated by O_2 diffusion, meaning that the phenomenon is both controlled by activation polarization, close to equilibrium and consequently by concentration polarization due to O_2 diffusion. The Ecorr values are slightly lower for S690 proving lower tendency for corrosion. Icorr values are lower for AH36 leading to lower corrosion rate.

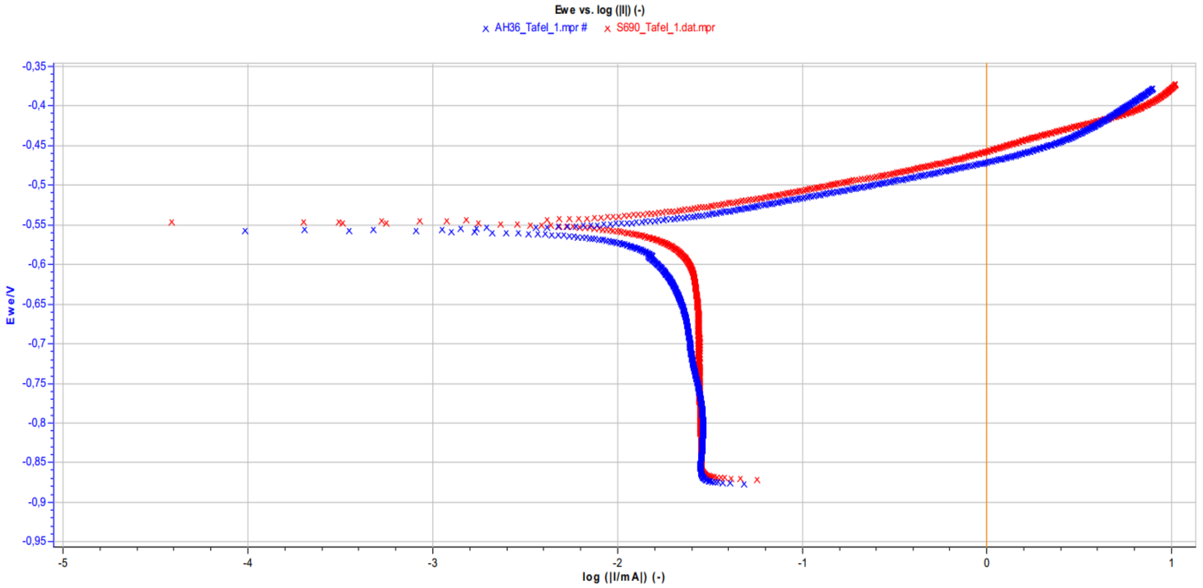

Fig.[7.4] Comparison of Potentiodynamic Polarization for parent metals **AH36** and **S690**, **Blue:** AH36. **Red:** S690.

Table [7.3] Average corrosion and Tafel parameters for parent metal tested.

	Ecorr (mV)	**Icorr ($\mu A/cm^2$)**	**Corrosion rate (mpy)**	**Corrosion rate Stdev (mpy)**
AH36	-566.6	17.833	8.203	1.101
S690	-505.2	24.817	11.470	0.888

7.2.2. Weldments

In the present paragraph, the summary diagrams, Fig.[7.5] and Fig.[7.6] and corrosion parameters tables, Table[7.4] and Table [7.5] of the weldments AH36-AH36 and AH36-S690 are presented, along with comparison diagram, Fig.[7.7] and Table [7.6].

Homogeneous weldment AH36-AH36 presents Ecorr of -646 mV and Icorr of 18 μA/cm^2. These values are quite similar for both the Ecorr and Icorr to the ones of the parent metal.
These values prove that the welding procedure has not affected significantly the corrosion parameters of the specimen.
The only evident difference is that the cathodic branch presents more activation controlled behaviour and less evident diffusion controlled. All the experiments present good repeatability, as shown in Fig.[7.5].

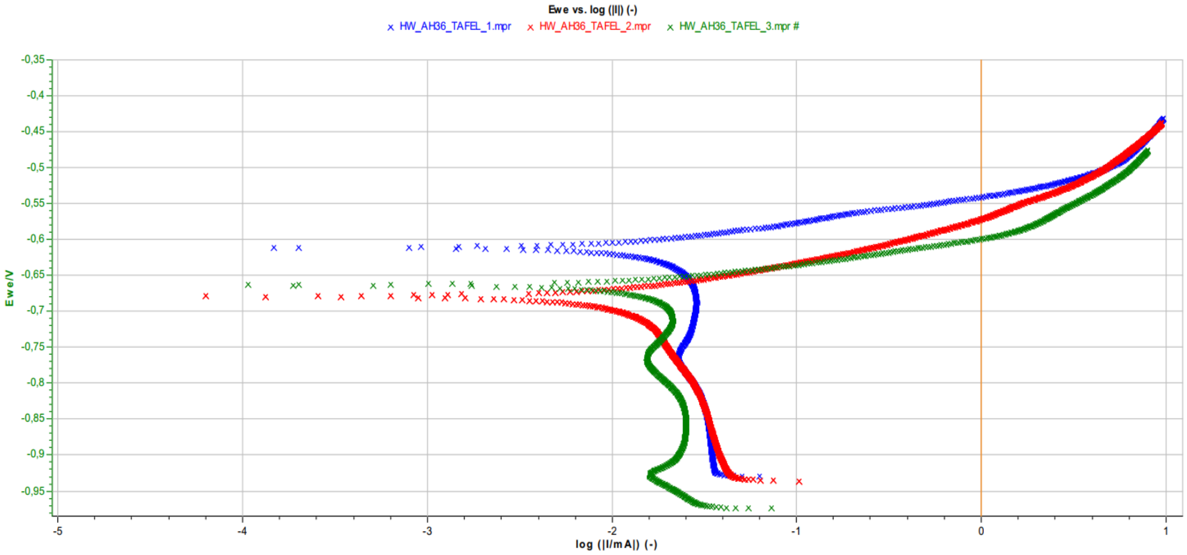

Fig.[7.5] Polarization curves **AH36-AH36**, all 3 experiments. **Blue**: exp.1. **Red**: exp. 2. **Green** exp. 3.

Table [7.4] Corrosion and Tafel parameters for each AH36-AH36 experiment.

	Ecorr (mV)	**Icorr (μA/cm^2)**	**βc (mV)**	**βa (mV)**	**Corrosion rate (mpy)**
AH36-AH36.1	-675.2	17.342	624.5	57.3	8.002
AH36-AH36.2	-601.4	19.182	1136.2	36.1	8.851
AH36-AH36.3	-660.3	16.520	1306.0	34.0	7.622
Average	**-645.6**	**17.681**	**1022.2**	**42.5**	**8.158**
Stdev	39.0	1.363	354.8	12.9	0.629

Concerning the heterogeneous weldment AH36-S690 the corrosion potential Ecorr is -594 mV, which is higher than the relative value of each distinct metal. This shows higher tendency for corrosion for the AH36-S690 weld. The average value of Icorr = 20 μA/cm^2 shows that the weldment is in between the constituting parent metals: lower than S690, higher than AH36. Another distinct difference is the cathodic part which seems to be controlled by charge transfer (activation polarization). All the experiments present very good repeatability.

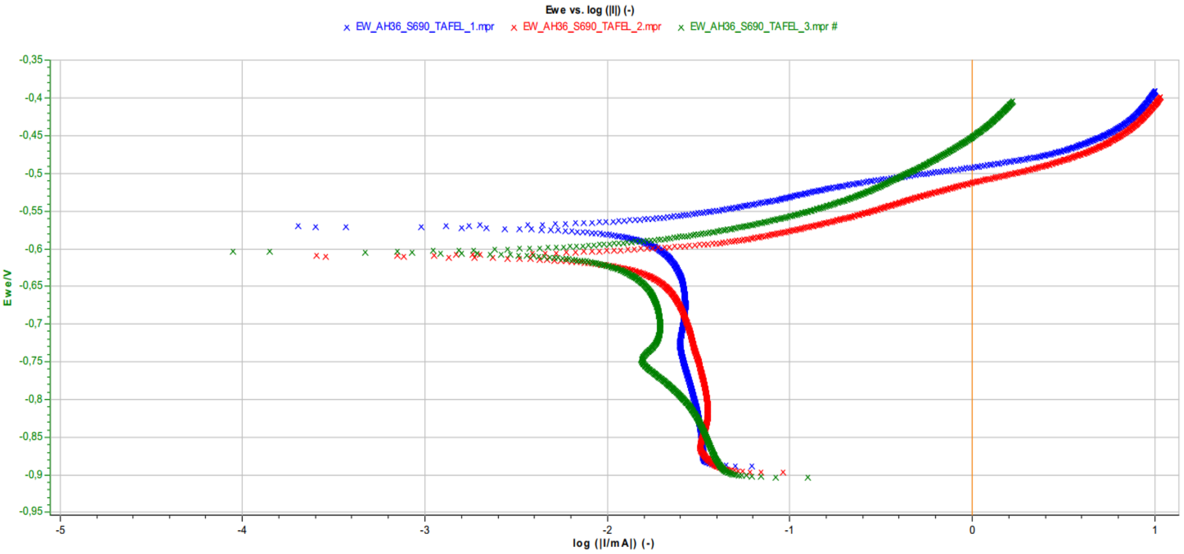

Fig.[7.6] Polarization curves **AH36-S690**, all 3 experiments. **Blue**: exp.1. **Red**: exp. 2. **Green** exp. 3.

Table [7.5] Corrosion and Tafel parameters for each AH36-AH36 experiment.

	Ecorr (mV)	**Icorr (μA/cm^2)**	**βc (mV)**	**βa (mV)**	**Corrosion rate (mpy)**
AH36-S690.1	-616.6	21.840	843.0	62.3	10.071
AH36-S690.2	-556.7	21.989	1868.6	40.1	10.140
AH36-S690.3	-609.4	15.252	1260.2	70.2	7.033
Average	**-594.2**	**19.694**	**1323.9**	**57.5**	**9.081**
Stdev	32.7	3.847	515.8	15.6	1.774

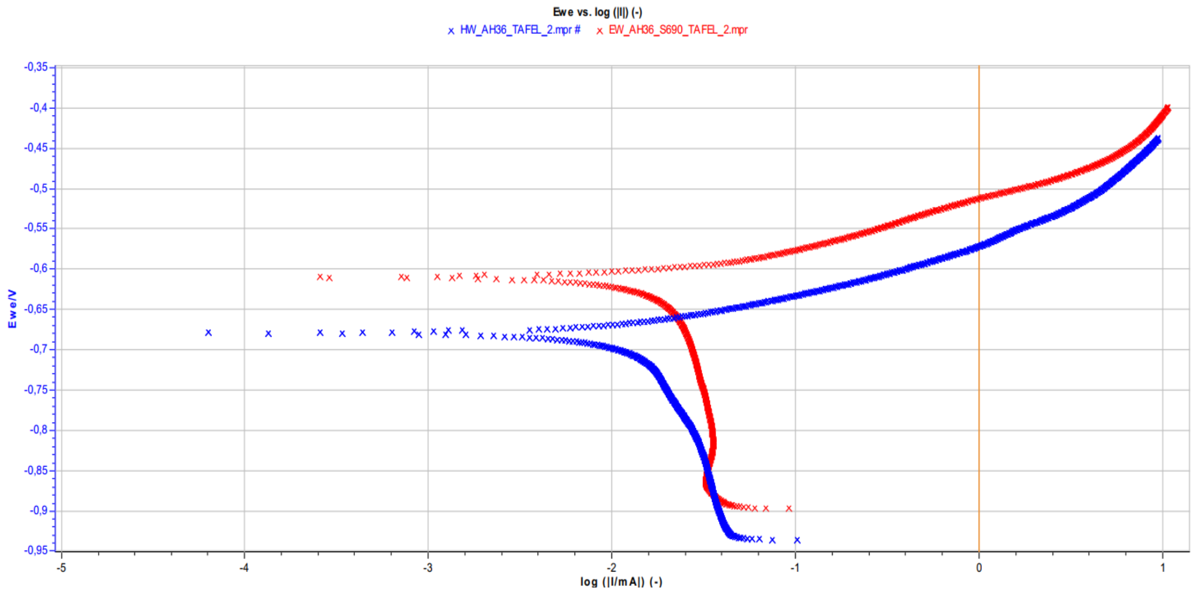

Fig.[7.7] Comparison of Potentiodynamic Polarization for the welds **AH36-AH36** and **AH36-S690**, **Blue:** AH36-AH36. **Red:** AH36-S690.

Table [7.6] Average corrosion and Tafel parameters for weldment tested.

	Ecorr (mV)	**Icorr ($\mu A/cm^2$)**	**Corrosion rate (mpy)**	**Corrosion rate Stdev (mpy)**
AH36-AH36	-645.6	17.681	8.158	0.629
AH36-S690	-594.2	19.694	9.081	1.774

7.3. Total results- Conclusions

The potentiodynamic polarization measurements performed on the parent metals AH36, S690 and the welds AH36-AH36 and AH36-S690 provided important results concerning both the corrosion mechanism and the corrosion parameters.

Firstly, all of our steel samples were characterized by an increase of current density with increasing potential in the anodic region, without presenting any passivation behavior in the 3.5% NaCl solution. According to this both parent metals and welds present similar anodic dissolution determined by charge transfer (activation polarization). The cathodic curve shows that the phenomenon is dominated by O_2 diffusion, meaning that the phenomenon is controlled by activation polarization, close to equilibrium and consequently by concentration polarization due to O_2 diffusion further than equilibrium. In particular for S690, but also for its weld AH36-S690 the transition from equilibrium to concentration polarization is faster and the cathodic curve presenting O_2 diffusion is a straight line vertical to I current (y) axis.

Comparing the parent metals, the Ecorr values do not present significant differences, while the Icorr values and the corrosion rate are higher for S690 (Icorr = 25$\mu A/cm^2$), indicating worse corrosion behavior than AH36 (Icorr = 18$\mu A/cm^2$), .

Comparing the different weldments, the Ecorr values as well as the the Icorr values and the corrosion rate are similar for both weldments AH36-S690 (Icorr = 19μA/cm^2), AH36-AH36, (Icorr = 17μA/cm^2).

In addition, comparing the parent metals with the two weldments we observe that the differences between the corrosion rates and the Icorr values of two weldments are almost negligible in comparison with the differences between the corrosion rates and the Icorr values of two parent metals. Also, the weldment of AH36-AH36 presents almost the same Icorr and corrosion rate as the parent metal AH36, whereas the difference between the parent metal S690 and the heterogeneous weldment is more significant.

Finally, comparing the values of the Tafel parameter βc, which is responsible for the cathodic polarization curve's slope and therefore, the reaction's oxygen diffusion level, we observe that the values of AH36, AH36-AH36 and AH36-S690 were almost equal and significantly smaller than the βc value of S690, indicating that the last has a higher level of oxygen diffusion in that case.[58]

In the present paragraph, the summary diagram, Fig.[7.8] and corrosion parameters table, Table[7.7] of the parent metals AH36 and S690 and the weldments AH36-AH36 and AH36-S690 are presented.

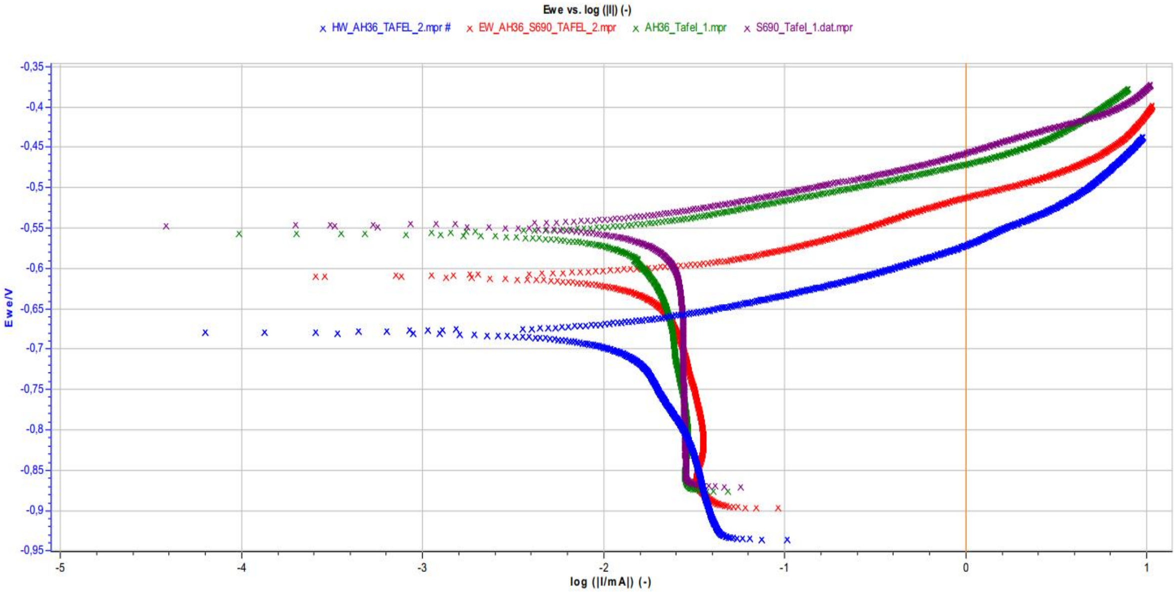

Fig.[7.8] Comparison of Potentiodynamic Polarization of all the specimens,
Blue: AH36-AH36. **Red:** AH36-S690. **Green**: AH36. **Purple**: S690.

Table [7.7] Average values of corrosion and Tafel parameters for each specimen tested.

	Ecorr (mV)	**Icorr (μA/cm^2)**	**βc (mV)**	**βa (mV)**	**Corrosion rate (mpy)**
AH36	-566.6	17.833	1516.3	56.5	8.203
S690	-505.2	24.817	5850.7	33.6	11.470
AH36-AH36	-645.6	17.681	1022.2	42.5	8.158
AH36-S690	-594.2	19.694	1323.9	57.5	9.081

8. ELECTROCHEMICAL IMPEDANCE SPECTROSCOPY

8.1. Introduction

Electrochemical Impedance Spectroscopy (EIS) is an effective technique for detecting the different electrochemical processes at the interfaces between the electrodes and the electrolytes and can provide valuable information on the corrosion behaviour of the system, as already mentioned in Chapter 4.
The impedance $Z(\omega)$ may be expressed in terms of real, $Z'(\omega)$, and imaginary, $Z''(\omega)$, components.

$$Z(\omega) = Z'(\omega) + Z''(\omega) \tag{8.1}$$

The impedance behaviour of an electrode may be expressed in Nyquist plots of $Z''(\omega)$ as a function of $Z'(\omega)$ or in Bode plots of log |Z| and θ versus frequency f in cycles per sec (hertz), where $\omega = 2\pi f$. These plots for a simple parallel connected resistance – capacitance circuit are shown schematically in Fig.[8.1]. This circuit is often an adequate representation of a simple corroding surface under activation control. The Nyquist plot shows a semicircle, with increasing frequency in a counter clockwise direction. At very high frequency the imaginary component Z'' disappears, leaving only the solution resistance, R_Ω. At very low frequency, Z'' again disappears, leaving a sum of R_Ω and the faradaic reacting resistance or polarization resistance, R_p. The Bode plot gives analogous results. At intermediate frequencies, the capacitance plots linear with a slope of -1 and maximum phase angle θ.

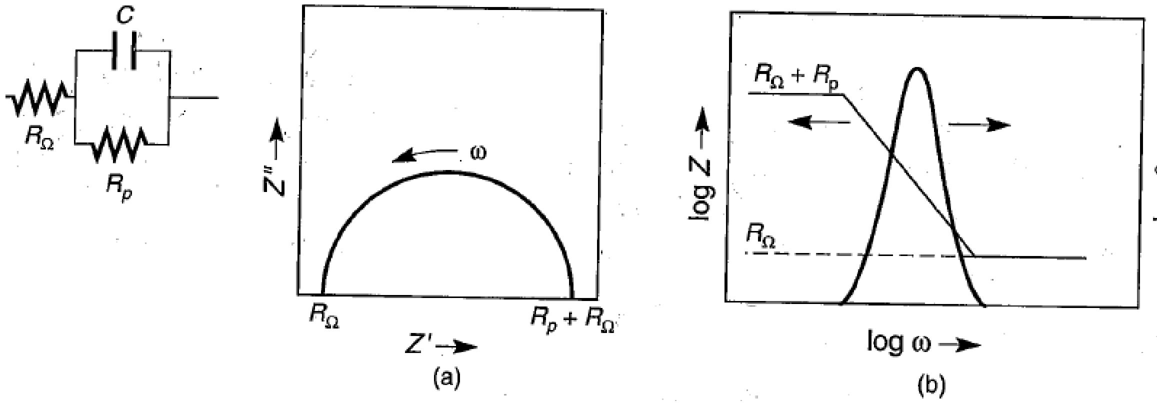

Fig.[8.1] Data display for electrochemical impedance spectroscopy for a corroding electode simulated by a parallel – connected resistance Rp and capacitance C (a) Nyquist plot, (b) Bode plot, both schematic.

The faradaic reaction resistance or polarization resistance R_p, is inversely proportional to the corrosion rate. It is evident that the R_Ω measured at high frequency can be subtracted from the sum of R_p+R_Ω at low frequency to give a compensated value of Rp free of ohmic interferences.

In the frequent case of control by diffusion in the electrolyte (concentration polarization) or in a surface film or coating, an additional resistive element called Warburg impedance, W, must be included in the circuit, *W* is evidenced at low frequencies on the Nyquist plot by a straight line superimposed at 45^{o}C to both axes in Fig.[8.2].

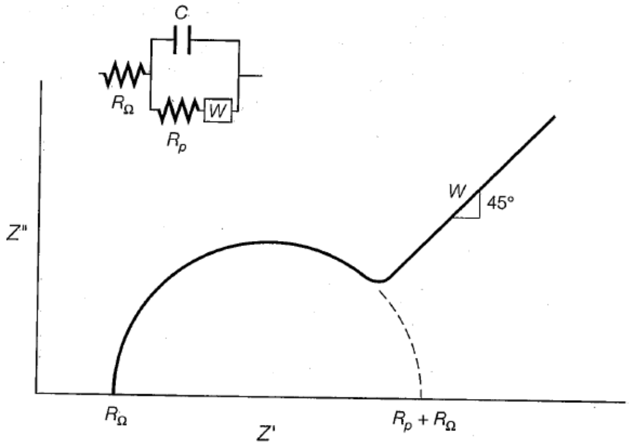

Fig.[8.2] Schematic Nyquist plot showing effects of partial diffusion control with Warburg impedance W.

In the present thesis EIS experiments are performed both on parent metals AH36, S690 and weldments AH36-AH36 and AH36-S690 (1st series of experiments). Moreover, trying to elucidate the corrosion mechanism over time, EIS experiments were also performed for the aforementioned specimens (2nd series of experiments) :

- In the first series, three (3) EIS experiments, of same duration were conducted back to back for each kind of specimen after a 30-minute-long Open Circuit Corrosion experiment in 0.6M NaCl solution. These experiments provided one Nyquist and two Bode diagrams each. In this chapter, only one of them is presented (the one with values that are closer to the average values of the three experiments), along with the common diagrams of all the three experiments. The rest of the diagrams are presented in Chapter 12. Annex (12.2.3).
- In the second series, six (6) EIS experiments of same duration were conducted but with a different method than the previous case. Each EIS was conducted in different time (t=0 hours, t=2 hours, t=4 hours, t= 8 hours, t= 16 hours and t=24 hours) and an Open Circuit Corrosion experiment was conducted between each EIS. For the second series of experiments, the solution was of 0.05M NaCl. This lower concentration of NaCl was expected to better reveal the corrosion mechanism through time. In this chapter, only a common Nyquist diagram with all the six (6) EIS experiments is presented, along with the values for each experiment, in order to compare the results over time. One Nyquist and two Bode diagrams were also obtained by each EIS experiment and they are presented in Chapter 12. Annex (12.2.3).

The fittings and the simulations in the EIS experiments were performed employing EC Lab software.

8.2. Results

In the following paragraphs the Nyquist and the Bode plots of parent metals AH36 and S690 are presented. For all the Nyquist plots, -Z"/Ohm is presented on y-axis, vs Z'/Ohm on x-axis. The Bode diagrams in this thesis consist of two types of curves. For all the Bode plots of the first category, log(|Z|/Ohm) is presented on y_1-axis (left side), vs log(f/Hz) on x-axis. The Bode plots of the second category, θ/degrees is presented on y_2-axis (right side), vs log(f/Hz) on x-axis.

In both Nyquist and Bode plot, the Z of high frequency implies solution resistance, whereas the Z of low frequency is total resistance including solution and polarization resistance. The interpretation of EIS plots provides information of surface/electrolyte solution interface.

In Fig.[8.3] an example of a Nyquist fitting via EC Lab software is presented, whereas, in Fig.[8.4] an example of the Bode fitting is presented, in order to help with the comprehension of the EIS method used for the data elaboration which are presented in the following paragraphs.

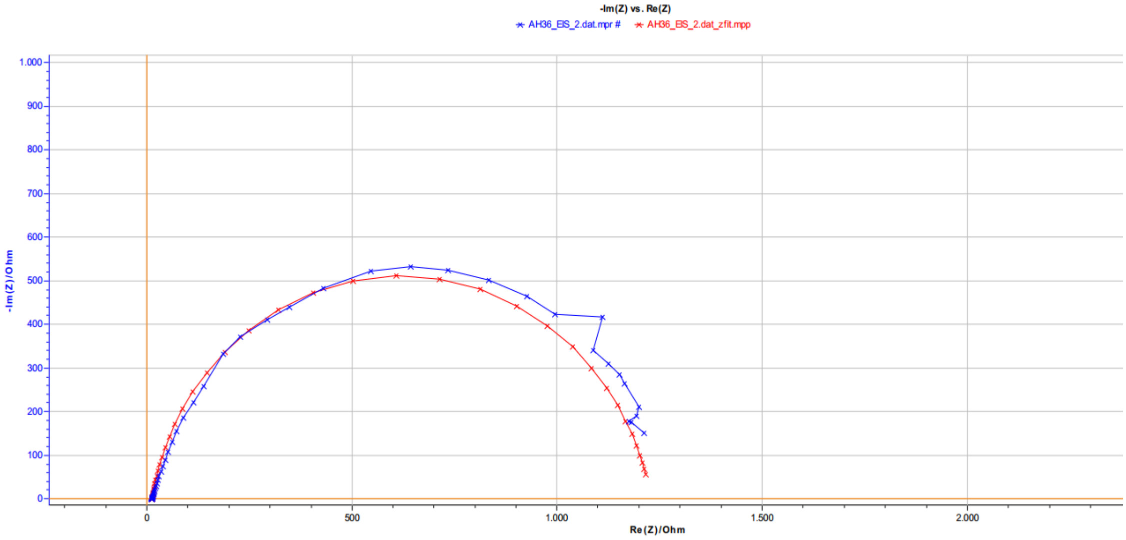

Fig.[8.3] Nyquist plot for parent metal **AH36**, exp.1.
Blue: data experiment, **Red:** Nyquist fitting.

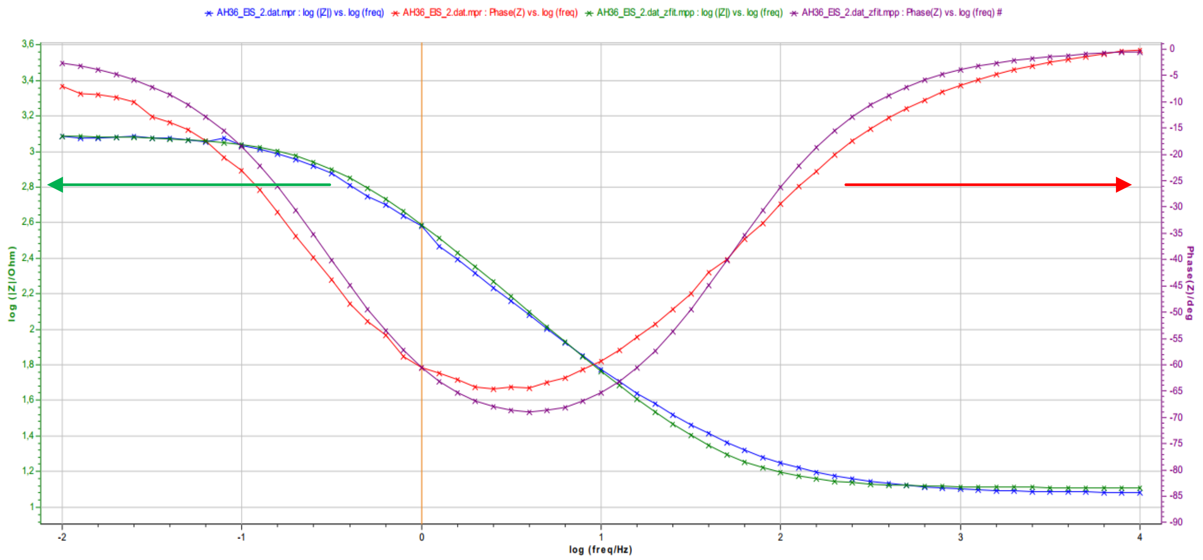

Fig.[8.4] Bode plots for parent metal **AH36**, exp. 1.
Blue: experiment data of log(|Z|), **Green:** fitting.
Red: experiment data of θ, **Purple:** Bode fitting.

8.2.1. Parent metals

In the present paragraph, the summary diagrams, Fig.[8.5], Fig.[8.6], Fig.[8.9] and Fig.[8.10] and the corrosion parameters tables Table [8.1] and Table [8.3] of the first series of experiments for the parent metals AH36 and S690 are presented, along with comparison diagrams, Fig.[8.12] and Fig.[8.13] and the respective table, Table [8.5].

The shape of the Nyquist plot for AH36 displays only one capacitive semicircle. This type of diagram is usually interpreted as a mechanism of charge transfer on an inhomogeneous surface. The diameter of the capacitive semi-circle is almost the same for the three experiments, Fig.[8.5]. Deviations at the low frequency end of the semi-circle are due to changes in impedance during the long times required to conduct measurements at low frequencies. Moreover, no indication of Warburg impedance line is indicated.

Similarly, the Bode plots of the steel samples shows only one time constant as in Fig.[8.6].

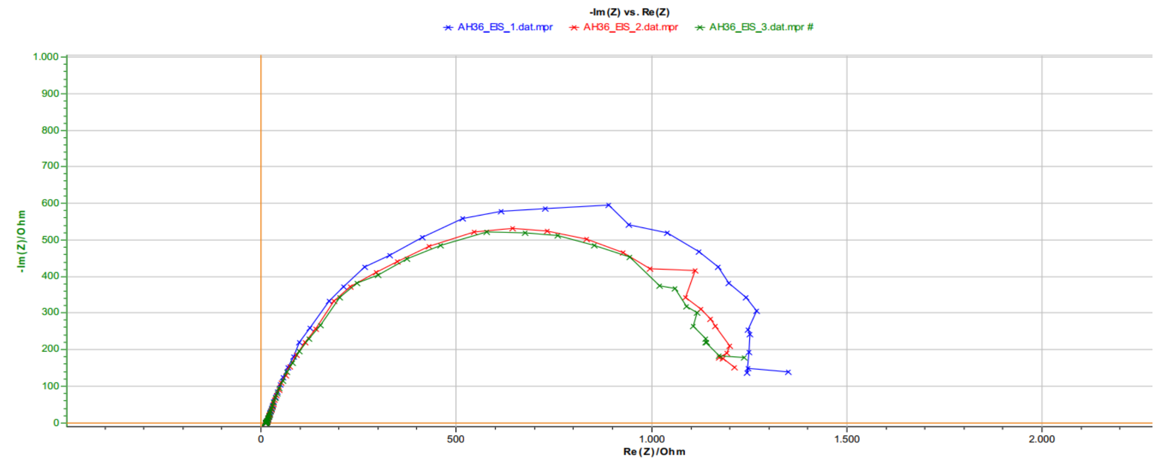

Fig.[8.5] Nyquist plots of the 1st series of experiments for parent metal **AH36**, all experiments. **Blue:** exp1, **Red:** exp.2. **Green:** exp.3.

The values of the equivalent circuit elements are presented in Table [8.1], along with the rest of the experiments performed for AH36, which present similar behavior. All the data present very good repeatability and the value of Rct i.e. the Rp, reaches the average value of 1230 Ohms.

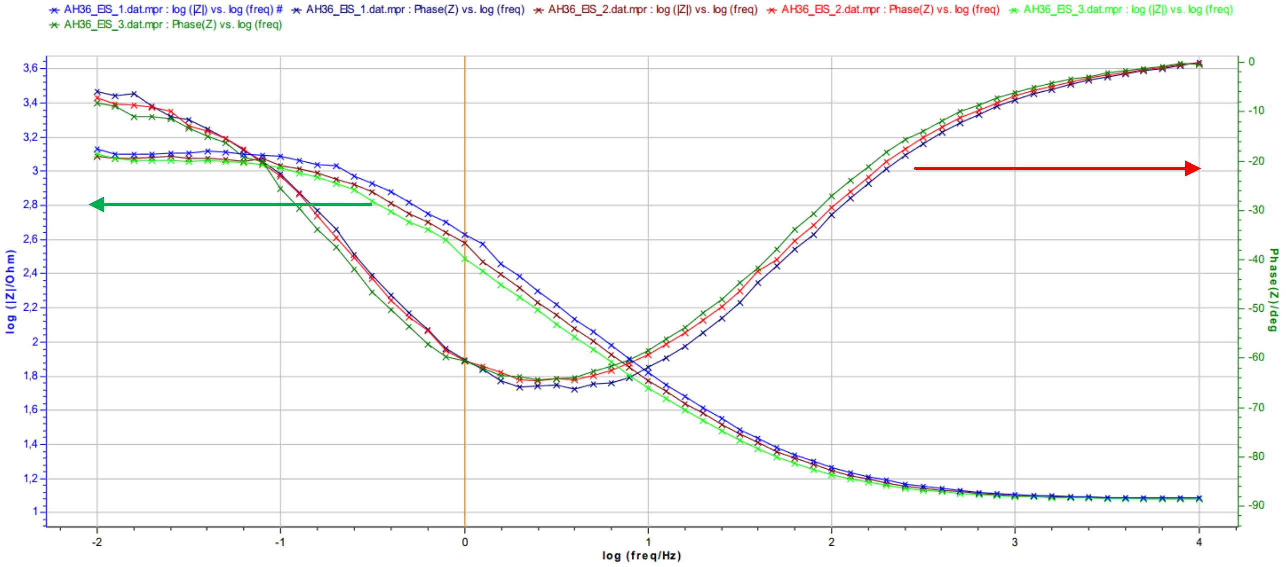

Fig.[8.6] Bode plots of the 1st series of experiments for parent metal **AH36**, all experiments. Experiment data of log(|Z|). **Blue:** exp.1, **Maroon:** exp.2, **Lime:** exp.3. Experiment data of θ. **Navy:** exp.1, **Red:** exp.2, **Green:** exp.3.

To describe the impedance response of the corrosion behaviour of AH36 in chloride environments, the equivalent circuit analysis was performed employing EC Lab software. The equivalent circuit model from the literature was used for the EIS results (Fig.[8.7]). In the circuits, *R*s and *R*ct indicate solution resistance and charge transfer resistance of the electrolyte–substrate interface, respectively. For perfect semi-circles the element Q is well represented by the capacitor C associated with the double layer capacitance. However, in AH36, the shape of the Nyquist curve is not a perfect semicircle centred on the Z’ axis at the (R/2, 0) point. It presents a deviation from the Resistance Capacitor behaviour and there is a deformation and broadening of the semicircle. For this reason, in the equivalent modelled circuit the capacitor C is substituted by the Constant Phase Element Q, still parallel with the resistor Rct. This deformation is attributed to the roughness of the electrode-electrolyte interfaces or to inhomogeneities in the local distribution of defects in the vicinity of grain boundaries.

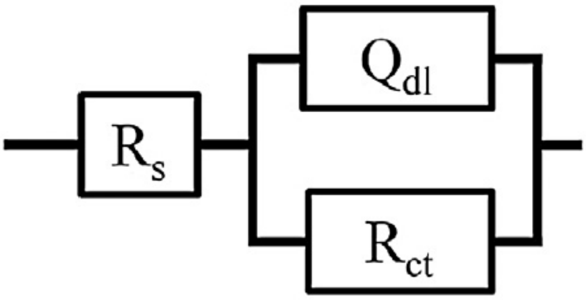

Fig.[8.7] Equivalent circuit (Randles) to fit impedance data.

In the following table (Table [8.1]), the electrical elements of the impedance fitting via EC Lab are presented. In general, *R*ct, is inversely proportional to the corrosion rate of a given metal. For AH36 the average value of Rct is 1227 Ohms, while Rs is stable at 13 Ohms.

Table [8.1] Corrosion and EIS parameters of the first series of EIS experiments for each AH36 experiment.

	R_S (Ohm)	**Q (*10^{-3} F)**	**R_{CT} (Ohm)**
AH36.1	12.81	0.4567	1215
AH36.2	12.87	0.3328	1264
AH36.3	12.66	0.5371	1203
Average	**12.78**	**0.4422**	**1227**
Stdev	0.11	0.1029	32

For the 24-hours experiments, the summary diagram, Fig.[8.8] is presented, along with the corrosion parameters Table [8.2].

The Nyquist plots for the 24h experiments present smaller diameters for longer exposure periods of the specimen to the solution. Thus, after 2 hours the diameter is almost half. It proves that Rct is lower, proving that the anodic dissolution of the specimen is continuing. The same behavior is apparent for the 4 hours curve. Though, the 8 hours, the 16 hours and the 24 hours curve are almost stable implying that corrosion products are formed on the surface halting the dissolution of the specimen. Moreover, at the high frequency end the semicircles are depressed below the horizontal Z' axis. This behaviour has been explained assuming metal dissolution under a corrosion product film with oxygen reduction within the film pores (Fig.[8.8]).

The values of the electric elements in Table [8.2], show that the resistance of the solution is stable Rs and Rct is diminishing with time.

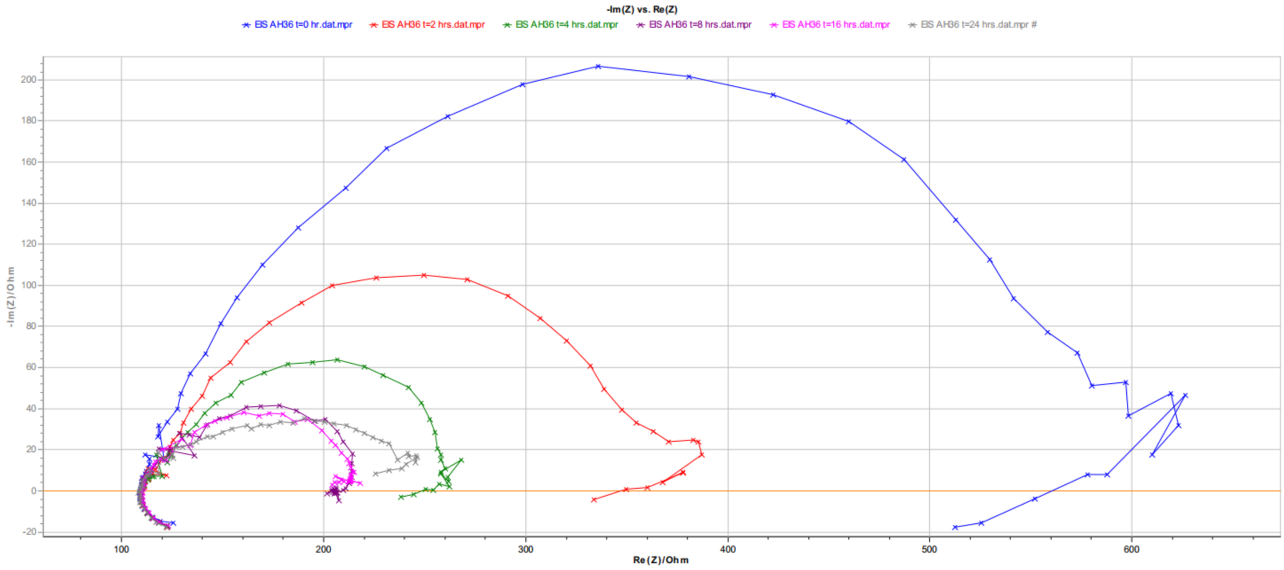

Fig.[8.8] Common Nyquist plot of the 2nd series of EIS experiments for parent metal **AH36.** **Blue:** t=0 hrs, **Red:** t=2 hrs, **Green:** t=4 hrs, **Purple:** t=8 hrs, **Pink:** t=16 hrs, **Grey:** t=24 hrs.

Table [8.2] Corrosion and EIS parameters of the second series of EIS experiments for each AH36 experiment.

	R_S (Ohm)	**Q (*10^{-3} F)**	**R_{CT} (Ohm)**
AH36, t=0 hrs	113.7	0.3577	476.3
AH36, t=2 hrs	114.4	1.014	261.6
AH36, t=4 hrs	113.3	0.6482	143.5
AH36, t=8 hrs	113.9	0.1773	92.8
AH36, t=16 hrs	111.9	0.2870	101.0
AH36, t=24 hrs	108.4	1.9110	140.2

For parent metal S690, as in the parent metal AH36, both plots Nyquist and Bode present only one capacitive semicircle, leading to the conclusion that the mechanism of corrosion is determined by the charge transfer and in fact on an inhomogeneous surface (Fig.[8.9]). The same observations are obtained from the Bode Plot (Fig.[8.10]). For S690, the shape of the Nyquist curve is not a perfect semicircle; in fact it is more deformed than AH36. Thus, the equivalent circuit analysis provided the same circuit model, Fig[8.9].

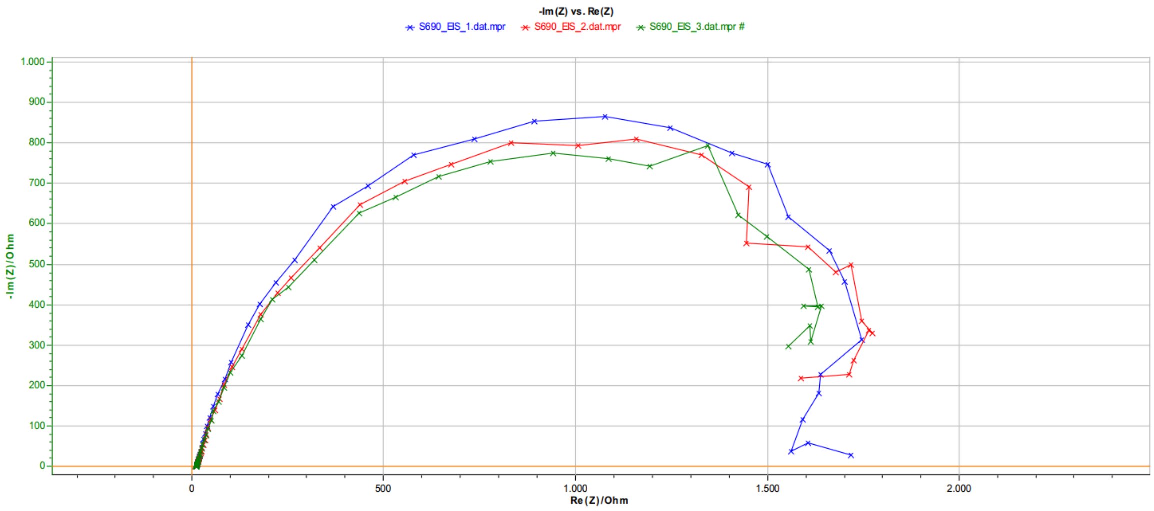

Fig.[8.9] Nyquist plots of the 1st series of experiments for parent metal **S690**, all experiments. **Blue:** exp1, **Red:** exp.2. **Green:** exp.3.

The values obtained from this modelling is provided in Table [8.3]. The values present very good repeatability for all the experiments performed, and the average Rct value is as high as 1710 Ohm.

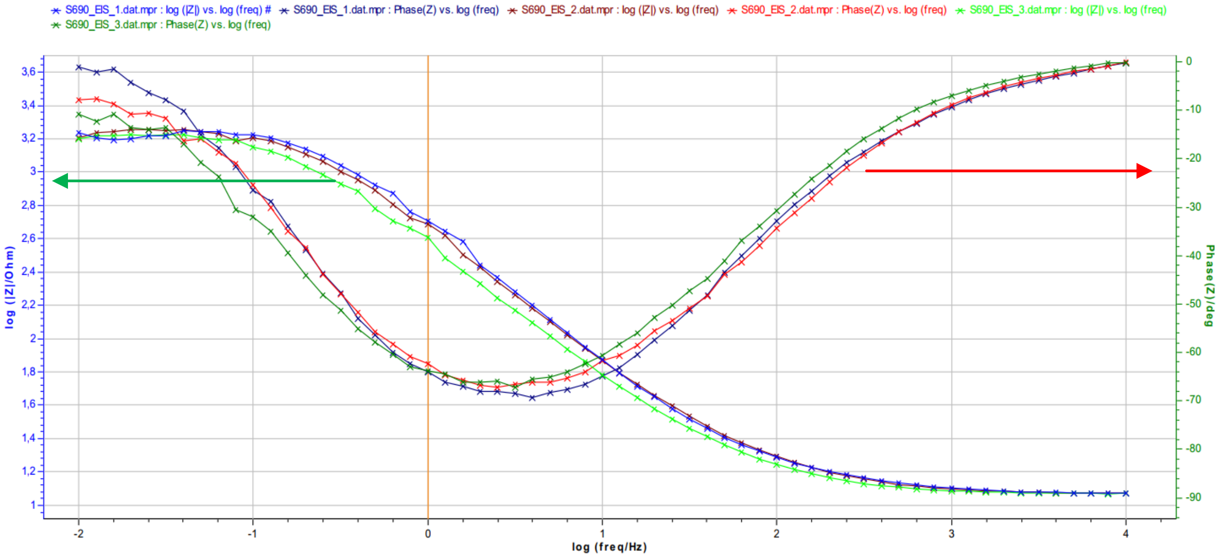

Fig.[8.10] Bode plots of the 1st series of experiments for parent metal **S690**, all experiments. Experiment data of log(|Z|). **Blue:** exp.1, **Maroon:** exp.2, **Lime:** exp.3. Experiment data of θ. **Navy:** exp.1, **Red:** exp.2, **Green:** exp.3.

Table [8.3] Corrosion and EIS parameters of the first series of EIS experiments for each S690 experiment.

	R_S (Ohm)	**Q ($*10^{-3}$ F)**	**R_{CT} (Ohm)**
S690.1	12.97	0.2632	1732
S690.2	11.09	0.3237	1748
S690.3	10.71	0.3915	1642
Average	**11.59**	**0.3261**	**1707**
Stdev	1.21	0.0642	67

For the 24-hours experiment on S690, the summary diagrams, Fig.[8.11] is presented, along with the corrosion parameters tables, Table [8.4].

The Nyquist plots for the 24h experiments present smaller diameters for longer exposure periods of the specimen to the solution. Thus, after 2 hours the diameter is half. It proves that Rct is lower, proving that the anodic dissolution of the specimen is continuing. The same behavior is apparent for the 4 and the 8 hours curves. At the 16 hours and the 24 hours curve are almost stable implying that corrosion products are formed on the surface halting the dissolution of the specimen. These two last curves present one more capacitive semicircle. This second semicircle is attributed to the presence of the corrosion products on surface of the specimen. (Fig.8.11).

The equivalent circuit of these curves is the one presented in Fig.[8.7]. The values of the electric elements in Table [8.4], show that the resistance of the solution is rather stable with small diminution Rs and Rct is diminishing significantly with time.

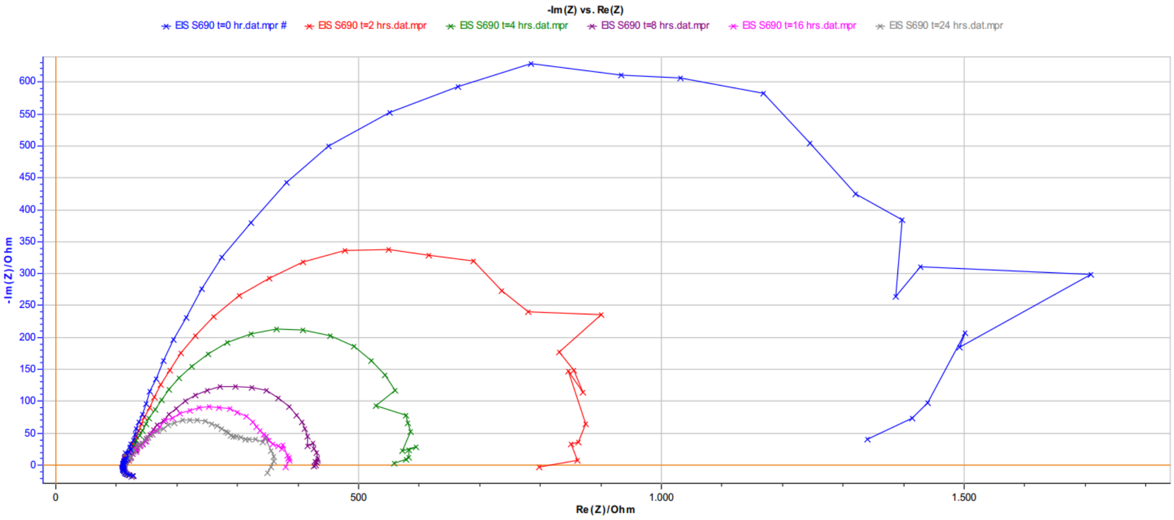

Fig.[8.11] Common Nyquist plot of the 2nd series of EIS experiments for parent metal **S690.** **Blue:** t=0 hrs, **Red:** t=2 hrs, **Green:** t=4 hrs, **Purple:** t=8 hrs, **Pink:** t=16 hrs, **Grey:** t=24 hrs.

Table [8.4] Corrosion and EIS parameters of the second series of EIS experiments for each S690 experiment.

	R_S (Ohm)	Q (*10^{-3} F)	R_{CT} (Ohm)
S690, t=0 hrs	115.0	0.452	1398.0
S690, t=2 hrs	117.5	0.601	750.1
S690, t=4 hrs	114.4	0.807	472.1
S690, t=8 hrs	116.4	0.902	323.7
S690, t=16 hrs	113.5	1.018	273.1
S690, t=24 hrs	111.8	1.620	253.8

In Fig.[8.12], the comparison of the Nyquist plots for both parent metals AH36 and S690 is presented. This plot and the relevant values of the electric elements of the circuit model show that the shape of the plot is the same showing that both corrosion mechanisms are charge transferred. However, the diameter of the semicircles and the values of the models show that the Rct values are higher for S690 implying that the Rct which is inversely proportional to corrosion rate is higher for this metal.

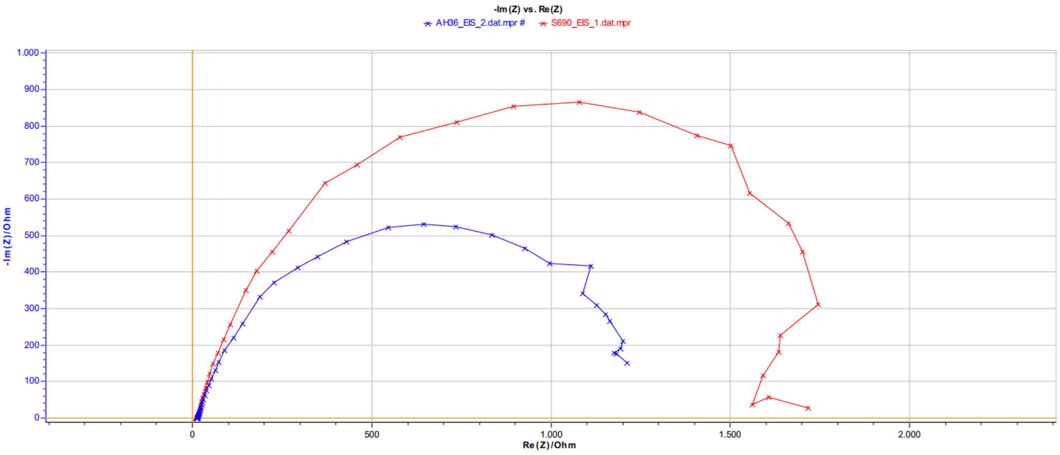

Fig.[8.12] Comparison of of the 1st series of experiments Nyquist plots for parent metals **AH36** and **S690**. **Blue:** AH36, **Red:** S690.

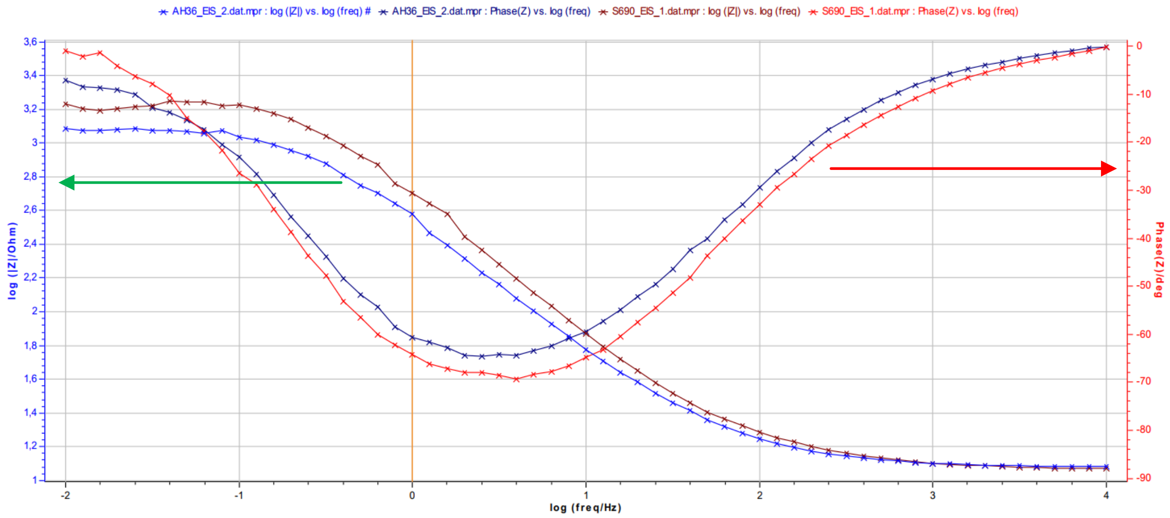

Fig.[8.13] Comparison of of the 1st series of experiments Bode plots for parent metals **AH36** and **S690**.

Experiment data of log(|Z|). **Blue**: AH36, **Maroon:** S690.

Experiment data of θ. **Navy:** AH36, **Red:** S690.

Table [8.5] Average corrosion and EIS parameters of the first series of EIS experiments for parent metal.

	R_S (Ohm)	**Q (*10^{-3} F)**	**R_{CT} (Ohm)**	**R_{CT} Stdev (Ohm)**
AH36	12.78	0.4422	1227	32
S690	11.59	0.3261	1707	67

8.2.2. Weldments

In the present paragraph, the summary diagrams, Fig.[8.14], Fig.[8.15], Fig.[8.17] and Fig.[8.18] and the corrosion parameters tables Table [8.6] and Table [8.8] of the first series of experiments for the weldments AH36-AH36 and AH36-S690 are presented, along with comparison diagrams, Fig.[8.20] and Fig.[8.21] and the respective table, Table [8.10]. For the 24-hours experiments, the summary diagrams, Fig.[8.16] and Fig.[8.19] are presented, along with the corrosion parameters tables, Table [8.7] and Table [8.9].

As for the homogeneous weld, AH36-AH36 weld present Nyquist with only one capacitive semicircle, implying charge transfer corrosion mechanism (Fig.[8.14], Fig.[8.15]). The equivalent circuit model is the same Randles cell presented for the parent metal AH36 in Fig.[8.7]. All the three experiments present very good repeatability. The values of the electric parameters for the circuit model equivalent are equal to 1170 Ohm (Table [8.6]).

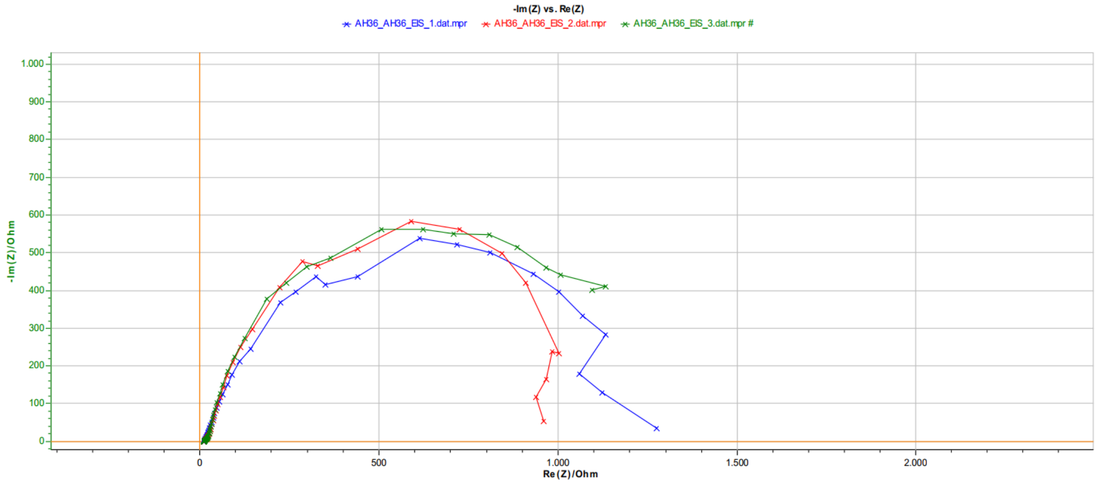

Fig.[8.14] Nyquist plots of the 1st series of experiments for homogeneous weld **AH36-AH36**, all experiments. **Blue:** exp1, **Red:** exp.2. **Green:** exp.3.

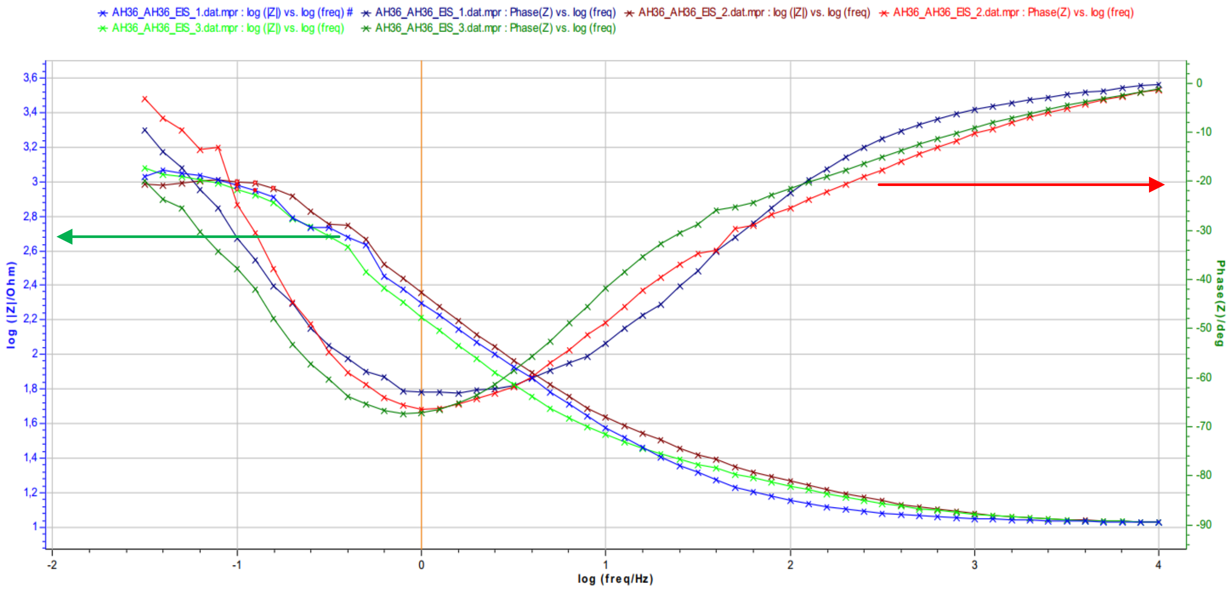

Fig.[8.15] Bode plots of the 1st series of experiments for homogeneous weld **AH36-AH36**, all experiments.

Experiment data of log(|Z|). **Blue:** exp.1, **Maroon:** exp.2, **Lime:** exp.3.

Experiment data of θ. **Navy:** exp.1, **Red:** exp.2, **Green:** exp.3.

Table [8.6] Corrosion and EIS parameters of the first series of EIS experiments for each AH36-AH36 experiment.

	R_S (Ohm)	Q (*10^{-3} F)	R_{CT} (Ohm)
AH36-AH36.1	11.37	0.8675	1190
AH36-AH36.2	11.43	0.6492	1073
AH36-AH36.3	12.54	0.9296	1250
Average	**11.78**	**0.8154**	**1171**
Stdev	0.66	0.1473	90

For the weld of AH36-AH36, the Nyquist plots show that the value of Rct is lowering until the 8 hours curve, while after that, the Rct is getting higher values and is rather stable at 16h and 24hours. It implies that at 8 hours a corrosion product film is formed on the surface of the specimen, limiting the dissolution of the specimen. This film is stable even in the last 24 hours curve limiting the dissolution of the specimen. And this film is stable and stronger in the 24 hours curve limiting further the corrosion dissolution (Fig.[8.16]). These findings are supported by the values of the electric elements in Table [8.7].

At the low end of the frequencies the semicircles are depressed below the horizontal Z' axis and this can be explained assuming metal dissolution under a corrosion product film with oxygen reduction within the film pores.

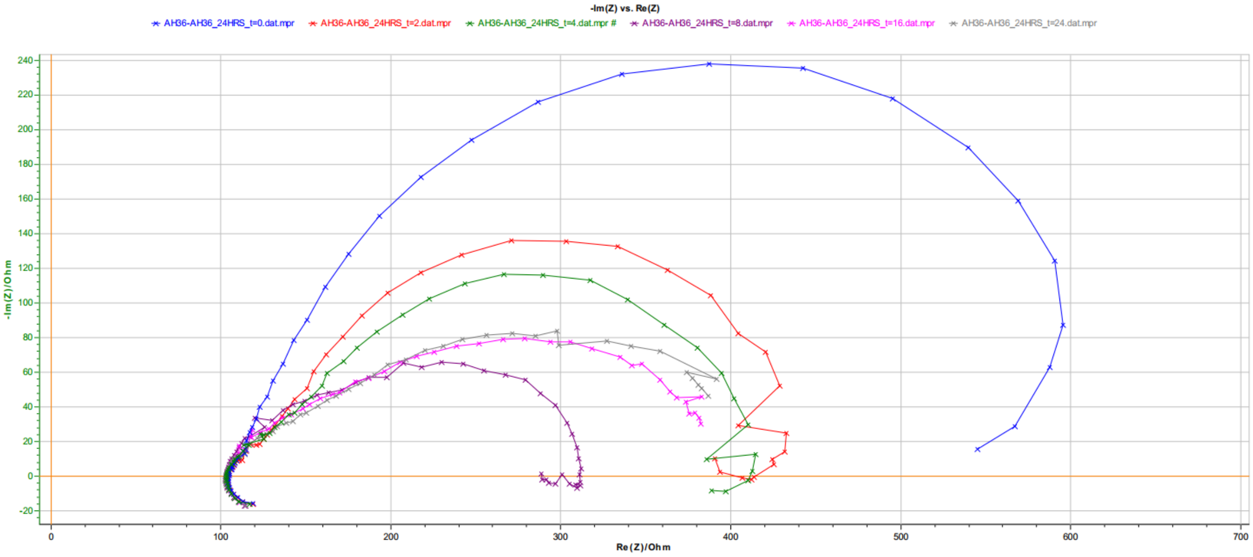

Fig.[8.16] Common Nyquist plot of the 2nd series of EIS experiments for homogeneous weld **AH36-AH36** .**Blue:** t=0 hrs, **Red:** t=2 hrs, **Green:** t=4 hrs, **Purple:** t=8 hrs, **Pink:** t=16 hrs,**Grey:** t=24 hrs.

Table[8.7] Corrosion and EIS parameters of the second series of EIS experiments for each AH36-AH36 experiment.

	R_S (Ohm)	**Q (*10^{-3} F)**	**R_{CT} (Ohm)**
AH36-AH36, t=0 hrs	104.5	0.4634	453.8
AH36-AH36, t=2 hrs	110.5	1.0130	315.0
AH36-AH36, t=4 hrs	108.1	1.1440	312.7
AH36-AH36, t=8 hrs	107.1	0.3820	197.4
AH36-AH36, t=16 hrs	102.2	1.5460	304.9
AH36-AH36, t=24 hrs	102.7	3.0250	356.2

In the following paragraphs the Nyquist and Bode plots are presented for AH36-S690 weld. Here also as in the previous experiments, only one capacitive semicircle, implying charge transfer corrosion mechanism (Fig.[8.17]). The equivalent circuit model is the same Randles cell (Fig.[8.7]). However, these experiments for AH36-S690 weld do not present repeatability. The Rct values range from 1100 to 2186 Ohms, presenting deviation of 586 Ohms. These deviations can be attributed to the microstructure of the AH36-S690 weld.

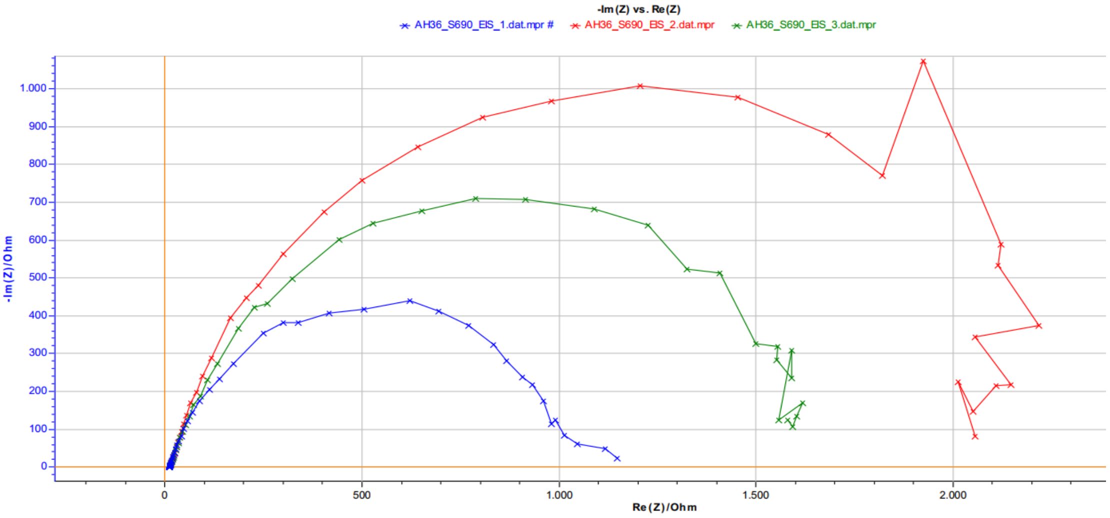

Fig.[8.17] Nyquist plots of the 1st series of experiments for heterogeneous weld **AH36-S690**, all experiments. **Blue:** exp1, **Red:** exp.2. **Green:** exp.3.

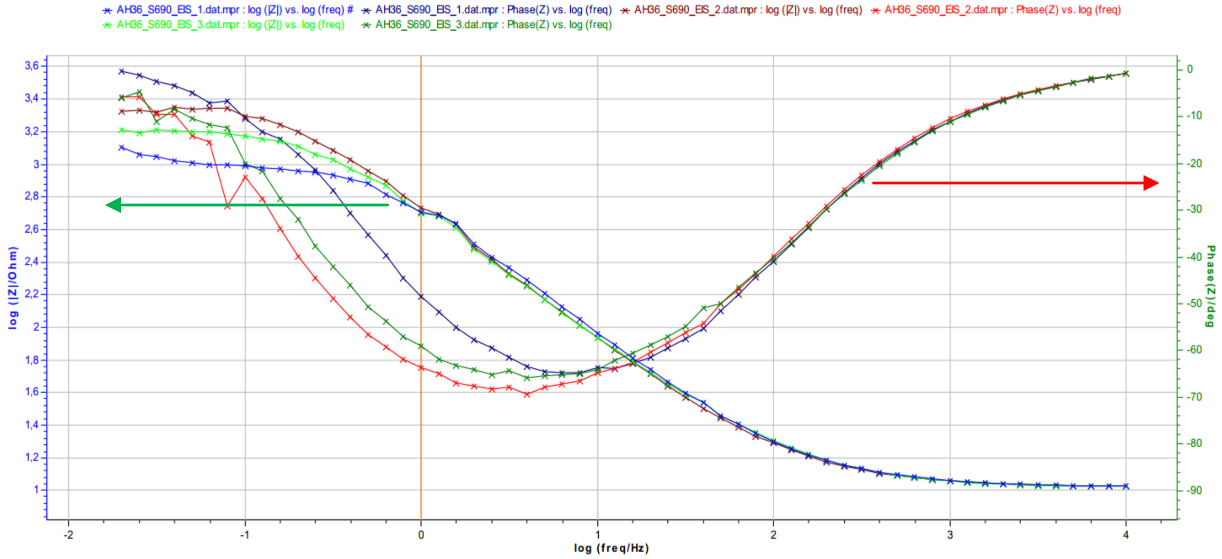

Fig.[8.18] Bode plots of the 1st series of experiments for heterogeneous weld **AH36-S690**, all experiments.

Experiment data of log(|Z|). **Blue:** exp.1, **Maroon:** exp.2, **Lime:** exp.3.

Experiment data of θ. **Navy:** exp.1, **Red:** exp.2, **Green:** exp.3.

Table [8.8] Corrosion and EIS parameters of the first series of EIS experiments for each AH36-S690 experiment.

	R_S (Ohm)	Q (*10^{-3} F)	R_{CT} (Ohm)
AH36-S690.1	11.89	0.3621	1675
AH36-S690.2	10.77	0.3940	1108
AH36-S690.3	11.51	0.3257	2186
Average	**11.39**	**0.3606**	**1656**
Stdev	0.57	0.0342	539

The semi-circles of the AH36-S690 weld are also far from perfect semi-circles. The curves of the longer time exposures show that the value of Rct is lowering until the 8 hours curve. After that, the curve of 16hours is almost identical and finally at 24 hours the Rct is lower. It indicates that at 8 hours a corrosion product film is formed on the surface of the specimen, limiting the dissolution of the specimen. And this film is stable and stronger in the 24 hours curve limiting further the corrosion dissolution (Fig.[8.19]). These findings are supported by the values of the electric elements in Table [8.9].

At the low end of the frequencies the semicircles are depressed below the horizontal Z' axis and this can be explained assuming metal dissolution under a corrosion product film with oxygen reduction within the film pores.

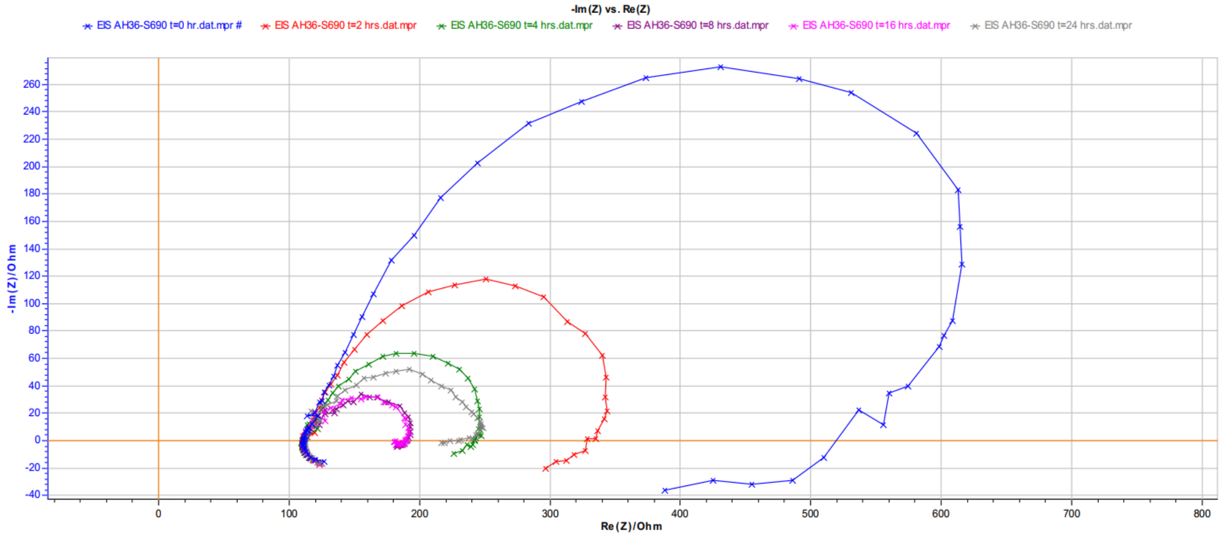

Fig.[8.19] Common Nyquist plot of the 2nd series of EIS experiments for weld **AH36-S690** .**Blue:** t=0 hrs, **Red:** t=2 hrs, **Green:** t=4 hrs, **Purple:** t=8 hrs, **Pink:** t=16 hrs,**Grey:** t=24 hrs.

Table [8.9] Corrosion and EIS parameters of the second series of EIS experiments for each AH36-S690 experiment.

	R_S **(Ohm)**	**Q** **($*10^{-3}$ F)**	**R_{CT}** **(Ohm)**
AH36-S690, t=0 hrs	113.9	0.6394	480.7
AH36-S690, t=2 hrs	113.5	0.8989	216.3
AH36-S690, t=4 hrs	113.6	0.6041	124.7
AH36-S690, t=8 hrs	114.3	0.2316	71.5
AH36-S690, t=16 hrs	115.7	0.1336	70.4
AH36-S690, t=24 hrs	115.4	0.2728	122.3

The significant scatter in the Nyquist and Bode plots and in the resulting values for the AH36-S690 weld does not allow for safe comparison between the two weldments. However, it seems that AH36-AH36 presents lower Rct values, thus higher corrosion rates.

In addition, comparing the behaviour of the two weldments through time, at the end of the experiment AH36-AH36 weld is more resistant to corrosion (Fig.[8.20], Fig.[8.21], Table [8.10]). One can support that through time the Rct values are lower at least until the 8 hours curve implying the autocatalytic nature of the corrosion process. Only after the 8 hours curve the formation of the corrosion product film inhibits the corrosion process providing higher Rct.

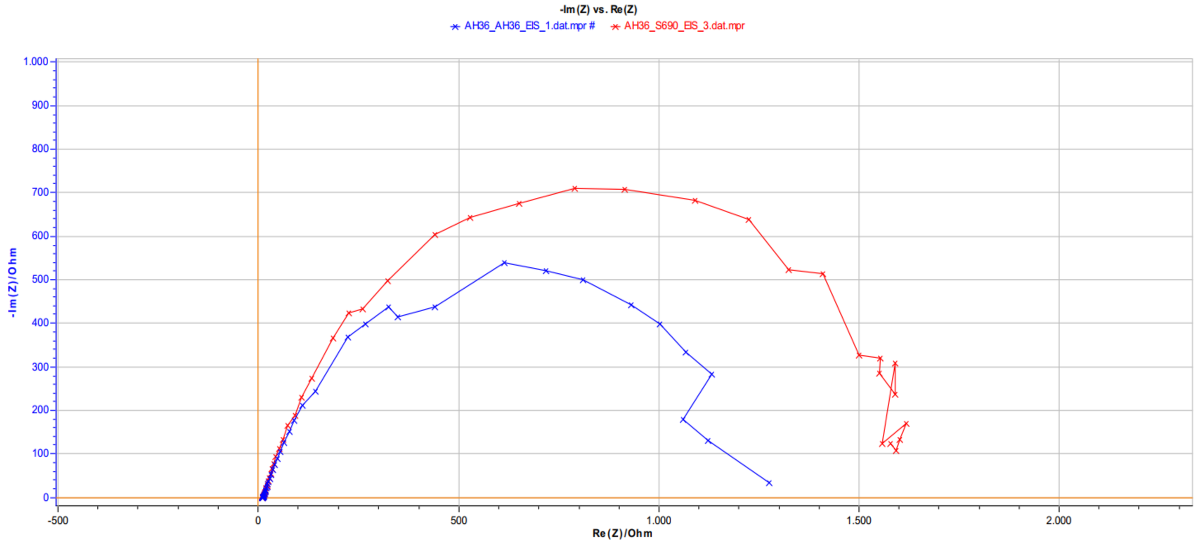

Fig.[8.20] Comparison of of the 1st series of experiments Nyquist plots for weldments.
Blue: AH36-AH36, **Red:** AH36-S690.

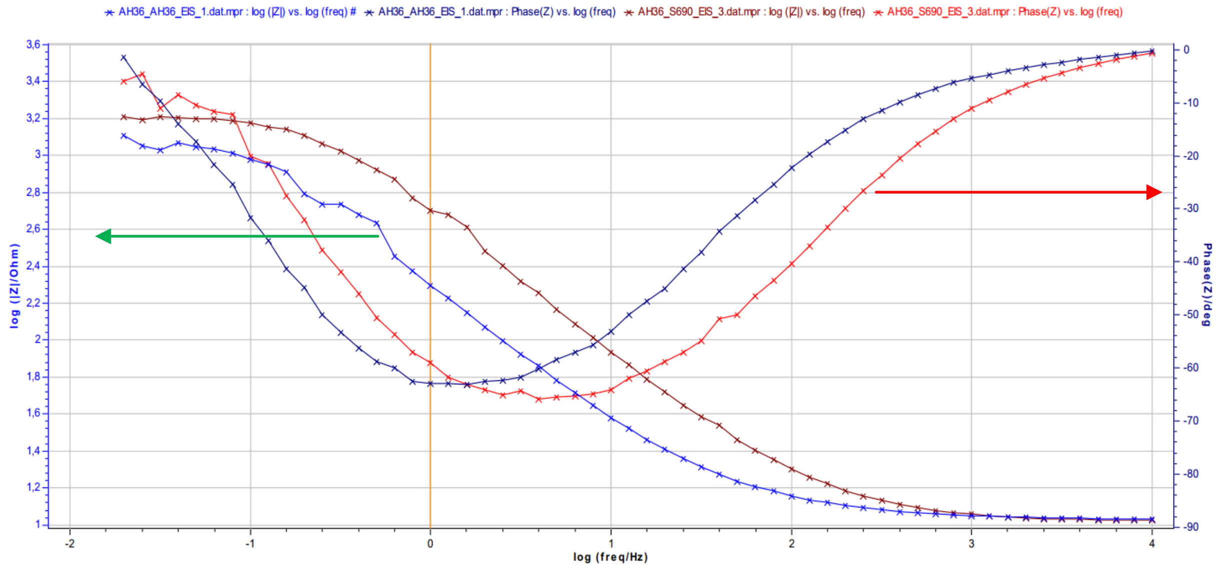

Fig.[8.21] Comparison of of the 1st series of experiments Bode plots for weldments.
Experiment data of log(|Z|). **Blue:** AH36-AH36, **Maroon:** AH36-S690.
Experiment data of θ. **Navy:** AH36-AH36, **Red:** AH36-S690.

Table [8.10] Corrosion and EIS parameters of the first series of EIS experiments for each weldment.

	R_S (Ohm)	**Q (*10^{-3} F)**	**R_{CT} (Ohm)**	**R_{CT} Stdev (Ohm)**
AH36-AH36	11.78	0.8154	1171	90
AH36-S690	11.39	0.3606	1656	539

8.3. Total Results- Conclusions

In the present paragraph, the summary diagrams, Fig.[8.22] and Fig.[8.23] and corrosion parameters table, Table [8.11] of the parent metals AH36 and S690 and the weldments AH36-AH36 and AH36-S690 are presented. Also, the diagrams of the Constant Phase Elements versus Time of all the specimens, Fig.[8.24] and Fig.[8.25], are presented.

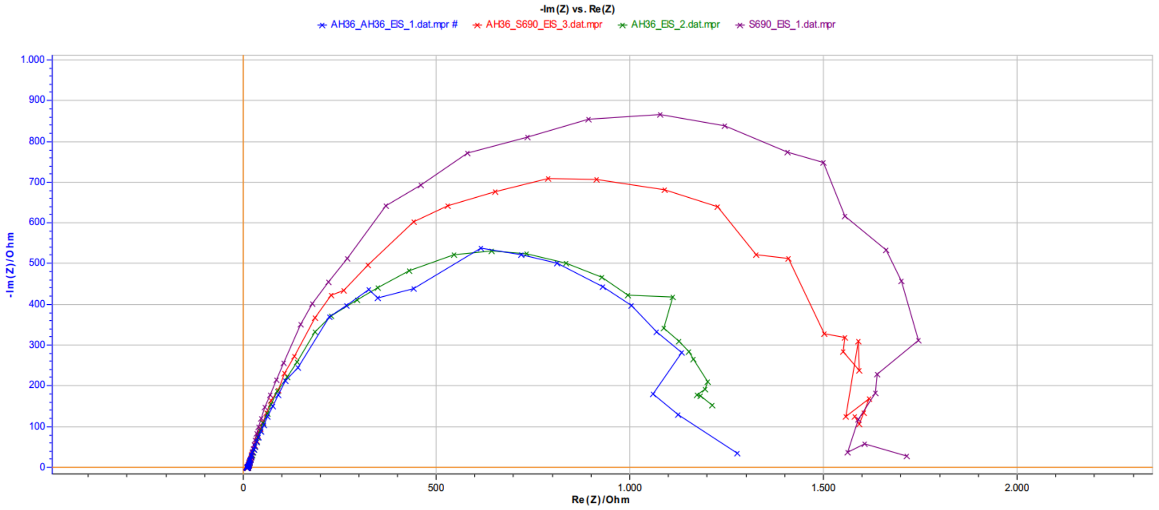

Fig.[8.22] Comparison of of the 1^{st} series of experiments Nyquist plots for all the specimens. **Blue:** AH36-AH36, **Red:** AH36-S690, **Green:** AH36, **Purple:** S690.

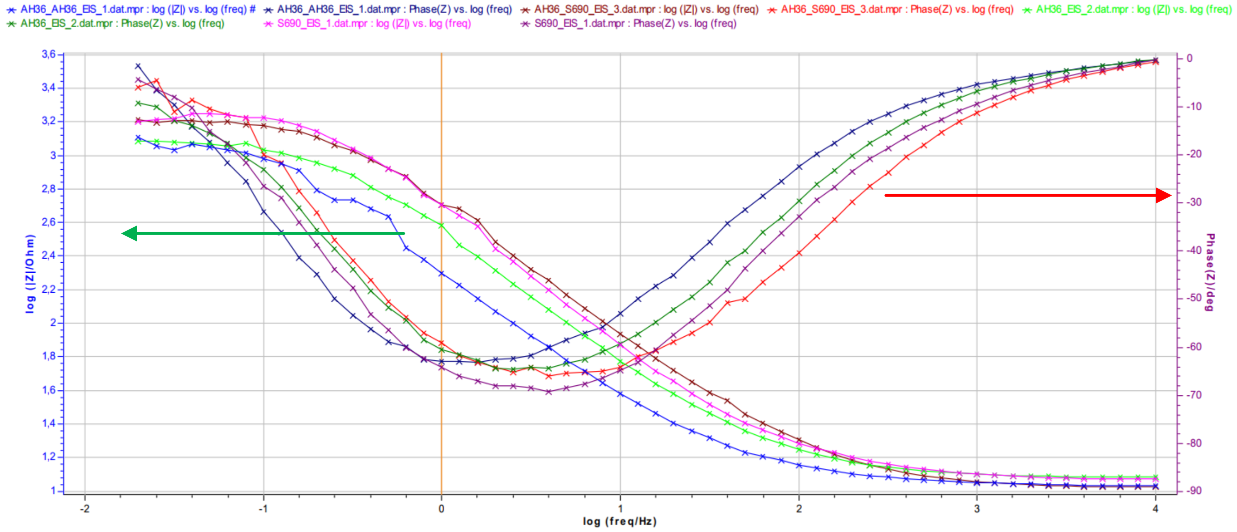

Fig.[8.23] Comparison of of the 1^{st} series of experiments Bode plots for all the specimens. log(|Z|): **Blue:** AH36-AH36, **Maroon:** AH36-S690, **Lime:** AH36, **Pink:** S690.
θ: **Navy:** AH36-AH36, **Red:** AH36-S690, **Green:** AH36, **Purple:** S690.

Table [8.11] Average polarization resistance for the first series of EIS experiments for every specimen.

	Rp (Ohm)
AH36	1227
S690	1707
AH36-AH36	1171
AH36-S690	1656

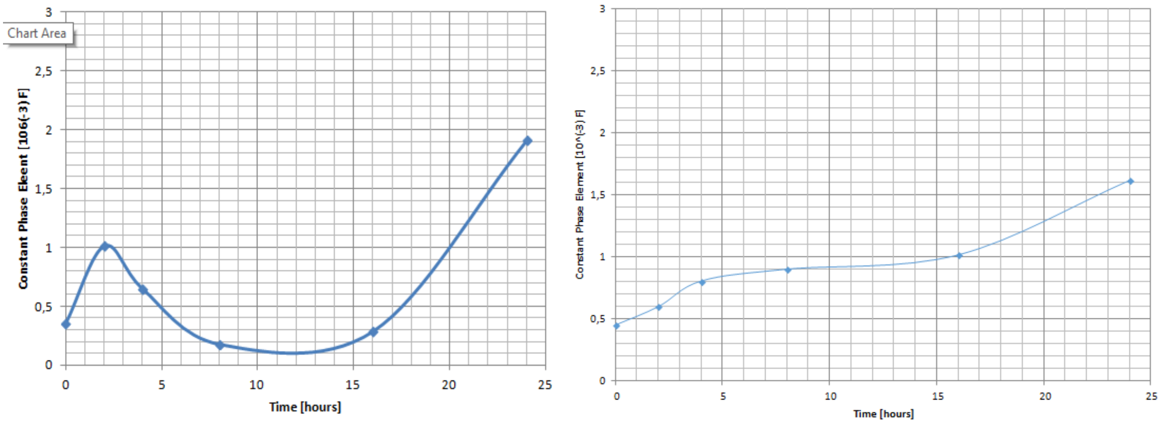

a) b)

Fig.[8.24] Constant Phase Element over time for 2nd series experiments for parent metal a) **AH36**, b) **S690**. CPE (10^{-3} F) (y-axis) vs Time (hours) (x-axis).

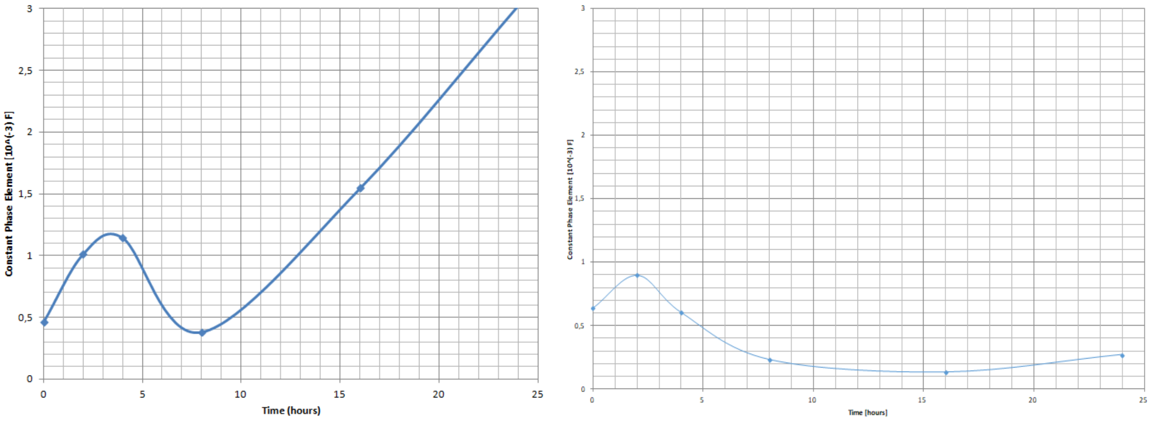

a) b)

Fig.[8.25] Constant Phase Element over time for 2nd series experiments for weldments a) **AH36-AH36**, b) **AH36-S690**. CPE (10^{-3} F) (y-axis) vs Time (hours) (x-axis).

First series of experiments, EIS experiments (three) for parent metals AH36, S690 and welds AH36-AH36, AH36-S690 (back to back).

The shape of the Nyquist plot for both parent metals AH36 and S690 displays only one capacitive semicircle. This type of diagram is usually interpreted as a mechanism of charge transfer on an inhomogeneous surface. The equivalent circuit chosen consists of *R*s and *R*ct indicate solution resistance and charge transfer resistance of the electrolyte–substrate interface, respectively. the shape of the Nyquist curve is not a perfect semicircle centred on the Z’ axis at the (R/2, 0) point. It presents a deviation from the Resistance Capacitor behaviour and there is a deformation and broadening of the semicircle. For this reason, in the equivalent modelled circuit the capacitor C is substituted by the Constant Phase Element Q, still parallel with the resistor Rct. This deformation is attributed to the roughness of the electrode-electrolyte interfaces or to inhomogeneities in the local distribution of defects in the vicinity of grain boundaries.

Concerning the values of the electric elements of the circuit, parent metals present well-defined differences, with S690 (1700 Ohms) presenting the higher resistance to corrosion than AH36 (1200 Ohms).

For the weldments, the plots are similar and are well presented by the Randles cell, here too. Thus, concerning the two weldments, the Rp values present some differences, but the lack of the repeatability in AH36-S690 weld does not allow for sound conclusions. Though, we can safely presume that AH36-S690 presents higher resistance to corrosion than AH36-AH36.

Comparing the parent metal with their weldments, we observe that the Rct values of AH36 are very similar with those of the weldment AH36-AH36 and that the Rct values of S690 are respectively similar to those of the weldment AH36-S690. This leads to the conclusion that the contribution of S690 as constituent metal, affects the corrosion behavior of the heterogeneous weld.

In each case, the 3 values of the Constant Phase Element (CPE-Q) were very similar to one another presenting only a very small deviation.

Second series of experiments, EIS experiments (six) in function with time in 24 hours period

In all the specimens, we observed that the Rp value is decreasing significantly over time.

For **AH36**, the anodic dissolution of the specimen is continuing until the 4 hours curve. Though, the 8 hours, the 16 hours and the 24 hours curve are almost stable implying that corrosion products are formed on the surface halting the dissolution of the specimen.

For **S690**, the anodic dissolution is not limited until the 16hours curve and on the 16 and 24hours curve one more capacitive semicircle, which can be attributed to the presence of the corrosion products on surface of the specimen.

For the weld of **AH36-AH36**, the Nyquist plots show that the value of Rct is lowering until the 8 hours curve, while after that, the Rct is getting higher values and is rather stable at 16h and 24hours. It implies that at 8 hours a corrosion product film is formed on the surface of the specimen, limiting the dissolution of the specimen. This film is stable even in the last 24 hours curve.

Concerning the **AH36-S690**, weld the curves of the longer time exposures show that the value of Rct is lowering until the 8 hours curve. After that, the curve of 16hours is almost identical and finally at 24 hours the Rct is lower. It indicates that at 8 hours a corrosion product film is formed on the surface of the specimen, limiting the dissolution of the specimen, and this film is stable and stronger in the 24 hours curve limiting further the corrosion dissolution

In Fig.[8.27] and Fig.[8.28], the change of Q element of the circuit in function with time is presented. Q, constant phase element represents the capacity of the double layer of the experiment, i.e. the electrode/electrolyte interface.

Finally, comparing the t=0 experiment in 0.6M NaCl (3.5% w/v) and in 0.05M NaCl solution, it is obvious that for lower salt concentration, the values of the Rct are relatively lower for all the parent metals and the welds .

9. CYCLIC POTENTIODYNAMIC POLARIZATION

9.1. Introduction

To study the surface condition of the samples (susceptibility to pitting corrosion) it was necessary to perform the cyclic potentiodynamic polarization (CPP) test, followed by observation employing Scanning Electron Microscopy.

A cyclic polarization scan is performed like a potentiodynamic scan, but with an addition: the voltage is swept across a range, but then reversed back to the starting potential. This allows a return to the original potential. Along with the continuous scanning potential, the current response is monitored.

The shape of the cyclic polarization curve indicates if the sample is in the passive or active state, and can also show the pitting potential and the re-passivation or protection potential. In a passive system, the potential at which the current sharply increases is defined as the pitting potential (Epit) and where the loop closes on the reverse scan is the protection or re-passivation potential (Epro). If these two potentials are the same, there is a little tendency to pitting. If Epro is more positive than Epit, there is no tendency to pitting. On the other hand, if Epro is more negative than Epit, the pitting could happen. Furthermore, the size of the pitting loop can be used as an indication of pitting tendency. The larger loop and the values of current density in the reverse scanning show more tendency for pitting. [10,11].

9.2. Results

In the following paragraphs the Cyclic Polarization curves and the results obtained of the parent metals AH36, S690 and the welded specimens AH36-AH36 and AH36-S690 are presented. In particular, for the parent metals AH36 and S690 observation of the surface of the specimens after the polarization has been performed, trying to define the pits developed on the surface.

The experiment was performed in aerated solution of 3.5% NaCl, with scan rate of 1 mV/sec and the maximum potential applied was 1.2V vs Ref. For all the graphs, current is presented as log(|I/mA|) on x-axis and potential is presented as Ewe/V on y-axis.

9.2.1. Parent metals

In the present paragraph, Cyclic Polarization Curves of the parent metal AH36 Fig.[9.1] along with its SEM observations, Fig.[9.2] are presented. Consequently the same data are presented for S690 parent metal: Cyclic polarization curves for S690 Fig.[9.3] and SEM SEM observations, Fig.[9.4]. In the end comparison diagram of the two parent metals is presented, Fig.[9.5].

Cyclic polarization curve of AH36 shows that, in the anodic polarization scan, scanning starts from corrosion potential after reaching the steady state. The anodic polarization curve presents a continuous increase in the anodic dissolution, implying that the oxide film formed is not stable with defects and that the surface presents defects that enhance the dissolution. Only after 200mV a passive region starts to appear. Considering the hysteresis loop no significant increase in the current density is observed, implying no significant pitting corrosion. This small loop shows that some pitting corrosion is developed, Fig.[9.1]. These results are confirmed by SEM observations, where some pits of average 120μm, Fig.[9.2].

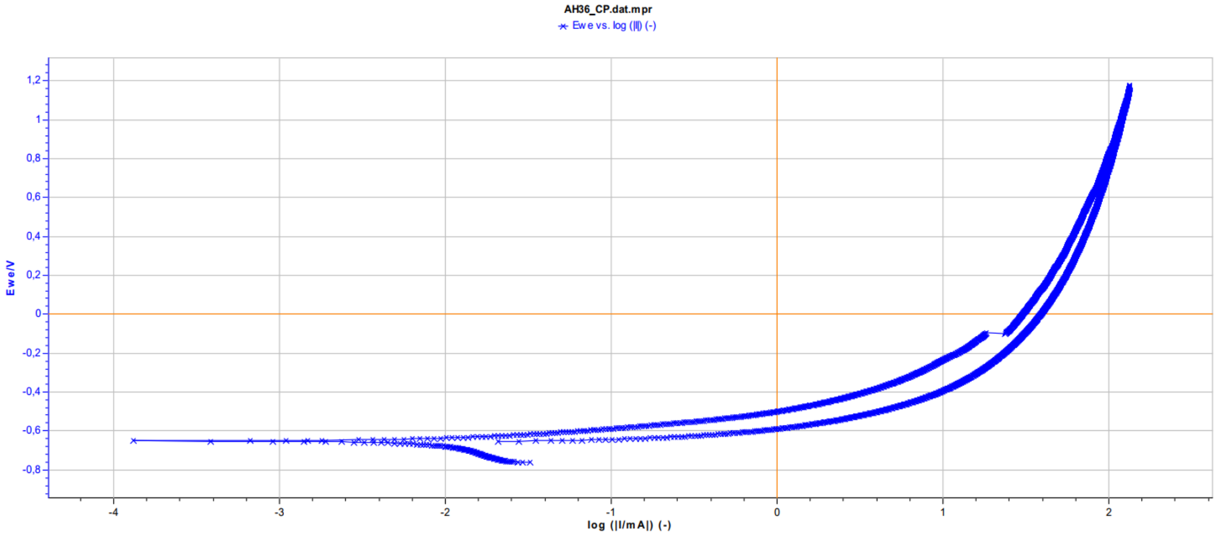

Fig.[9.1] Cyclic Polarization method of parent metal **AH36**.

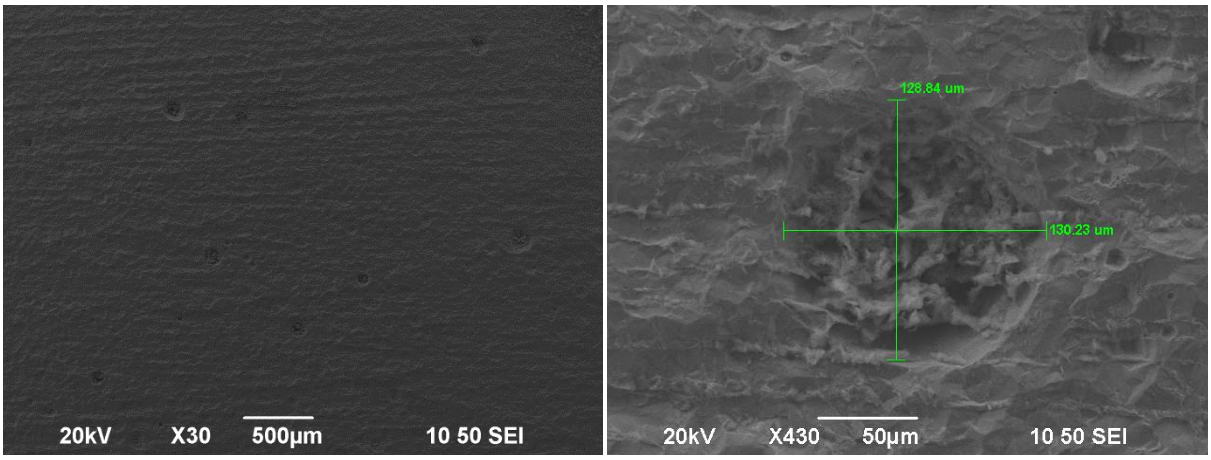

a) b)

Fig.[9.2] a) SEM pitting observation for parent metal AH36, x30, b) measurements of pits, x430.

As with AH36, analogous behavior is observed for S690, the anodic polarization curve presents a continuous increase in the anodic dissolution, implying that the oxide film formed is not stable with defects and that the surface presents defects that enhance the dissolution. After around 200mV a passive region starts to appear. In S690 a very narrow hysteresis close to Ecorr is observe, with no increase in the current density. This shape of CPP curve indicates very limited or no pitting corrosion, Fig.[9.3]. These results are confirmed by SEM observations, where some very limited number of pits is observed of average 60μm, Fig.[9.4].

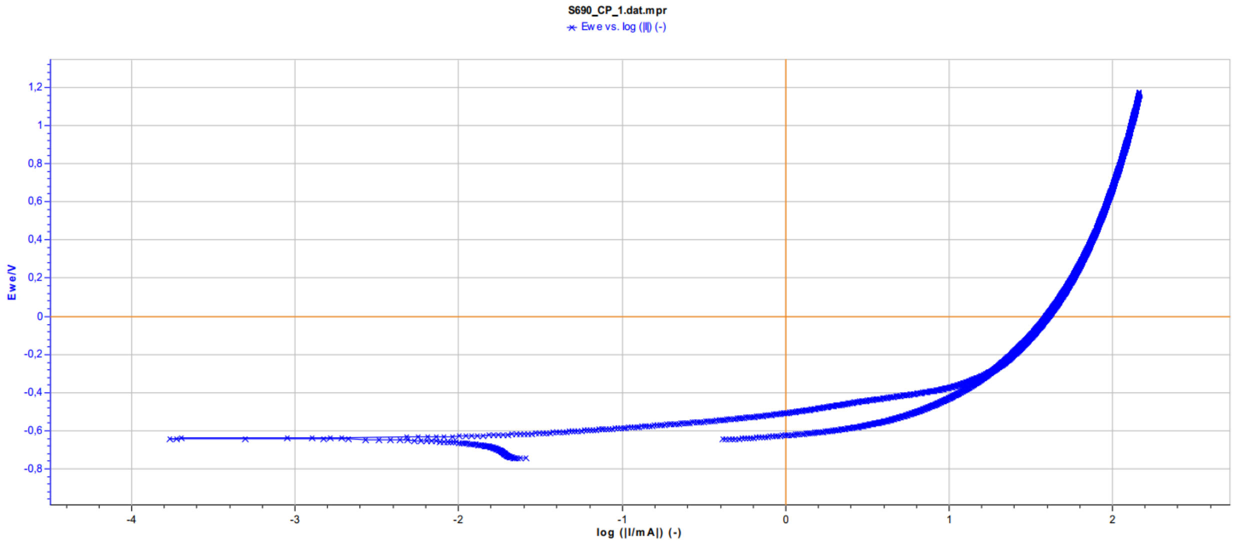

Fig.[9.3] Cyclic Polarization method of parent metal **S690**.

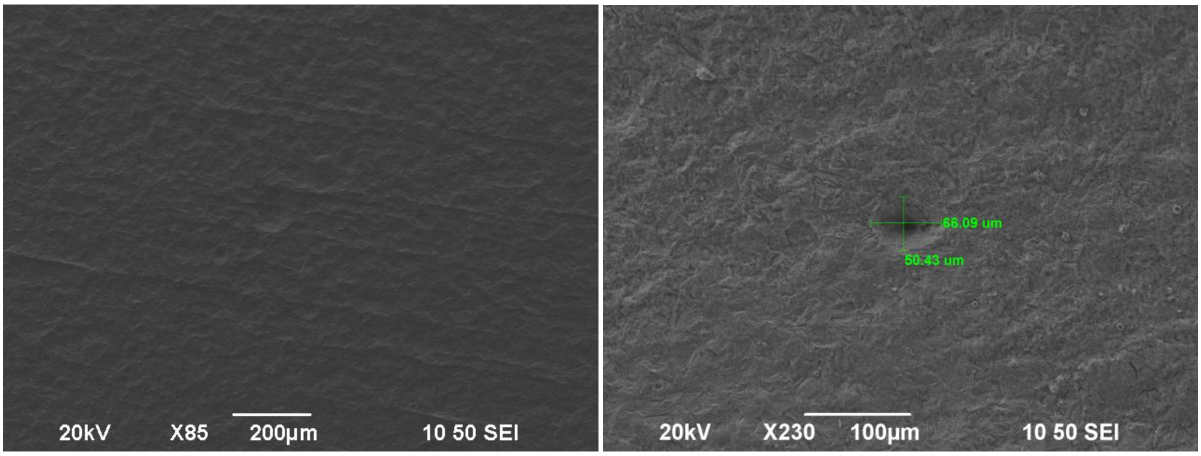

a) b)

Fig.[9.4] a) SEM pitting observation for parent metal S690, x85, b) measurements of pits, x230.

Comparing the CPP curves AH36 and S690 it is apparent that both metals do not present pitting corrosion. The narrow hysteresis loops show that these metals are not susceptible to pitting corrosion in these experimental conditions. In fact, some pitting is observed for AH36 and almost no pitting for S690.

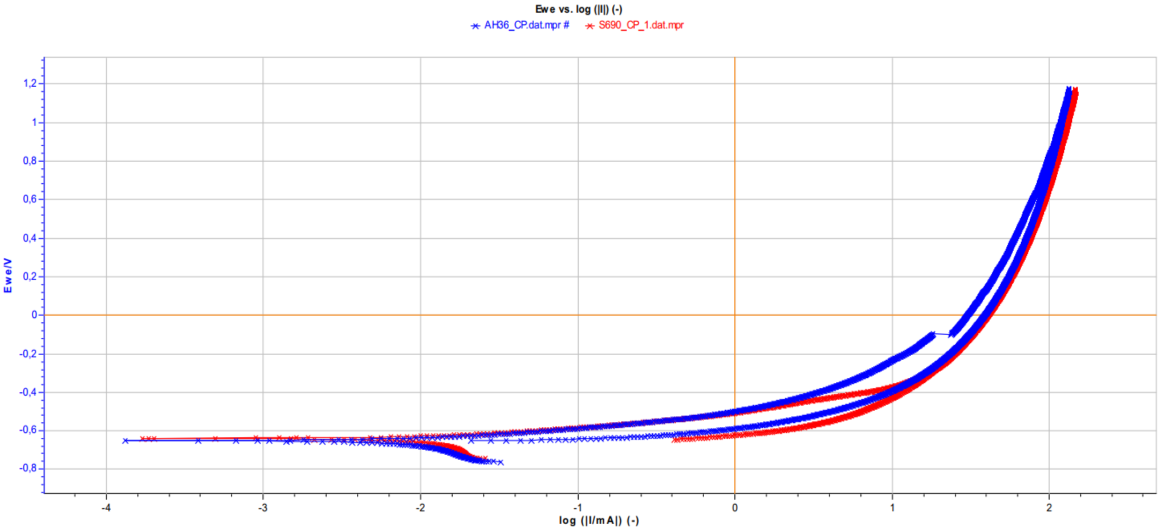

Fig.[9.5] Comparison of CP plots of parent metals **AH36** and **S690**.
Blue: AH36. **Red:** S690.

9.2.2. Weldments

In the present paragraph, the curves of Cyclic Potentiodynamic Polarization of AH36-AH36 and AH36-S690 are presented, along with their comparison. The curves in the weldments are very similar to the curves of the parent metals ones. For both weldments anodic dissolution is observed and some passivity is apparent after 200mV (Fig.[9.6], Fig.[9.7]). The hysteresis loop observed is even more narrow than the parent metals, indicating no susceptibility to pitting corrosion for both weldments, Fig.[9.8].

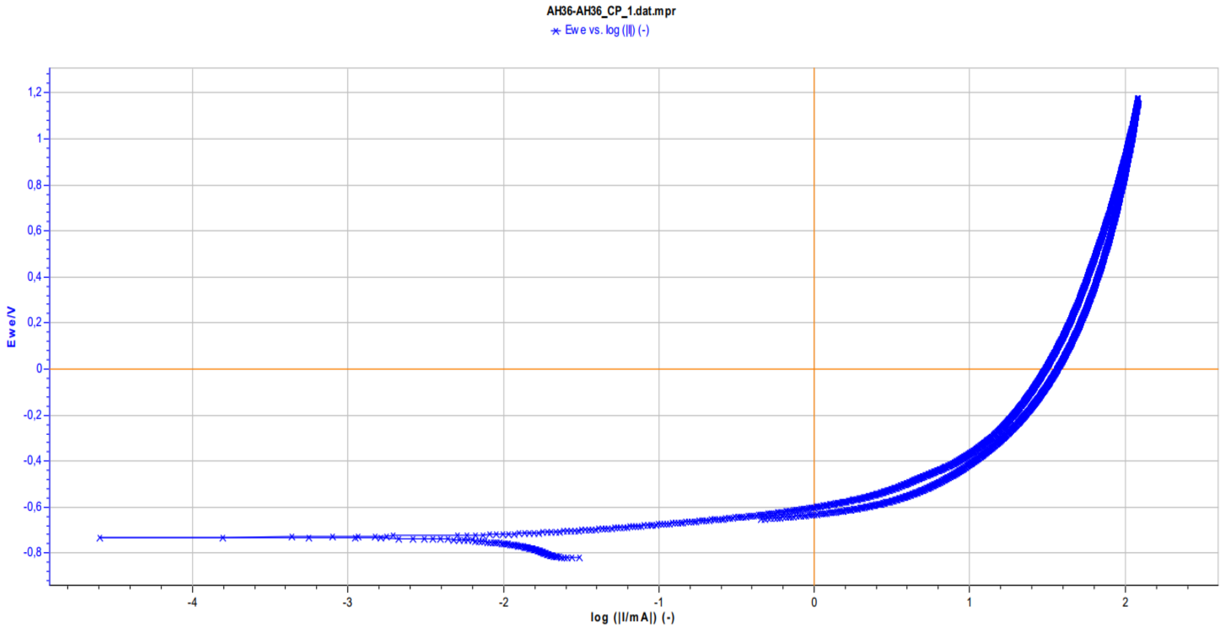

Fig.[9.6] Cyclic Polarization method of homogeneous weldment **AH36-AH36**.

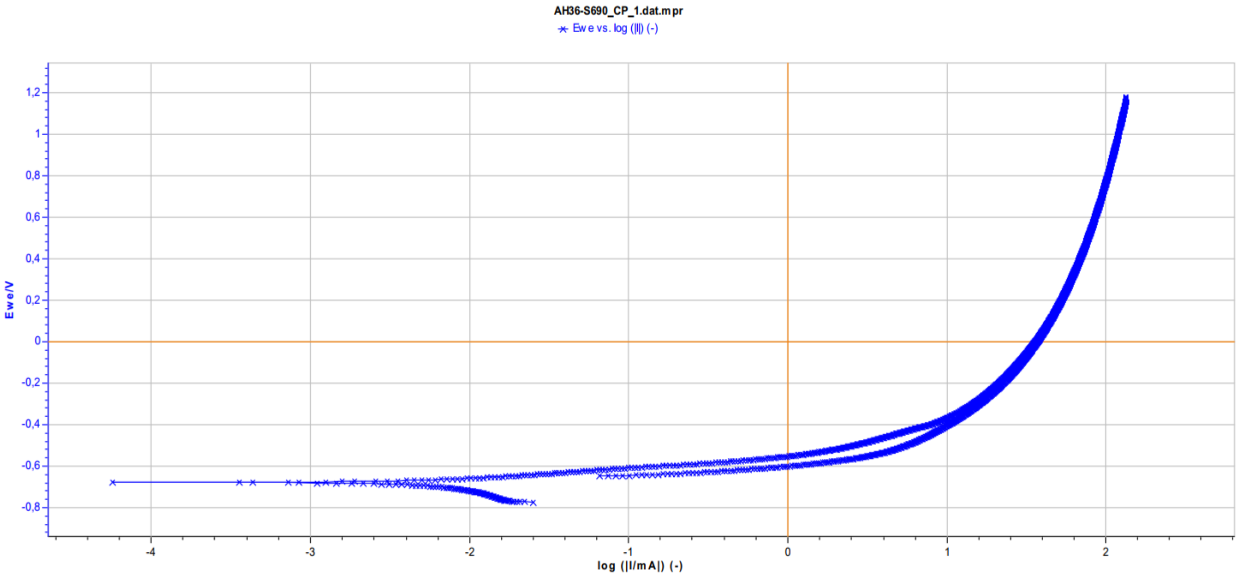

Fig.[9.7] Cyclic Polarization method of heterogeneous weldment **AH36-S690**.

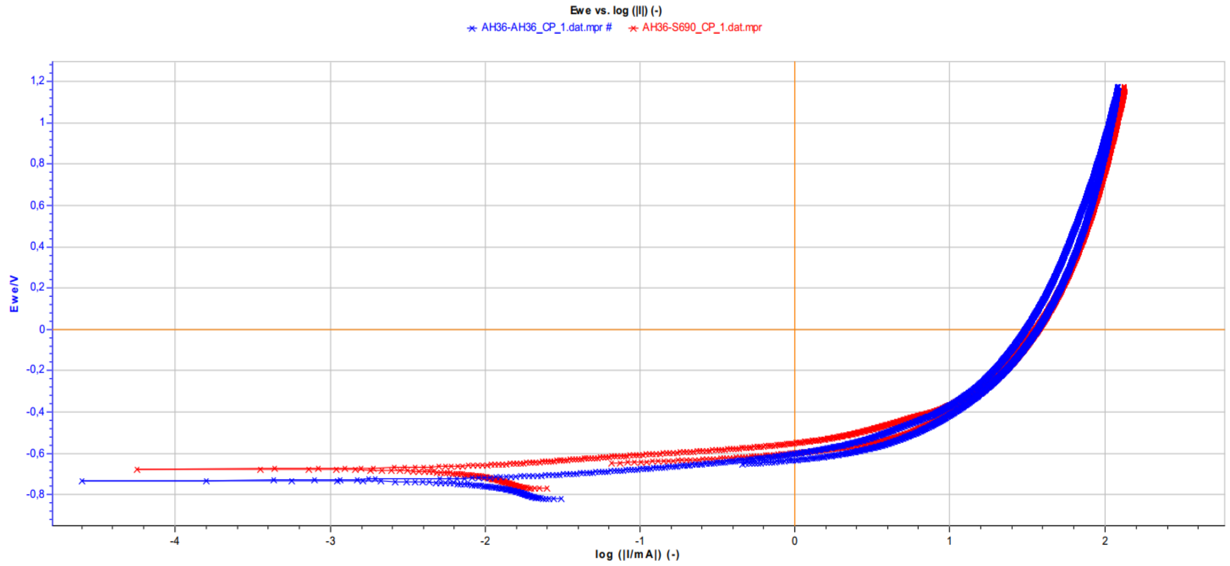

Fig.[9.8] Comparison of CP plots of weldments **AH36-AH36** and **AH36-S690**.
Blue: AH36-AH36. **Red:** AH36-S690.

9.3 Total Results- Conclusions

In the present paragraph, the summary diagram, Fig.[9.9] of the parent metals AH36 and S690 and the weldments AH36-AH36 and AH36-S690 is presented.

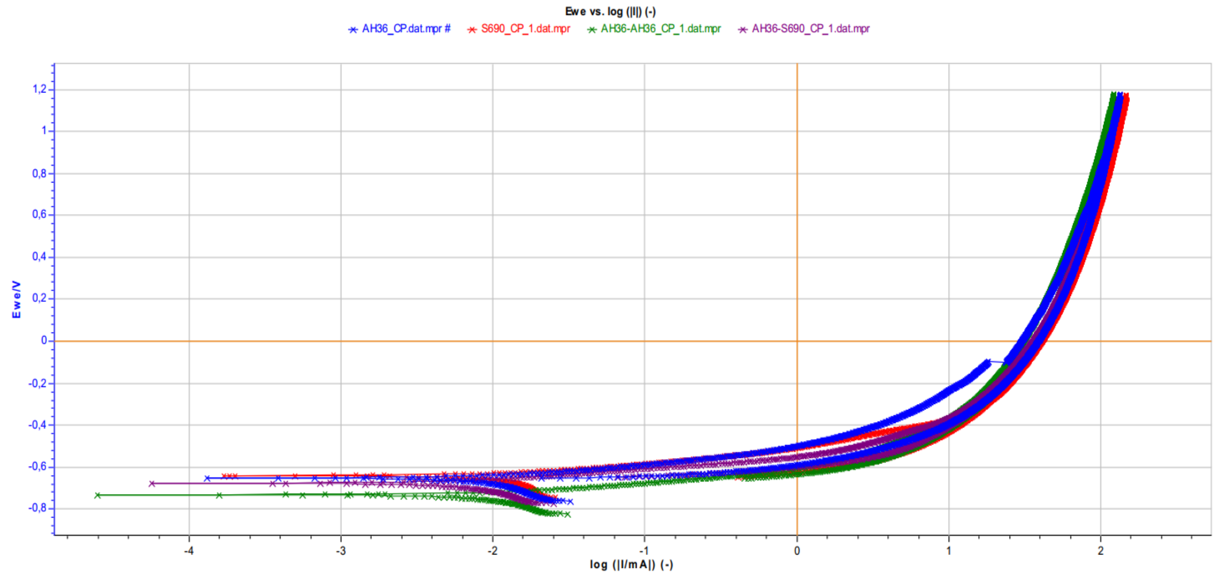

Fig.[9.9] Comparison of CP plots of all specimens.
Blue: AH36, **Red:** S690, **Green:** AH36-AH36, **Purple:** AH36-S690.

All of our specimens present a similar corrosion behavior, without significant differences comparing their CPP curves. This can easily be observed in Fig.[9.9], where all of the curves almost coincide. The anodic polarization curve presents a continuous increase in the anodic dissolution, implying that the oxide film formed is not stable with defects and that the surface presents defects that enhance the dissolution. Only after around 200mV a passive region starts to appear. Considering the hysteresis loop no significant increase in the current density is observed, implying no significant pitting corrosion, showing active surface and general corrosion.

In all of the cases, we observe that the pitting potential (Ept) coincides with the corrosion potential (Ecor), which occurs when there is an oxide film on the material surface prior to the polarization. Due to the intersection of the cathodic branch with the transpassive region of the anodic branch, the value of pitting potential is the same as corrosion potential.

If in the reverse scan, the anodic to cathodic transition potential is more noble than Ecorr, the passive layer will not be stable at Ecorr, Fig.[4.11], while the passivity will persist, if Ecorr gets more noble than the anodic to cathodic transition potential.

10. GENERAL CONCLUSIONS

10.1. Introduction

The aim of the present thesis is to study the corrosion behaviour of parent metals AH36, S690 as well as the weldments AH36-AH36 and AH36-S690. In order to accomplish it, electrochemical techniques were employed, applying DC and AC perturbation. However, electrochemical techniques should be accompanied by study of the micro-structure in order to arrive into sound conclusions. For this reason, study of the microstructure was performed in parent metals and weldments and the results of micro hardness performed by AIMEN are presented.

In the following paragraphs the conclusions obtained are presented along with suggestions for future research.

10.2. Conclusions

Micro structure – micro hardness

High strength steel **AH36** consists of alternate bands of ferrite 75% and pearlite 25% with intense orientation due to production process and the micro-hardness is equal to 153 HV. **S690** steel is a High Strength Low Alloy steel (HSLA) consisting of a homogeneous mixture of tempered martensite and bainite, along with ferrite. Micro-hardness equals to 280 HV.

Homogeneous weldment of **AH36-AH36**, the HAZ presents fine-grained austenite zone , while in the FZ, a ferrite-bainite microstructure was observed, with higher percentages of ferrite. The grains form dendrites while Widmanstätten ferrite is locally observed. Concerning micro-hardness HAZ is 250 HV, FZ follows with 210 HV and parent metal is 155 HV.

Concerning the heterogeneous weldment of **AH36-S690**, the region of the HAZ on the side of S690 presents tempered martensite, along with small amounts of remaining austenite, ferrite and bainite, while the FZ of the weldment presents a ferrite-bainite microstructure, with a higher percentage of ferrite. The micro-hardness reaches the value of 340 HV in the HAZ on the side of S690, while the FZ is 214 HV and the HAZ on AH36 side is 230 HV.

Corrosion mechanism - parameters

The electrochemical techniques employed, revealed valuable information on the mechanism of the corrosion and provided vales on critical parameters, for the parent metals AH36, S690 and the respective welds AH36-AH36, AH36-S690

Concerning the **mechanism of corrosion**, the potentiodynamic polarization showed that the steel specimens were characterized by an increase of current density with increasing potential in the anodic region, indicating active corrosion behavior without passivation in the 3.5% NaCl solution. According to this, both parent metals and welds present similar anodic dissolution determined by charge transfer (activation polarization). The cathodic curve shows that the phenomenon is dominated by O_2 diffusion, meaning that the phenomenon is controlled by activation polarization, close to equilibrium and consequently by concentration polarization due to O_2 diffusion further than equilibrium. In particular for S690, and its weld AH36-S690 the transition from equilibrium to concentration polarization is faster and the cathodic curve presenting O_2 diffusion is a straight line vertical to I current (y) axis.

Similar findings are provided by Cyclic Potential Polarization. The anodic polarization curve presents a continuous increase in the anodic dissolution, implying that the oxide film formed is not stable with defects and that the surface presents defects that enhance the dissolution. Only after around 200mV a passive region starts to appear. Considering the hysteresis loop, no significant increase in the current density is observed, implying no significant pitting corrosion, showing active surface and general corrosion.

The plots provided by Electrochemical Impedance Spectroscopy for all the specimens display only one capacitive semicircle. It is usually interpreted as a mechanism of charge transfer on an inhomogeneous surface. The equivalent circuit chosen consists of *R*s and *R*ct indicate solution resistance and charge transfer resistance of the electrolyte–substrate interface, respectively. However, the shape of the Nyquist curve is not a perfect semicircle and it presents a deviation from the Resistance Capacitor behaviour with deformation and broadening of the semicircle. For this reason, the capacitor C is substituted by the Constant Phase Element Q, still parallel with the resistor Rct. This deformation is attributed to the roughness of the electrode-electrolyte interfaces or to inhomogeneities in the local distribution of defects in the vicinity of grain boundaries. The experiments in function of time showed that for AH36, the AH36-AH36 and the AH36-S690 weld, the 8 hours curve imply the formation of corrosion products on the surface, halting the dissolution of the specimen. For S690 this is observed on the 16 hours curve.

The **corrosion parameters** show that AH36 is rather more corrosion resistant comparing to S690 with no significant difference. This can be attributed to the harder microstructure of S690, consisting of tempered martensite and bainite, along with ferrite. The Icorr values are similar for the parent metals and the welds and only AH36-AH36 weld presents higher corrosion susceptibility in Tafel extrapolation method. However, in EIS technique S690 appears as the most corrosion resistant material. This difference can be explained by the difference of the perturbation applied on the specimen, with EIS. In particular :

According to LPR

- S690 presents higher I_{corr} (Icorr =18μA/cm^2) than AH36 (Icorr =15μA/cm^2).
- AH36-AH36 presents higher I_{corr} (30μA/cm^2) than AH36-S690 (19μA/cm^2).
- Relevant differences are presented for Rp values

According to Potentiodynamic Polarization

- Icorr values are higher for S690 (Icorr = 25μA/cm^2), than AH36 (Icorr = 18μA/cm^2).
- Icorr values are similar for both weldments AH36-S690 (Icorr = 19μA/cm^2) and AH36-AH36, (Icorr = 17μA/cm^2).
- Icorr for parent metal AH36 is almost the same (Icorr = 18μA/cm^2) with AH36-AH36 weld (Icorr = 17μA/cm^2).

According to EIS :

- S690 presents higher corrosion resistance Rct= 1700 Ohms, than AH36 (Rct =1200 Ohms).
- Despite the lack of the repeatability in AH36-S690 (Rct = 1656 Ohms) experiments, we can safely presume that it presents higher corrosion resistance than AH36-AH36 (Rct =1171 Ohms).

10.3. Suggestions for future research

A lot of issues came up in the present thesis that serve as suggestions for future research:

- The sensitivity of the electrochemical techniques showed that it is interesting to study the correlation of the obtained parameters from the different electrochemical techniques and employ more sophisticated analysis of the parameters i.e. Tafel extrapolation method, limiting current i_L, other circuits for EIS, etc.
- It is very useful to try to correlate parameters of the microstructure with the corrosion i.e orientation, inclusions, employing more sophisticated techniques e.g. EBSD, detailed SEM on welds with micro electrochemical cells.
- For the shipbuilding industry it will be very useful to study the corrosion behavior in combination with mechanical phenomena, as fatigue, i.e. to study the corrosion behavior under cyclic loading conditions.

11. REFERENCES

[1] AA Clinic, (2019), Corrosion of Materials, Version 1.0.3, Powered be Andromo, Build version 5.1.2/476.

[2] Al-Shammary F.K.W., (2012), Electrochemical Kinetics of Corrosion, University of Babel, 2012.

[3] ASM International, (1993), ASM Handbook Vol. 6: Welding, Brazing and Soldering, American Society of Metals.

[4] ASM International, (2011), ASM Handbook Vol. 6A: Welding Fundamentals and Processes, American Society of Metals.

[5] ASM International, (1987), ASM Handbook Vol. 13: Corrosion, American Society of Metals.

[6] ASM International, (2003), ASM Handbook Vol. 13A: Corrosion: Fundamentals, Testing, Protection, American Society of Metals

[7] AWS, (2004), Welding Handbook Vol.2: Welding Processes, Part 1, American Welding Society.

[8] Bard A.J., Faulkner L.R., (2001), Electrochemical Methods: Fundamentals and applications, Second edition, John Wiley & Sons.

[9] BBN Ship Steel Factory, AH36 Shipbuilding Steel Plate, Xicheng Science &Technology Building High-Tech Development zone, China.

[10] Berradja A., (2019), Electrochemical Techniques for Corrosion and Tribocorrosion Monitoring: Methods for the Assessment of Corrosion Rates, IntechOpen.

[11] Bhadeshia H.K.D.H., Honeycombe R.W.K., (2017), Steels- Microstructure and properties, Fourth edition, Butterworth-Heinemann,Elsevier

[12] Biologic Sciences Instruments, (2014), EC-Lab® Software User's Manual - Version 10.38.

[13] BorTec, Common Alloying Elements for Steel and their Effects.

[14] Boutsali V.G., (2016), (Thesis), Study of microstructure and corrosion behavior of AH36 FSW welds and HSLA S690 arc welds, School of Naval Architecture and Marine Engineering, National Technical University of Athens.

[15] BUEHLER, Vickers Hardness Testing

[16] Chakrabati D, (2007), (PhD Thesis), Development of bimodal grain structures and their effect on toughness in HSLA steel, University of Birmingham.

[17] CGE Academy, BowTie XP, Visual Risk Assessment, CGE Risk Management Solutions.

[18] Correa C.A., Mastelari N., (2014), Effect of welding parameters in flux core arc welding (FCAW) with conventional and pulsed current in the efficiency and fusion rate of melting coating, Academic Journals.

[19] D&D Coatings, What is pitting corrosion?, D&D Coatings, Industrial & Decorative Painting Specialists.

[20] Efthymiou A., Study of microstructure and corrosion behavior of AH36 and HSLA S690 FSW welds, (Thesis), School of Naval Architecture and Marine Engineering, National Technical University of Athens.

[21] Esmailzadeh S., Aliofkhazraei M., Sarlak H., (2017), Interpretation of Cyclic Potentiodynamic Polarization Test Results for Study Behavior of Metals: A Review, Pleiades Publishing.

[22] Favi C., Cambi F., Germani M., Mandolini M., (2019), A Data Framework for Environmental Assessment of Metal Arc Welding Processes and Welded Structures During the Design Phase, The International Journal of Advanced Manufacturing Technology.

[23] FISCHER, X-Ray Fluorescence Measuring Systems

[24] Fourkas V., Corrosion behavior of super-hydrophobic surfaces on copper substrate in 3.5% NaCl solution, (Thesis), School of Naval Architecture and Marine Engineering, National Technical University of Athens.

[25] Gale W.F., Totemeier T.C., (2004), Smithells Metals Reference Book, 8th edition, Elsevier Butterworth-Heinemann.

[26] Gladman T., (1997), The physical metallurgy of microalloyed steels, 1st edition, The University Press, Cambridge.

[27] Gogou E., (2012), (Thesis Master), Use of High Strength Steel Grades for Economical Bridge Design, Delft University.

[28] Gummow R.A., Segall S., Fingas D., (2020), An Alternative View of the Cathodic Protection Mechanism on Buried Pipelines, MP Materials Performance.

[29] Haribalaji V., Boopathi S., Balamurugan S., (2014), Effect of welding processes on mechanical and metallurgical properties of HSLA steel joints, International Journal of Innovation and Scientific Research.

[30] Hascelik, Impact of Alloy Elements on Steel Structure.

[31] Hirotomo S., (2010), Corrosion of metallic biomaterials, Metals for Biomedical Devices.

[32] Huang W.H., Yen H.W., Lee Y.L., (2019), Corrosion behavior and surface analysis of 690MPa-grade offshore steels in chloride media, Journals of Materials Research and Technology, Elsevier.

[33] Jones D.A., (1996), Principles and Prevention of Corrosion, Second edition, Prentice Hall.

[34] Kakaei K., Esrafili M., Ehsani A., (2019), Interface Science and Technology vol. 27: Graphene Surfaces: Particles and Catalysts, Interface Science and Technology, Elsevier.

[35] Kemplon Engineering, (2015), Stress Corrosion Cracking (SCC): A Capriciously Insidious Material Killer, USA.

[36] Kou S., (1987), Welding Metallurgy, John Wiley & Sons.

[37] Liadi P., (2018), (Thesis), Susceptibility to corrosion of AH36 and S690 weldments in shipbuilding industry, School of Naval Architecture and Marine Engineering, National Technical University of Athens.

[38] Loder D., Michelic S.K., Bernhard C., (2017), Acicular Ferrite Formation and Its Influencing Factors- A Review, Journal Science Research, Vol.6, No. 1, Montanuniversitaet Leoben, Austria.

[39] McCafferty E., (2005), Validation of corrosion rates measured by the Tafel extrapolation method, Corrosion Science.

[40] Metinvest International, Plates of S690Q steel grade - Fine-grain structural steel after quenching and tempering, Italy.

[41] Microscope Detective, How Does a Stereo Microscope Work?

[42] Microscope Master, How Does A Microscope Works?

[43] Morrison W.B., (2000), Overview of Microalloying in Steels, academia.edu

[44] Myrdal R., (2010), Corrosion Inhibitors - State of the art, COIN Project report 22-2010, SINTEF Building and Infrastructure.

[45] NanoScience Instruments, Scanning Electron Microscopy.

[46] Pantelis D.I., Chrysoulakis G., (2008), Materials Science and Technology, Second Edition, Papasotiriou (in Greek).

[47] Pantelis D.I., Papazoglou V.I., Chaidemenopoulos G.N., (2017), Welding Science and Technology, Second Edition, Tziola (in Greek).

[48] Pantelis D.I., Tsiourva D.E, (2001), Corrosion and Protection of Shipbuilding and Mechanical Constructions, School of Naval Architecture and Marine Engineering, National Technical University of Athens (in Greek).

[49] Pantelis D.I., Tsiourva D.E., (2017), Trends in Oil and Gas Corrosion Research and Technologies, Chapter 10, Shipbuilding Technology Laboratory, School of Naval Architecture and Marine Engineering, National Technical University of Athens, Greece.

[50] Pearson C., (1998), Conservation of marine archaeological objects, Butterworths, London.

[51] Pinto H., Corpas M., Guio J.A., Pyzalla A.R., Jahn A., Standfub J., (2008), Microstructure and Residual Stress Formation in Induction-Assisted Laser Welding of the Steel S690QL, Materials Technology,Germany

[52] Popov B.N., (2015), Basics of Corrosion Measurements, Corrosion Engineering, Elsevier.

[53] RAMSSES, (2019), Realization and Demonstration of Advanced Material Solutions for Sustainable and Efficient Ships, Internal Report 19.4, 4th Internal report.

[54] Ribeiro D.V., Souza C.A.C., Abrantes J.C.C., (2015), Use of Electrochemical Impedance Spectroscopy (EIS) to monitoring the corrosion of reinforced concrete, IBRACON Structures and Materials Journal.

[55] Sastri V.S., (2015), Challenges in Corrosion: Costs, Causes, Consequences and Control, John Wiley & Sons.

[56] Shi S. (2014), Evaluating the structural integrity of High Strength Low Alloy Steels considered for shipbuilding using acoustic emission, University of Birmingham.

[57] SIGRAY, AttoMap X-ray Fluorescence Microscope

[58] Silverman D.C., (2011), Practical Corrosion Prediction Using Electrochemical Techniques, Argentum Solutions.

[59] Skobir D.A., (2011), High-Strength Low-Alloy (HSLA) Steels, Institute of Metals and Technology.

[60] Slater C., Davis D., Papaelias M., Hatzidouros E., Pantelis D, Papazoglou V., Lopez A., Rodriguez E., Przydatek J., (2013), HSLA Steel Selection and Characterization, University of Birmingham, NTUA, AIMEN, LR. MOSAIC.

[61] STI Group, (2015), Welding Processes: A Closer Look at FCAW.

[62] Subsidiary of Hitachi Metals, Effects of Common Alloying Elements in Steel, DIEHL Tool Steel, America.

[63] TEC Eurolab, Uniform Corrosion, TEC Eurolab, Siglacom, Italy.

[64] The Welding Institute Ltd, What is galvanic corrosion and how can it be prevented?, United Kingdom.

[65] Tuz L., (2018), Evaluation of microstructure and selected mechanical properties of laser beam welded S690QL High-Strength Steel, Sciendo,Advances in materials science, vol.18

[66] WeldersLab, What are the five basic types of welding joints?

[67] Wirth K., Barth A., X-Ray Fluorescence (XRF), Geochemical Instrumentation and Analysis.

[68] Wu W., Hao W.K., Liu Z.Y., Li X.G., Du C.W., Liao W.J., (2015), Corrosion Behavior of E690 High-Strength Steel in Alternating Wet-Dry Marine Environment with Different pH Values, Journals of Materials Engineering and Performance, Springer.

[69] Xinyu Welding, (2014), The advantages and disadvantages of flux cored arc welding, Hebei Xinyu Welding Co., Ltd.

[70] Yusheng Iron and Steel CO. LTD, ABS Grade AH36, ABS Grade EH36, ABS Grade DH36, ABS Grade FH36 steel plate for shipbuilding and repairing.

C. APPENDIX

12. ANNEX

12.1. Optical observation after corrosion

12.1.1. Tafel Extrapolation Method

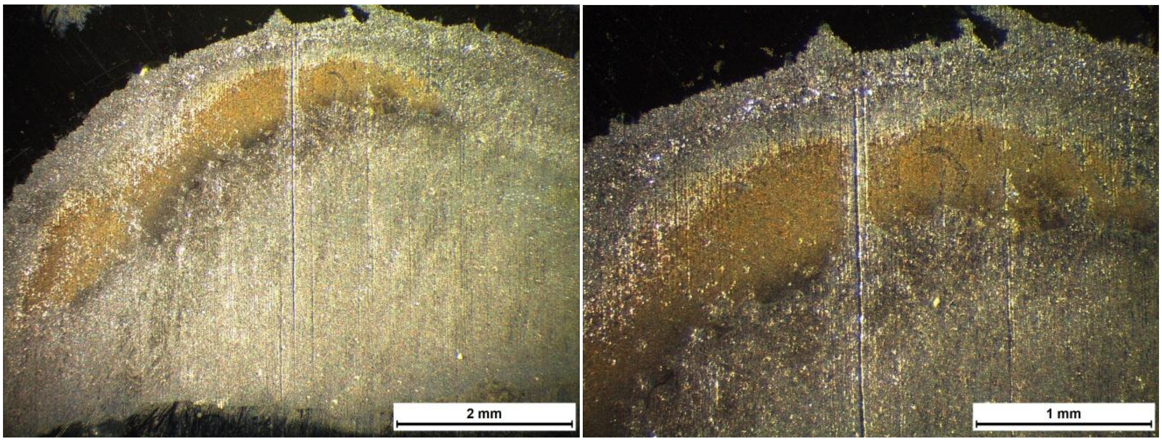

a) b)

Fig.[12.1] Optical observation of parent metal AH36 after Tafel Extrapolation Method a) x2.0, b) x4.0.

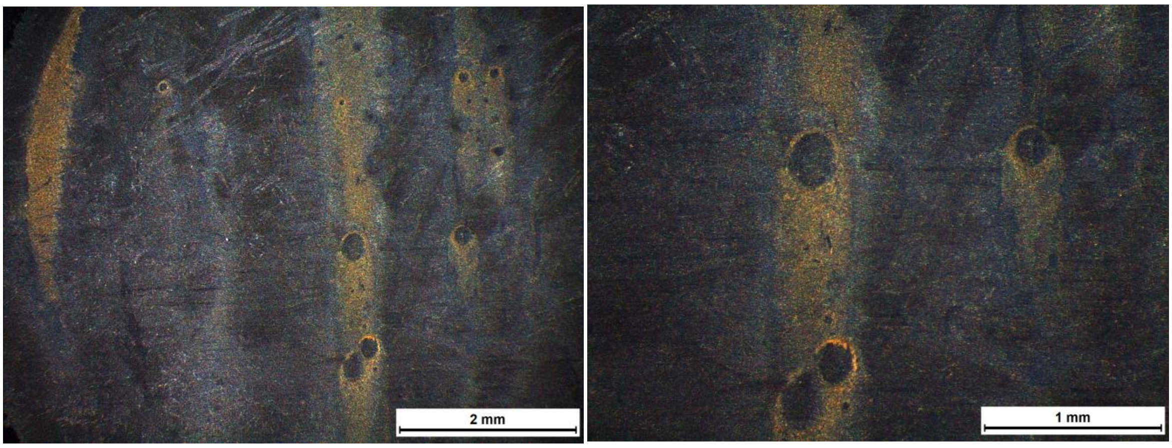

a) b)

Fig.[12.2] Optical observation of parent metal S690 after Tafel Extrapolation Method a) x2.0, b) x4.0.

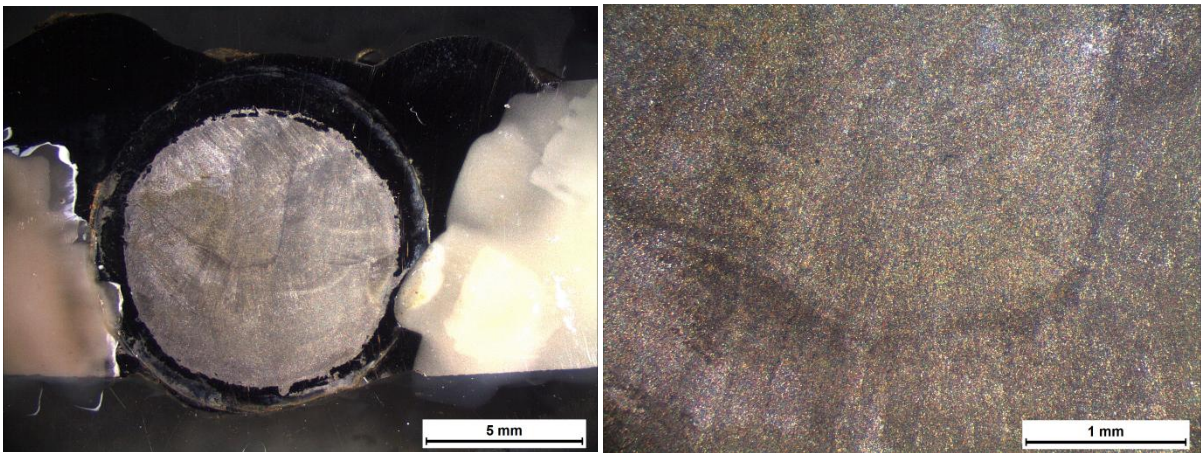

a) b)

Fig.[12.3] Optical observation of homogeneous weldment of AH36-AH36 after Tafel Extrapolation Method a) x0.63, b) x3.2.

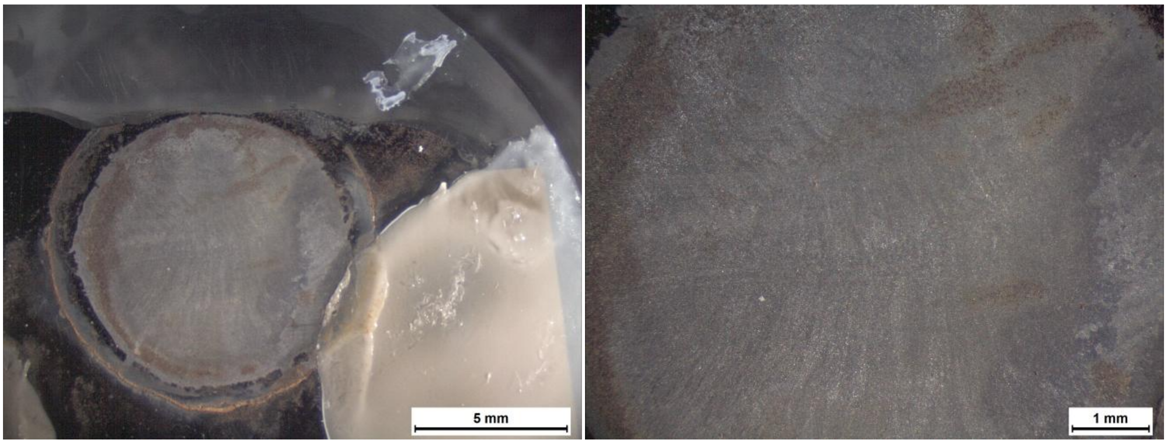

a) b)

Fig.[12.4] Optical observation of heterogeneous weldment of AH36-S690 after Tafel Extrapolation Method a) x0.63, b) x1.6.

12.1.2. Electrochemical Impedance Spectroscopy

a) b)

Fig.[12.5] Optical observation of parent metal AH36 after the first series of Electrochemical Impedance Spectroscopy a) x1.0, b) x2.0.

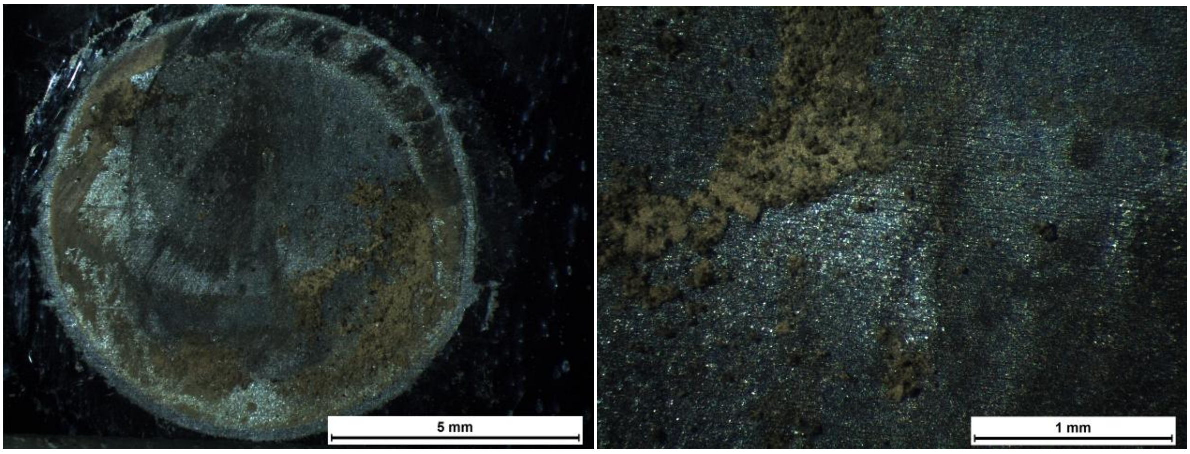

a) b)

Fig.[12.6] Optical observation of parent metal AH36 after the second series of Electrochemical Impedance Spectroscopy a) x1.0, b) x4.0.

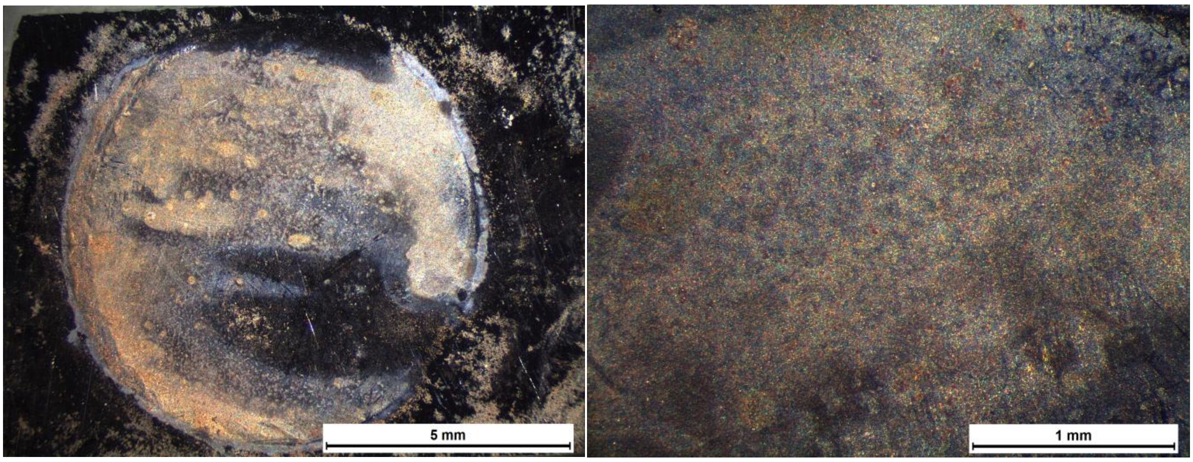

a) b)

Fig.[12.7] Optical observation of parent metal S690 after the first series of Electrochemical Impedance Spectroscopy a) x1.0, b) x4.0.

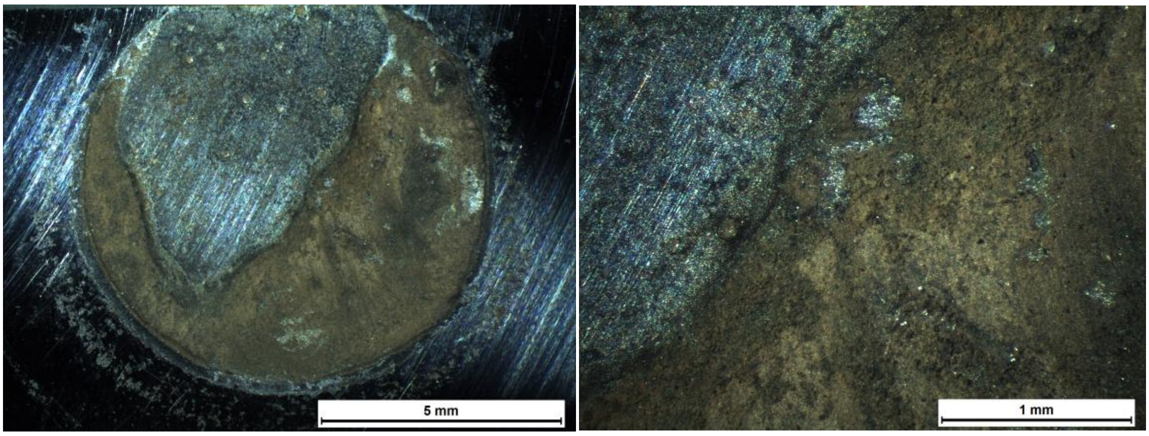

Fig.[12.8] Optical observation of parent metal S690 after the second series of Electrochemical Impedance Spectroscopy a) x1.0, b) x4.0.

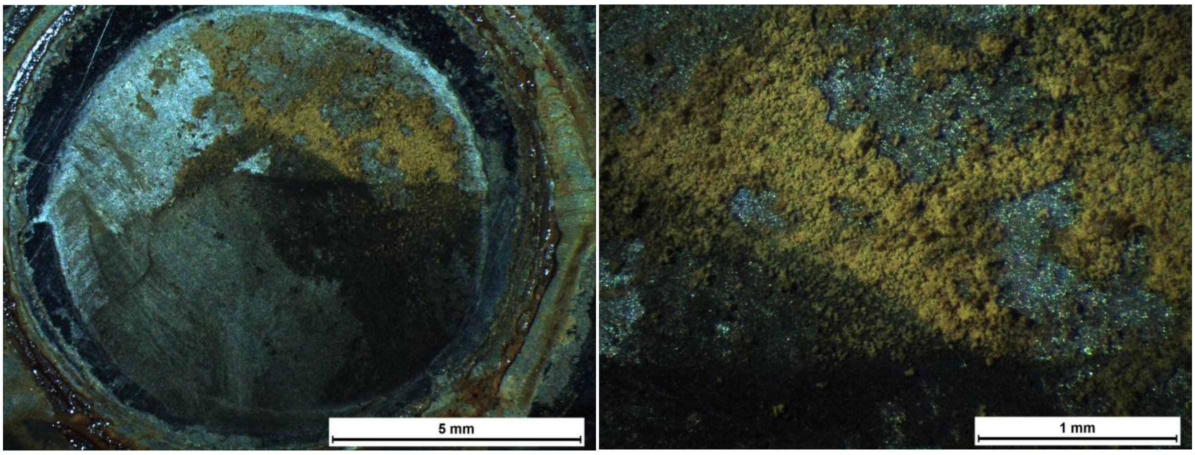

a) b)

Fig.[12.9] Optical observation of homogeneous weldment AH36-AH36 after the second series of Electrochemical Impedance Spectroscopy a) x1.0, b) x4.0.

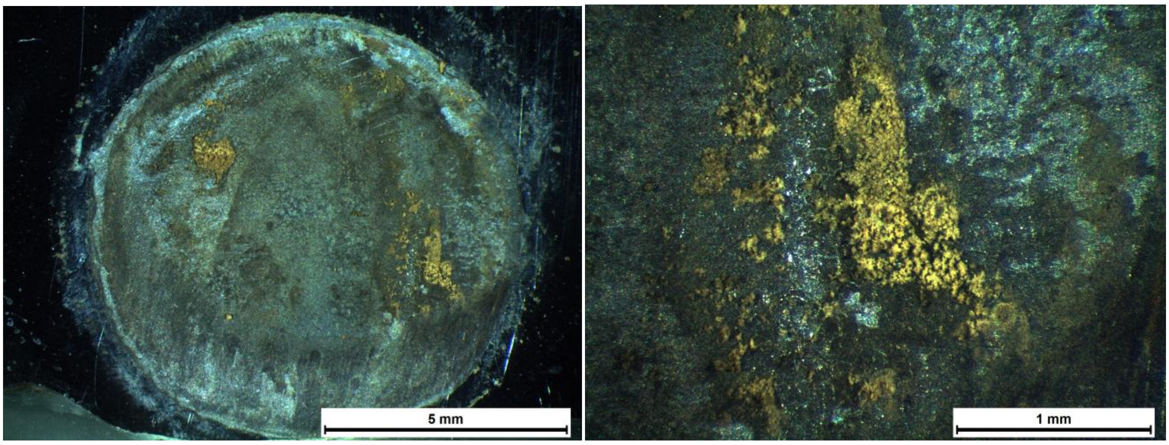

a) b)

Fig.[12.10] Optical observation of heterogeneous weldment AH36-S690 after the second series of Electrochemical Impedance Spectroscopy a) x1.0, b) x4.0.

12.2. Supplementary diagrams

12.2.1. Linear Polarization Resistance

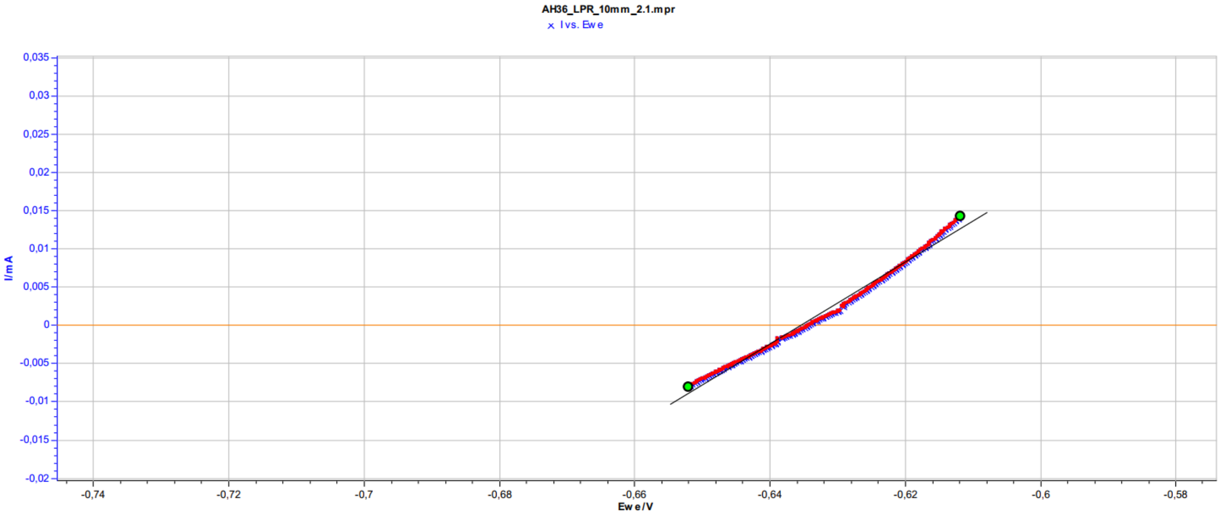

Fig.[12.11] LPR plot of parent metal AH36, exp.1, **Blue**/**Red** trace: points, **Black** line LPR fit.

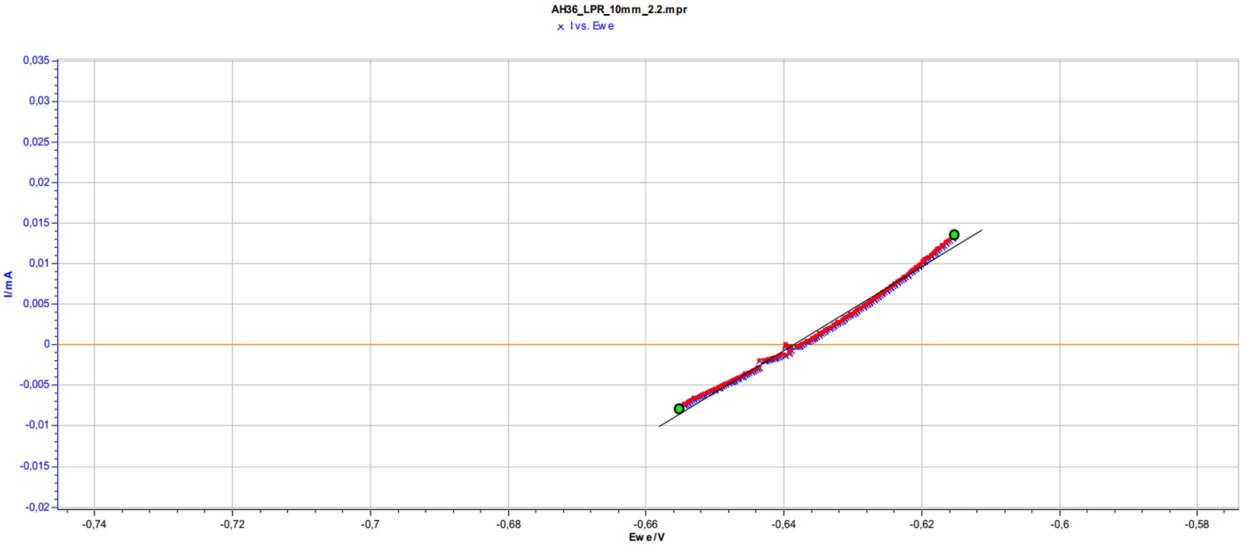

Fig.[12.12] LPR plot of parent metal AH36, exp.2, **Blue**/**Red** trace: points, **Black** line LPR fit.

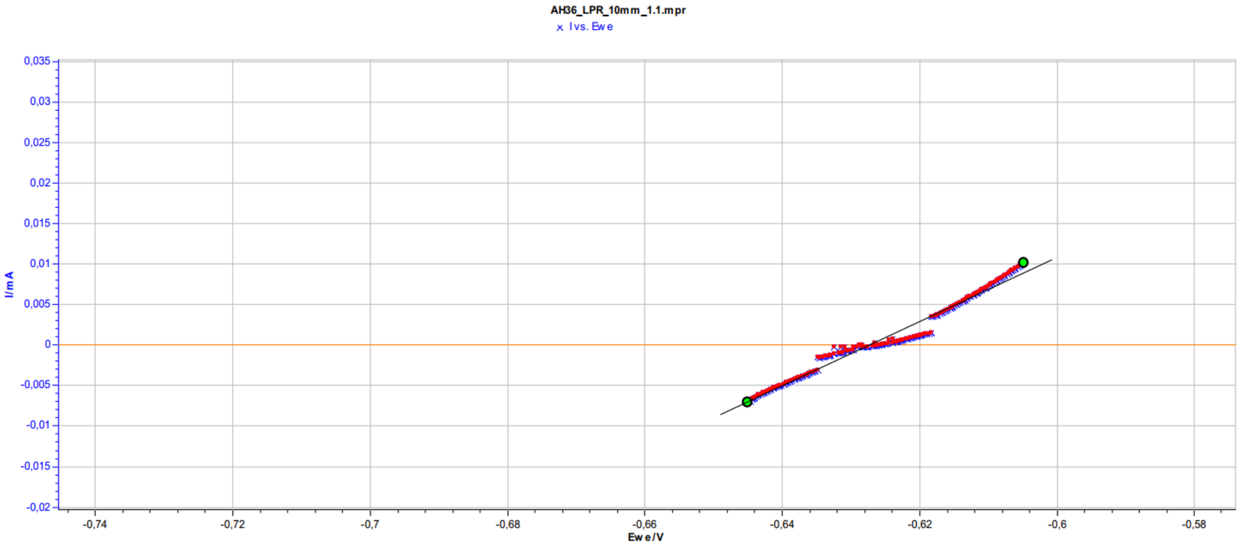

Fig.[12.13] LPR plot of parent metal AH36, exp.3, **Blue**/**Red** trace: points, **Black** line LPR fit.

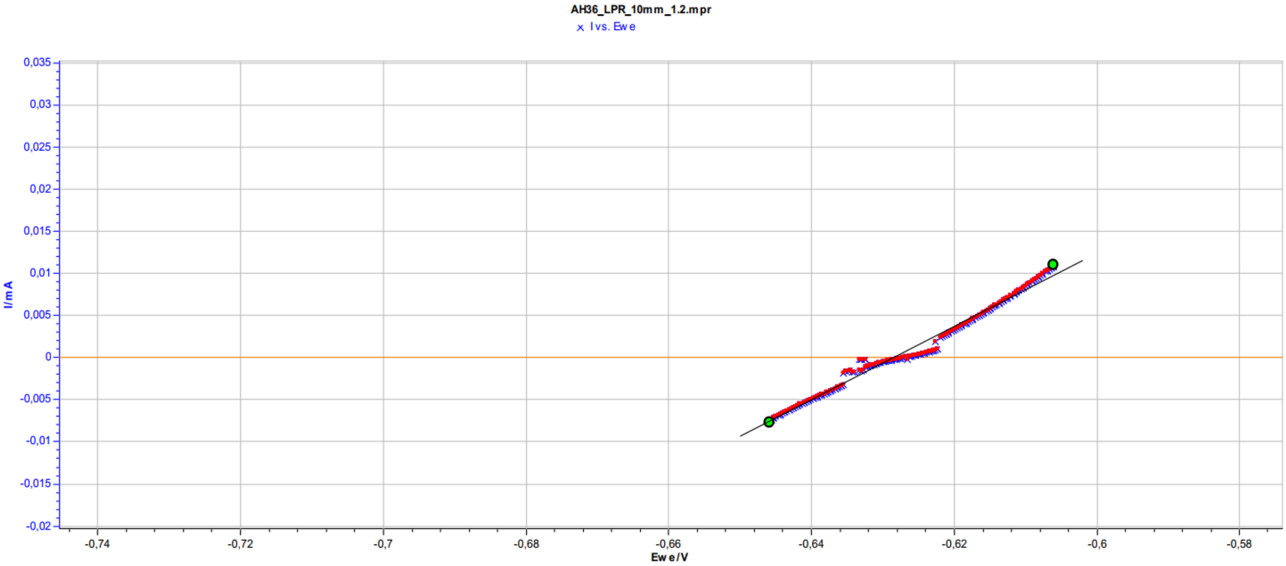

Fig.[12.14] LPR plot of parent metal AH36, exp.4, **Blue**/**Red** trace: points, **Black** line LPR fit.

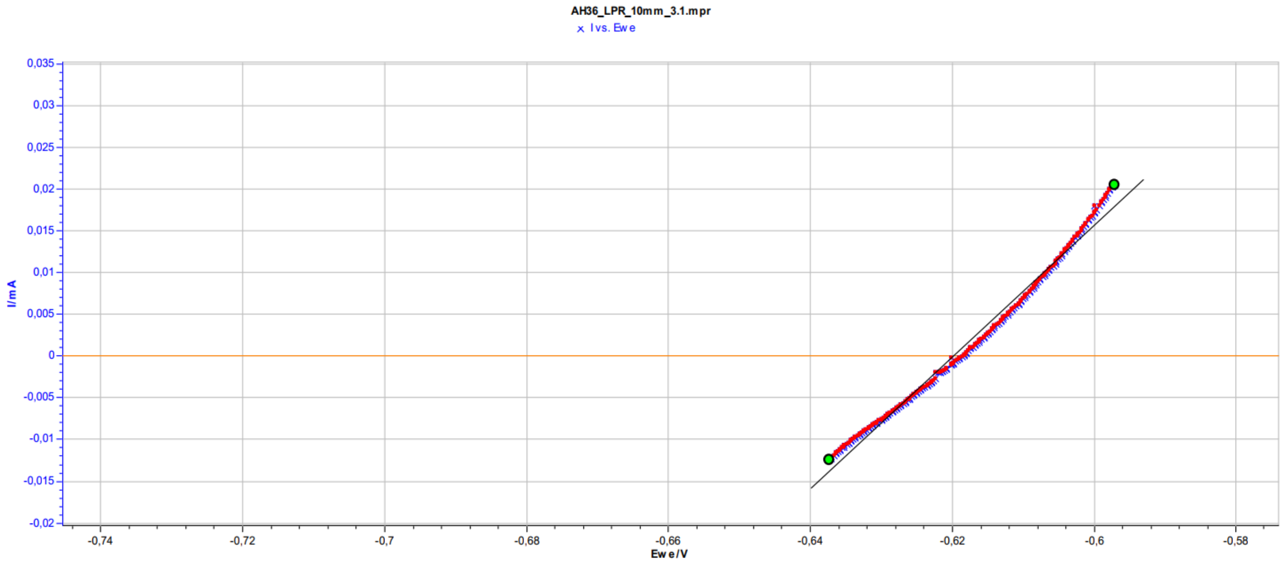

Fig.[12.15] LPR plot of parent metal AH36, exp.5, **Blue**/**Red** trace: points, **Black** line LPR fit.

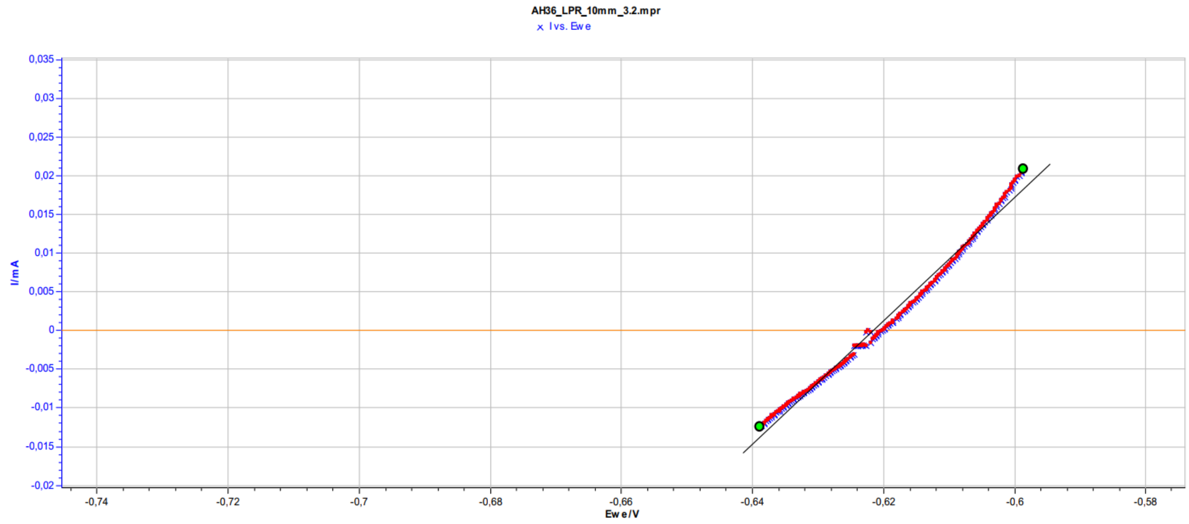

Fig.[12.16] LPR plot of parent metal AH36, exp.6, **Blue**/**Red** trace: points, **Black** line LPR fit.

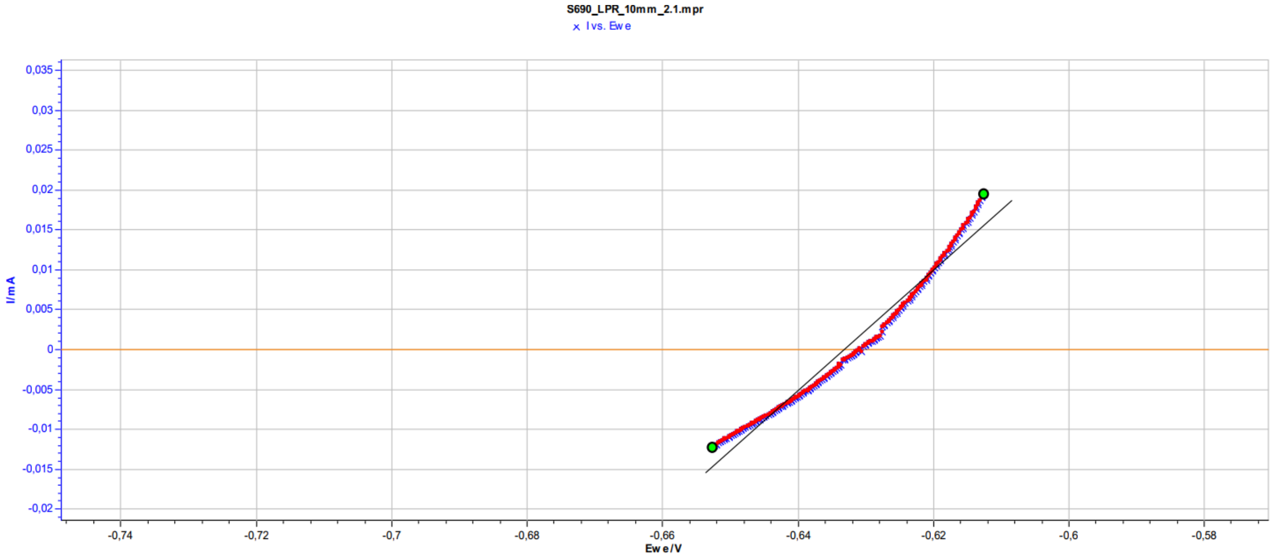

Fig.[12.17] LPR plot of parent metal S690, exp.1, **Blue**/**Red** trace: points, **Black** line LPR fit.

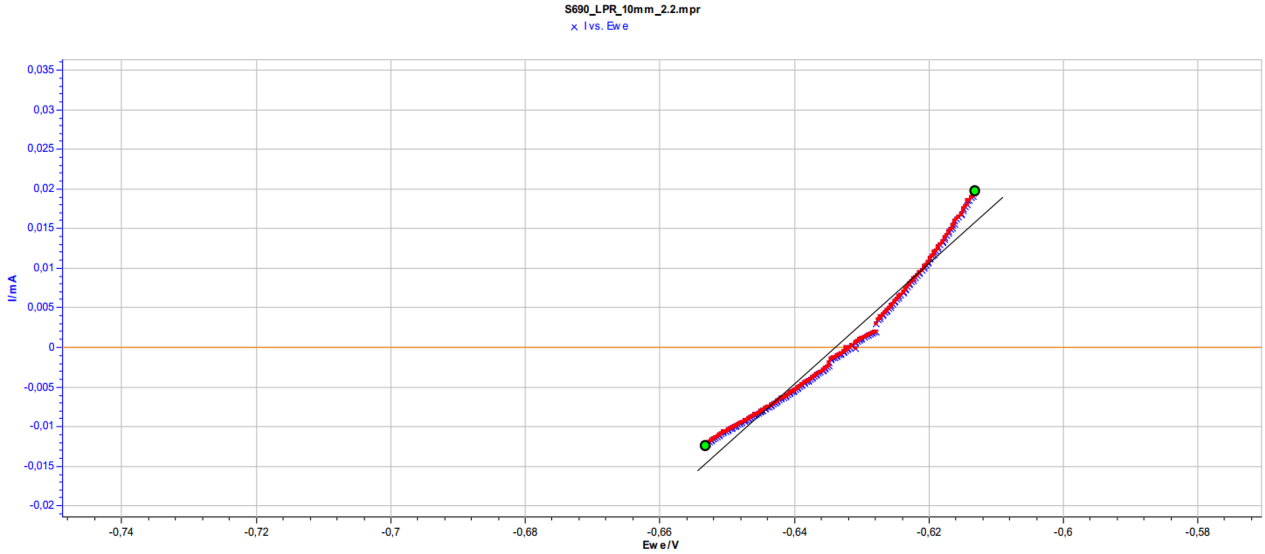

Fig.[12.18] LPR plot of parent metal S690, exp.2, **Blue**/**Red** trace: points, **Black** line LPR fit.

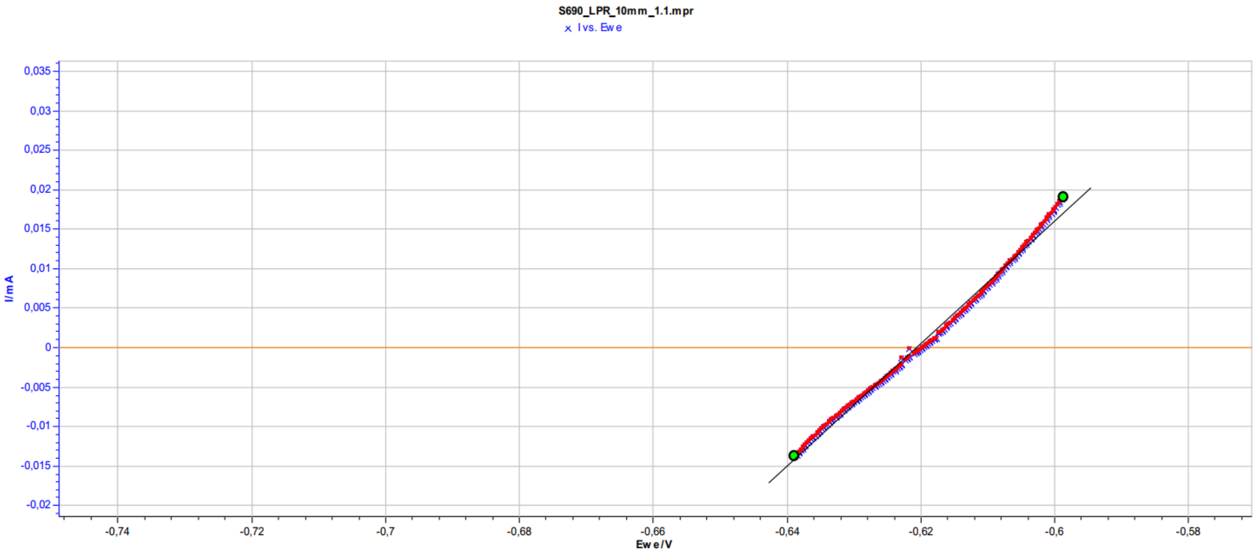

Fig.[12.19] LPR plot of parent metal S690, exp.3, **Blue**/**Red** trace: points, **Black** line LPR fit.

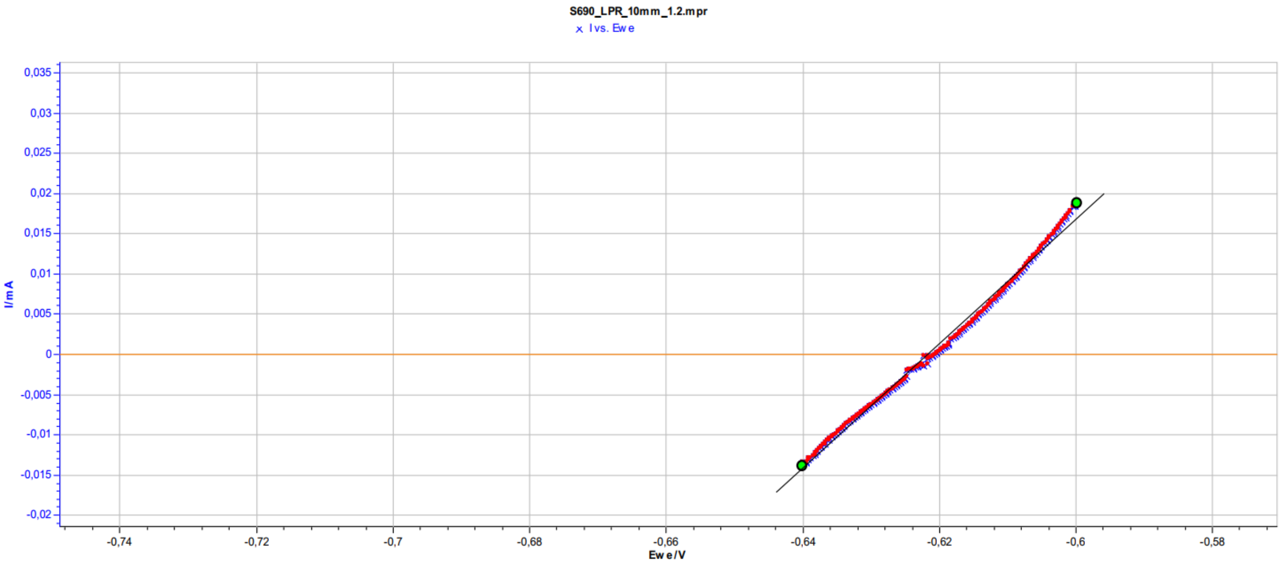

Fig.[12.20] LPR plot of parent metal S690, exp.4, **Blue**/**Red** trace: points, **Black** line LPR fit.

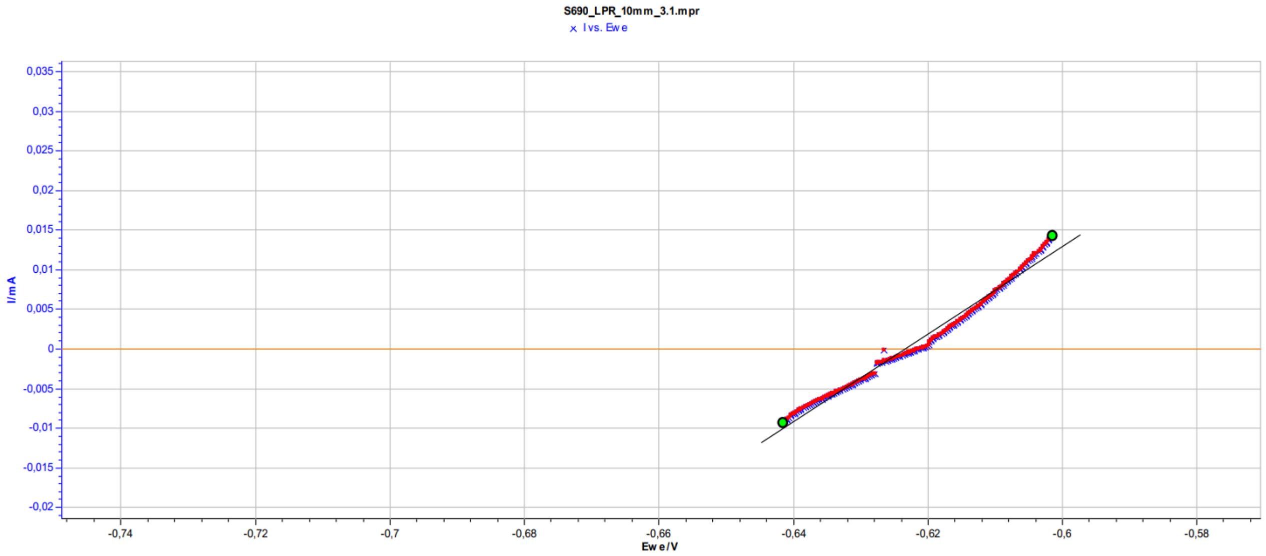

Fig.[12.21] LPR plot of parent metal S690, exp.5, **Blue**/**Red** trace: points, **Black** line LPR fit.

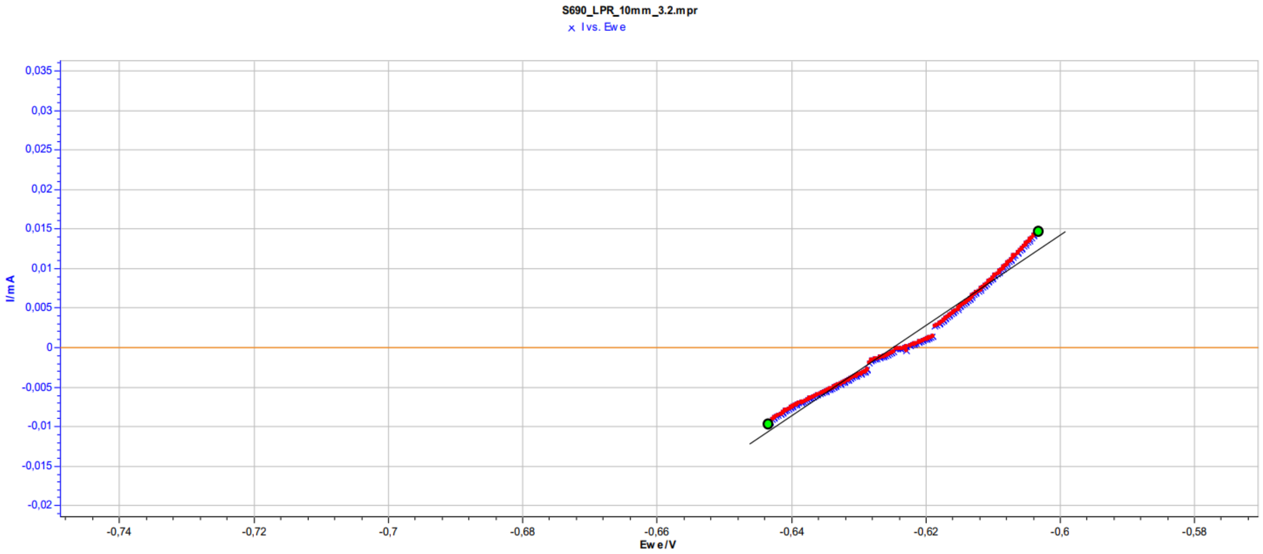

Fig.[12.22] LPR plot of parent metal S690, exp.6, **Blue**/**Red** trace: points, **Black** line LPR fit.

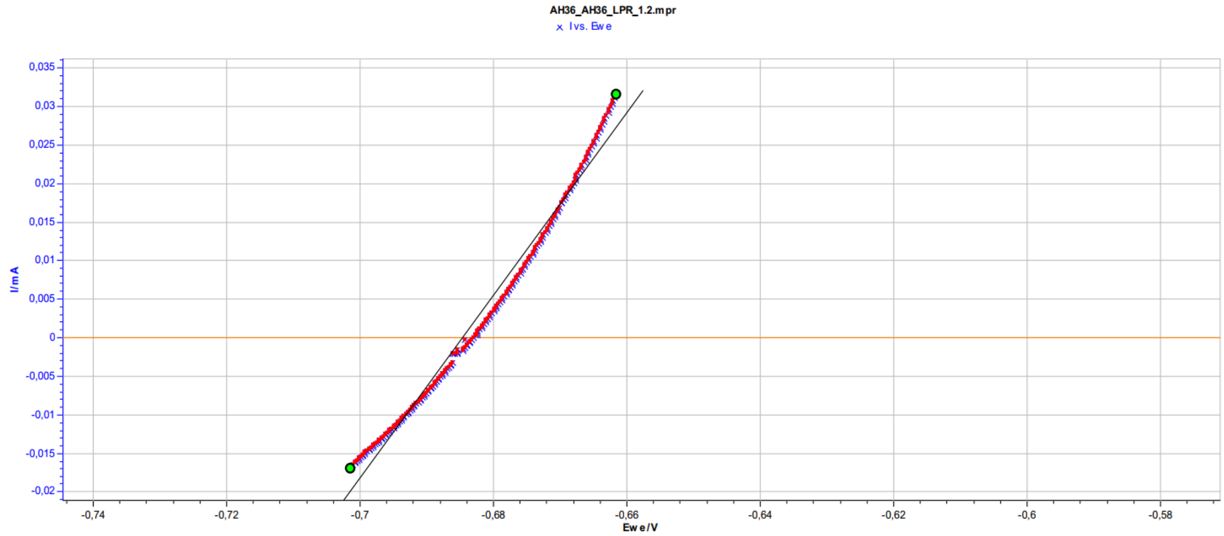

Fig.[12.23] LPR plot of homogeneous weldment AH36-AH36, exp.1,
Blue/**Red** trace: points, **Black** line LPR fit.

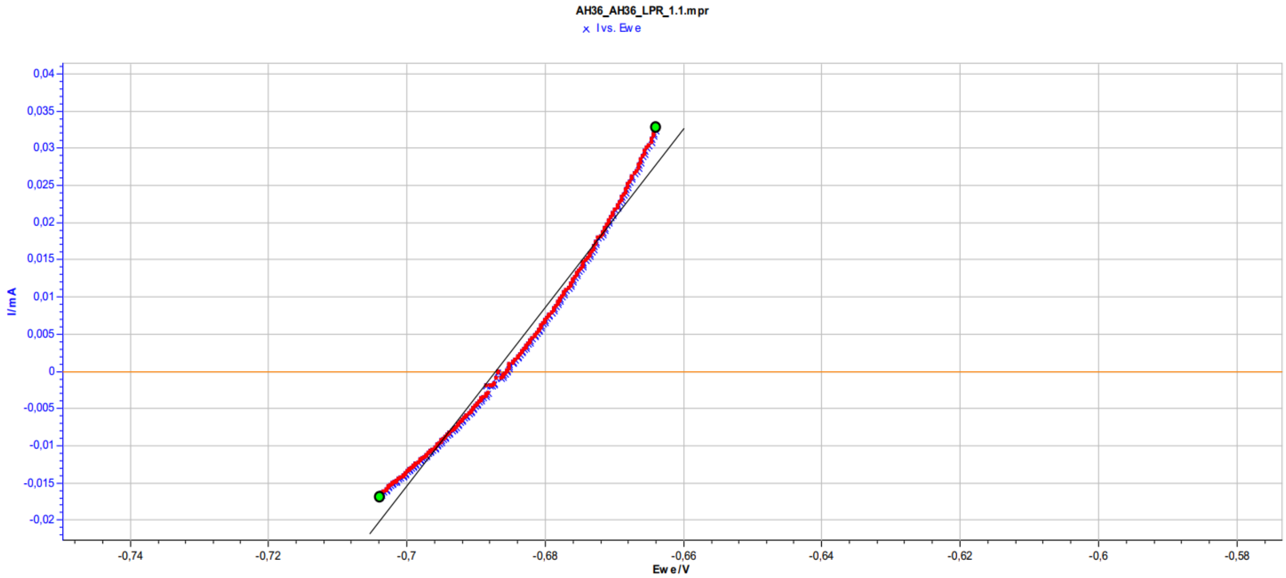

Fig.[12.24] LPR plot of homogeneous weldment AH36-AH36, exp.2,
Blue/**Red** trace: points, **Black** line LPR fit.

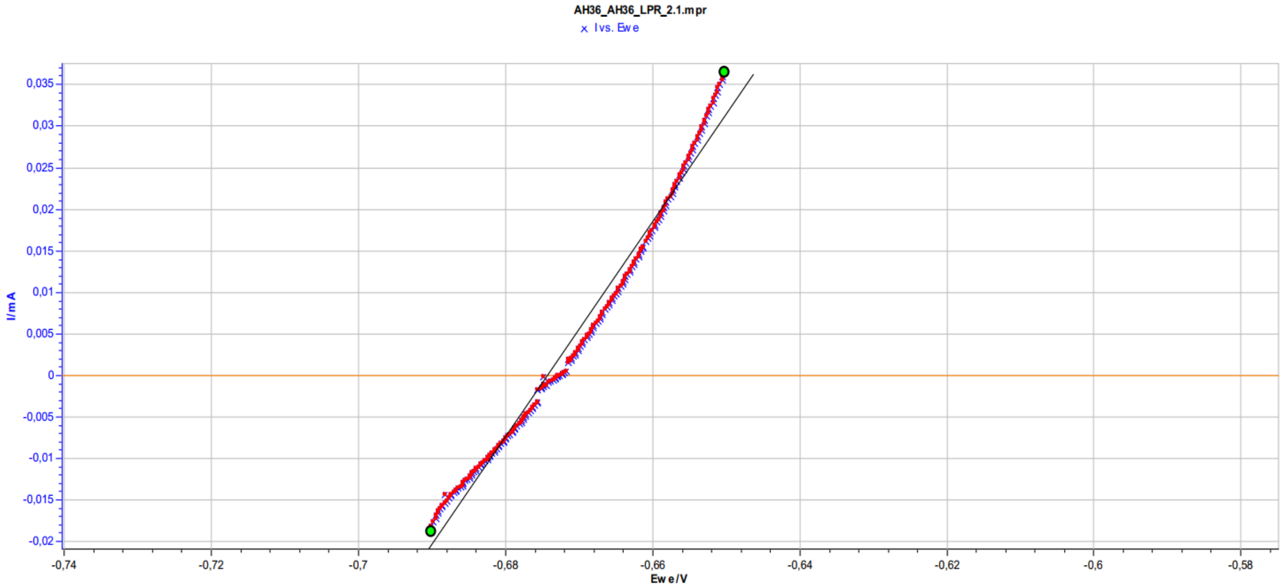

Fig.[12.25] LPR plot of homogeneous weldment AH36-AH36, exp.3,
Blue/**Red** trace: points, **Black** line LPR fit.

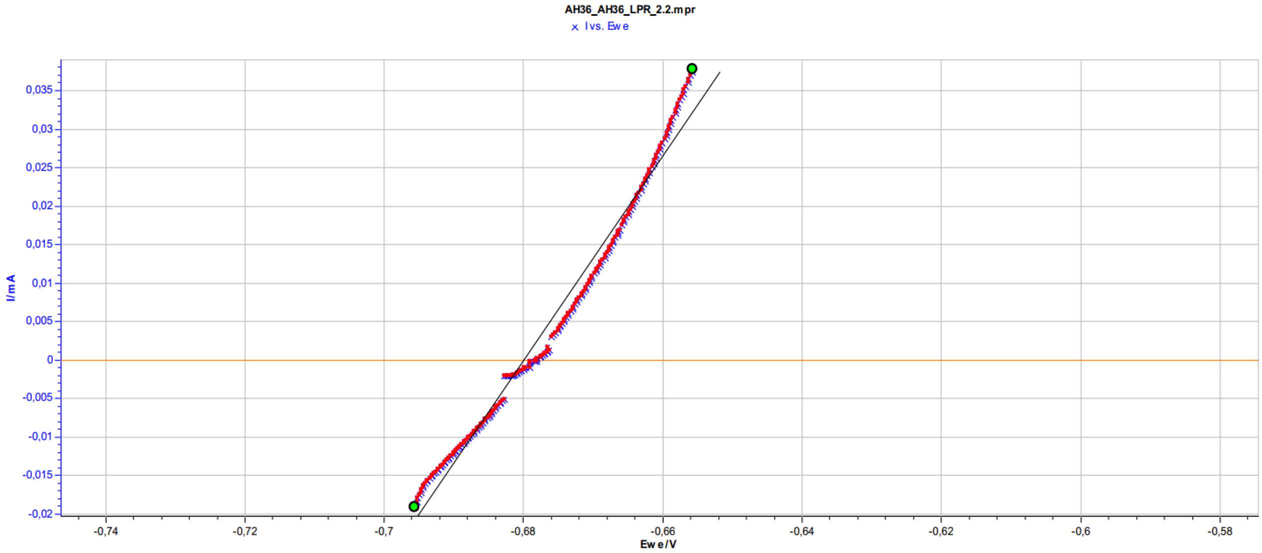

Fig.[12.26] LPR plot of homogeneous weldment AH36-AH36, exp.4,
Blue/**Red** trace: points, **Black** line LPR fit.

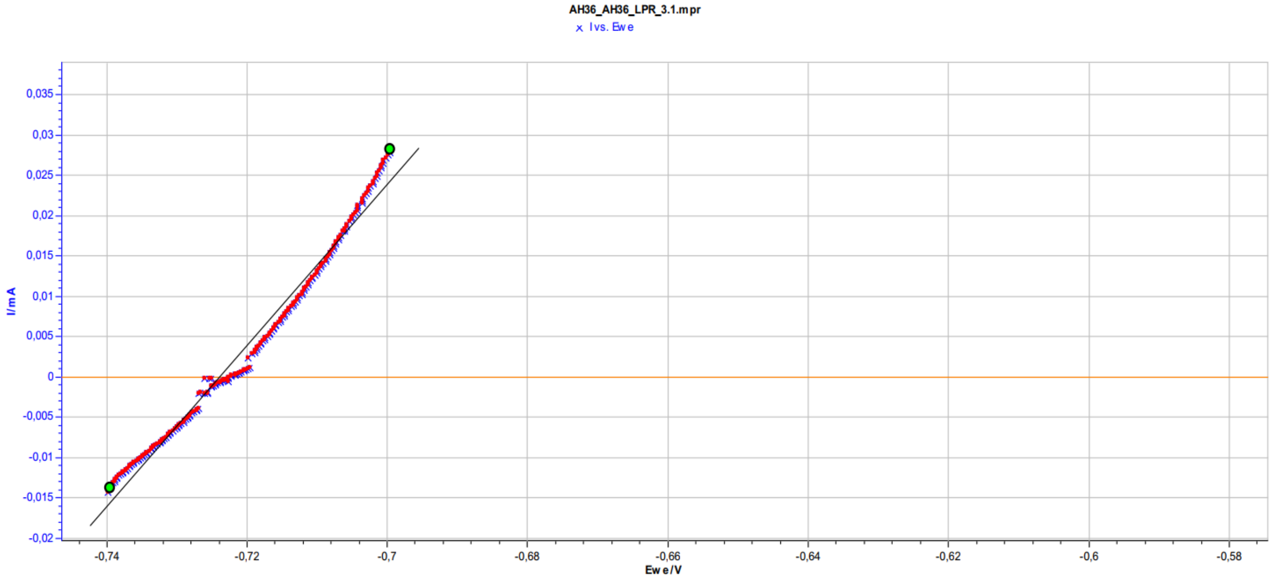

Fig.[12.27] LPR plot of homogeneous weldment AH36-AH36, exp.5, **Blue**/**Red** trace: points, **Black** line LPR fit.

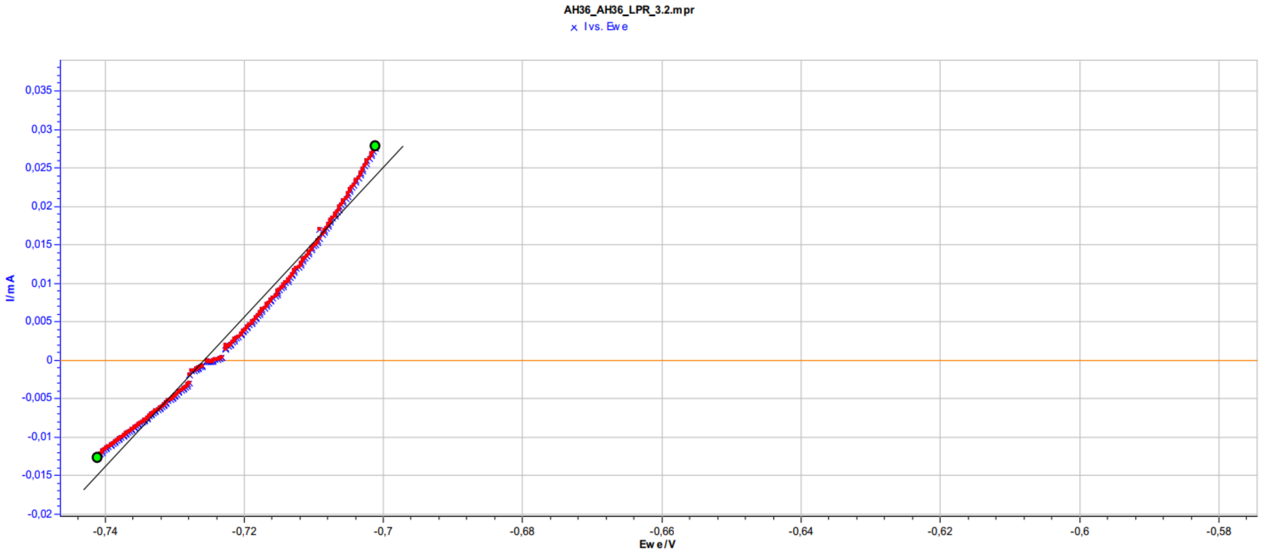

Fig.[12.28] LPR plot of homogeneous weldment AH36-AH36, exp.6, **Blue**/**Red** trace: points, **Black** line LPR fit.

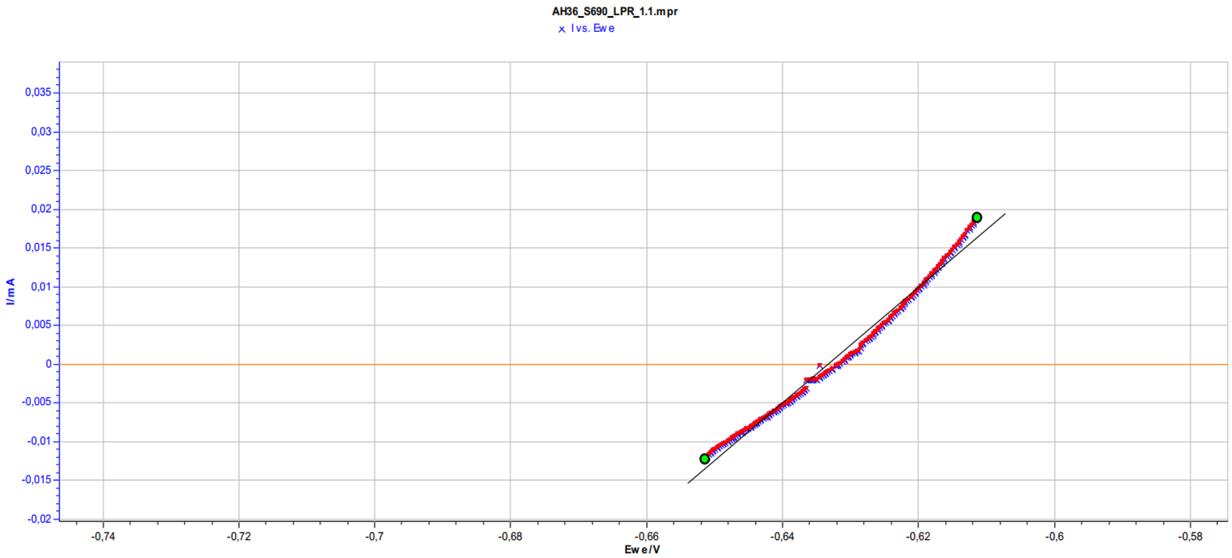

Fig.[12.29] LPR plot of heterogeneous weldment AH36-S690, exp.1,
Blue/**Red** trace: points, **Black** line LPR fit.

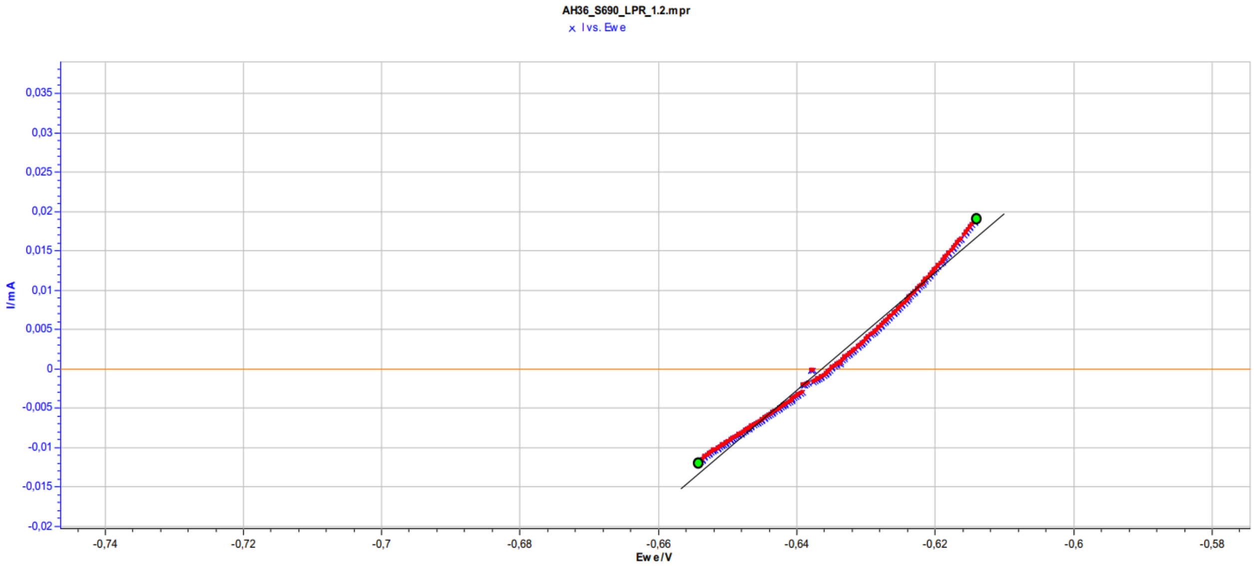

Fig.[12.30] LPR plot of heterogeneous weldment AH36-S690, exp.2,
Blue/**Red** trace: points, **Black** line LPR fit.

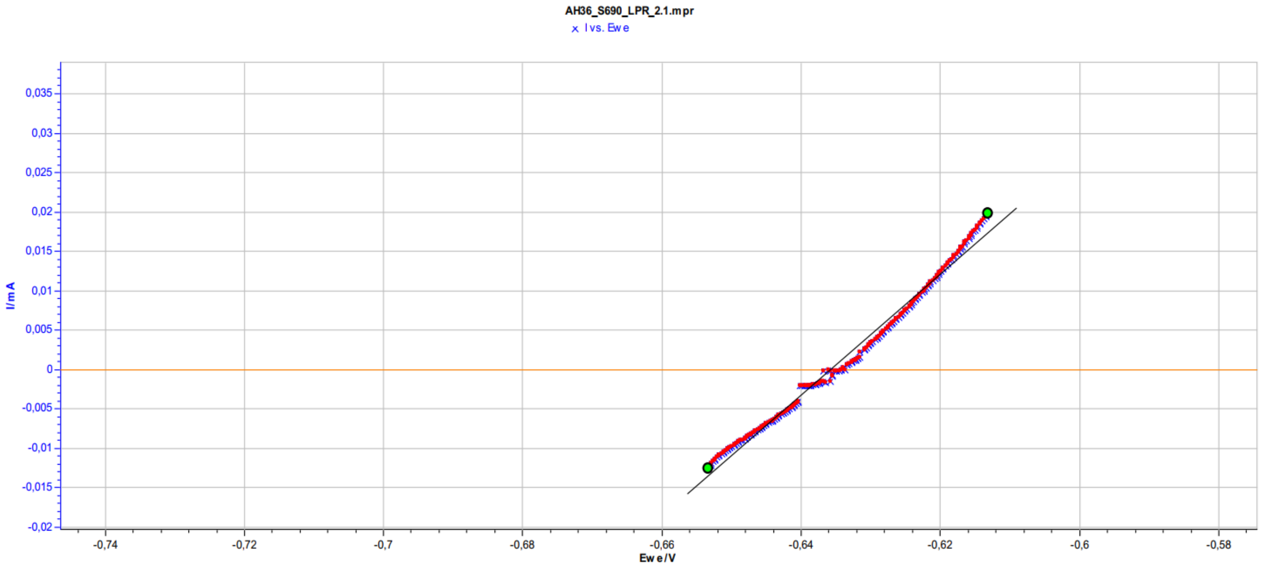

Fig.[12.31] LPR plot of heterogeneous weldment AH36-S690, exp.3,
Blue/**Red** trace: points, **Black** line LPR fit.

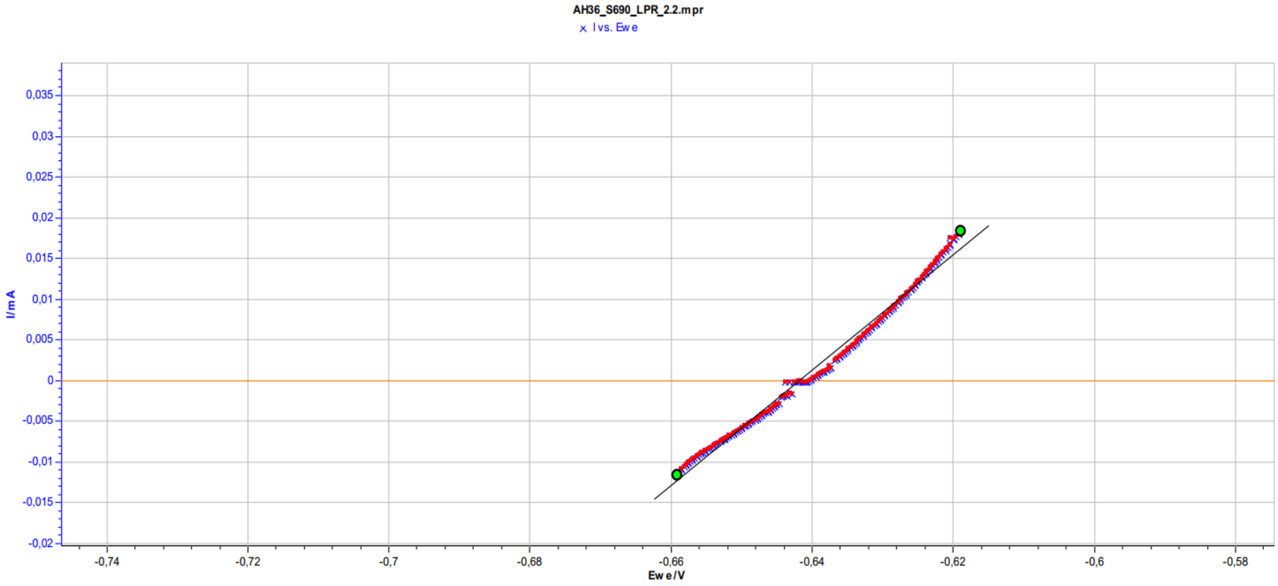

Fig.[12.32] LPR plot of heterogeneous weldment AH36-S690, exp.4,
Blue/**Red** trace: points, **Black** line LPR fit.

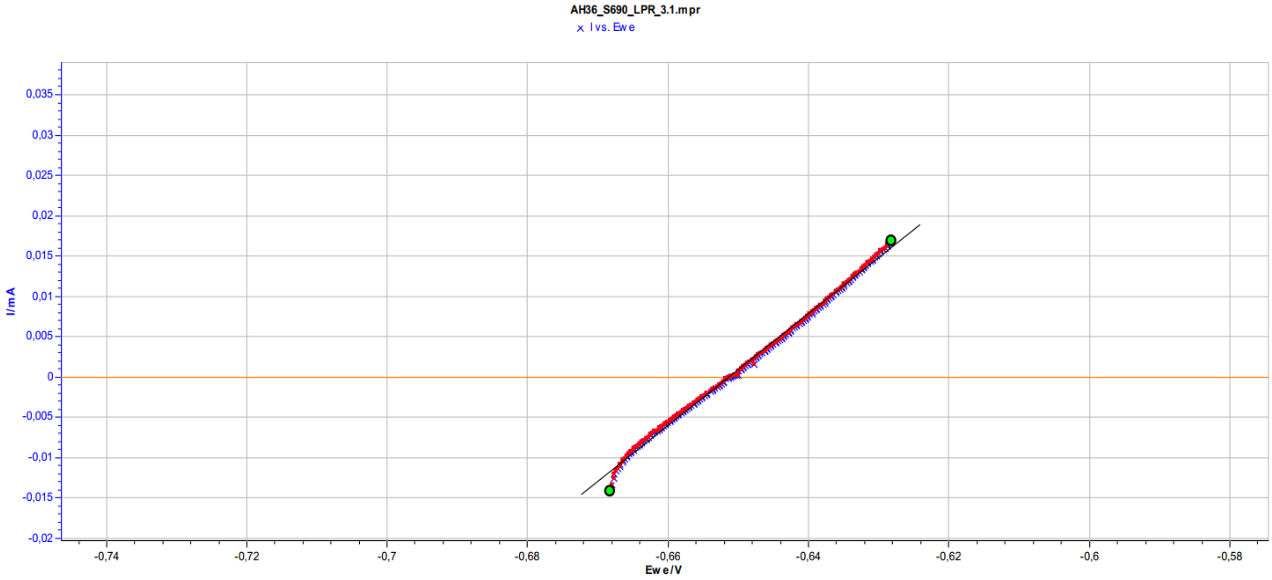

Fig.[12.33] LPR plot of heterogeneous weldment AH36-S690, exp.5,
Blue/**Red** trace: points, **Black** line LPR fit.

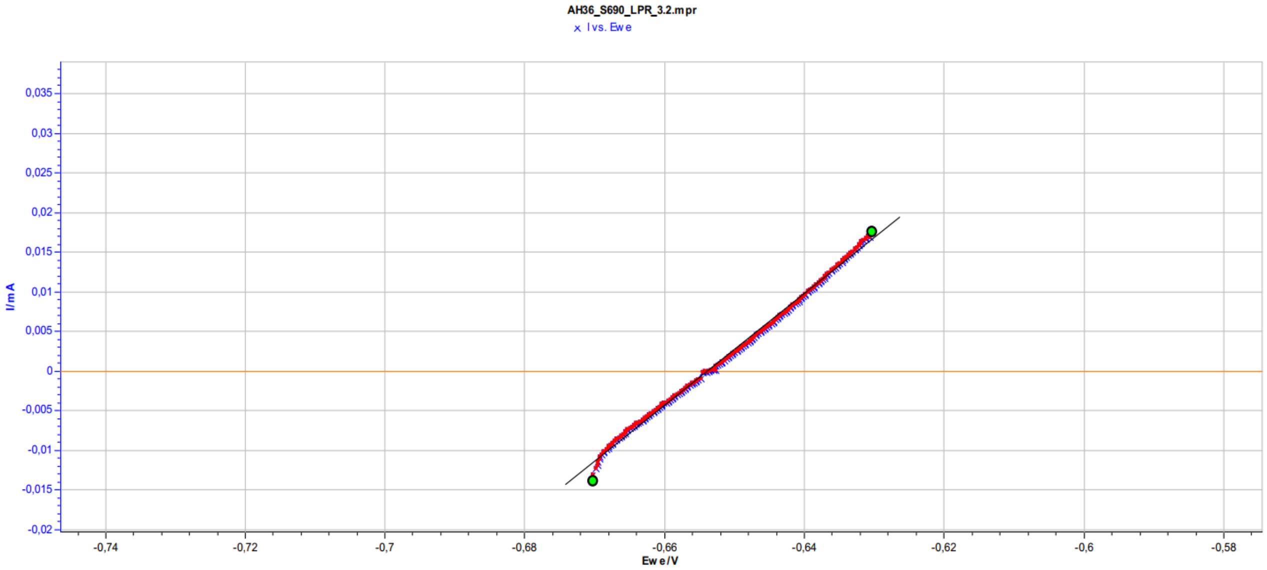

Fig.[12.34] LPR plot of heterogeneous weldment AH36-S690, exp.6,
Blue/**Red** trace: points, **Black** line LPR fit.

12.2.2. Tafel Extrapolation Method

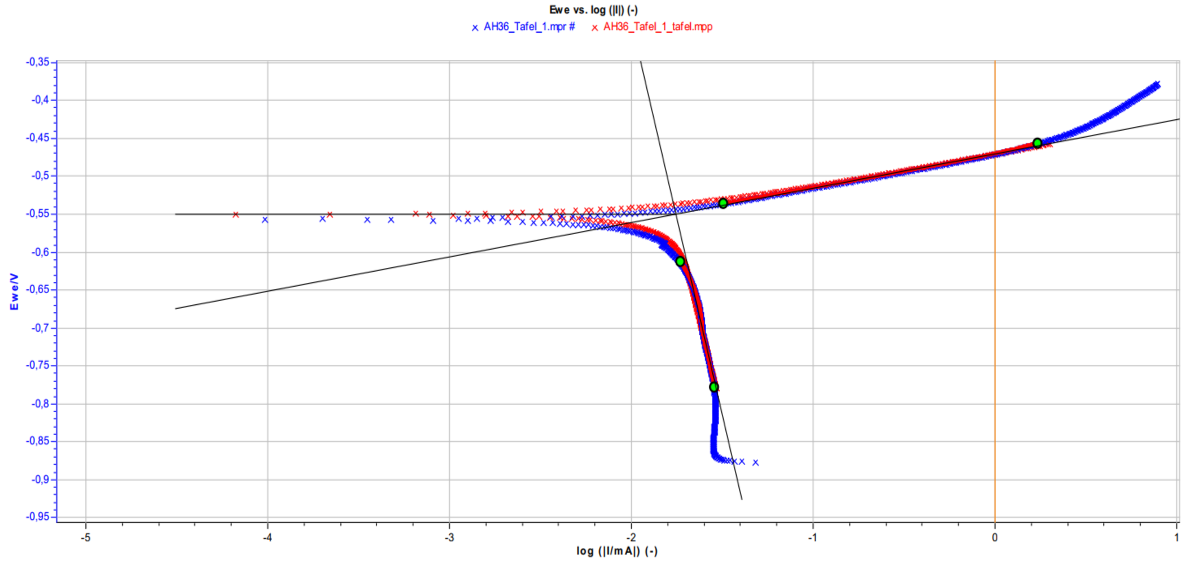

Fig.[12.35] Polarization curves and Tafel extrapolation method of parent metal **AH36**, exp.1.
Blue: AH36, **Red**: Tafel fitting via EC Lab.

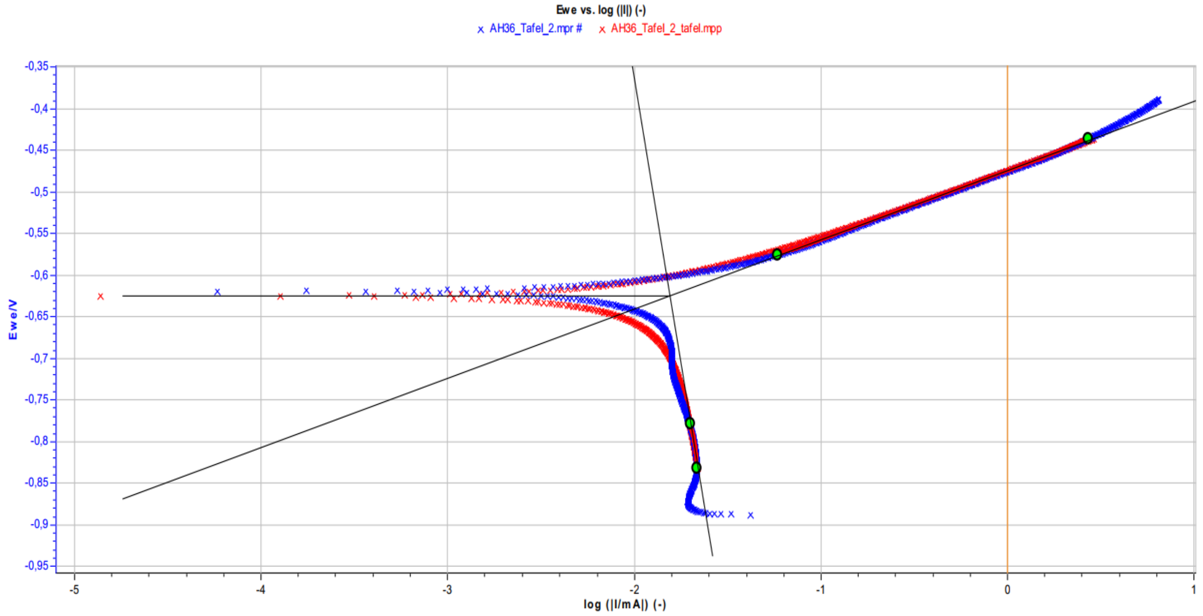

Fig. [12.36] Polarization curves and Tafel extrapolation method of parent metal **AH36**, exp.2.
Blue: AH36, **Red**: Tafel fitting via EC Lab.

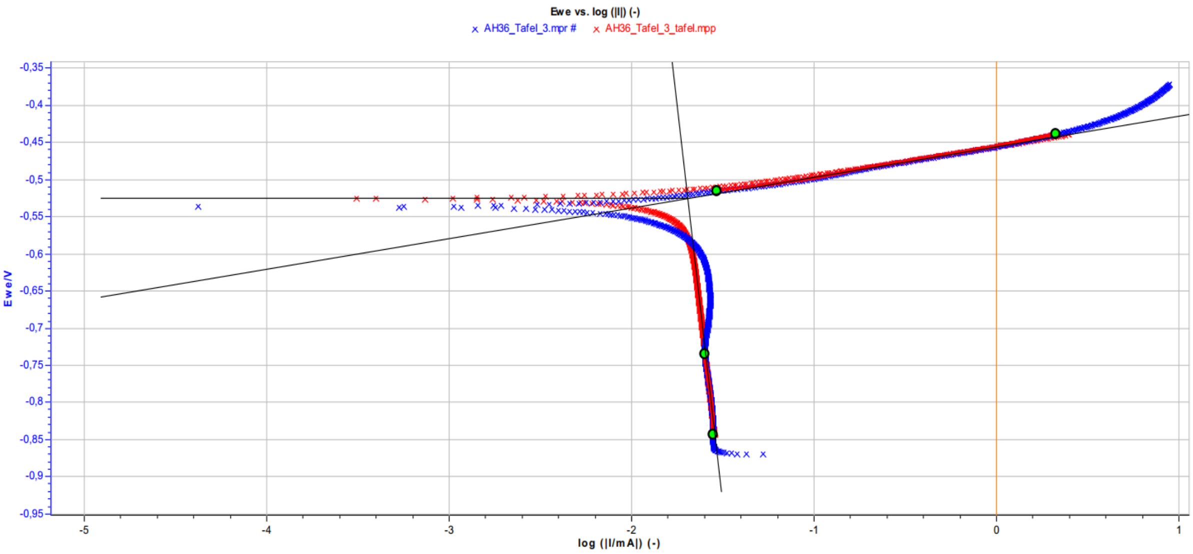

Fig.[12.37] Polarization curves and Tafel extrapolation method of parent metal **AH36**, exp.3.
Blue: AH36, **Red**: Tafel fitting via EC Lab.

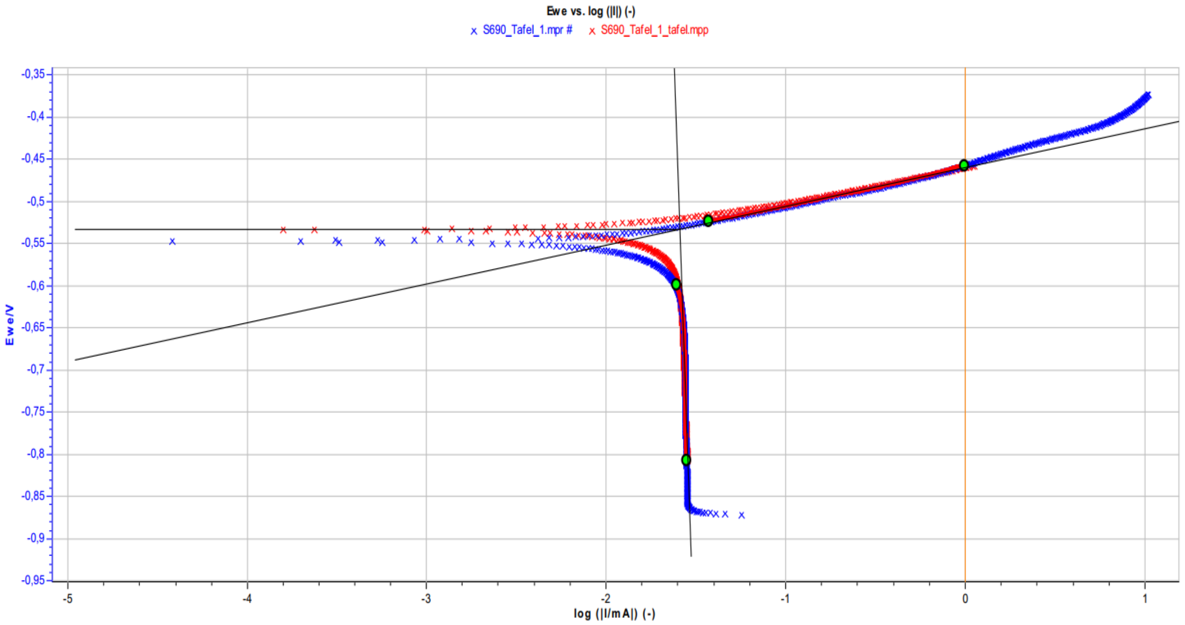

Fig.[12.38] Polarization curves and Tafel extrapolation method of parent metal **S690**, exp.1.
Blue: AH36, **Red**: Tafel fitting via EC Lab.

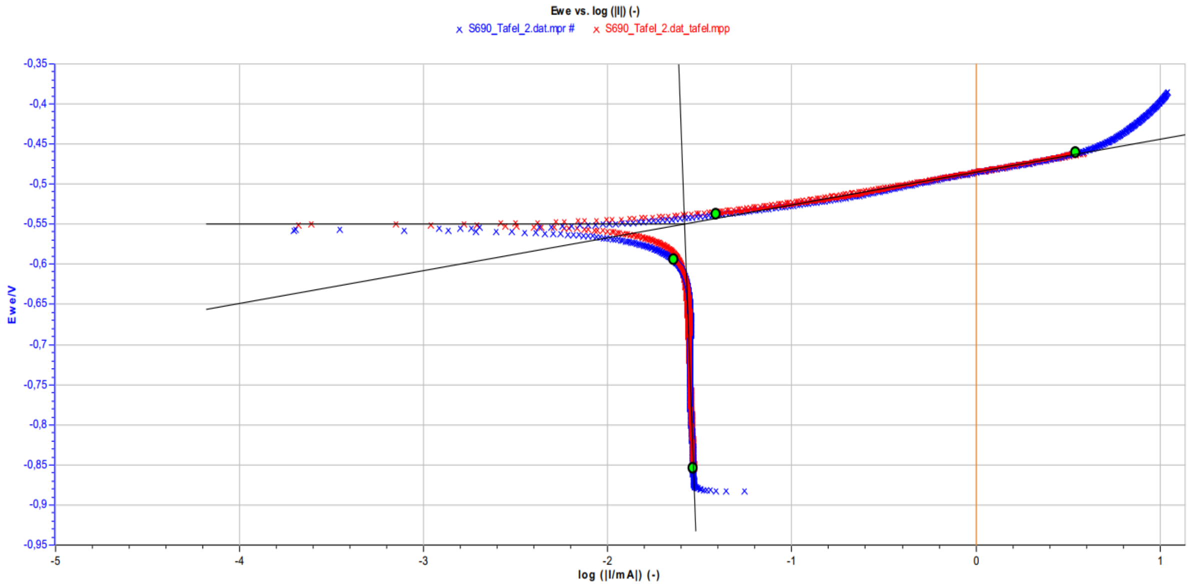

Fig.[12.39] Polarization curves and Tafel extrapolation method of parent metal **S690**, exp.2.
Blue: AH36, **Red**: Tafel fitting via EC Lab.

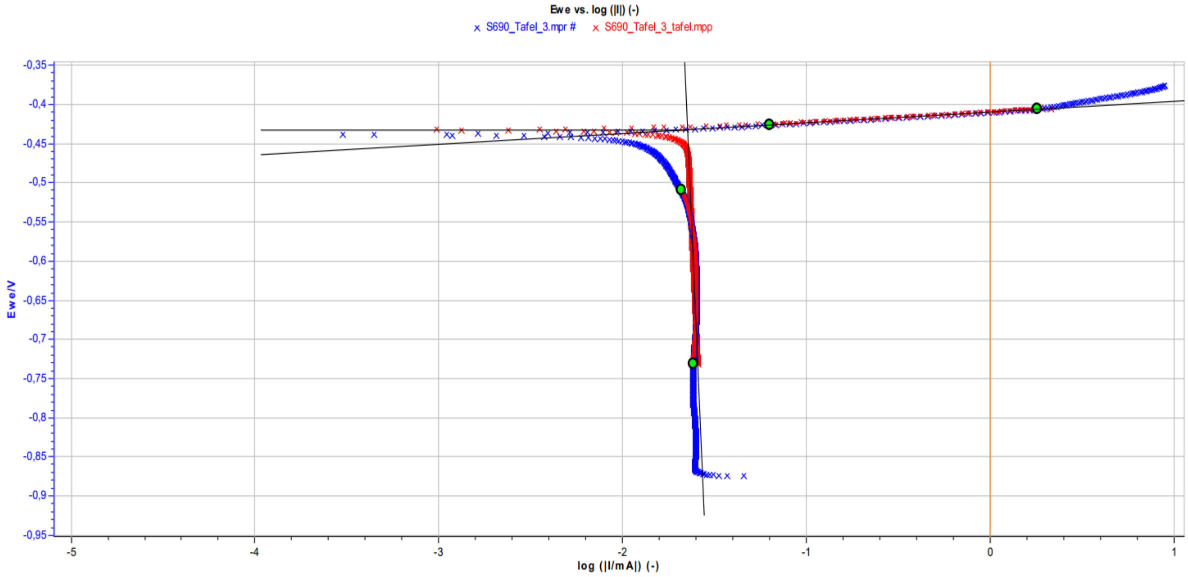

Fig.[12.40] Polarization curves and Tafel extrapolation method of parent metal **S690**, exp.3.
Blue: AH36, **Red**: Tafel fitting via EC Lab.

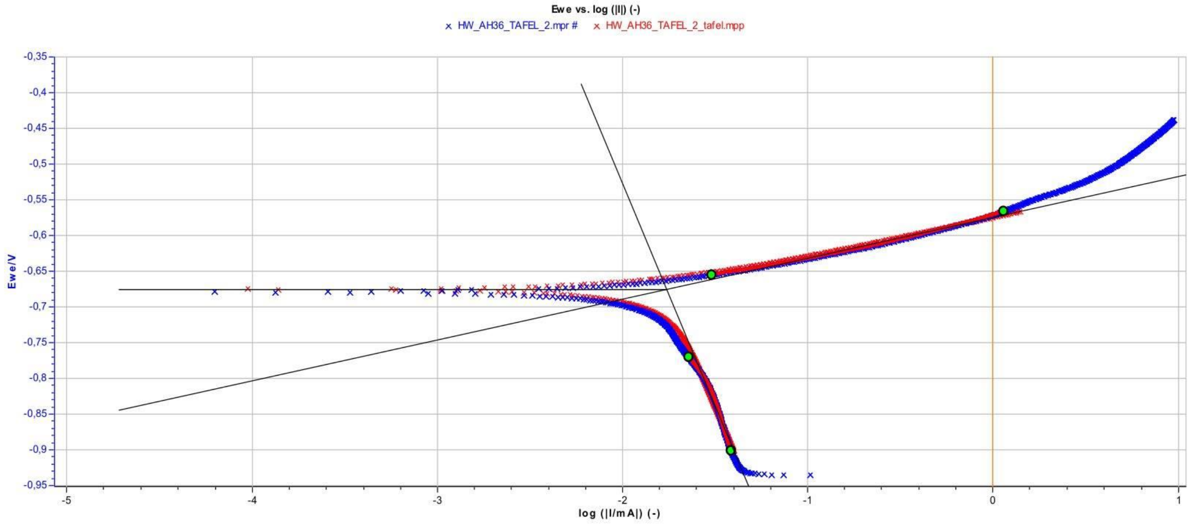

Fig.[12.41] Polarization curves and Tafel extrapolation method of homogeneous weldment **AH36-AH36**, exp.1. **Blue**: AH36, **Red**: Tafel fitting via EC Lab.

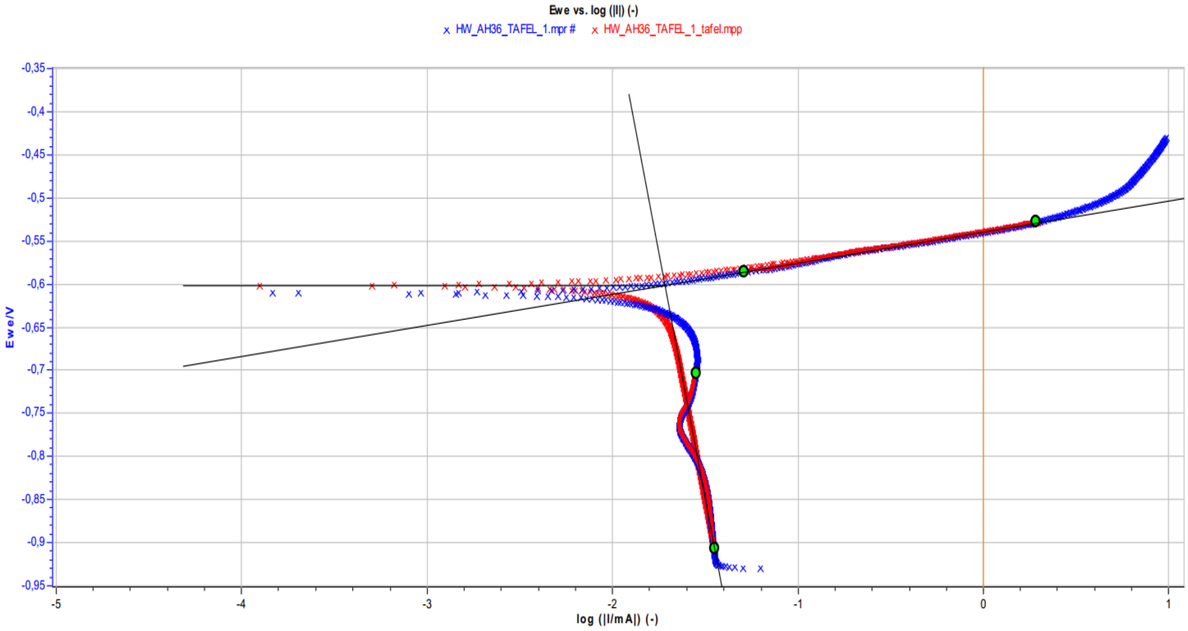

Fig.[12.42] Polarization curves and Tafel extrapolation method of homogeneous weldment **AH36-AH36**, exp.2. **Blue**: AH36, **Red**: Tafel fitting via EC Lab.

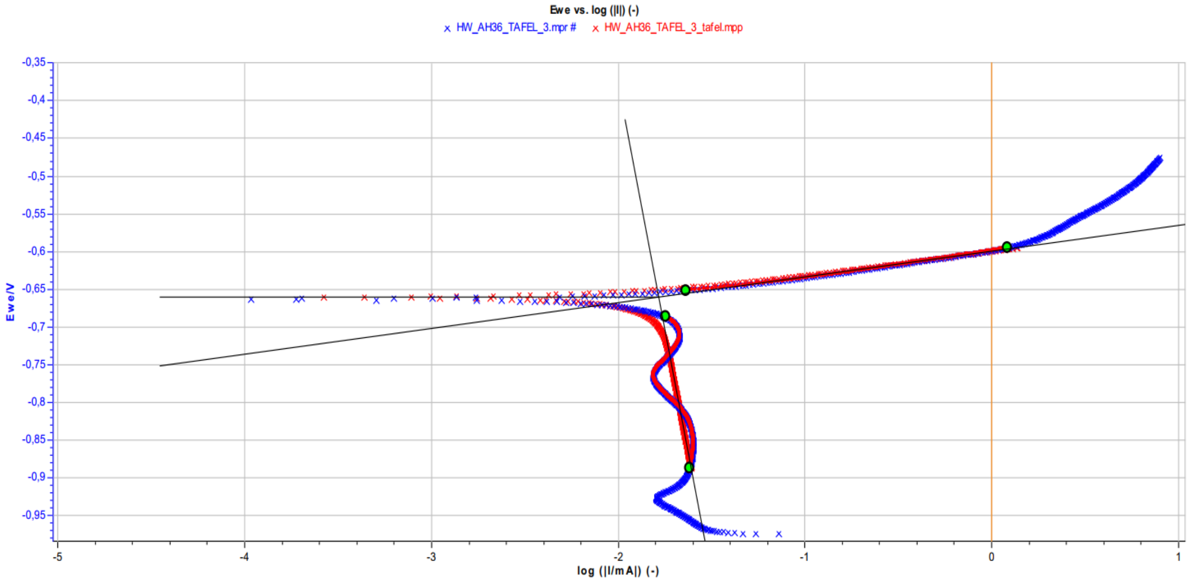

Fig.[12.43] Polarization curves and Tafel extrapolation method of homogeneous weldment **AH36-AH36**, exp.3. **Blue**: AH36, **Red**: Tafel fitting via EC Lab.

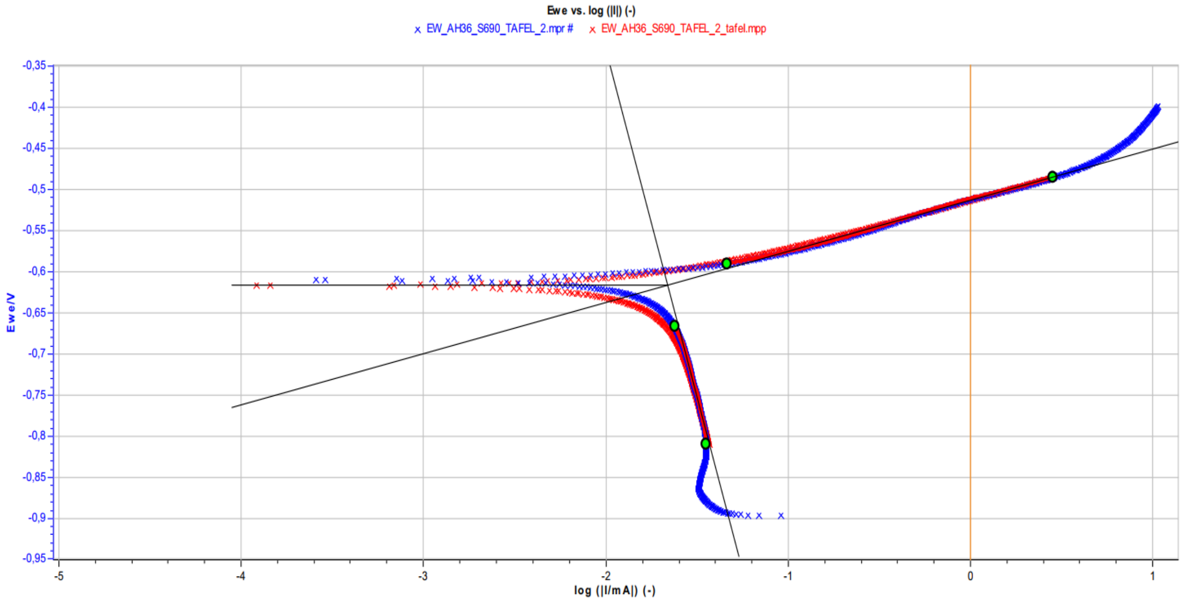

Fig.[12.44] Polarization curves and Tafel extrapolation method of heterogeneous weldment **AH36-S690**, exp.1. **Blue**: AH36, **Red**: Tafel fitting via EC Lab.

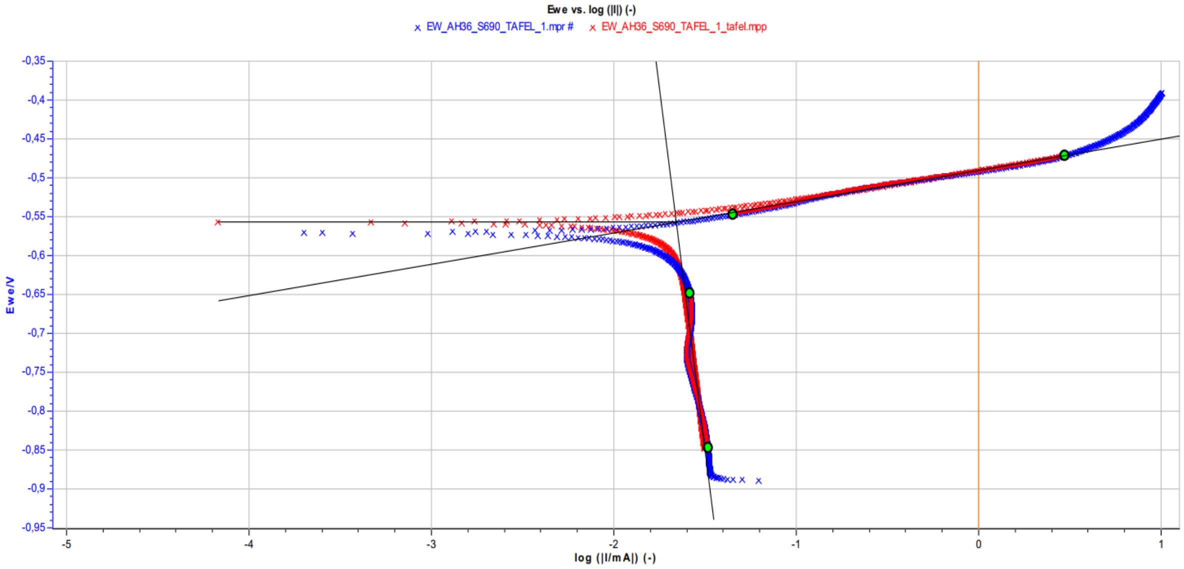

Fig.[12.45] Polarization curves and Tafel extrapolation method of heterogeneous weldment **AH36-S690**, exp.2. **Blue**: AH36, **Red**: Tafel fitting via EC Lab.

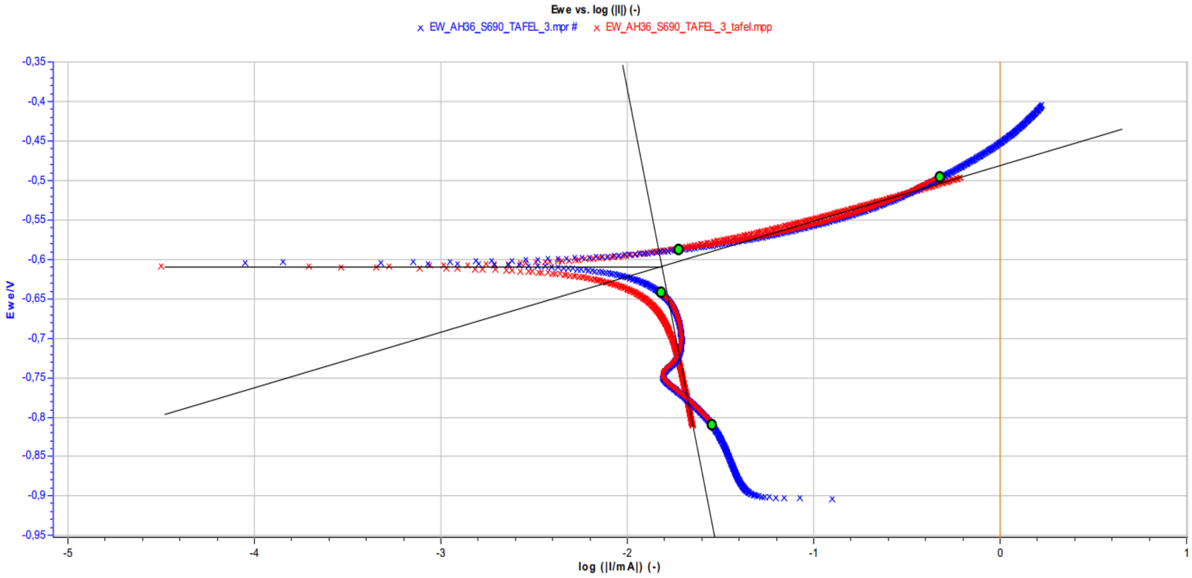

Fig.[12.46] Polarization curves and Tafel extrapolation method of heterogeneous weldment **AH36-S690**, exp.3. **Blue**: AH36, **Red**: Tafel fitting via EC Lab.

12.2.3. Electrochemical Impedance Spectroscopy

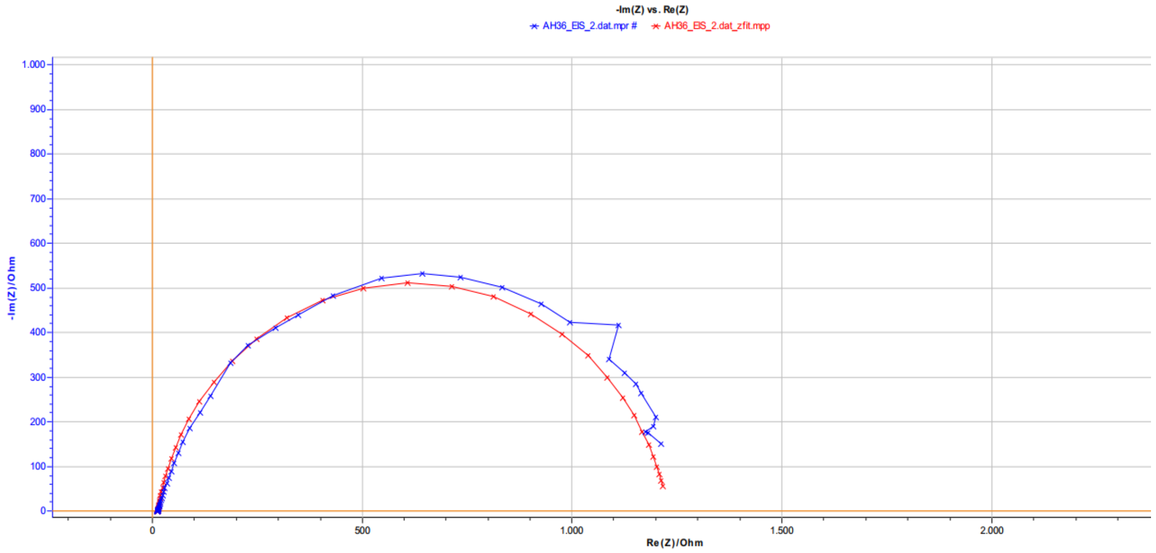

Fig.[12.47] Nyquist plot for parent metal **AH36**, exp.1.

Blue: data experiment, **Red:** Nyquist fitting.

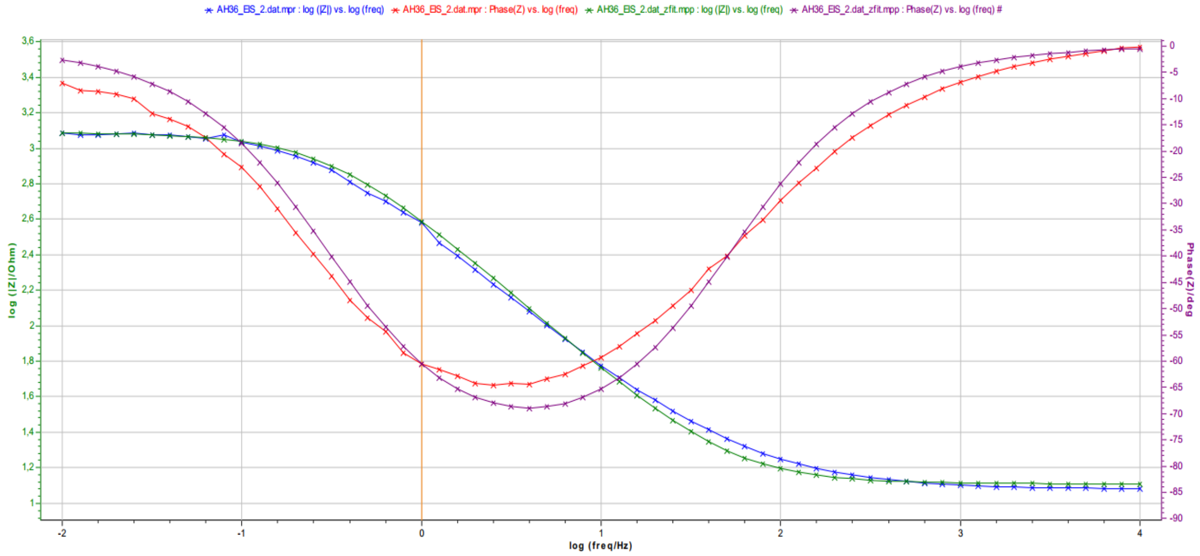

Fig.[12.48] Bode plots for parent metal **AH36**, exp. 1.

Blue: experiment data of log(|Z|), **Green:** fitting.

Red: experiment data of θ, **Purple:** Bode fitting.

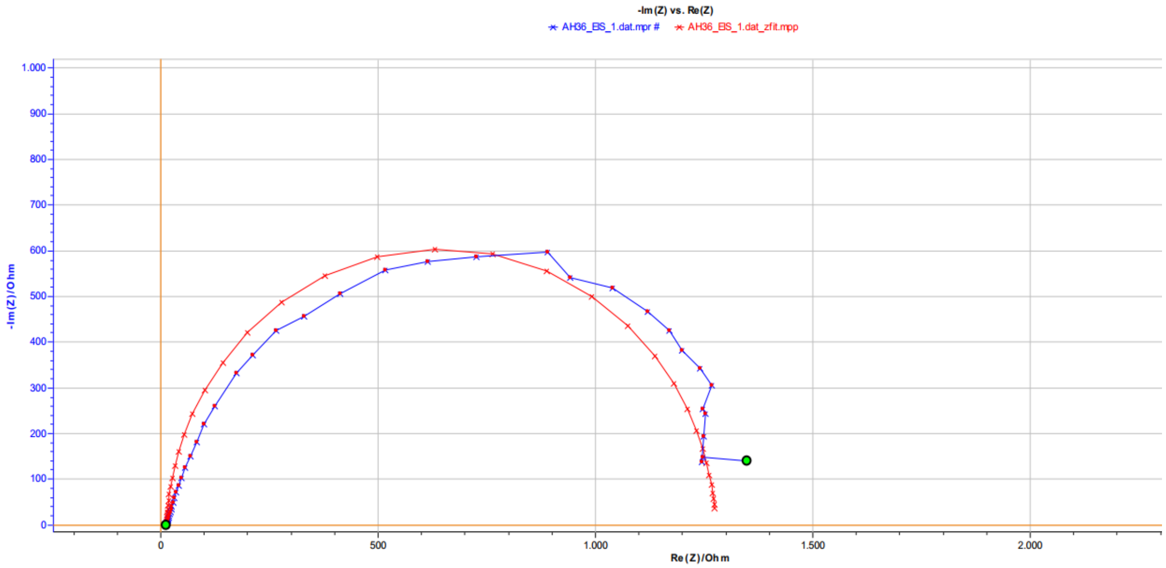

Fig.[12.49] Nyquist plot for parent metal **AH36**, exp.2.
Blue: data experiment, **Red:** Nyquist fitting.

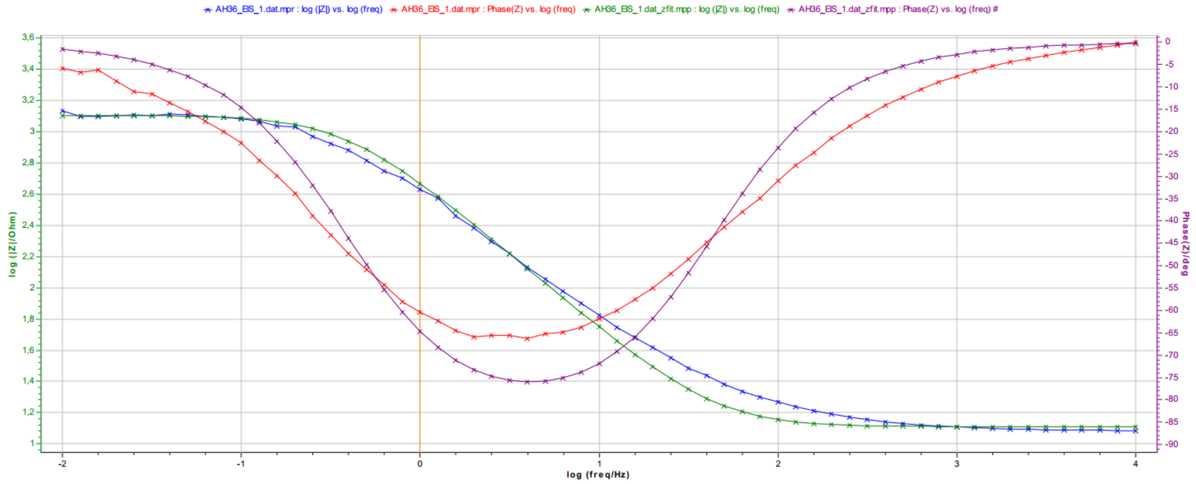

Fig.[12.50] Bode plots for parent metal **AH36**, exp.2.

Blue: experiment data of log(|Z|), **Green:** fitting.

Red: experiment data of θ, **Purple:** Bode fitting.

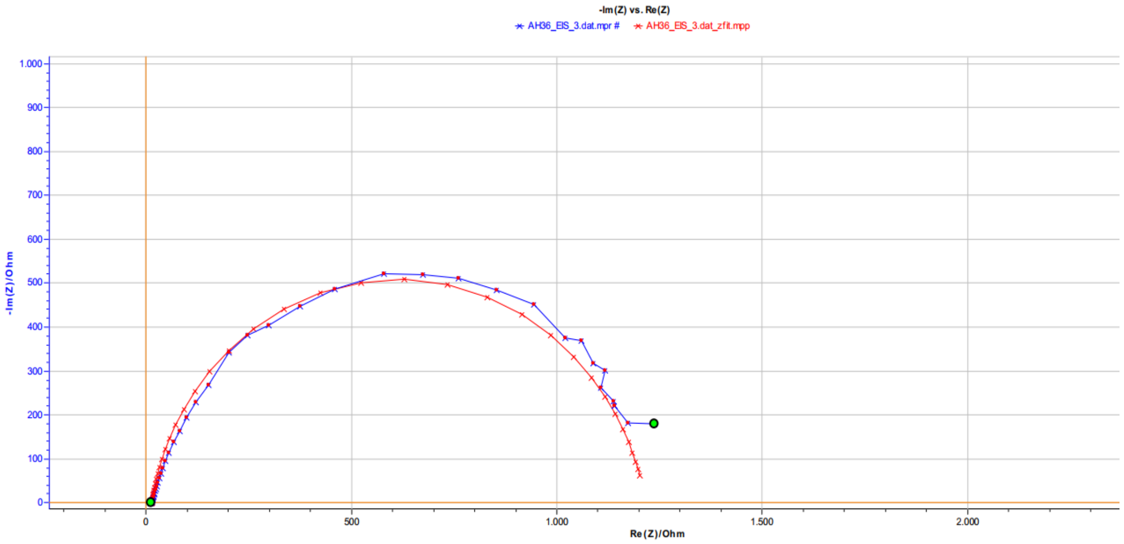

Fig.[12.51] Nyquist plot for parent metal **AH36**, exp.3.
Blue: data experiment, **Red:** Nyquist fitting.

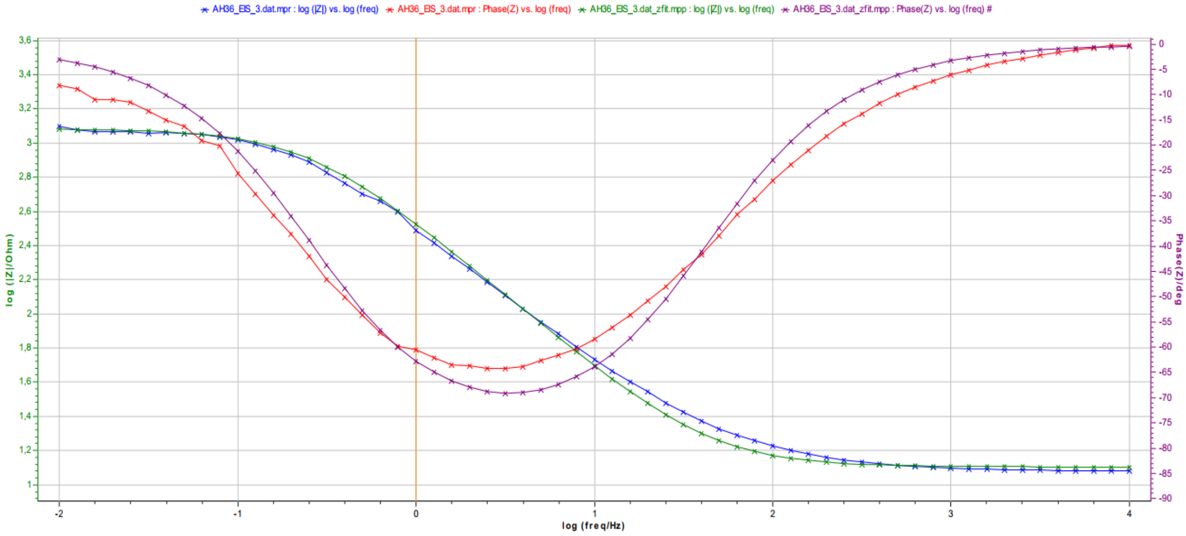

Fig.[12.52] Bode plots for parent metal **AH36**, exp. 3.

Blue: experiment data of log(|Z|), **Green:** fitting.

Red: experiment data of θ, **Purple:** Bode fitting.

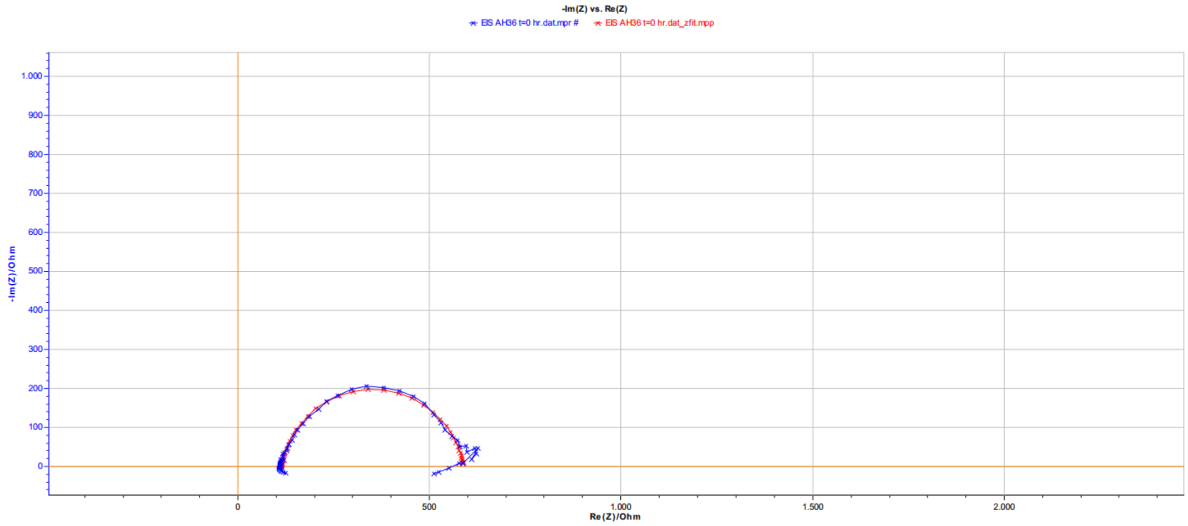

Fig.[12.53] Nyquist plot for the 2^{nd} series of parent metal **AH36**, t=0.
Blue: data experiment, **Red:** Nyquist fitting.

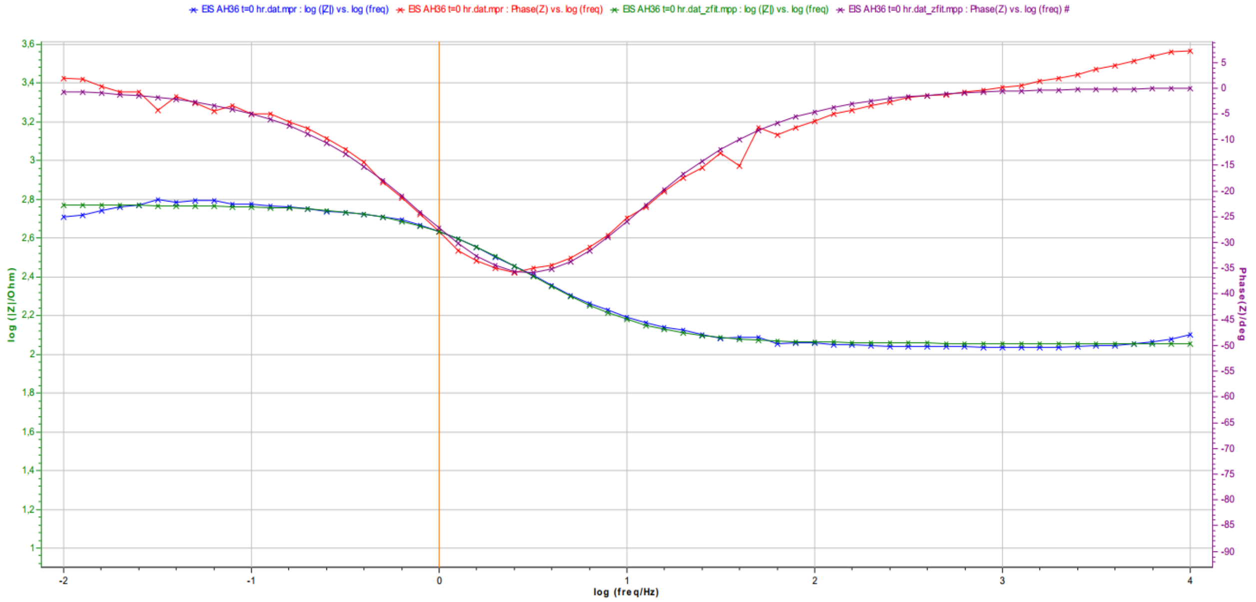

Fig.[12.54] Bode plots for the 2^{nd} series of parent metal **AH36**, t=0.

Blue: experiment data of log(|Z|), **Green:** fitting.

Red: experiment data of θ, **Purple:** Bode fitting.

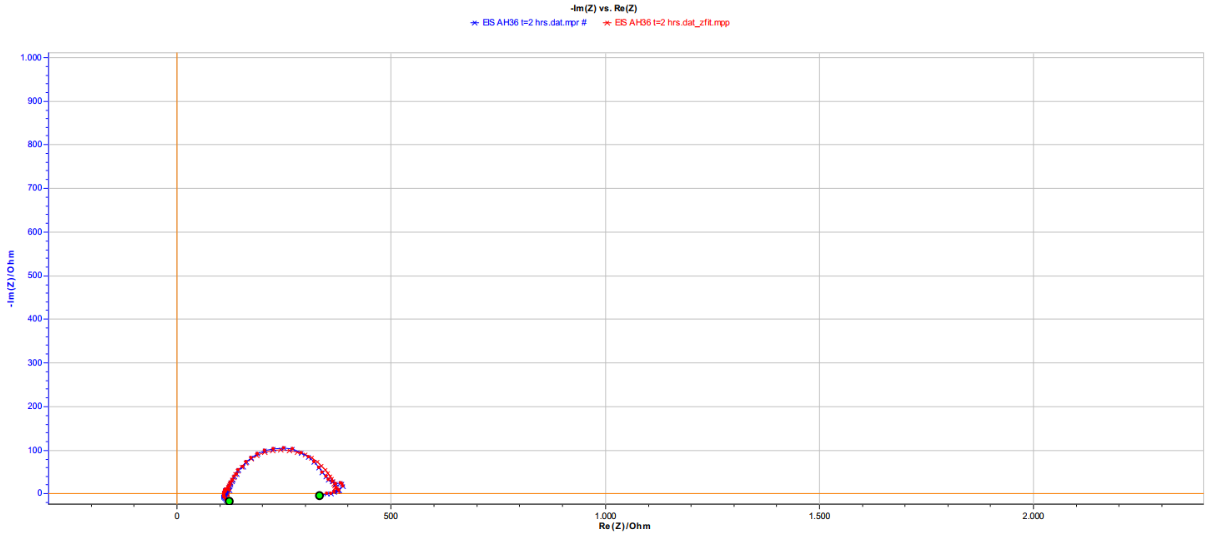

Fig.[12.55] Nyquist plot for the 2nd series of parent metal **AH36**, t=2 hrs.
Blue: data experiment, **Red:** Nyquist fitting.

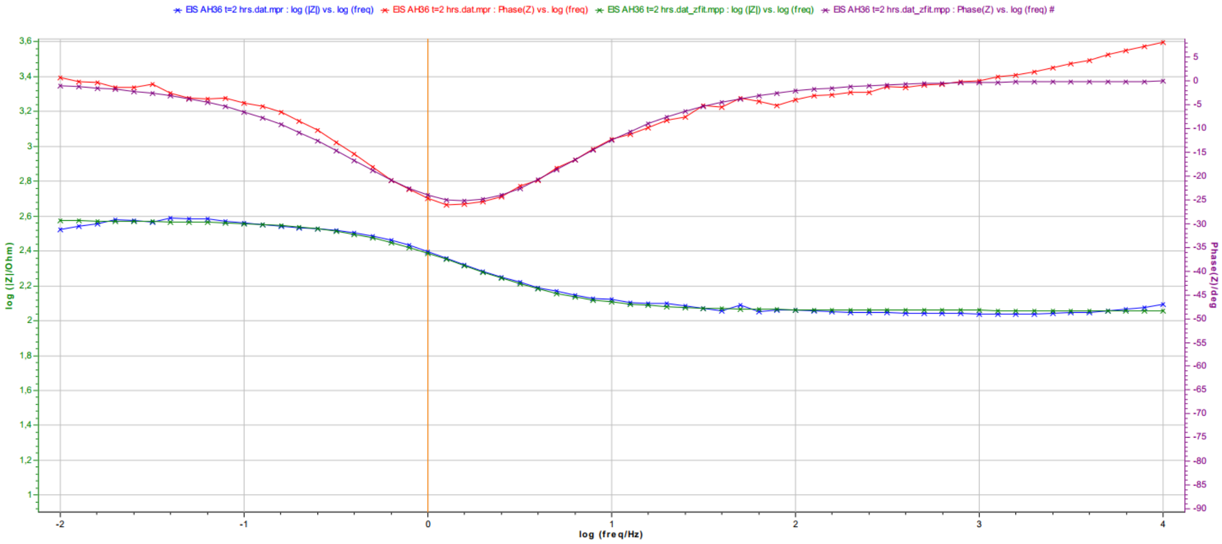

Fig.[12.56] Bode plots for the 2nd series of parent metal **AH36**, t=2 hrs.

Blue: experiment data of log(|Z|), **Green:** fitting.

Red: experiment data of θ, **Purple:** Bode fitting.

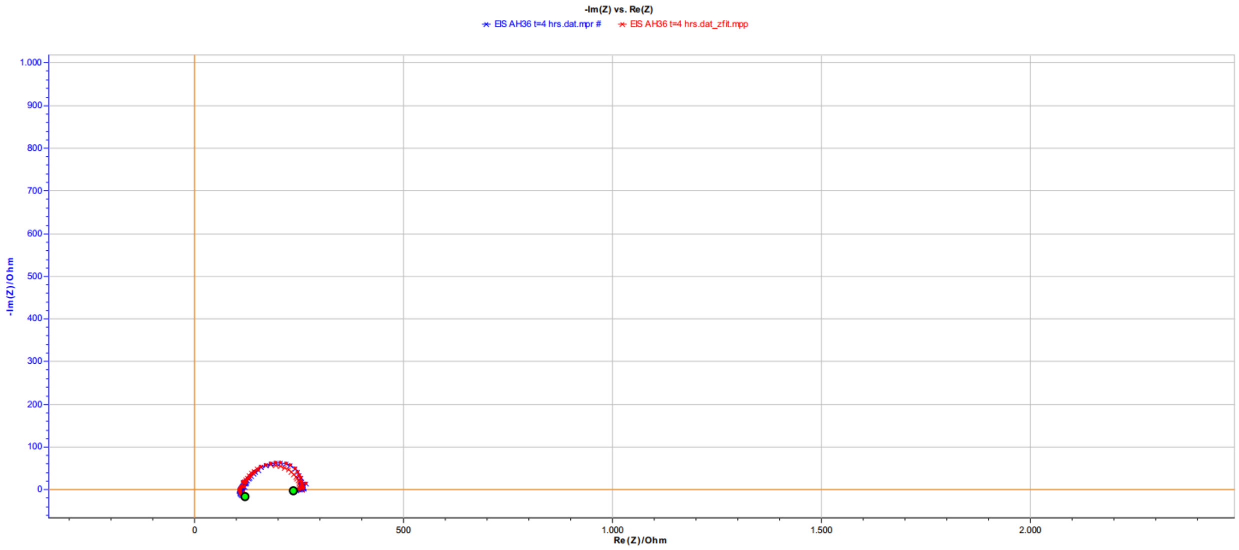

Fig.[12.57] Nyquist plot for the 2nd series of parent metal **AH36**, t=4 hrs.
Blue: data experiment, **Red:** Nyquist fitting.

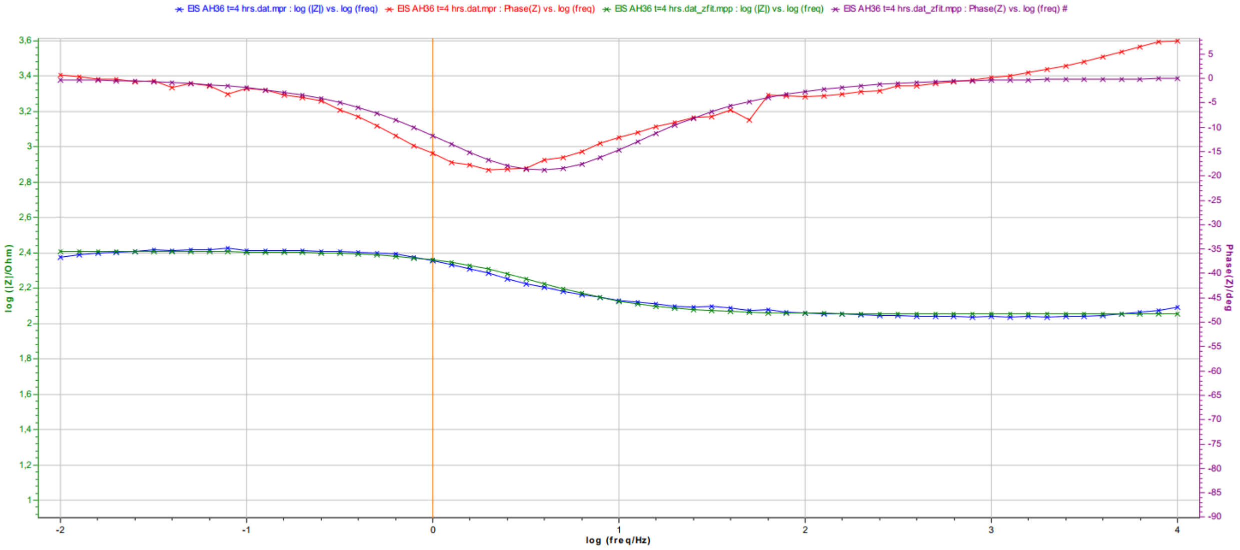

Fig.[12.58] Bode plots for the 2nd series of parent metal **AH36**, t=4 hrs.

Blue: experiment data of log(|Z|), **Green:** fitting.

Red: experiment data of θ, **Purple:** Bode fitting.

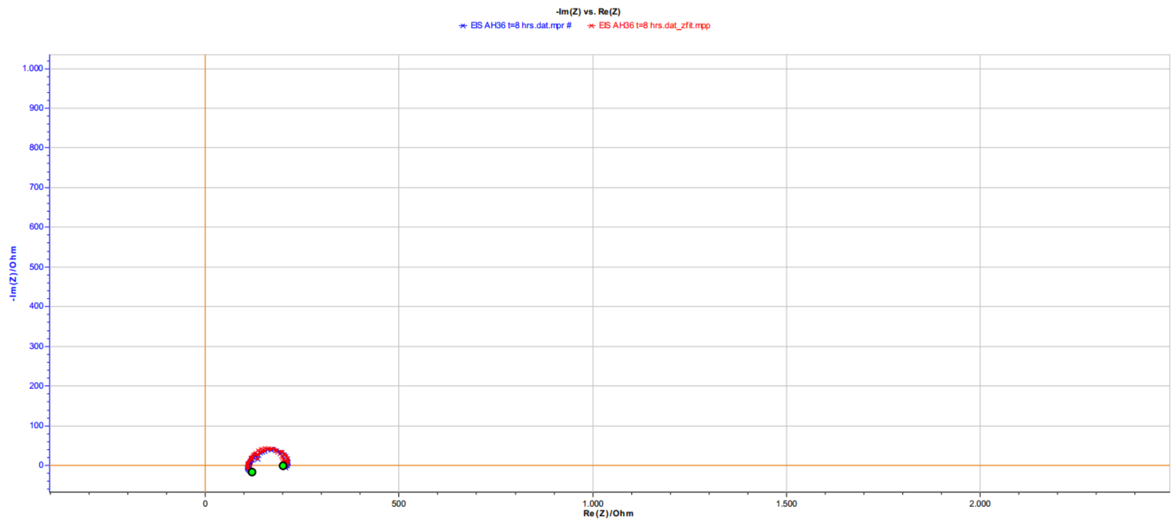

Fig.[12.59] Nyquist plot for the 2nd series of parent metal **AH36**, t=8 hrs.
Blue: data experiment, **Red:** Nyquist fitting.

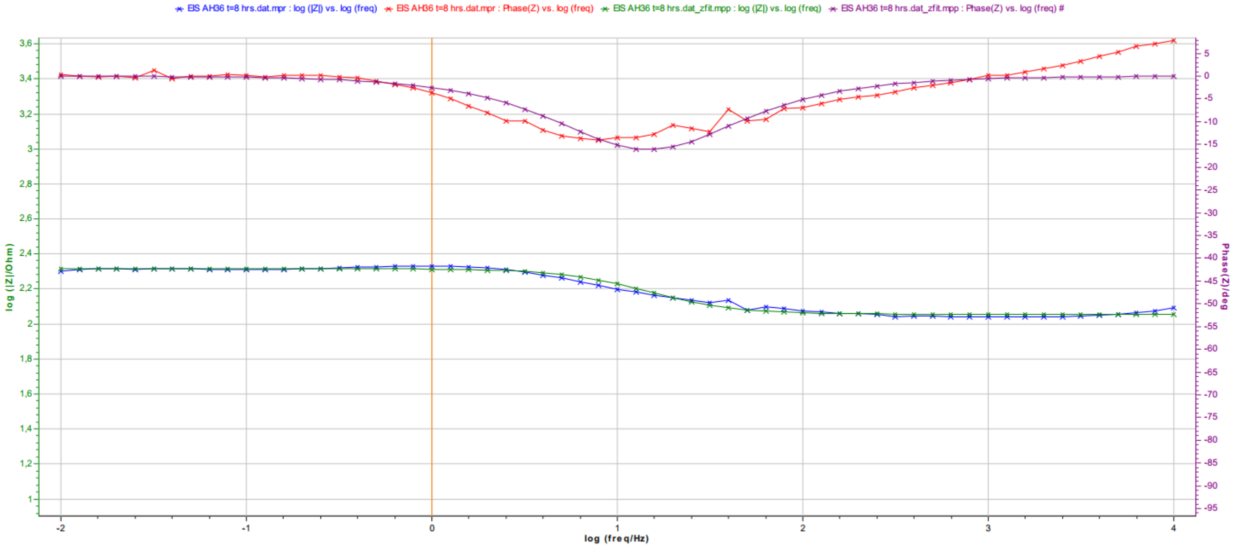

Fig.[12.60] Bode plots for the 2nd series of parent metal **AH36**, t=8 hrs.

Blue: experiment data of log(|Z|), **Green:** fitting.

Red: experiment data of θ, **Purple:** Bode fitting.

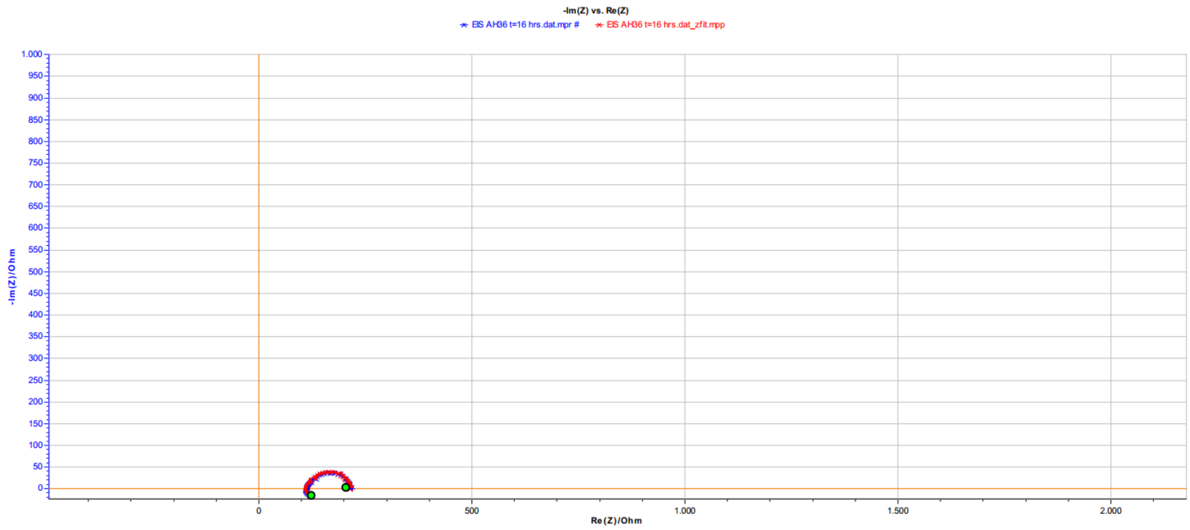

Fig.[12.61] Nyquist plot for the 2nd series of parent metal **AH36**, t=16 hrs.
Blue: data experiment, **Red:** Nyquist fitting.

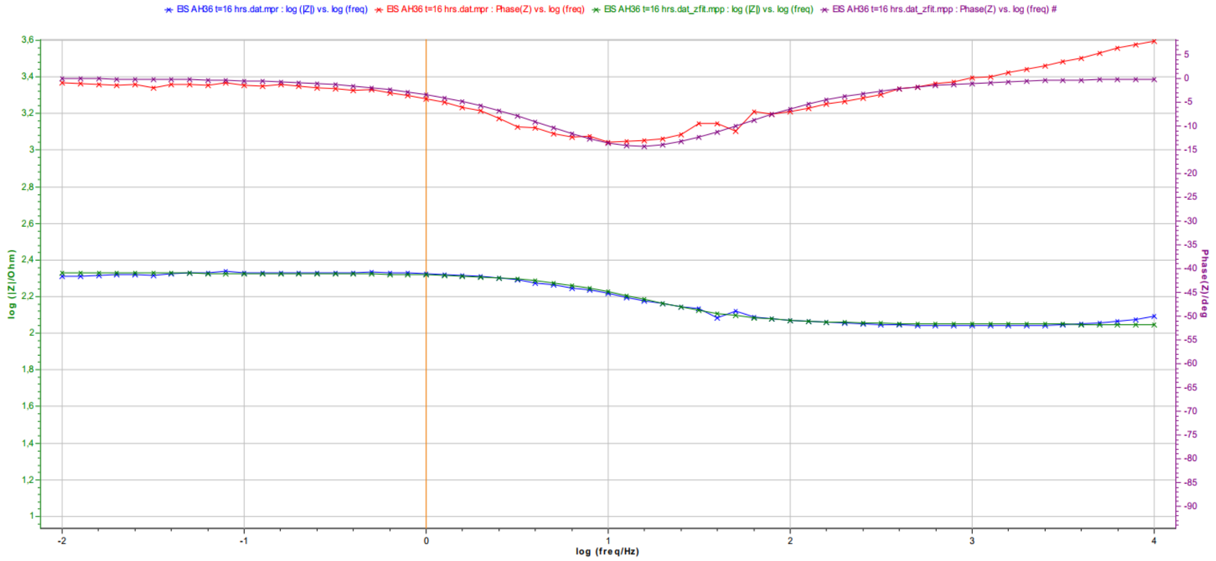

Fig.[12.62] Bode plots for the 2nd series of parent metal **AH36**, t=16 hrs.

Blue: experiment data of log(|Z|), **Green:** fitting.

Red: experiment data of θ, **Purple:** Bode fitting.

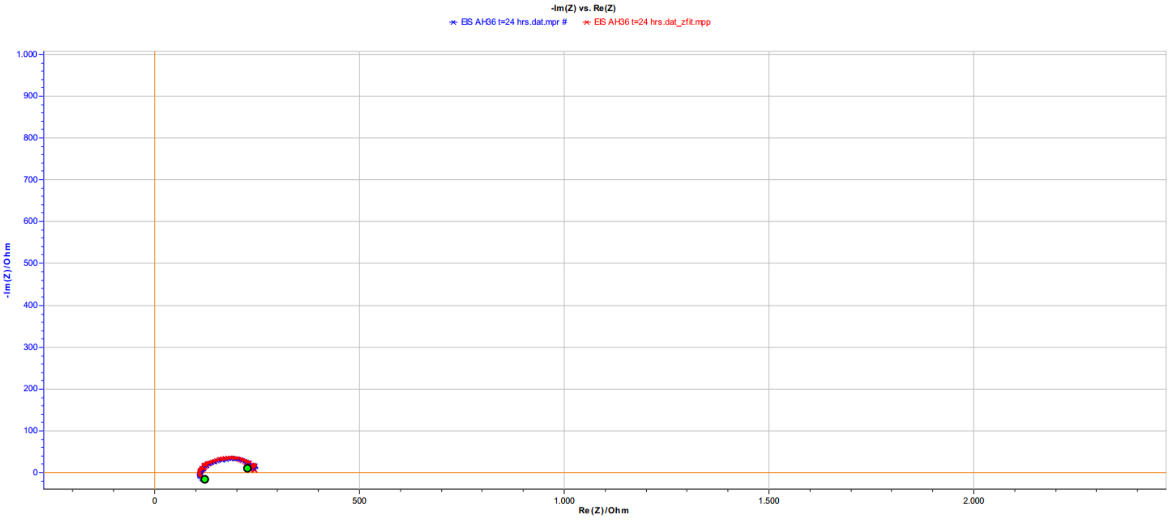

Fig.[12.63] Nyquist plot for the 2nd series of parent metal **AH36**, t=24 hrs.
Blue: data experiment, **Red:** Nyquist fitting.

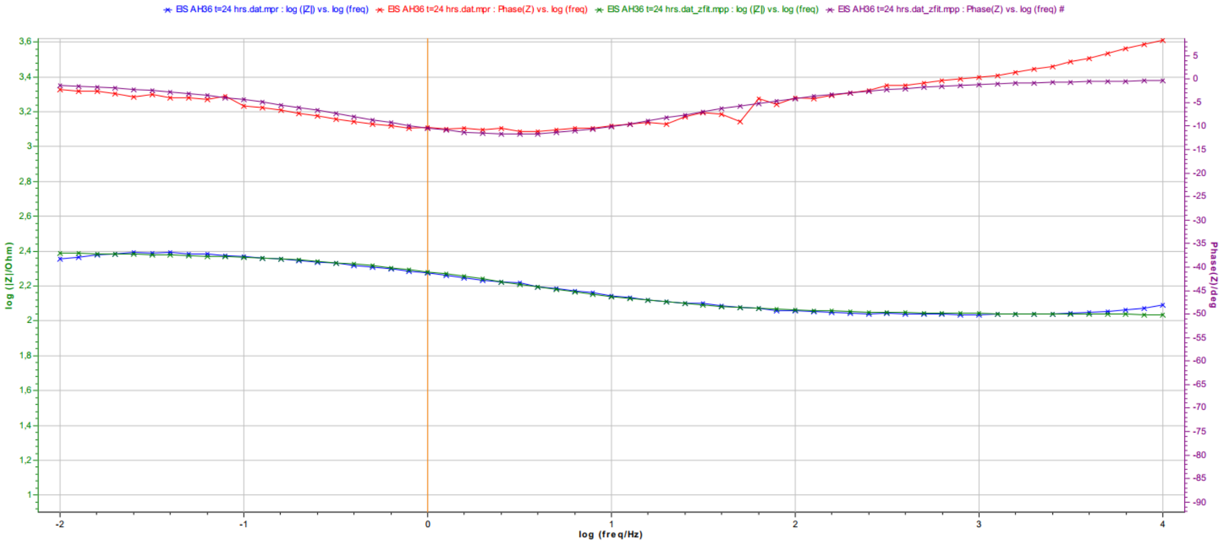

Fig.[12.64] Bode plots for the 2nd series of parent metal **AH36**, t=24 hrs.

Blue: experiment data of log(|Z|), **Green:** fitting.

Red: experiment data of θ, **Purple:** Bode fitting.

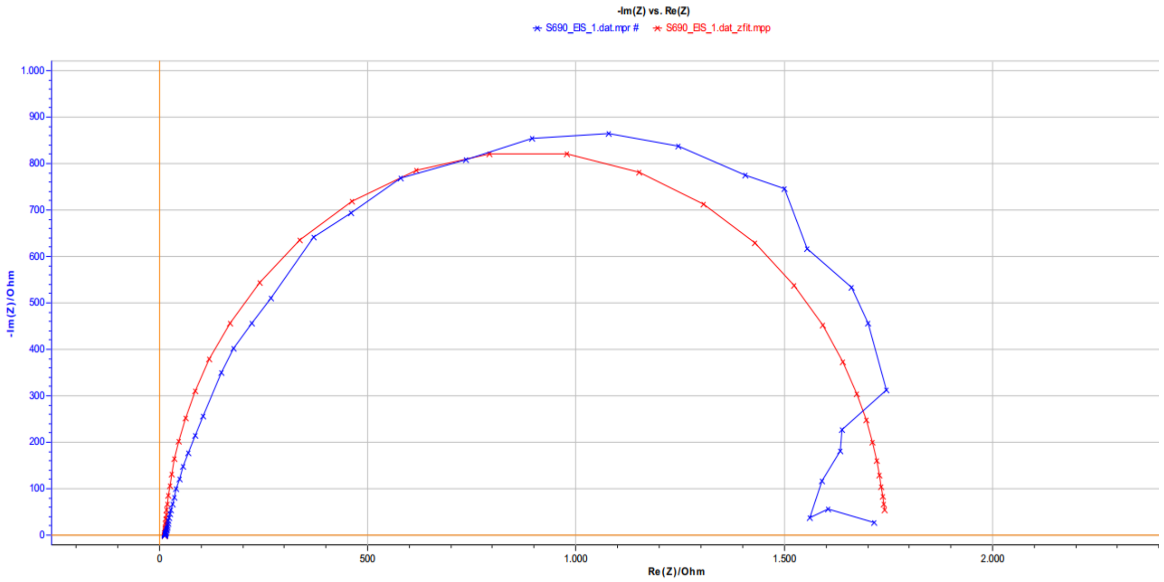

Fig.[12.65] Nyquist plot for parent metal **S690**, exp.1.

Blue: data experiment, **Red:** Nyquist fitting.

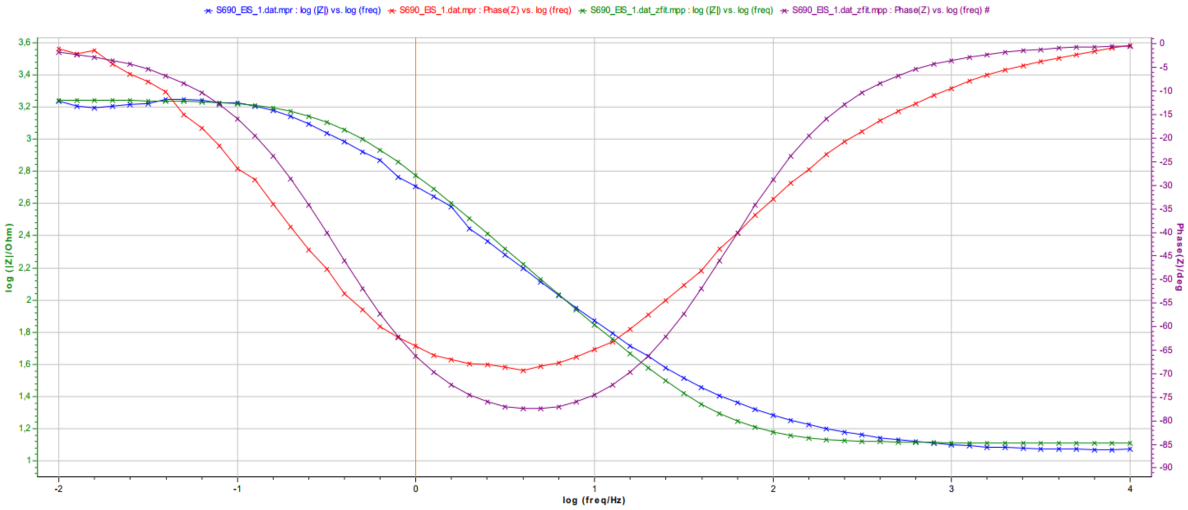

Fig.[12.66] Bode plots for parent metal **S690**, exp. 1.

Blue: experiment data of log(|Z|), **Green:** fitting.

Red: experiment data of θ, **Purple:** Bode fitting.

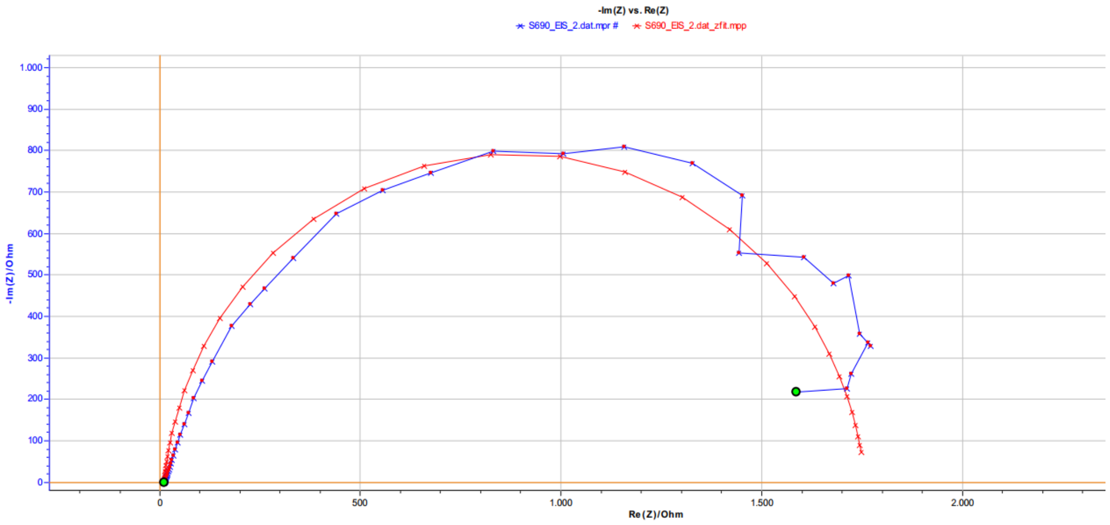

Fig.[12.67] Nyquist plot for parent metal **S690**, exp.2.
Blue: data experiment, **Red:** Nyquist fitting.

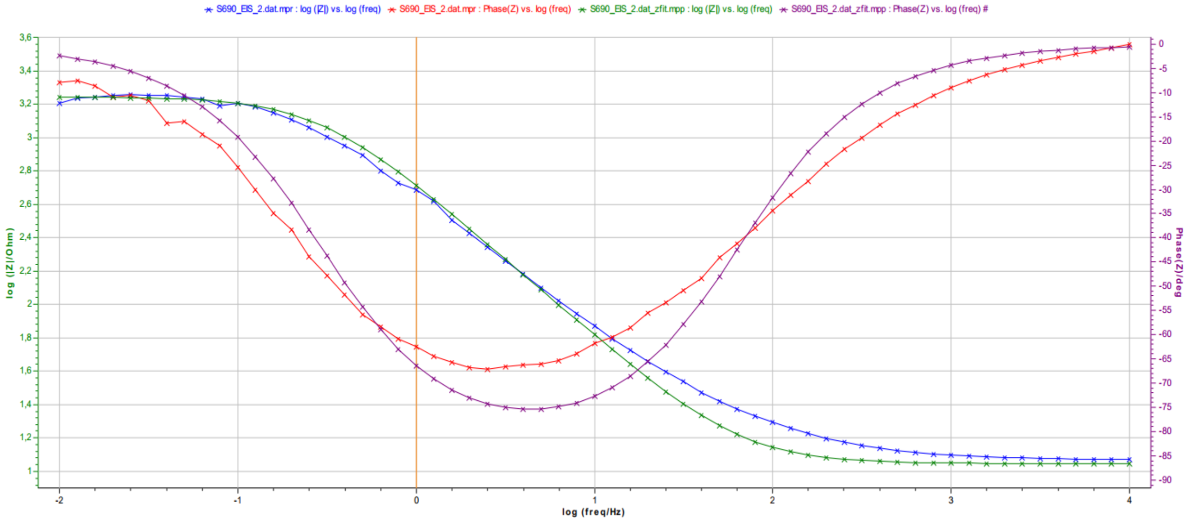

Fig.[12.68] Bode plots for parent metal **S690**, exp. 2.

Blue: experiment data of log(|Z|), **Green:** fitting.

Red: experiment data of θ, **Purple:** Bode fitting.

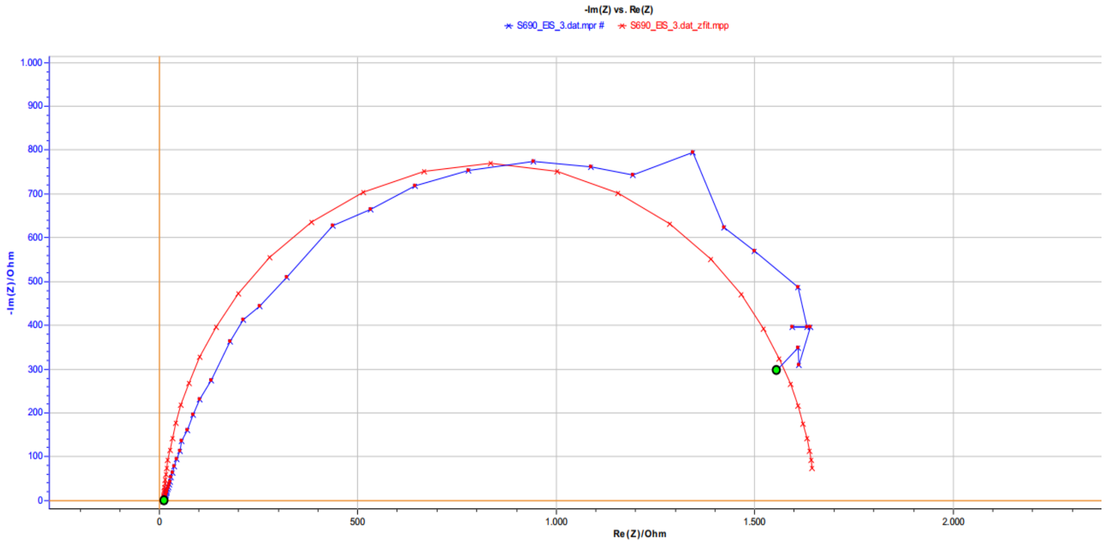

Fig.[12.69] Nyquist plot for parent metal **S690**, exp.3.
Blue: data experiment, **Red:** Nyquist fitting.

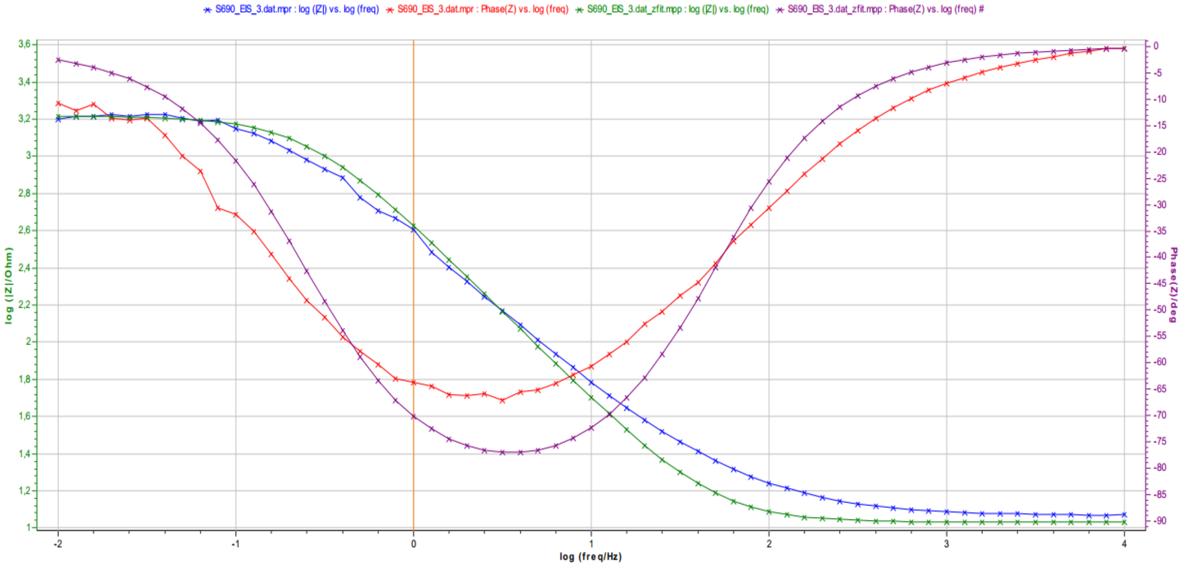

Fig.[12.70] Bode plots for parent metal **S690**, exp. 3.

Blue: experiment data of log(|Z|), **Green:** fitting.

Red: experiment data of θ, **Purple:** Bode fitting.

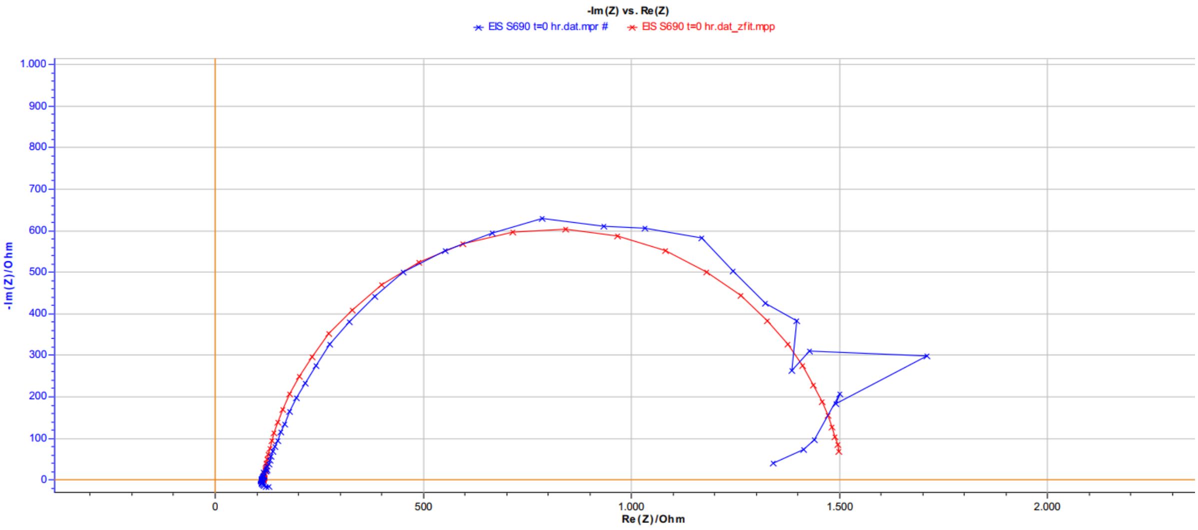

Fig.[12.71] Nyquist plot for the 2nd series of parent metal **S690**, t=0.
Blue: data experiment, **Red:** Nyquist fitting.

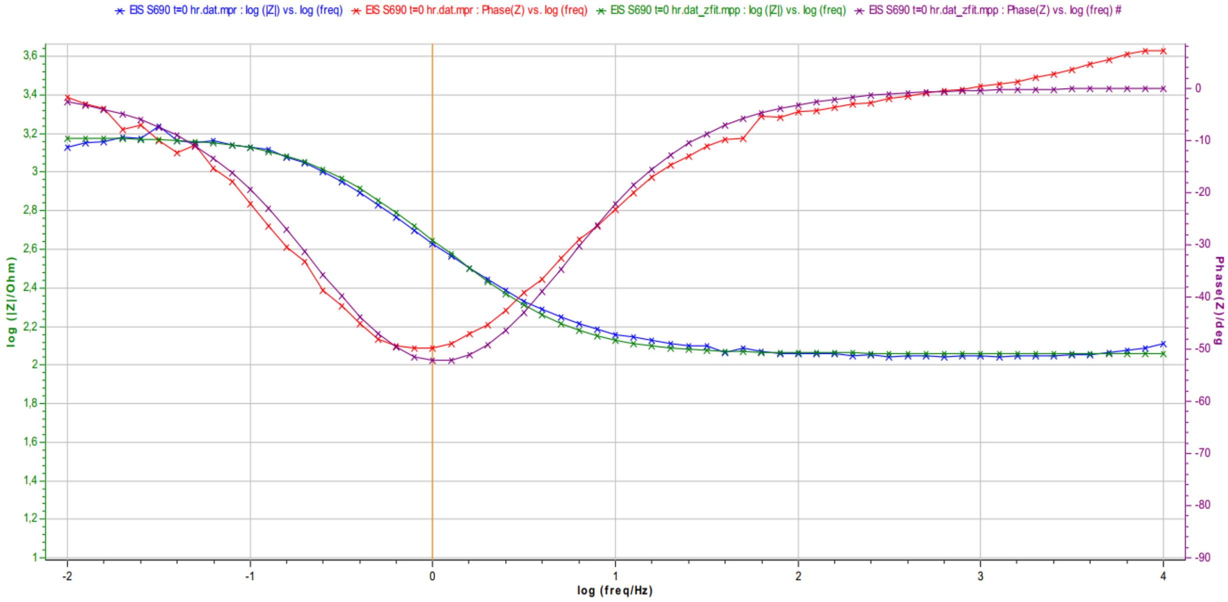

Fig.[12.72] Bode plots for the 2nd series of parent metal **S690**, t=0.

Blue: experiment data of log(|Z|), **Green:** fitting.

Red: experiment data of θ, **Purple:** Bode fitting.

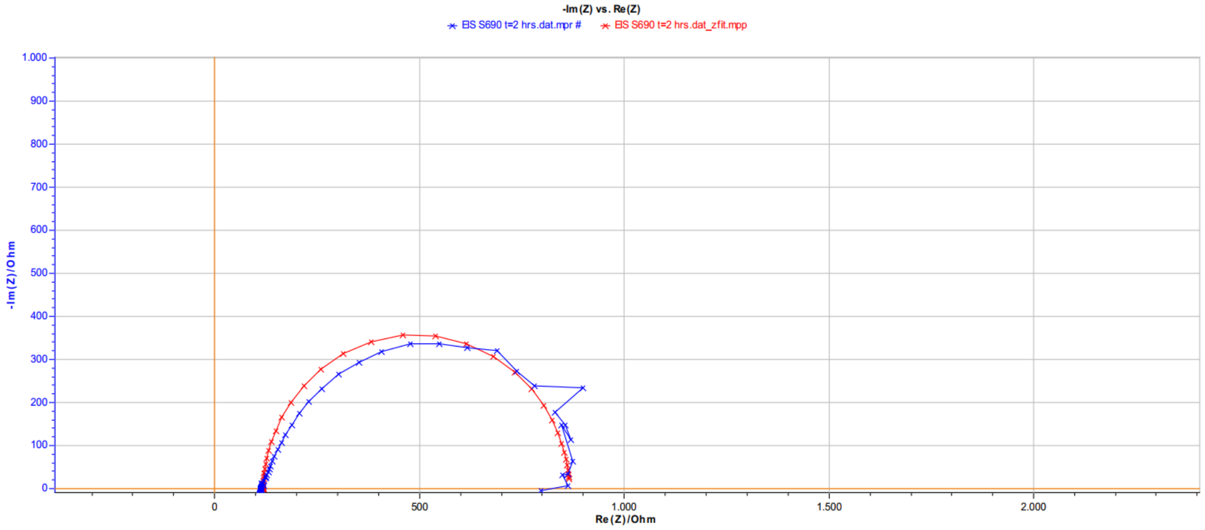

Fig.[12.73] Nyquist plot for the 2nd series of parent metal **S690**, t=2 hrs.
Blue: data experiment, **Red:** Nyquist fitting.

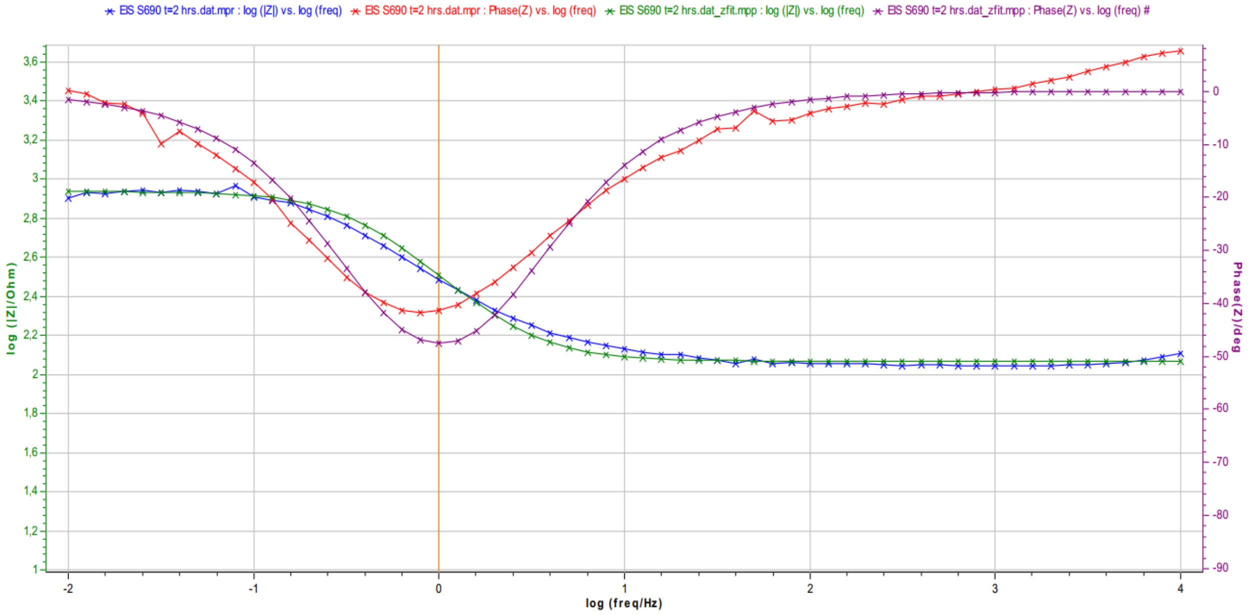

Fig.[12.74] Bode plots for the 2nd series of parent metal **S690**, t=2 hrs.

Blue: experiment data of log(|Z|), **Green:** fitting.

Red: experiment data of θ, **Purple:** Bode fitting.

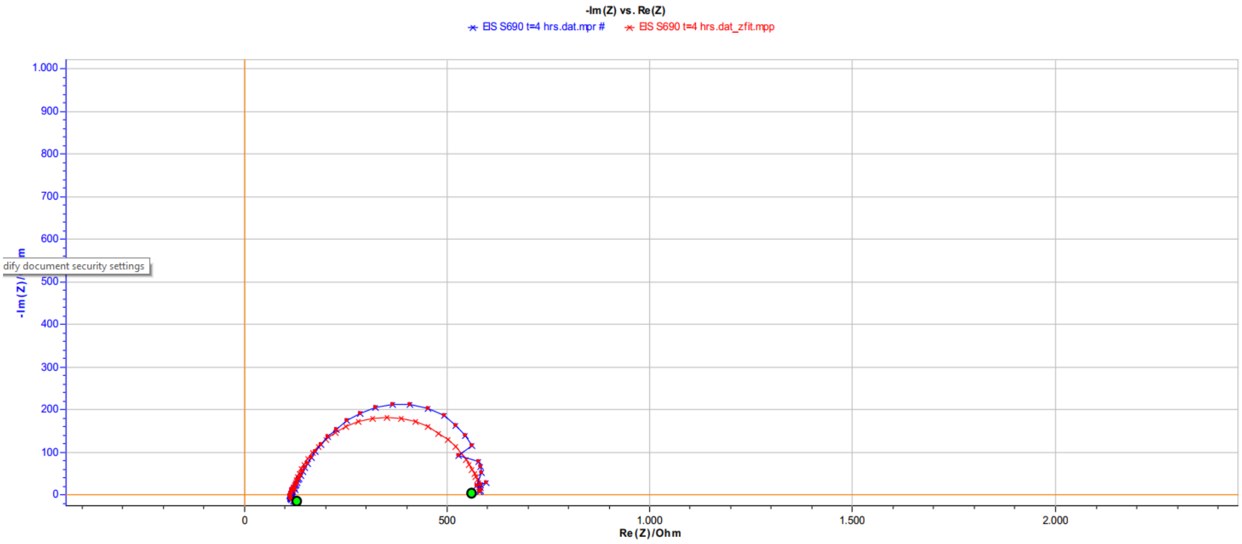

Fig.[12.75] Nyquist plot for the 2nd series of parent metal **S690**, t=4 hrs.
Blue: data experiment, **Red:** Nyquist fitting.

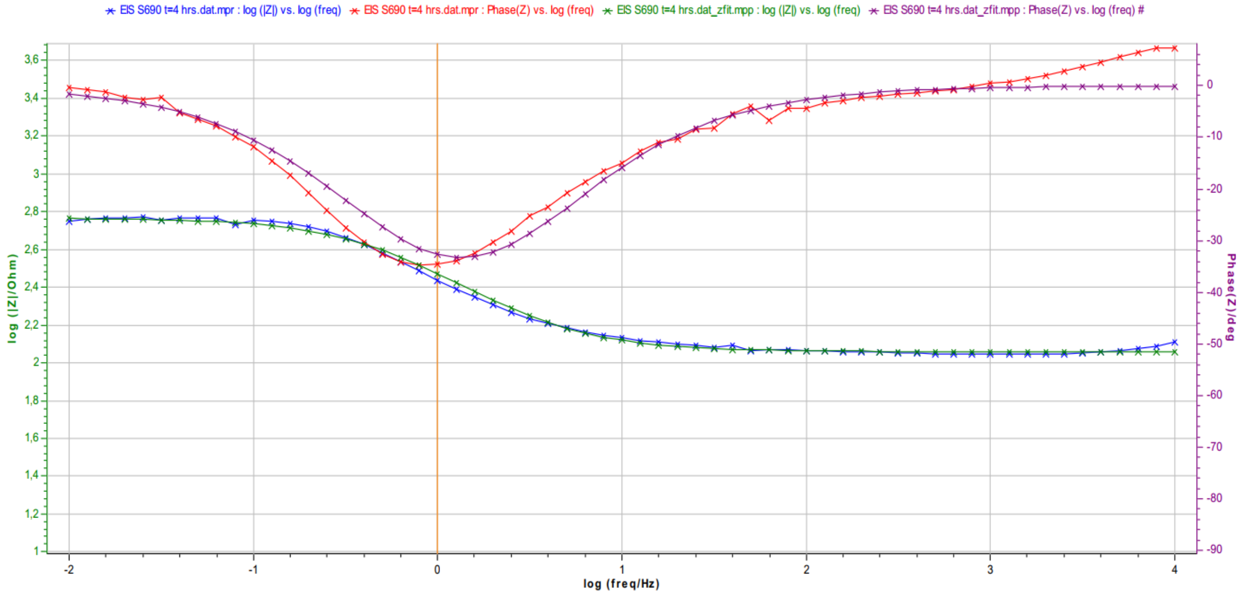

Fig.[12.76] Bode plots for the 2nd series of parent metal **S690**, t=4 hrs.

Blue: experiment data of log(|Z|), **Green:** fitting.

Red: experiment data of θ, **Purple:** Bode fitting.

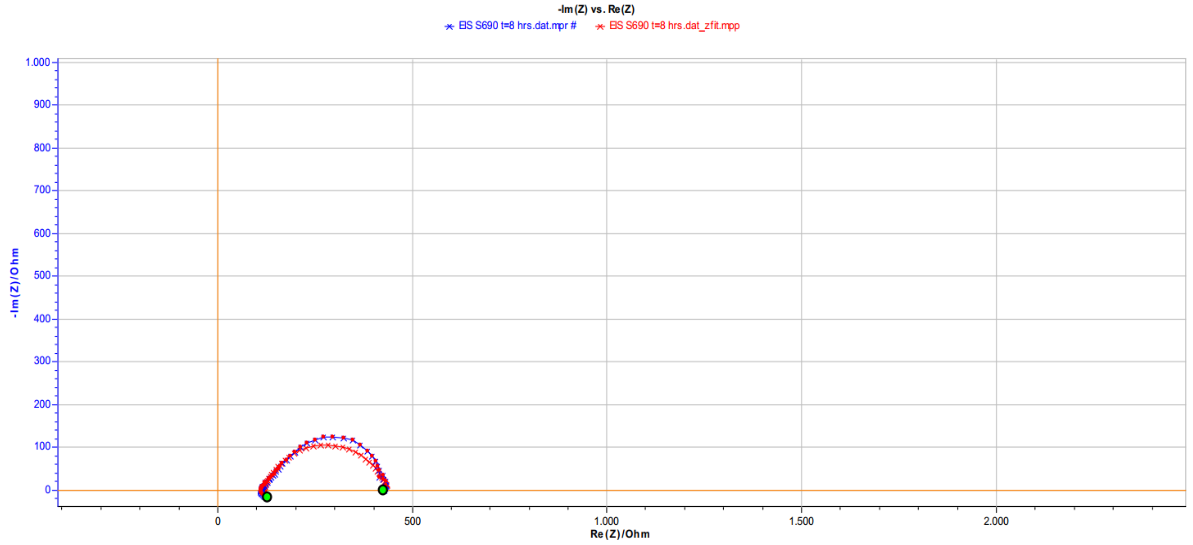

Fig.[12.77] Nyquist plot for the 2nd series of parent metal **S690**, t=8 hrs.
Blue: data experiment, **Red:** Nyquist fitting.

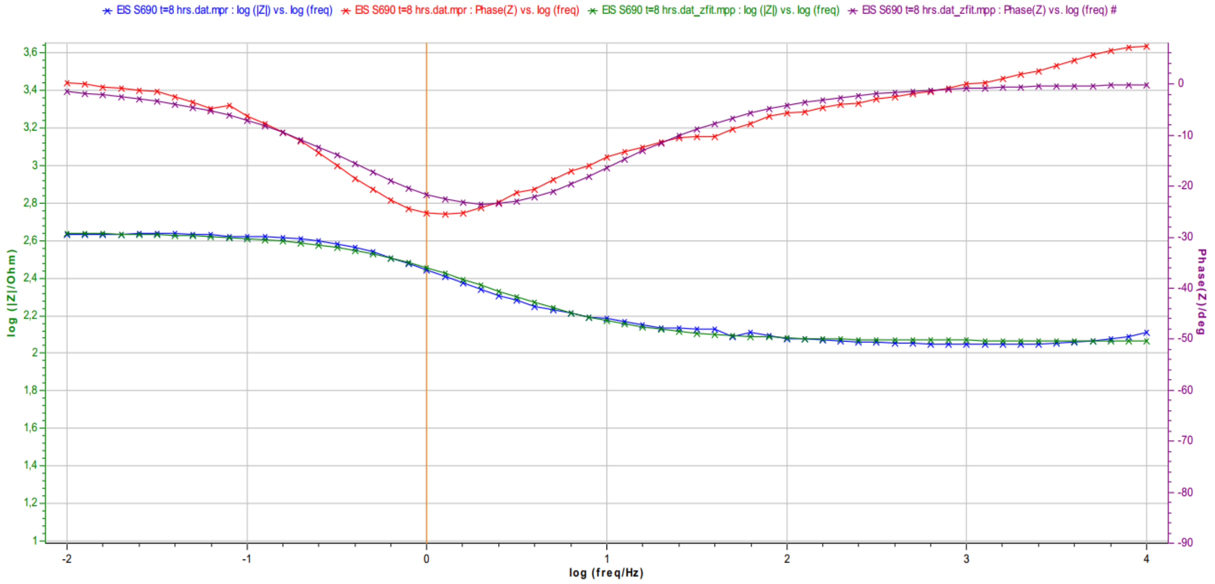

Fig.[12.78] Bode plots for the 2nd series of parent metal **S690**, t=8 hrs.

Blue: experiment data of log(|Z|), **Green:** fitting.

Red: experiment data of θ, **Purple:** Bode fitting.

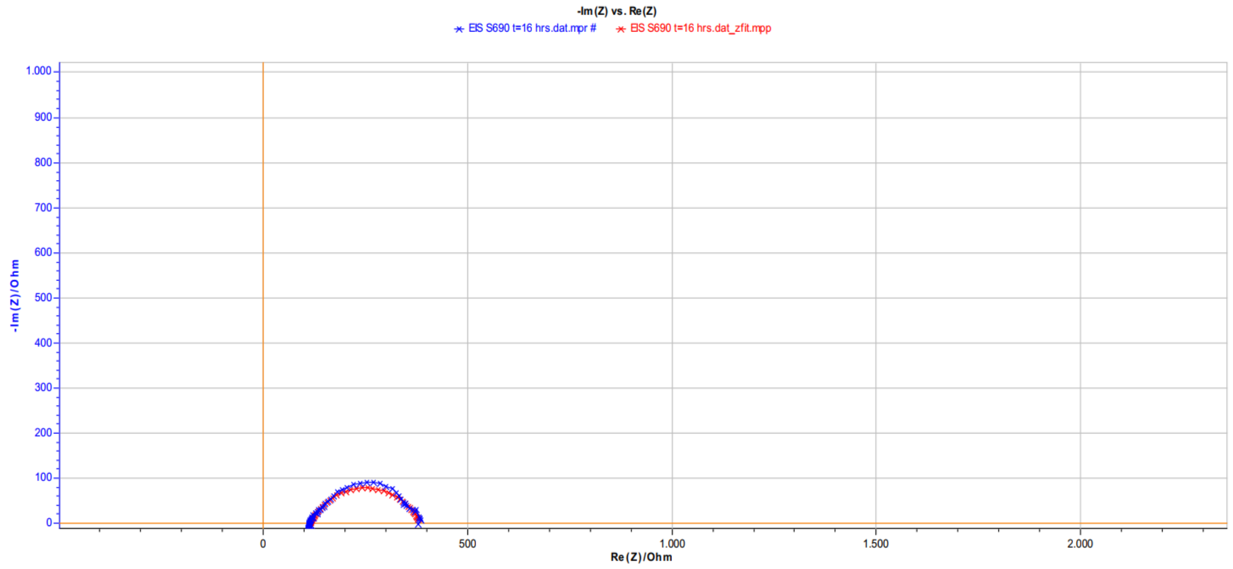

Fig.[12.79] Nyquist plot for the 2nd series of parent metal **S690**, t=16 hrs.
Blue: data experiment, **Red:** Nyquist fitting.

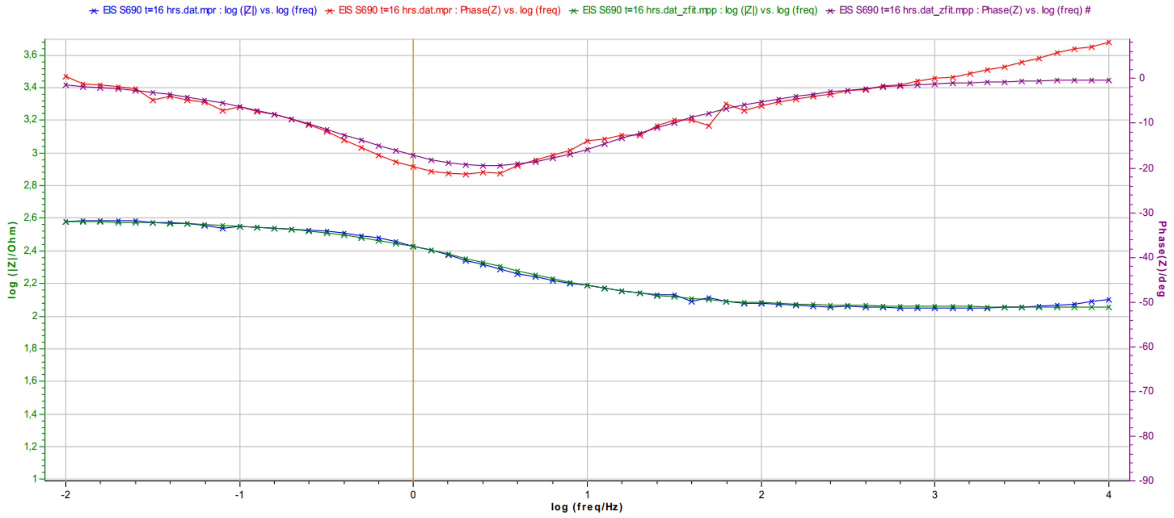

Fig.[12.80] Bode plots for the 2nd series of parent metal **S690**, t=16 hrs.

Blue: experiment data of log(|Z|), **Green:** fitting.

Red: experiment data of θ, **Purple:** Bode fitting.

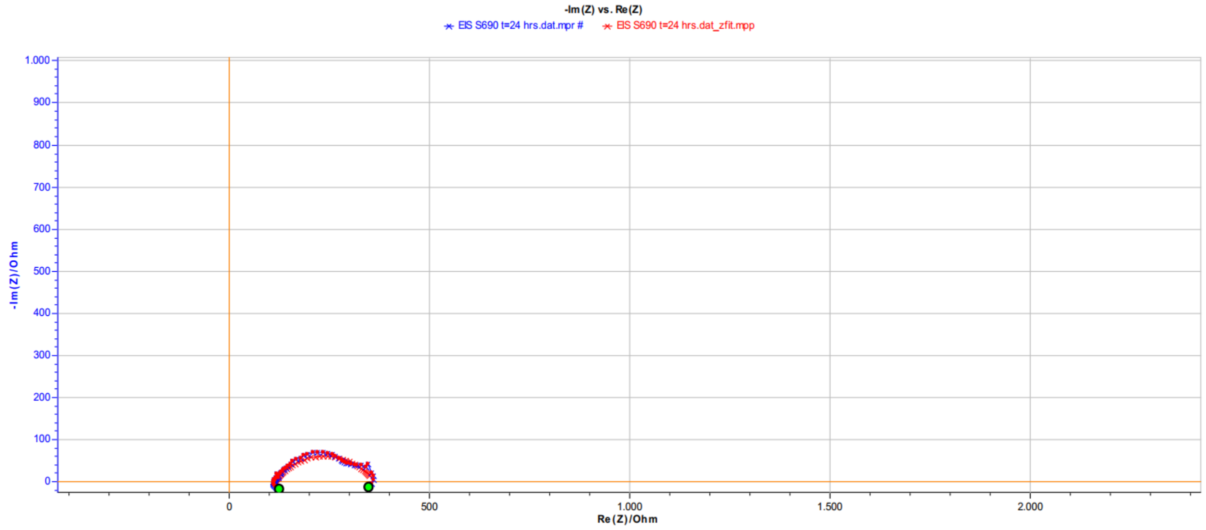

Fig.[12.81] Nyquist plot for the 2nd series of parent metal **S690**, t=24 hrs.
Blue: data experiment, **Red:** Nyquist fitting.

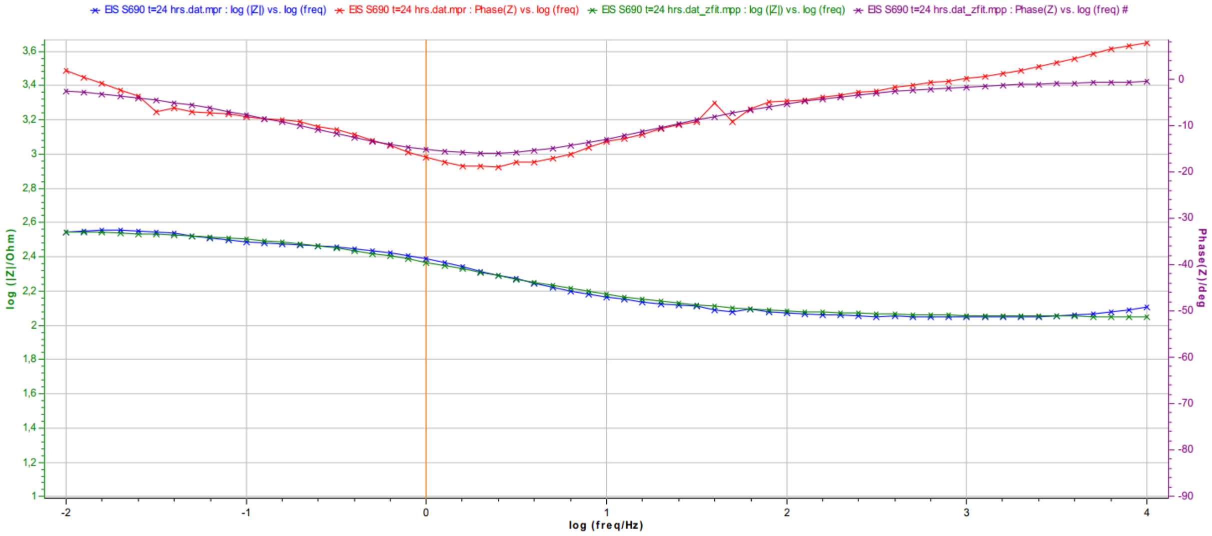

Fig.[12.82] Bode plots for the 2nd series of parent metal **S690**, t=24 hrs.

Blue: experiment data of log(|Z|), **Green:** fitting.

Red: experiment data of θ, **Purple:** Bode fitting.

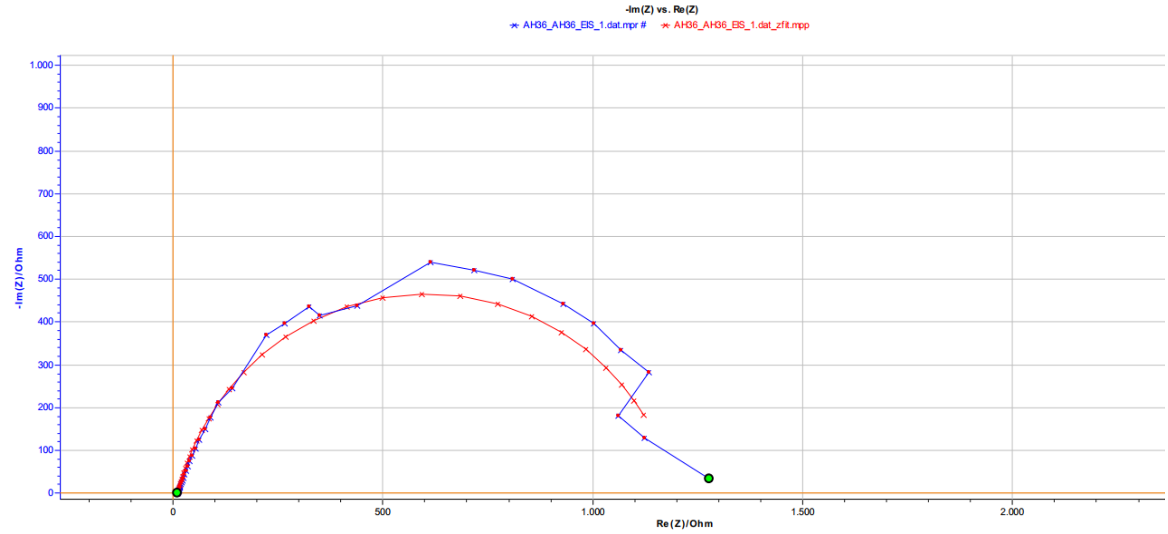

Fig.[12.83] Nyquist plot for homogeneous weldment **AH36-AH36**, exp.1.
Blue: data experiment, **Red:** Nyquist fitting.

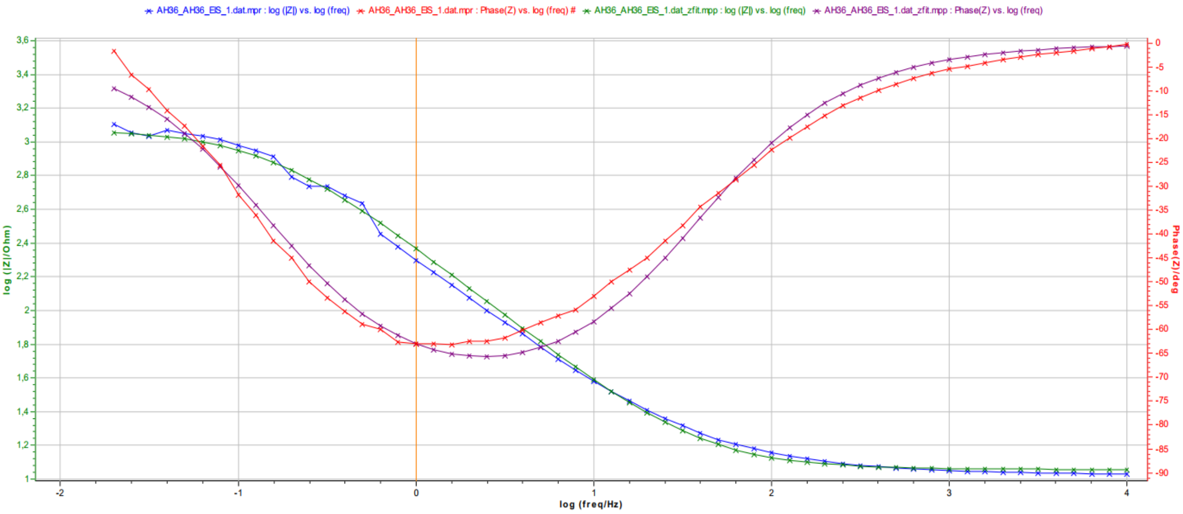

Fig.[12.84] Bode plots for homogeneous weldment **AH36-AH36**, exp. 1.

Blue: experiment data of log(|Z|), **Green:** fitting.

Red: experiment data of θ, **Purple:** Bode fitting.

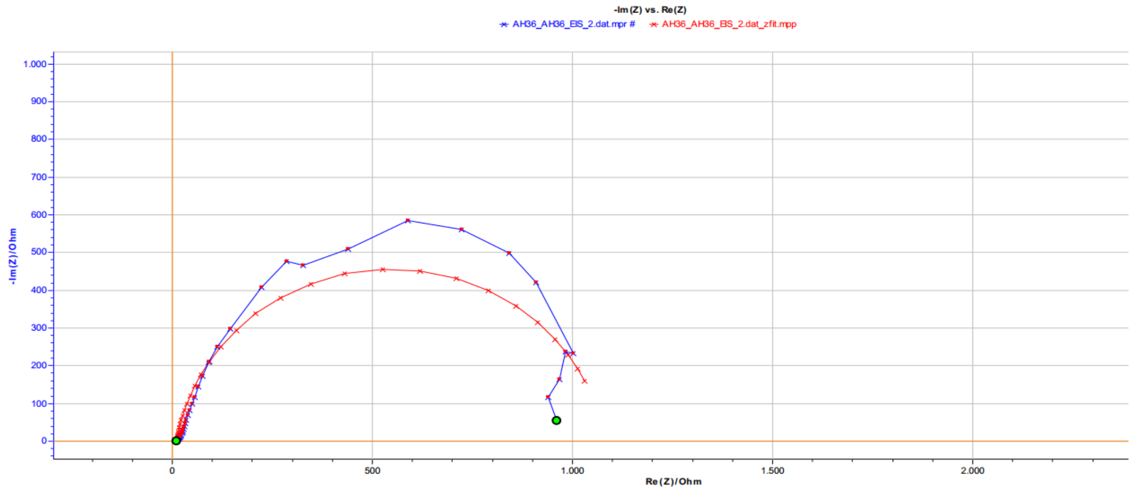

Fig.[12.85] Nyquist plot for homogeneous weldment **AH36-AH36**, exp.2.
Blue: data experiment, **Red:** Nyquist fitting.

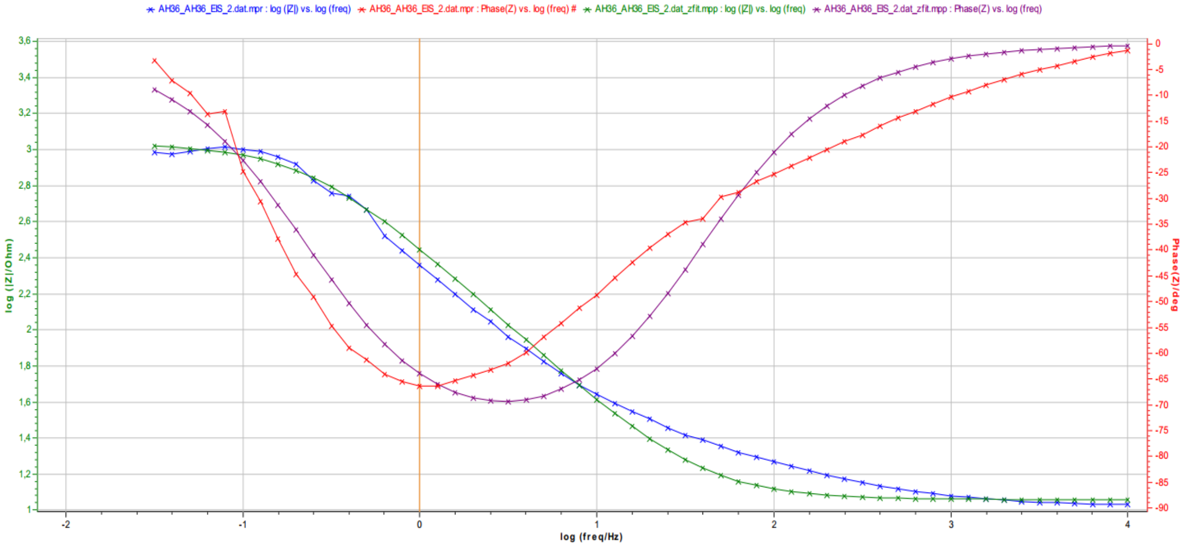

Fig.[12.86] Bode plots for homogeneous weldment **AH36-AH36**, exp. 2.

Blue: experiment data of log(|Z|), **Green:** fitting.

Red: experiment data of θ, **Purple:** Bode fitting.

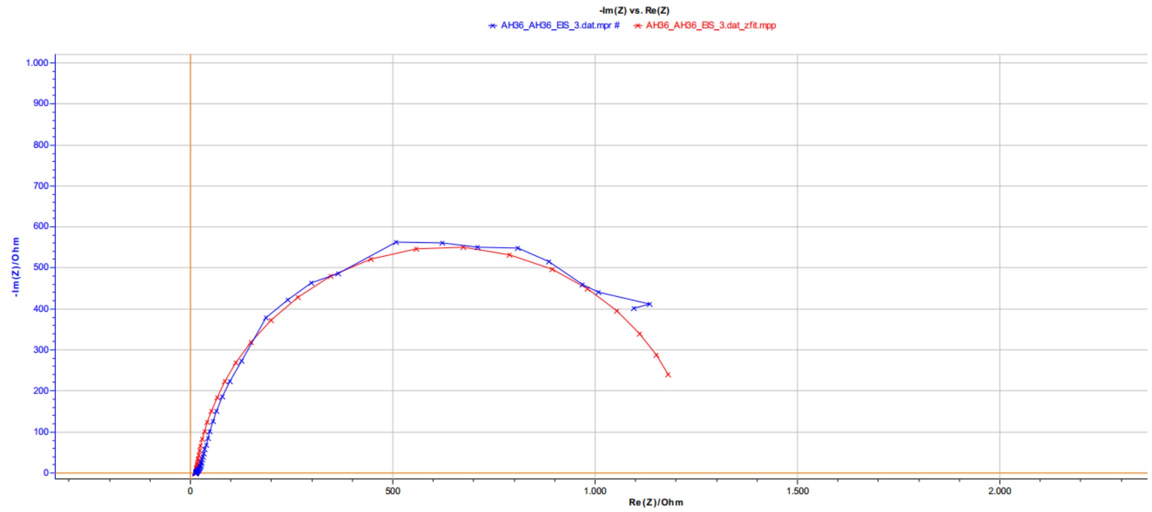

Fig.[12.87] Nyquist plot for homogeneous weldment **AH36-AH36**, exp.3.
Blue: data experiment, **Red:** Nyquist fitting.

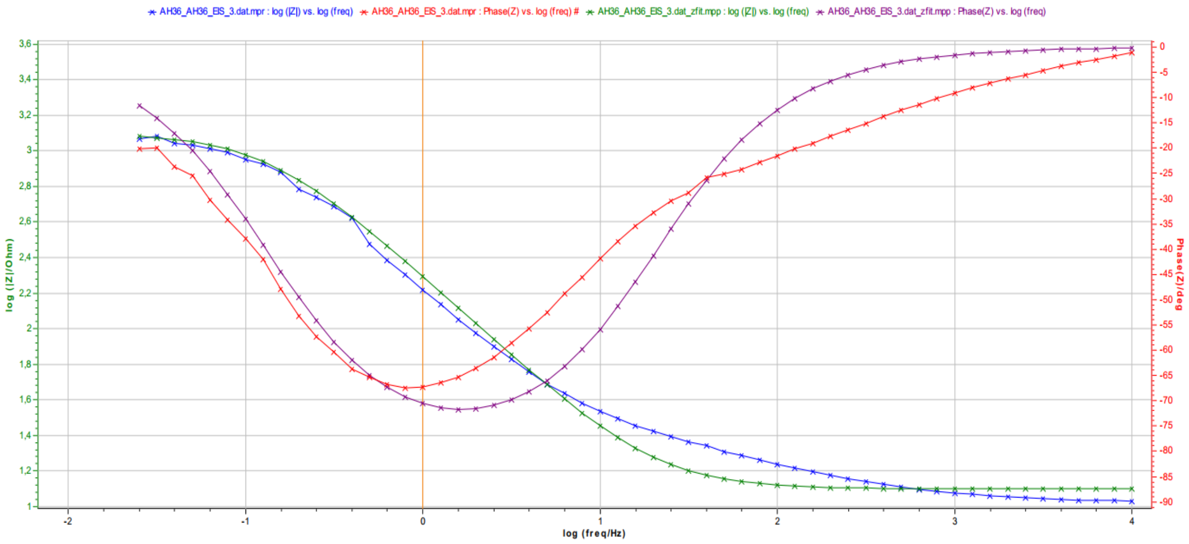

Fig.[12.88] Bode plots for homogeneous weldment **AH36-AH36**, exp. 3.

Blue: experiment data of log(|Z|), **Green:** fitting.

Red: experiment data of θ, **Purple:** Bode fitting.

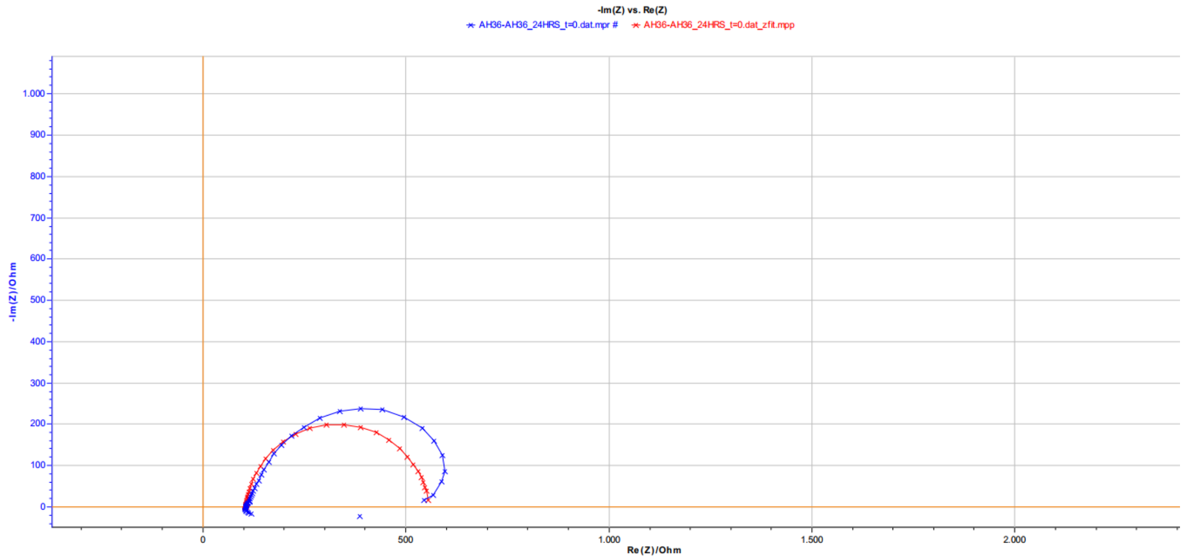

Fig.[12.89] Nyquist plot for the 2nd series of homogeneous weld of **AH36-AH36**, t=0. **Blue:** data experiment, **Red:** Nyquist fitting.

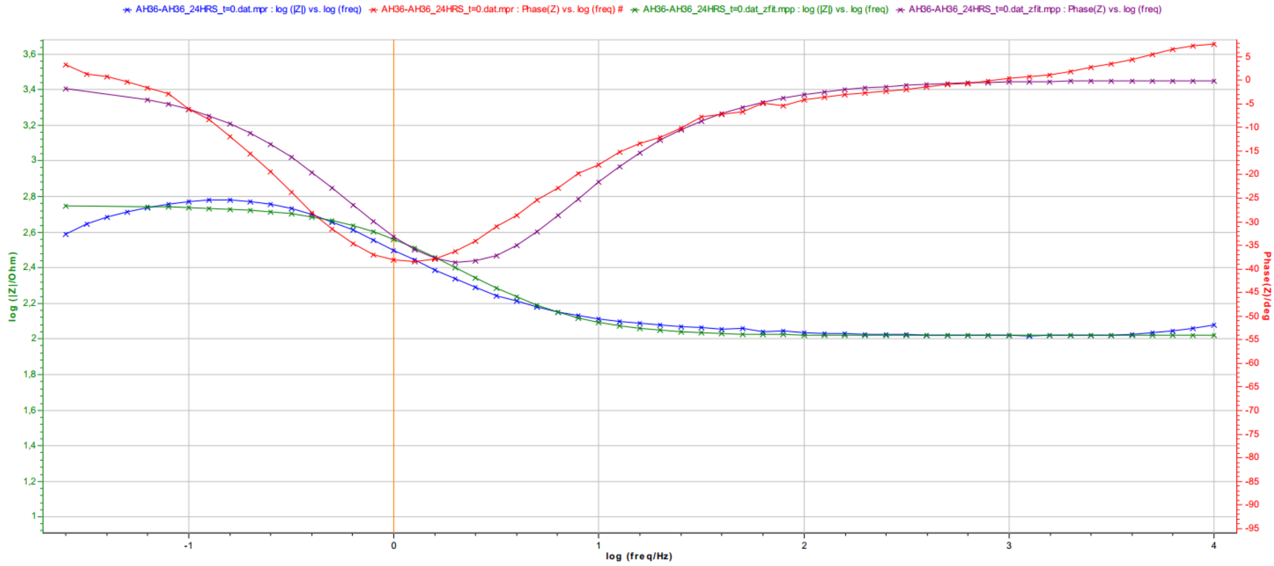

Fig.[12.90] Bode plots for the 2nd series of homogeneous weldment of **AH36-AH36**, t=0 hrs.

Blue: experiment data of log(|Z|), **Green:** fitting.

Red: experiment data of θ, **Purple:** Bode fitting.

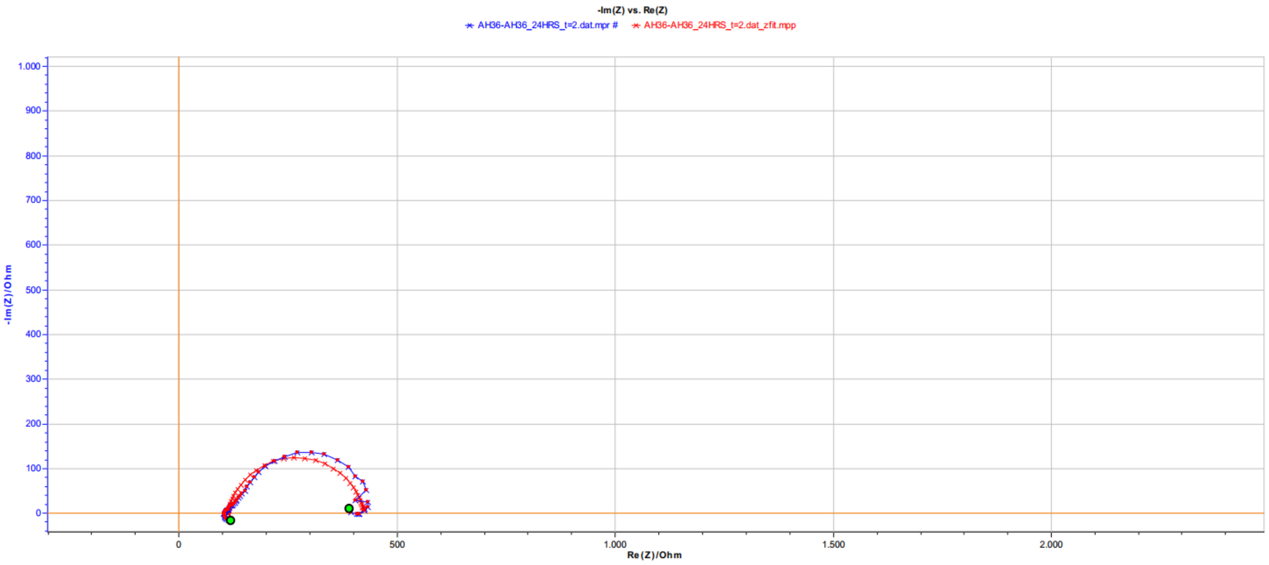

Fig.[12.91] Nyquist plot for the 2nd series of homogeneous weld of **AH36-AH36**, t=2 hrs.

Blue: data experiment, **Red:** Nyquist fitting.

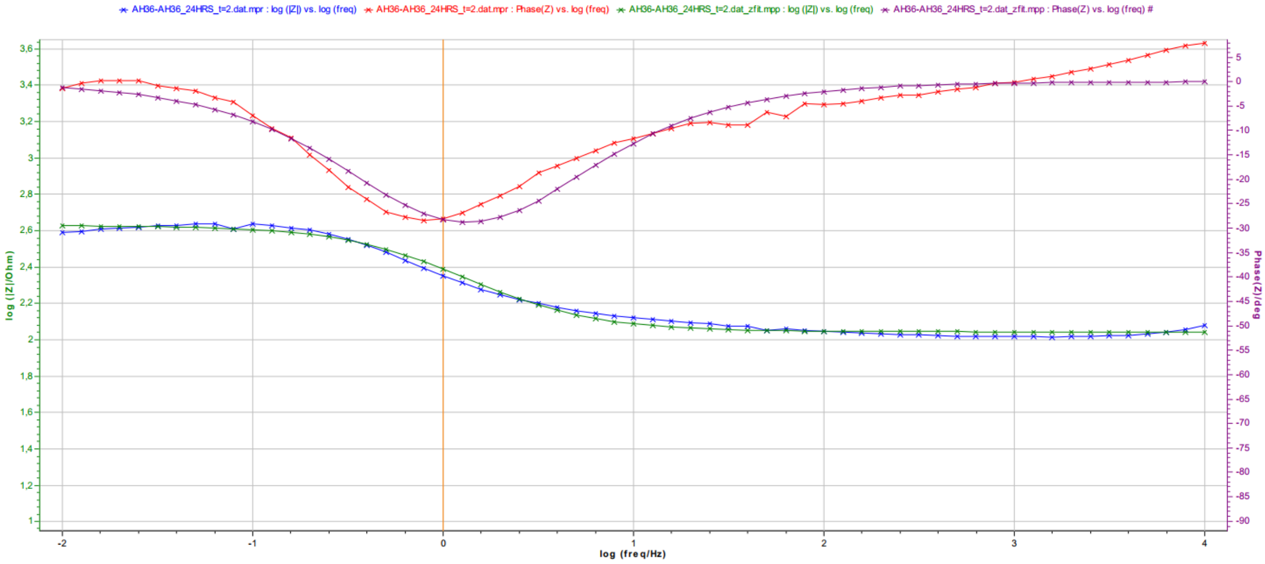

Fig.[12.92] Bode plots for the 2nd series of homogeneous weldment of **AH36-AH36**, t=2 hrs.

Blue: experiment data of log(|Z|), **Green:** fitting.

Red: experiment data of θ, **Purple:** Bode fitting.

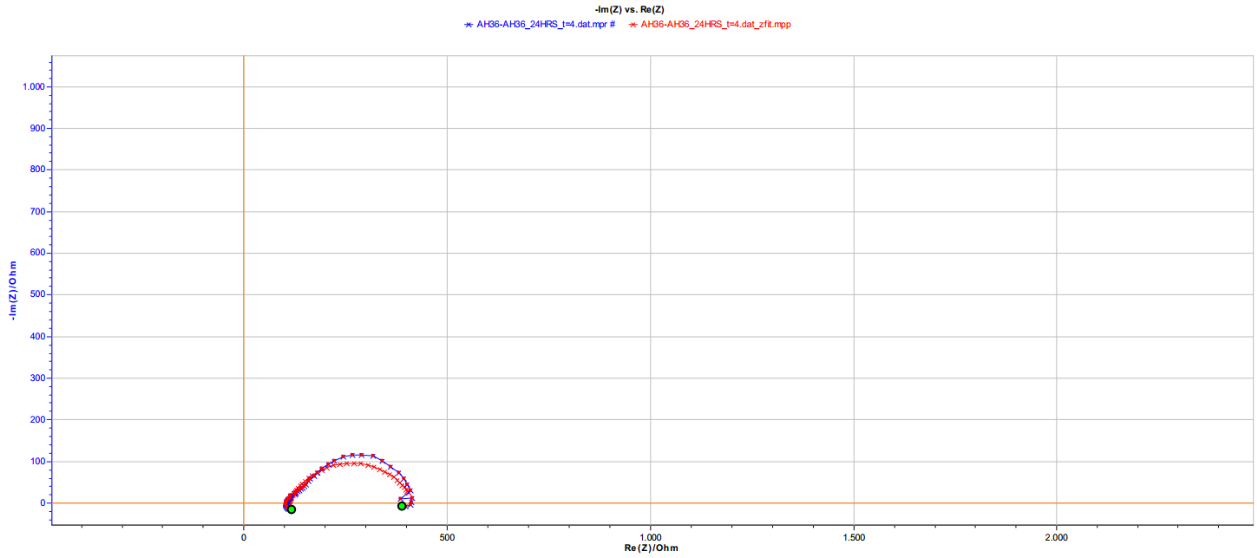

Fig.[12.93] Nyquist plot for the 2nd series of homogeneous weld of **AH36-AH36**, t=4 hrs.
Blue: data experiment, **Red:** Nyquist fitting.

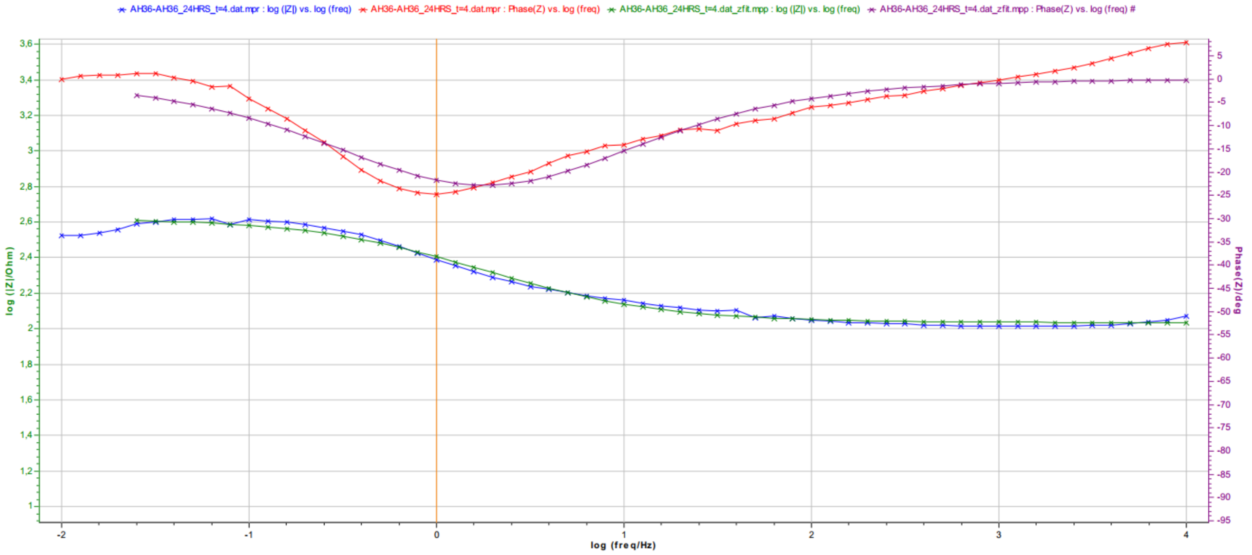

Fig.[12.94] Bode plots for the 2nd series of homogeneous weldment of **AH36-AH36**, t=4 hrs.

Blue: experiment data of log(|Z|), **Green:** fitting.

Red: experiment data of θ, **Purple:** Bode fitting.

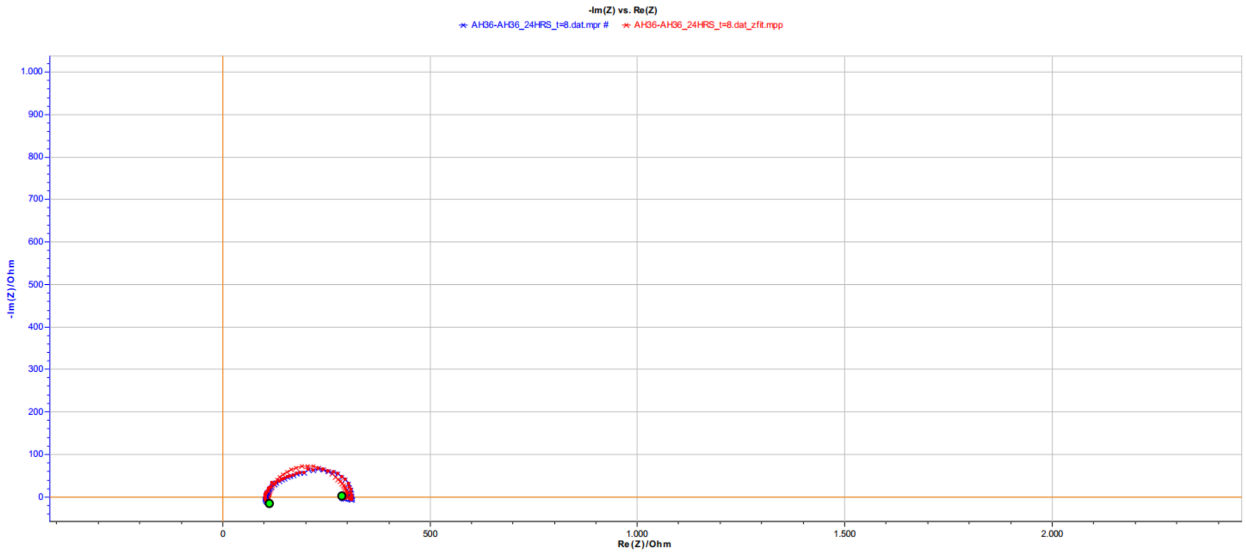

Fig.[12.95] Nyquist plot for the 2nd series of homogeneous weld of **AH36-AH36**, t=8 hrs. **Blue:** data experiment, **Red:** Nyquist fitting.

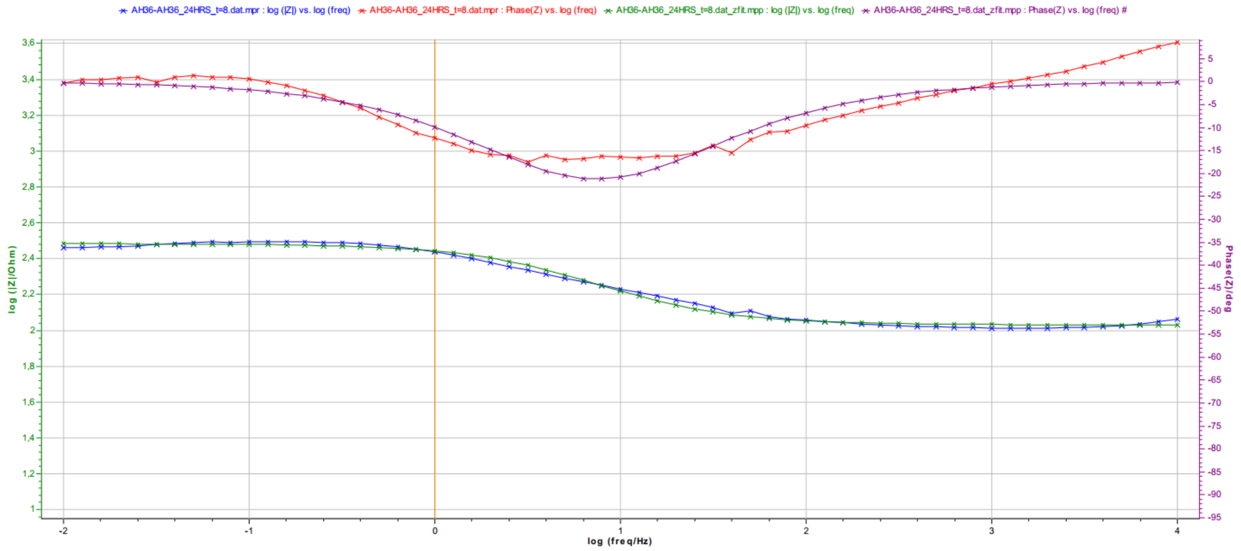

Fig.[12.96] Bode plots for the 2nd series of homogeneous weldment of **AH36-AH36**, t=8 hrs.

Blue: experiment data of log(|Z|), **Green:** fitting.

Red: experiment data of θ, **Purple:** Bode fitting.

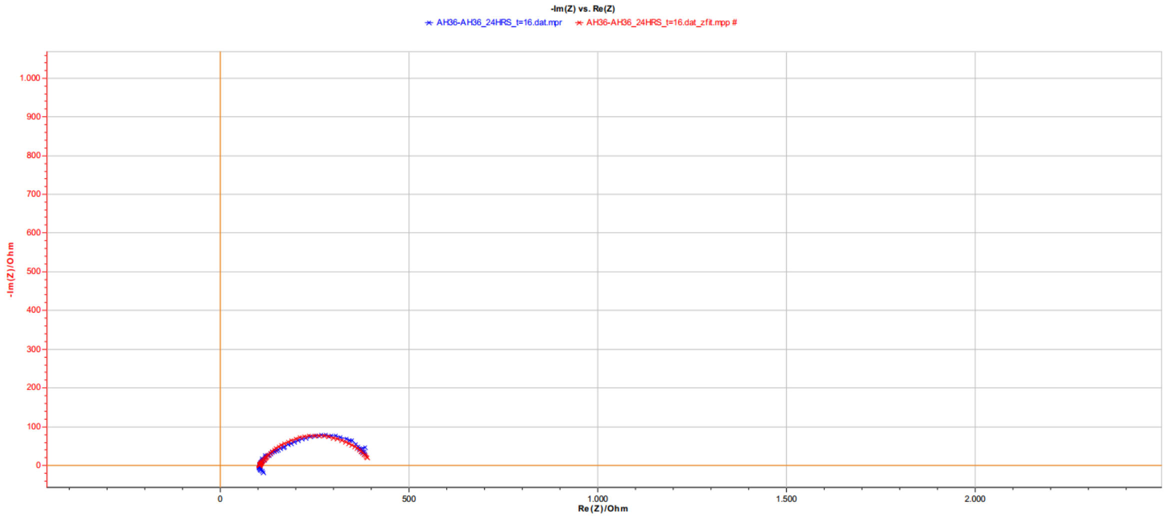

Fig.[12.97] Nyquist plot for the 2nd series of homogeneous weld of **AH36-AH36**, t=16 hrs. **Blue:** data experiment, **Red:** Nyquist fitting.

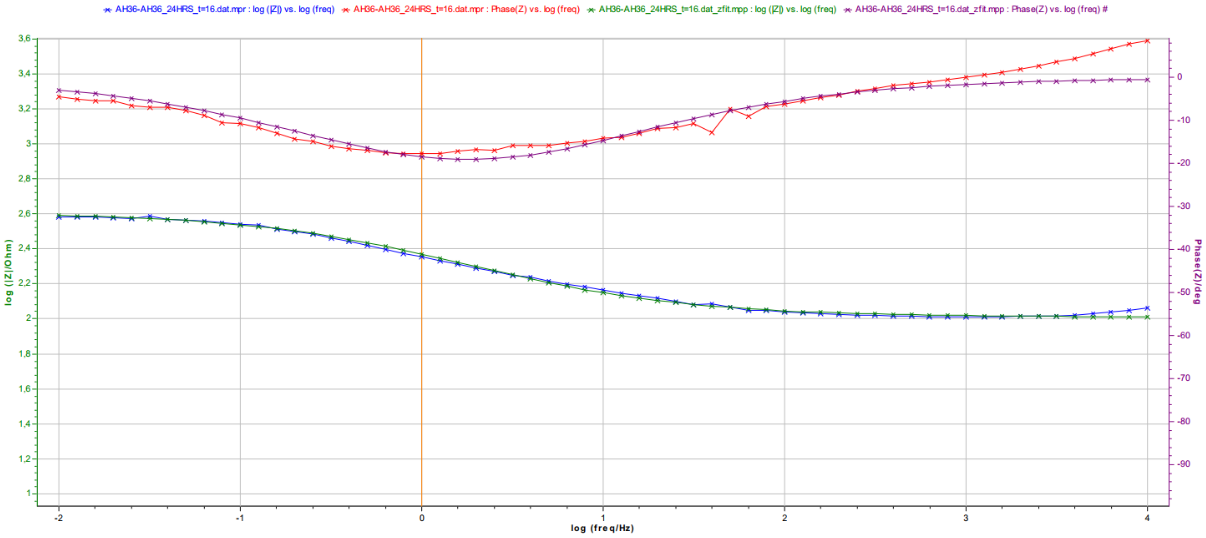

Fig.[12.98] Bode plots for the 2nd series of homogeneous weldment of **AH36-AH36**, t=16 hrs.

Blue: experiment data of log(|Z|), **Green:** fitting.

Red: experiment data of θ, **Purple:** Bode fitting.

`

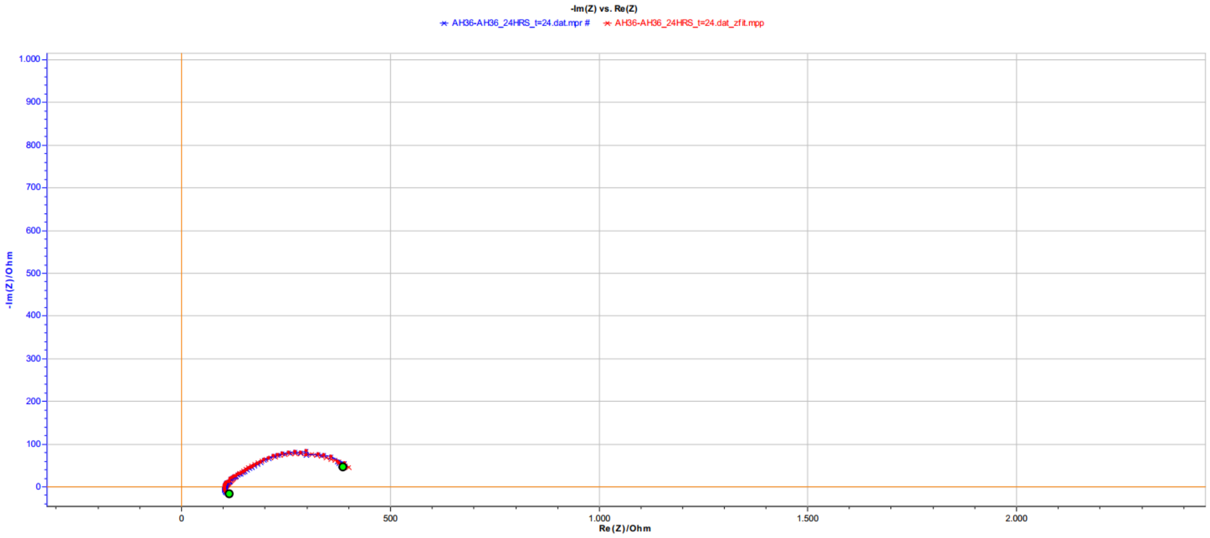

Fig.[12.99] Nyquist plot for the 2nd series of homogeneous weld of **AH36-AH36**, t=24 hrs. **Blue:** data experiment, **Red:** Nyquist fitting.

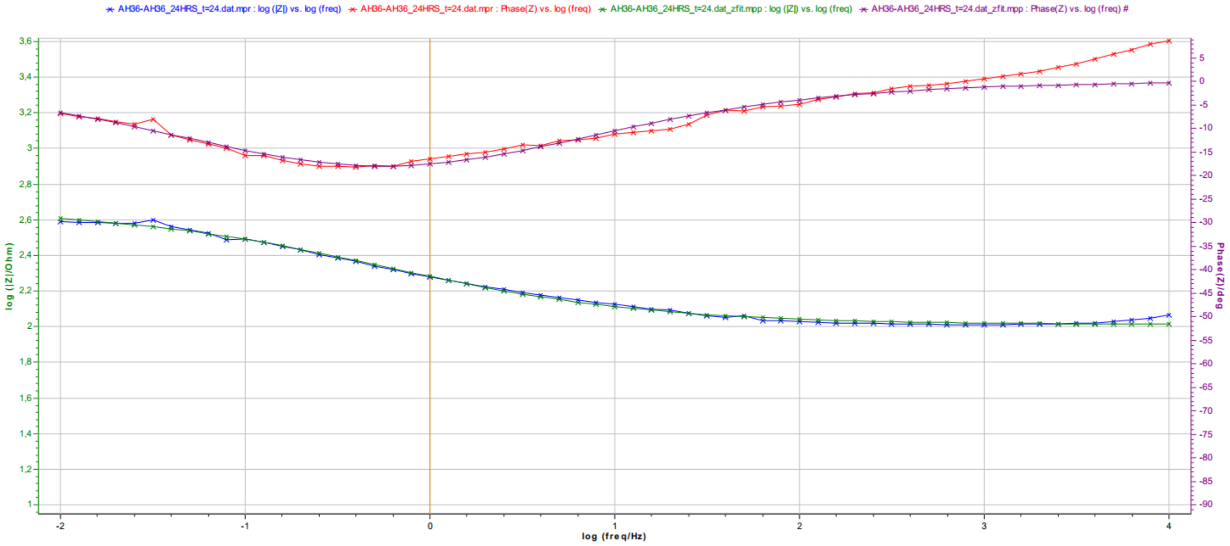

Fig.[12.100]Bode plots for the 2nd series of homogeneous weldment of **AH36-AH36**, t=24hrs.

Blue: experiment data of log(|Z|), **Green:** fitting.

Red: experiment data of θ, **Purple:** Bode fitting.

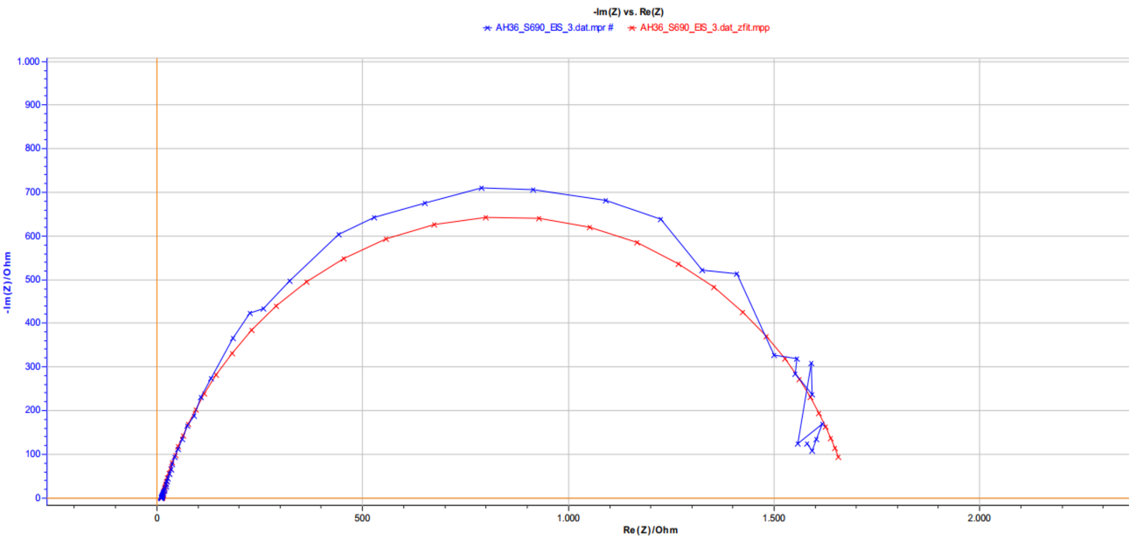

Fig.[12.101] Nyquist plot for heterogeneous weldment **AH36-S690**, exp.1.
Blue: data experiment, **Red:** Nyquist fitting.

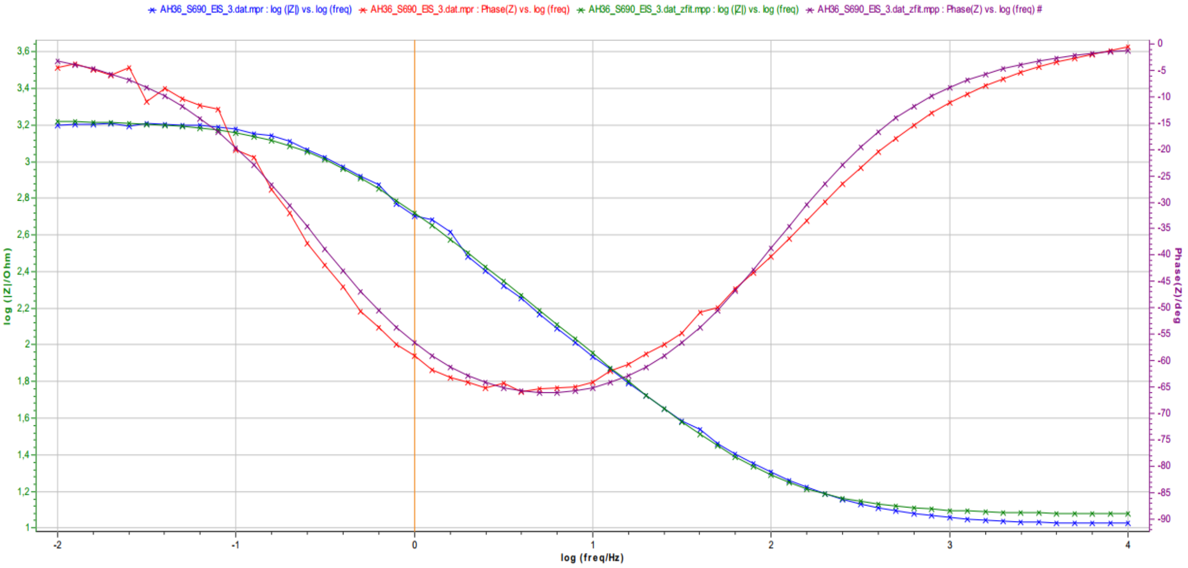

Fig.[12.102] Bode plots for heterogeneous weldment **AH36-S690**, exp. 1.

Blue: experiment data of log(|Z|), **Green:** fitting.

Red: experiment data of θ, **Purple:** Bode fitting.

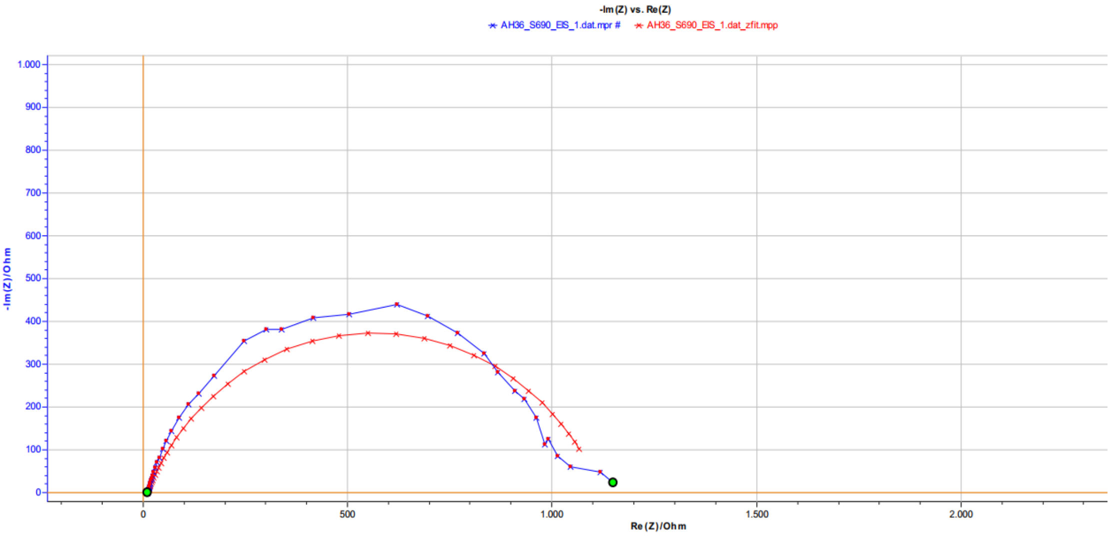

Fig.[12.103] Nyquist plot for heterogeneous weldment **AH36-S690**, exp.2.
Blue: data experiment, **Red:** Nyquist fitting.

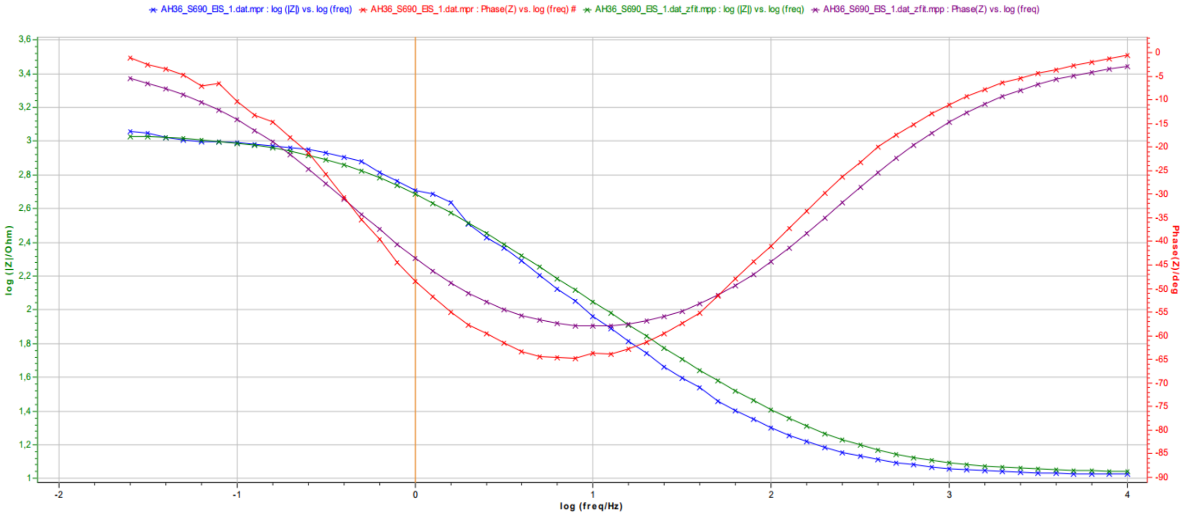

Fig.[12.104] Bode plots for heterogeneous weldment **AH36-S690**, exp. 2.

Blue: experiment data of log(|Z|), **Green:** fitting.

Red: experiment data of θ, **Purple:** Bode fitting.

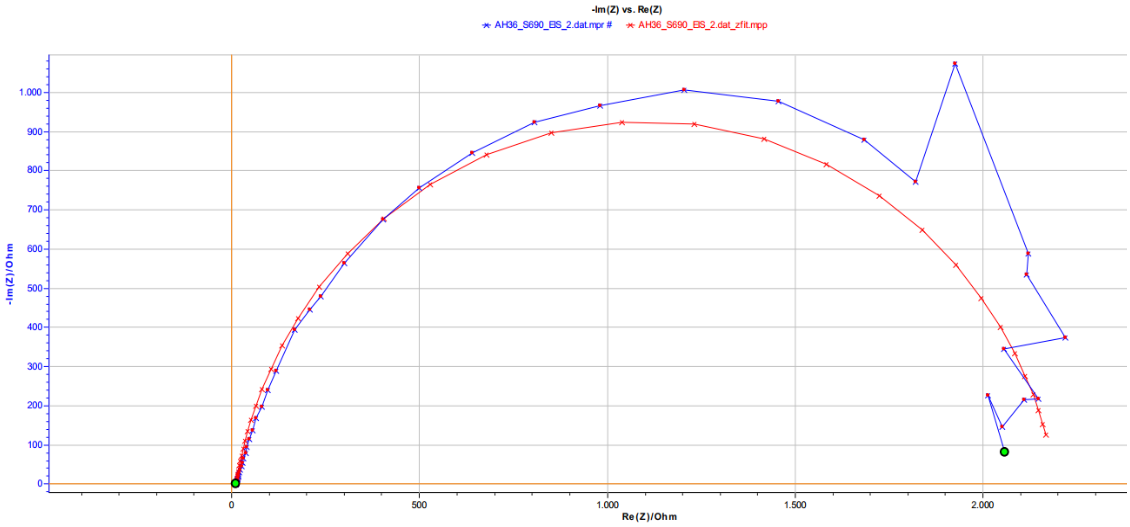

Fig.[12.105] Nyquist plot for heterogeneous weldment **AH36-S690**, exp.3.
Blue: data experiment, **Red:** Nyquist fitting.

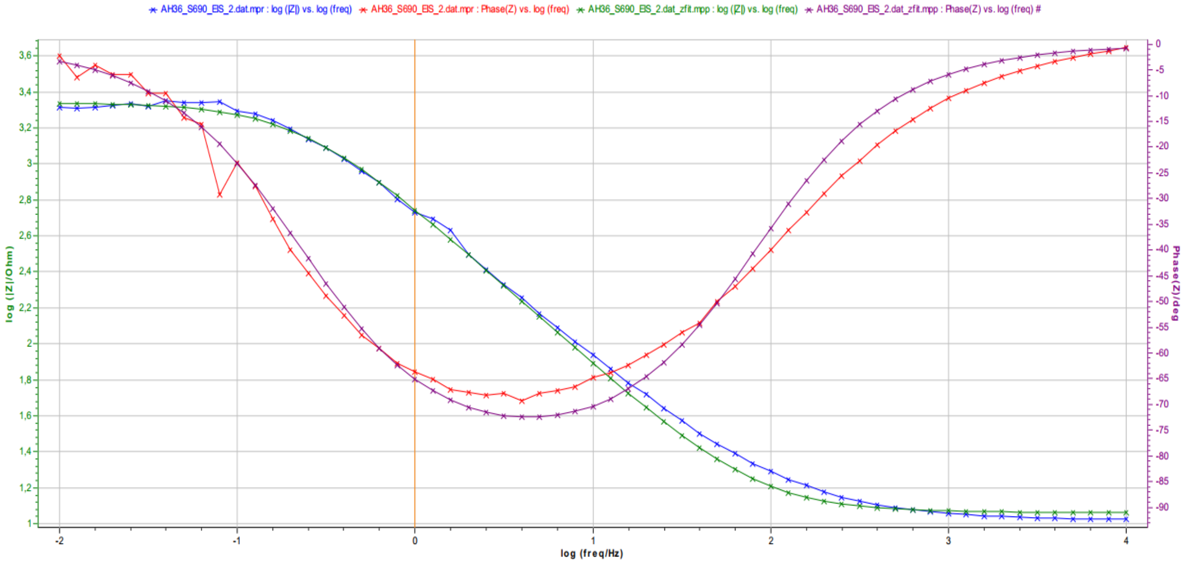

Fig.[12.106] Bode plots for heterogeneous weldment **AH36-S690**, exp. 3.

Blue: experiment data of log(|Z|), **Green:** fitting.

Red: experiment data of θ, **Purple:** Bode fitting.

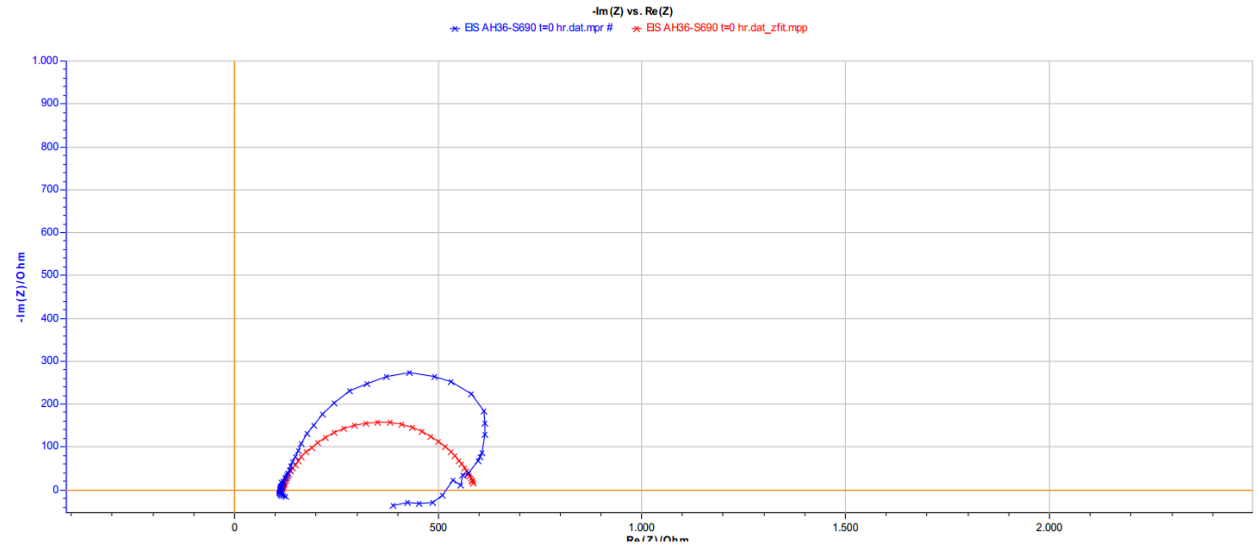

Fig.[12.107] Nyquist plot for the 2nd series of heterogeneous weld of **AH36-S690**, t=0.
Blue: data experiment, **Red:** Nyquist fitting.

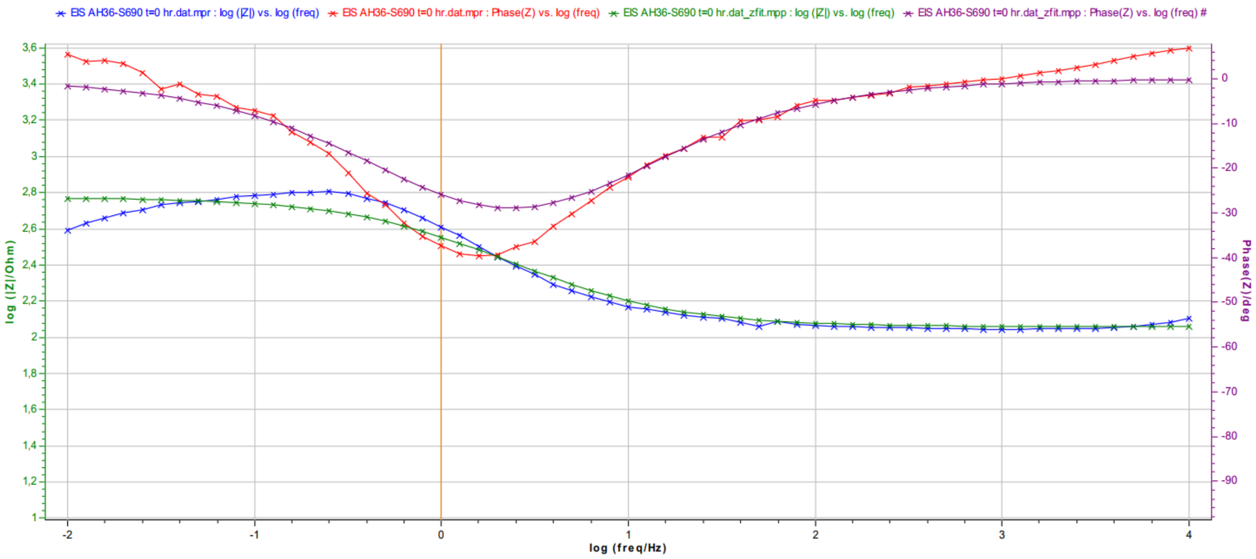

Fig.[12.108] Bode plots for the 2nd series of heterogeneous weldment of **AH36-S690**, t=0.

Blue: experiment data of log(|Z|), **Green:** fitting.

Red: experiment data of θ, **Purple:** Bode fitting.

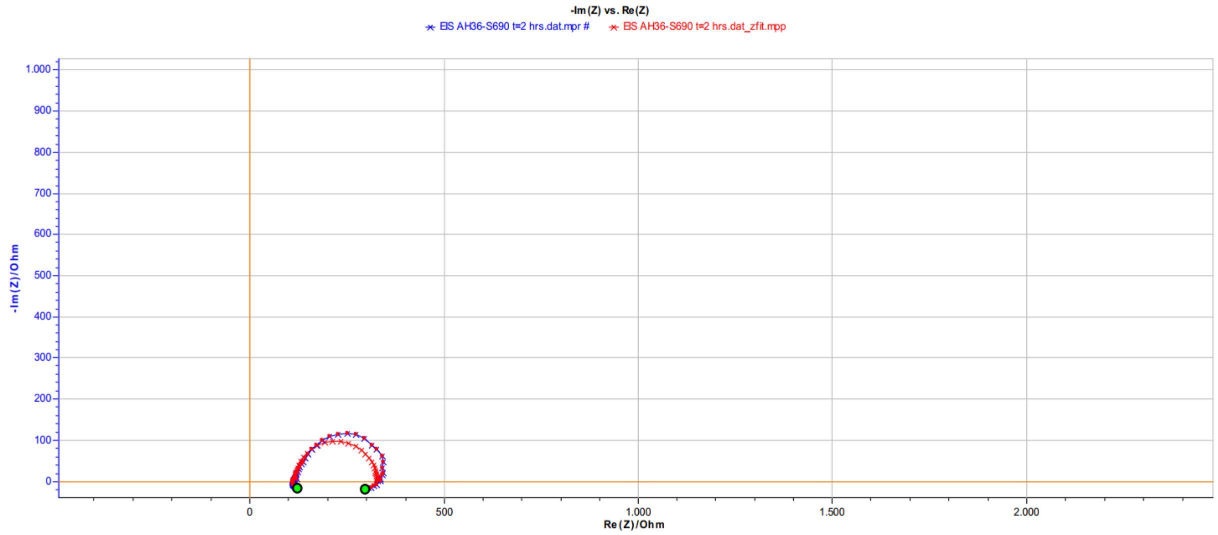

Fig.[12.109] Nyquist plot for the 2nd series of heterogeneous weld of **AH36-S690**, t=2 hrs. **Blue:** data experiment, **Red:** Nyquist fitting.

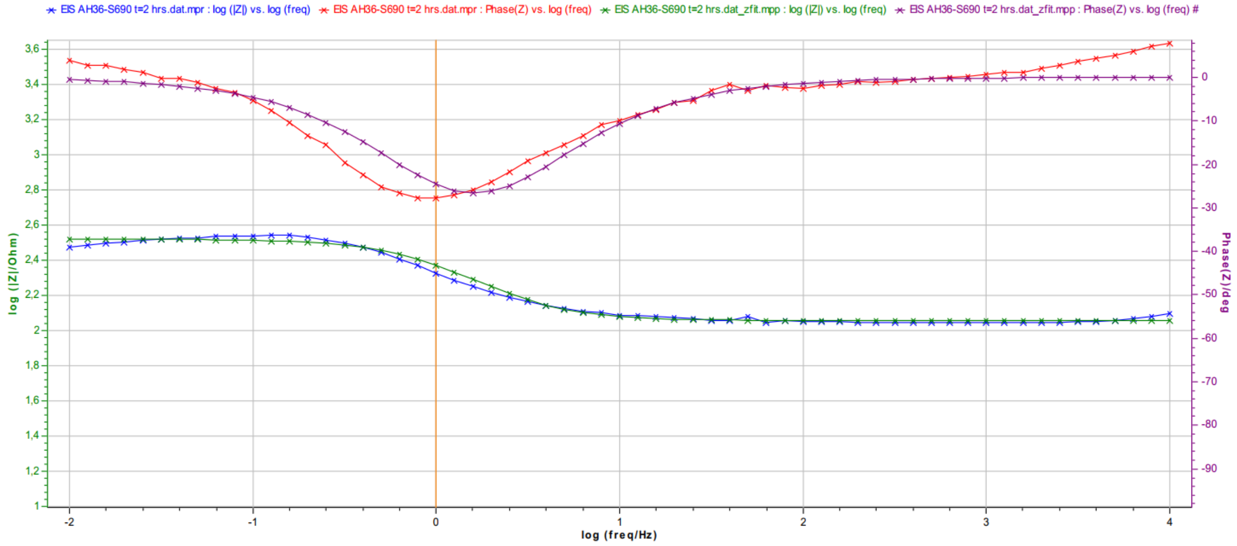

Fig.[12.110]Bode plots for the 2nd series of heterogeneous weldment of **AH36-S690**, t=2 hrs.

Blue: experiment data of log(|Z|), **Green:** fitting.

Red: experiment data of θ, **Purple:** Bode fitting.

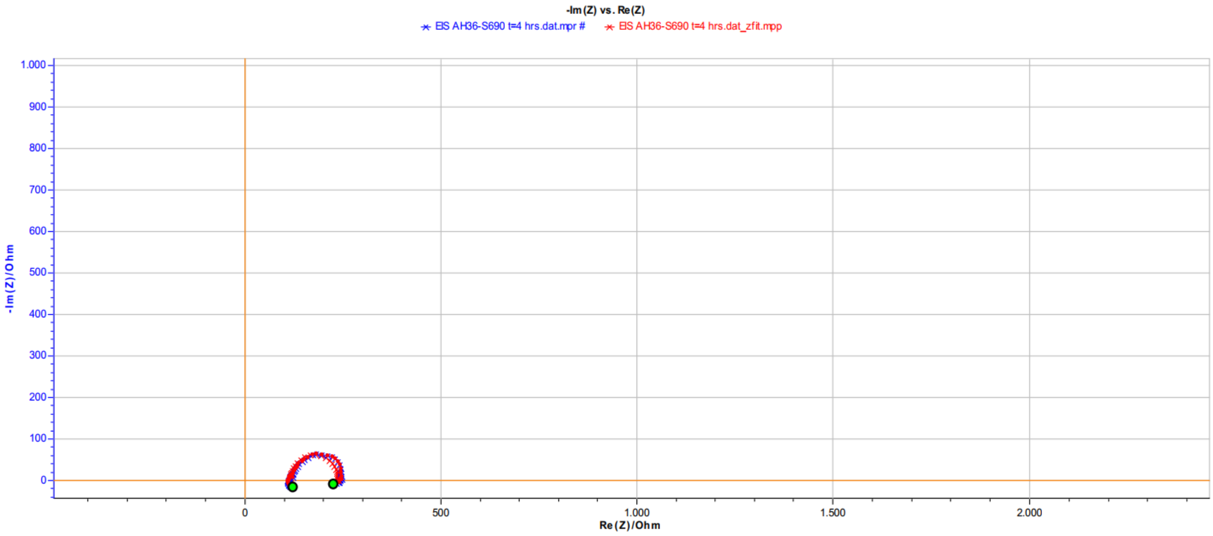

Fig.[12.111] Nyquist plot for the 2nd series of heterogeneous weld of **AH36-S690**, t=4 hrs.
Blue: data experiment, **Red:** Nyquist fitting.

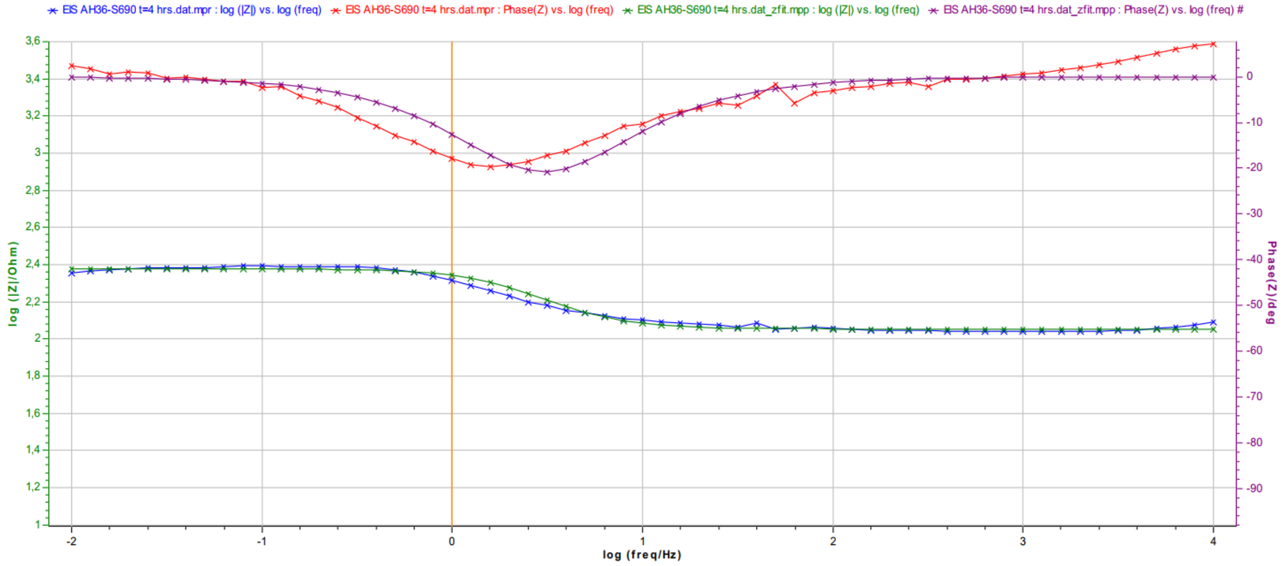

Fig.[12.112] Bode plots for the 2nd series of heterogeneous weldment of **AH36-S690**, t=4 hrs.

Blue: experiment data of log(|Z|), **Green:** fitting.

Red: experiment data of θ, **Purple:** Bode fitting.

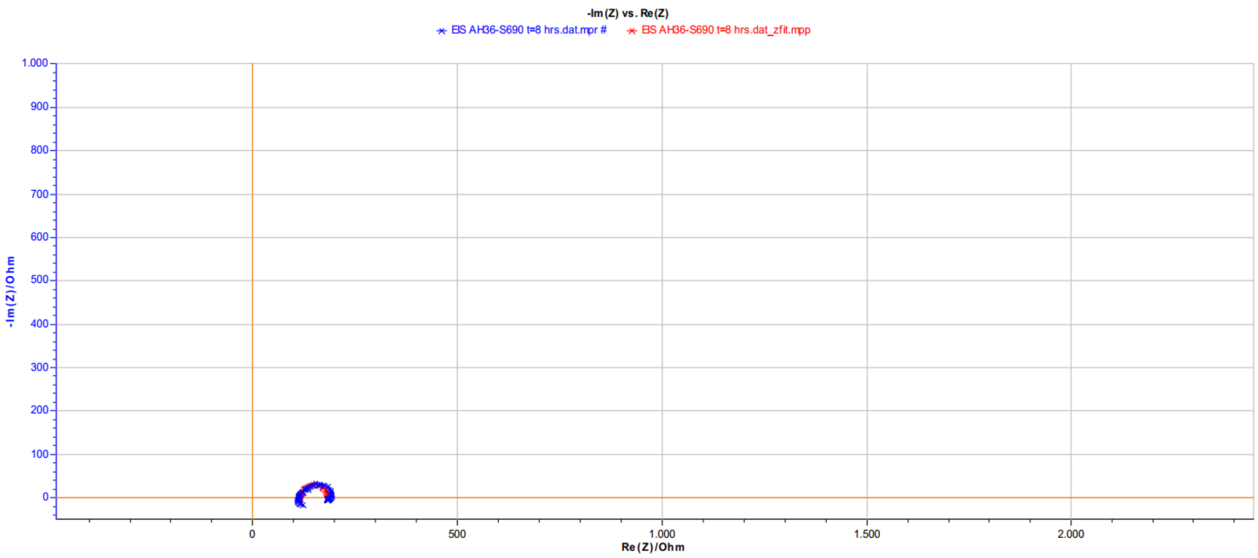

Fig.[12.113] Nyquist plot for the 2nd series of heterogeneous weld of **AH36-S690**, t=8 hrs. **Blue:** data experiment, **Red:** Nyquist fitting.

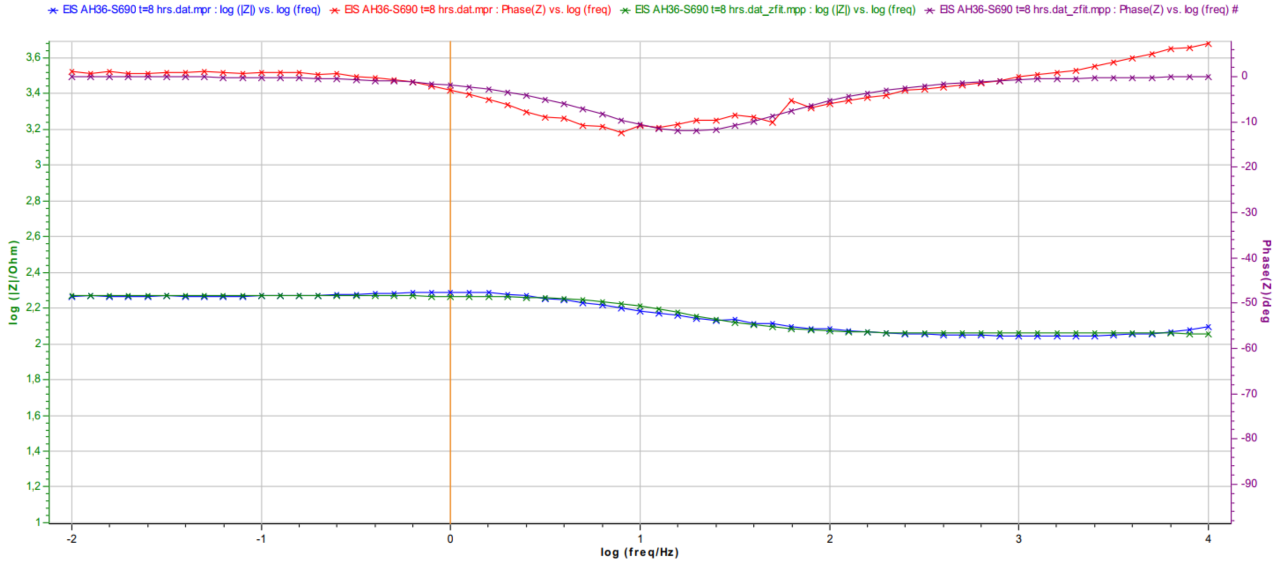

Fig.[12.114] Bode plots for the 2nd series of heterogeneous weldment of **AH36-S690**, t=8 hrs.

Blue: experiment data of log(|Z|), **Green:** fitting.

Red: experiment data of θ, **Purple:** Bode fitting.

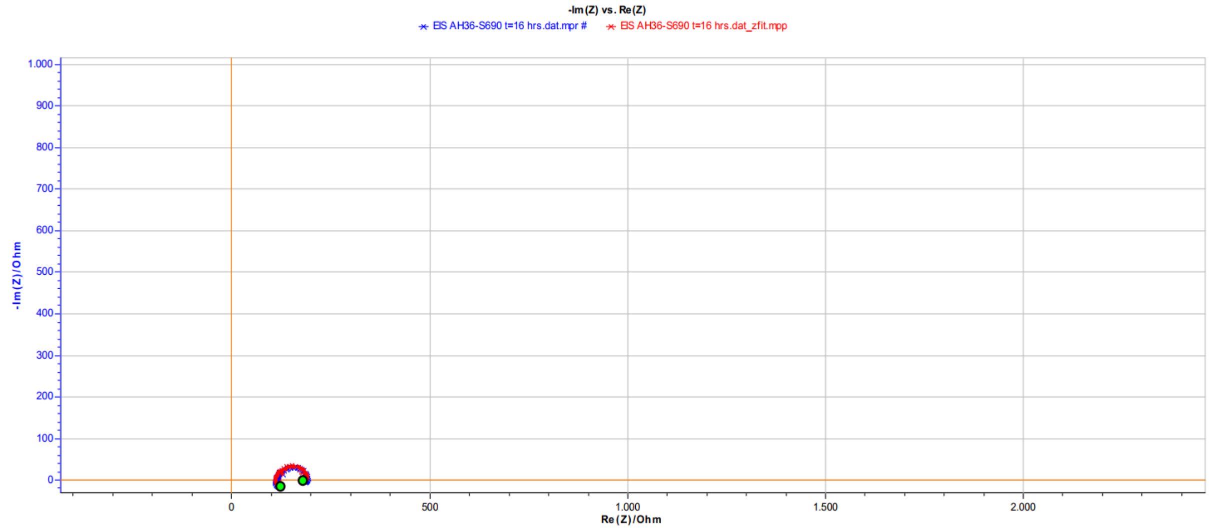

Fig.[12.115] Nyquist plot for the 2nd series of heterogeneous weld of **AH36-S690**, t=16 hrs. **Blue:** data experiment, **Red:** Nyquist fitting.

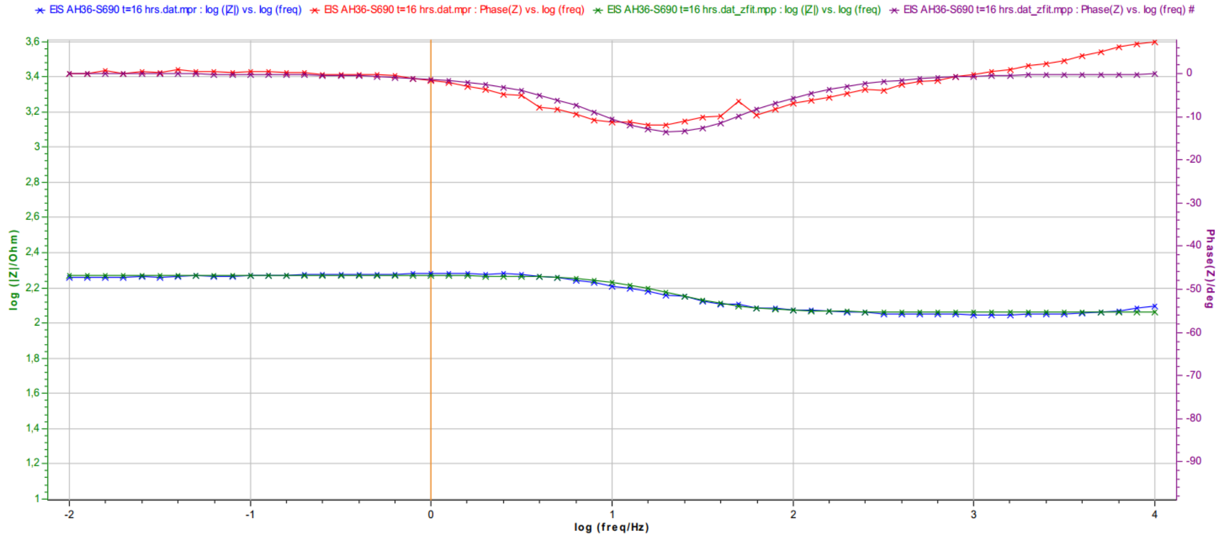

Fig.[12.116] Bode plots for the 2nd series of heterogeneous weldment of **AH36-S690**, t=16hrs.

Blue: experiment data of log(|Z|), **Green:** fitting.

Red: experiment data of θ, **Purple:** Bode fitting.

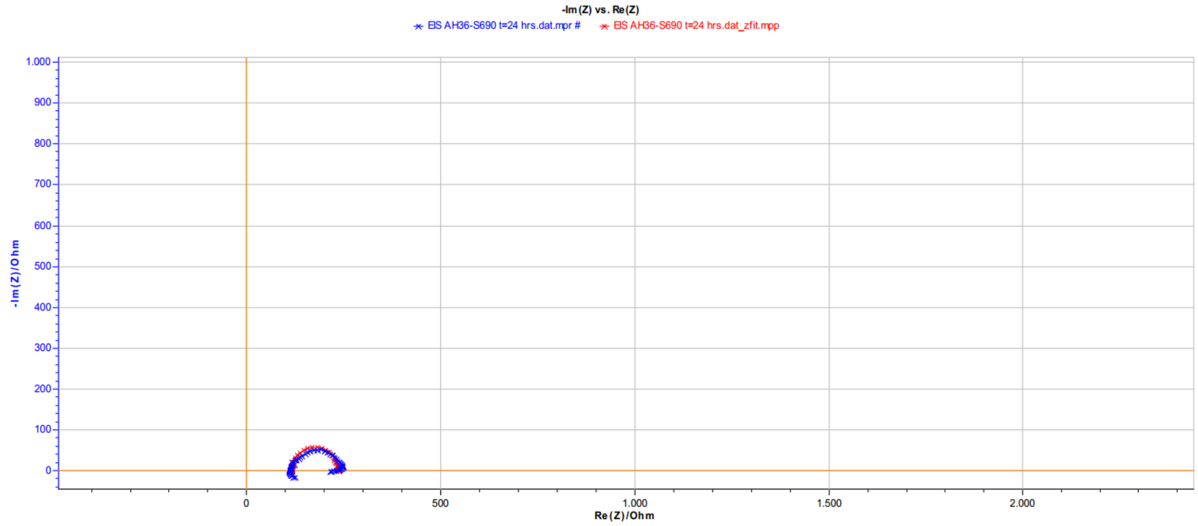

Fig.[12.117] Nyquist plot for the 2nd series of heterogeneous weld of **AH36-S690**, t=24 hrs. **Blue:** data experiment, **Red:** Nyquist fitting.

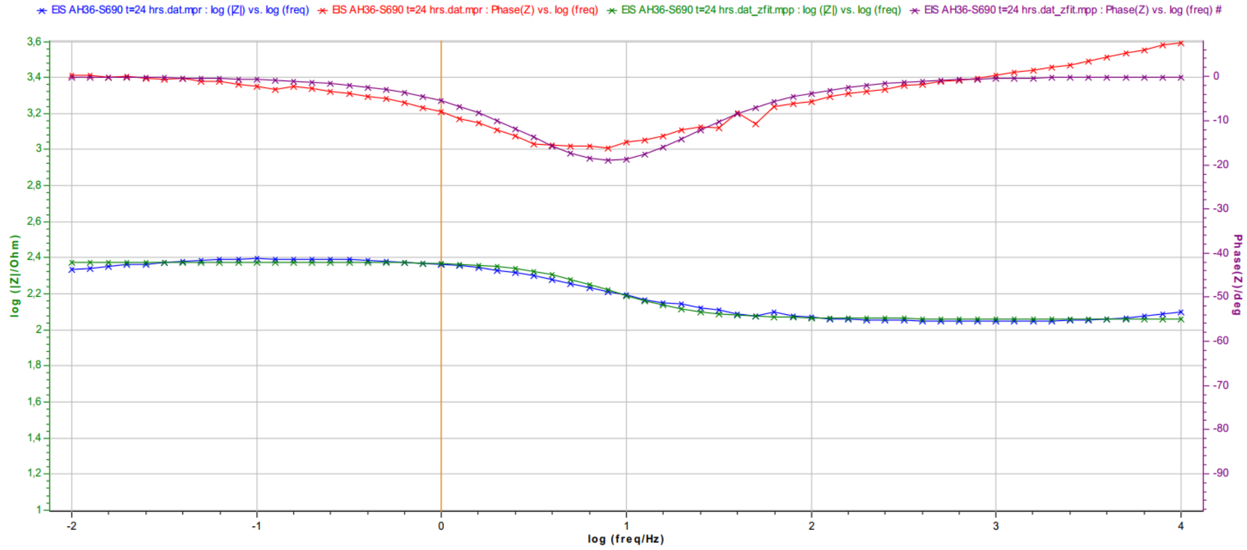

Fig.[12.118] Bode plots for the 2nd series of heterogeneous weldment of **AH36-S690**, t=24hrs.

Blue: experiment data of log(|Z|), **Green:** fitting.

Red: experiment data of θ, **Purple:** Bode fitting.